UNIVERSITÀ DELLA CALABRIA

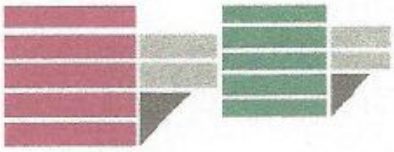

Dipartimento di Fisica

Doctorate School of Science and Technique
"Bernardino Telesio"

A thesis submitted for the degree of Doctor of Philosophy
in
Science and Technology of Mesophases and Molecular Materials

XXVI Cycle
FIS/07-02/B3

Absorptive Losses Mitigation in Gain-Plasmon Hybrid Systems as Optical Metamaterials

School Director
Prof. Roberto Bartolino

Curriculum Coordinator
Prof. Carlo C Versace

Supervisor
Prof. Giuseppe Strangi

Candidate
Alireza Rahimi Rashed

December 2013

To my Parents,

without them, life is meaningless.

Gözəl Ana və Atam üçün,

onlarsız yaşayış mənasızdır.

Acknowledgements

First of all, I would always be thankful to my supervisor Professor Giuseppe Strangi for providing the opportunity to involve in this inspiring research field in University of Calabria. His constant encouragement and support throughout my PhD helped me to pave confidence in this research study. In particular, his perfect comments and corrections regarding writing this thesis were really effective and appreciable.

I would also like to express my special gratitude towards Dr. Antonio De Luca whom I have learned so many valuable experimental and analytical points during my PhD in these three years. His warm hospitality and perfect helps in daily life has given me wonderful moments in Cosenza. I acknowledge Prof. Roberto Bartolino, Prof. Carlo Versace and Prof. Nicola Scaramuzza who never left me alone to deal with educational and personal life difficulties in whole days of my PhD.

I would like to thank my friends (in fact my brothers) Arash Hosseinzadeh and Rakesh Dhama who have offered me valuable helps and comments to write and complete this thesis.

I would like to thank Dr. Melissa Infusino, Dr. Roberto Caputo, Dr. Luciano De Sio, Dr. Riccardo Massareli and Dr. Allesandro Veltri. They helped me to have pleasant moments in working and daily life in University of Calabria.

I expand my gratitude to Dr. Massimo La Deda for his helps and efforts to get time-resolved spectroscopy results. I express my thanks Dr. Loredana Ricciadi and Dnyaneshwar Raut for their great helps regarding writing my thesis. I also would like to acknowledge Prof. Matteo Albani and Dr. Andrea Vallecchi for their warm hospitality and perfect training during two weeks in University of Siena.

I would like to thank all my friends and colleagues, in particular Caterina whose their presence always cheered me up and helped me to experience nice working moments. I really thank my best friends Massimiliano and Serafino which never have left me alone in my room to bore even during rainy and cold weekends of Cosenza.

I would like to appreciate kind Centro Residenziale staff who offered me good accommodation and food during these three years.

I hug my parents, my kind sister Mina and my brothers for their great help and support. They were always beside me in every moment of my life, in particular during these three years, out of home in Italy.

In the end, I am thankful to my god who has provided me this opportunity to experience new life and know new friends during these three years of my stay in Italy.

Table of Contents

Chapter 3: Overview on Fluorescence Spectroscopy

Chapter 4: Energy Transfer Processes in Hybrid Systems

Chapter 5: Experimental Instruments and Setups

Chapter 6: Experimental Instruments and Setups

Chapter 7: Optical Loss Mitigation in Meso-scaled Hybrid Systems

Chapter 8: Optical Loss Mitigation in Macro-scaled Hybrid Systems

Abstract

In the past decade, plasmonic nanoparticles (NPs) have gained a lot of interest due to their exceptional and fascinating properties which have been accomplishing vital role in emerging science and technology towards multifunctional applications. The extensive current research efforts in nanoplasmonics trigger towards various opto-electronic and medical applications such as invisibility, perfect lens, increasing the efficiency of solar cells, designing and extra-sensitive single-particle detection of biomolecular recognition and in particular optical metamaterials. The negative real part and the low value of the imaginary part of dielectric permittivity are crucial for applications of nanoparticles as subunits of optical metamaterials. However, the performance of plasmonic nanostructures is significantly limited by the intrinsic and strong energy dissipation in metals, especially in the visible range. In fact, regardless of the challenges to synthesize plasmonic nanostructures, the path to use them as building blocks of optical metamaterial is crossing through the finding a solution to mitigate their optical losses.

In this research thesis, it is demonstrated experimentally that the incorporation of gain material such as organic dye molecules and quantum dots in close proximity of enhanced local fields of various properly designed plasmonic systems makes it possible to induce resonant energy transfer processes from gain units to plasmonic nanoparticles, to accompanish loss compensation in optical metamaterials. Steady-state experiments and time resolved spectroscopy along with modification of Rayleigh scattering and optical transmission of a probe beam as a function of impinging energy are crucial evidences of mitigation of absorptive losses in different gain doped plasmonic systems.

The strategy that has been followed here towards mitigation of absorptive losses in optical metamaterials acts at different spatial scales from nano to macro (see Figure 1). The systems at nano-scale (10-100 nm) are based on dispersion of NPs, in particular, gain assisted (nanoparticle-dye dispersion), gain-functionalized core-shell gold NPs (encapsulated dye molecules into the shell) and dye grafted gold core multimeric nanostructures. The study of such nano-composites allows to recognize experimentally how the parameters such as the geometry and size of the metal nanostructures, inter-particle distance, overlap between emission spectrum of gain material and plasmon band of metal NPs, concentration and quantum yield of donor molecules are playing an important role to create more efficient nonradiative RET processes from donor molecules to acceptors.

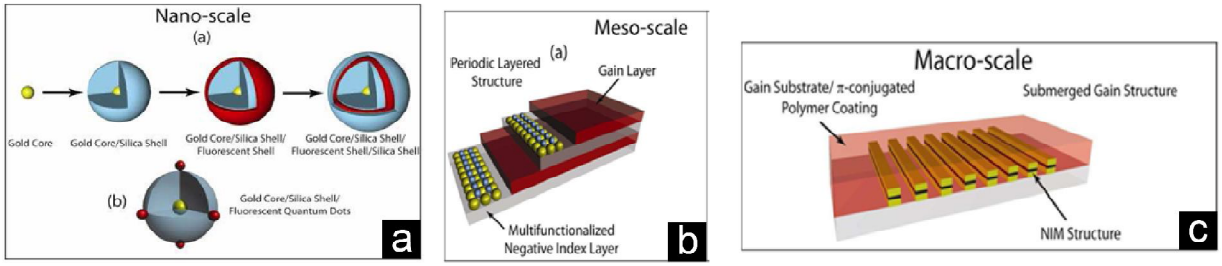

Figure 1 The followed spatial stages on this research study ranged from **(a)** nano-scale and **(b)** mesco scale towards **(c)** macro scale.

The obtained results in nano-scale generate further motivations to move forward to study meso-scale (100-900 nm) plasmonic systems which include both dispersion (nanoshell composites) and bulk (periodic layers of gain materials and lossy metal elements) systems. The nanoshells which are consisted of dye doped dielectric core coated gold shell dispersed in ethanol solution are designed with an optimized ratio of core diameter and metallic shell thickness. The time resolved fluorescence spectroscopy results along with pump-probe experiments on nanoshells are convincing evidences for optical loss mitigation. Finally in third stage, the optical properties of gain-plasmon composites dispersed in PDMS host matrix as an example for bulk samples at the macroscopic scale (1 μm and beyond) have been investigated. The achieved results on this stage can help to design and fabricate such plasmonic structures that lead from fundamental physics towards practical applications.

In this regard, the first four chapters provide the background concerning the main elements of this research work. The first chapter contains an introduction to the metamaterials. Second chapter describes the optical properties of plasmonic nanostructures. In third chapter, gain materials and the optical processes beyond these materials have been investigated. The

fourth chapter deals with the optical properties of hybrid systems consisted of active materials and nano-plasmonic elements. After providing a brief introduction regarding the applied setups and instruments in this research study in chapter five, the last three chapters represent the acquired experimental results in each mentioned spatial scale. In chapter six, the optical properties of nano-scaled gain-plasmon systems in solution including gain-assisted, gain-functionalized and dye grafted multimeric samples are investigated. Chapter seven explores the optical characteristics of dispersion of nanoshell sample as an example of the study in meso-scale. Finally, the thesis is completed with the study of the optical features of macro-scaled bulk samples based on core–shell type quantum dots and gold NPs dispersed in PDMS, and a short conclusion of this research study.

This study emphasizes effective progress in materials science and paves the way towards further promising scientific research aimed to enable the wide range of electromagnetic properties of plasmonic metamaterials.

Chapter 1

Overview on Metamaterials

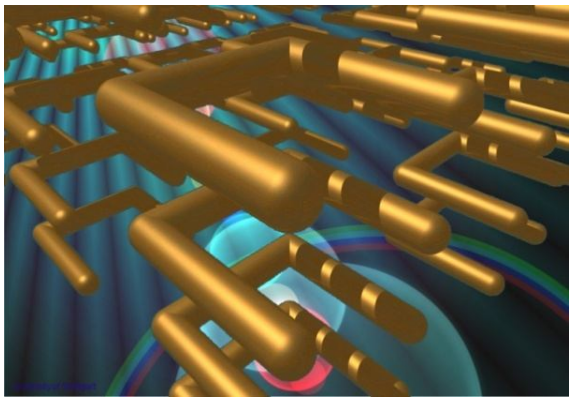

1.1 Introduction

This chapter deals with optical metamaterials, artificially structured materials with sub wavelength inclusions which represent strikingly unconventional properties at optical frequencies. First of all, a short history behind progress on metamaterials from medieval art works until flourishing of optical metamaterials in recent years have been provided. Then after providing a brief explanation for the optical properties of Left Handed Materials (LHM), the importance of low loss metamaterials is highlighted. Finally, this section has been completed by introducing some appropriate structures for fabrication of negative dielectric and magnetic inclusions based on bottom-up approach.

1.2 History of Metamaterials

Almost all electromagnetic phenomena and devices result from interactions between waves and materials. In fact, due to weak interactions of magnetic component of an electromagnetic wave with natural materials, it is the only electric component which plays an

important role to create various important electromagnetic phenomena. Previous theoretical studies suggested that such materials that can couple to both components of incident electromagnetic wave are expected to exhibit some extra-ordinary properties and fascinating applications, but these types of materials cannot be natural.

Thus, investigations to design such kind of artificially composites with novel electromagnetic properties are really motivating. For instance, negative refractive index as one of outstanding features of these materials can provide the ability to produce perfect lenses for observing small particles beyond the diffraction limit. Such artificial, functional materials engineered to fulfill unusual electromagnetic properties, are usually referred as "metamaterials". The prefix "meta" means "beyond," and in this sense the name "metamaterials" indicates such systems that are beyond conventional materials. Comprehensively, "metamaterials are artificially structured composites consisting of well-organized functional inclusions of sub-wavelength dimensions, with extraordinary electromagnetic properties not found in nature, which attain those unusual properties from the unit cells rather than the constituent materials" [1]. Since the dimension of unit cells and even the average distance between adjacent meta-atoms of such materials several times are smaller than the wavelength of incident electromagnetic waves, their electromagnetic responses are expressed in terms of homogenized, "effective" material parameters.

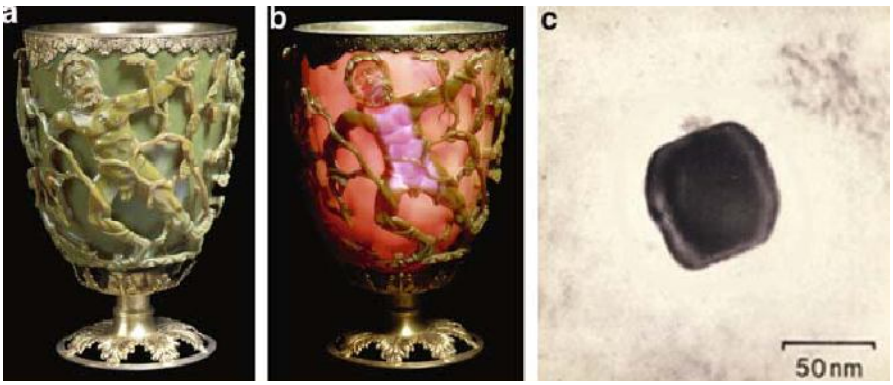

Figure 1-1 The Lycurgus Cup viewed **(a)** in reflected light and **(b)** in transmitted light. **(c)** A metallic nanoparticle used in these art works [2].

Historically, metamaterials have been used in art pieces centuries ago, without understanding the real physics behind them. A well-known example is medieval ruby cup exhibited in British Museum in London might be considered as the first optical metamaterial. Ruby glass which contains droplets of nano-scaled gold particles features an amazing property of changing color depending on the incident light over it [2]. In Figure 1-1, Lycurgus cup, the

Roman cup made of ruby glass, is shown. Reflected light makes it appear green, but reddish color is observed when light is transmitted through it.

In modern science, artificial electromagnetic metamaterials were designed and studied long before the term "metamaterial" introduced to scientific community. The proposal of Bose for fabricating an artificial chiral effect in 1898 [3] and the work of Kock on artificial dielectrics for microwave antenna lenses in 1945 have been considered as the oldest scientific works in the field of metamaterials [4].

In the area of modern metamaterials, three papers should be considered as fundamental research works. The first is Victor Veselago's paper on left-handed materials in 1968 [5]. His fantastic inspections on materials with negative material parameters, electric permittivity and magnetic permeability have opened a new window to generate artificial materials that are not forbidden by Maxwell's equations but are not observed in any conventional media. After three decades, the first experimental validation for theoretical prediction of Veselago medium has been demonstrated by D.R. Smith and his team [6]. It is feasible to say what we today call metamaterial was born in Smith's lab at the University of California at San Diego (UCSD) at the beginning of 21st century. However, before that, Sir. J. Pendry and his coworkers in 1999 have used the well-known split-ring resonators (SRR) to achieve the artificially magnetic plasma whose permeability was negative [7]. Also, they have applied periodic array of Thin Wires (TW) to obtain the desired electric response. What Smith and his team have presented, was the structure using the combination of TWs and SRRs, for the exhibiting simultaneously negative electric permittivity and negative magnetic permeability at a specific microwave range of frequencies. Figure 1-2 shows the first one dimensional and two dimensional LHM represented by UCSD team. The third seminal paper is Pendry's work on a perfect lens [8], which represents the initial attempt to fill the gap between novel metamaterials and exciting applications. Precise investigations of Pendry for the near and far fields of a source, in which interacts with the Veselago lens have shown that in principle the lens could refocus over both near and far fields radiated from an object. His stunning observation has represented that the Veselago lens was not subject to the diffraction limit of all other known optics. The planar negative-index slab has consequently been called a superlens. Interestingly, all the three papers that established the field of metamaterials were focused on negative index metamaterials. This fact is the major reason

that during first years of the research in metamaterials, the term of metamaterial was almost synonymous of left-handed material.

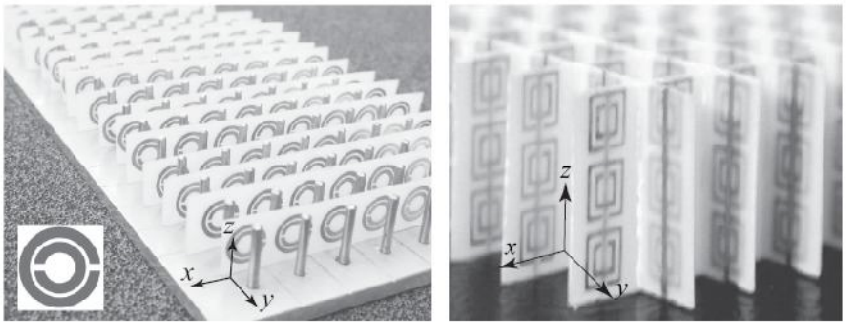

Figure 1-2 The first experimental structures to create LHM proposed by Smith and coworkers in 2000. **(a)** one dimensional metamaterial **(b)** two-dimensional metamaterial by combination of TWs and SPRs [7].

1.3 Optical Metamaterials

After the experimental realization of invisible cloak in the microwave regime, among all, optical metamaterials, in particular in visible wavelength have gained a lot of research interest. In order to expand the negative frequency response of metamaterials toward optical frequencies, fabricating process of constituent blocks must be modified beyond general technologies. Undoubtedly, the development of optical metamaterials is in debt to correlation between different research activities such as nanofabrication techniques with advances in nanoscale imaging and computational electromagnetic design. Due to their unconventional electromagnetic characteristics, new viewpoints for controlling and manipulating photons have been proposed and their potentials for creating revolution in various fields including optical sensing, miniature antennae, novel waveguides, sub-wavelength imaging, nanoscale photolithography and photonic circuits have been approved.

In order to progress and expand sciences of light beyond conventional optics, study of plasmonics for metamaterial applications is one of those frontiers to break limitations toward novel and wonderful applications. Plasmonic metamaterials are composites of metal-dielectric materials, designed to achieve astonishing optical properties that might be harnessed for practical use. This type of photonic metamaterials often derives their extraordinary properties from surface plasmon waves, which are collective oscillations of free electrons on the surface of metallic nanostructures. Application of plasmonic materials as unit cells of metamaterials provides a new toolset to control the flow of light at nano-scale range. Thus, fabrication of such metamaterials can be really vital to break the fundamental limits toward functional applications

of plasmonic devices. These designs require development of viable manufacturing and novel characterization techniques. Furthermore, the effective use of these tools in any real applications or technologies demands corresponding advancements in nanofabrication and materials technology. Luckily, nanofabrication has now matured to such an extent that many metamaterial geometries can be produced with relative ease.

However, a more fundamental hurdle is finding the right materials and taming their properties to enable effective, real-world applications of plasmonic metamaterials. In addition, the important point that should not be neglected is that the research field of photonic metamaterials is too young and broad inquiries need to be done to progress from there. They are usually highly dissipative (lossy), dispersive, anisotropic and with narrow desire frequency response. Nevertheless, the confirmed ability of optical metamaterials to exhibit novel and exciting applications has already convinced the scientist to put their efforts to investigate the new physics behind them and optimize their design toward practical purposes. Hence, in order to achieve prescribed functionalities the scientist society of metamaterials tries to find out about the new methods to tailor the structural units in shape and size, to tune their composition and morphology artificially, and to design inclusions in a predetermined manner.

1.4 Properties of Left Handed Materials

It is well-known that the electromagnetic properties of a material can be characterized by two material parameters: electric permittivity (ε) and a magnetic permeability (μ). Since the response of a material to external fields is largely determined only by these two material parameters, all possible properties for classifying of material can be illustrated in the ε –μ domain [9]. As shown in Figure 1-3, the first quadrant ($\varepsilon > 0$ and $\mu > 0$) represents right-handed materials (RHM). From the Maxwell's equations, for a RHM, the electric field **E**, the magnetic field **H**, and the wave vector **k** form a right-handed system and they support the forward propagating waves and transparent dielectric materials. The second and forth quadrant denote for the materials with one of two parameters of ε or μ with a negative value, resulting purely imaginary refractive index. For these kinds of materials, a negative value of ε (μ) indicates that the direction of the electric (magnetic) field induced inside the material is in the opposite direction to the incident field, and consequently, propagating waves cannot be supported by them. The electric plasma for materials with negative ε and positive μ can be found in second quadrant, which

supports only evanescent waves. The response of noble metals at optical frequencies is a good example for materials with negative ε.

Furthermore, the fourth quadrant refers to magnetic plasma with positive ε and negative μ, in which negative permeability can be found in ferromagnetic media near a resonance frequency [9].

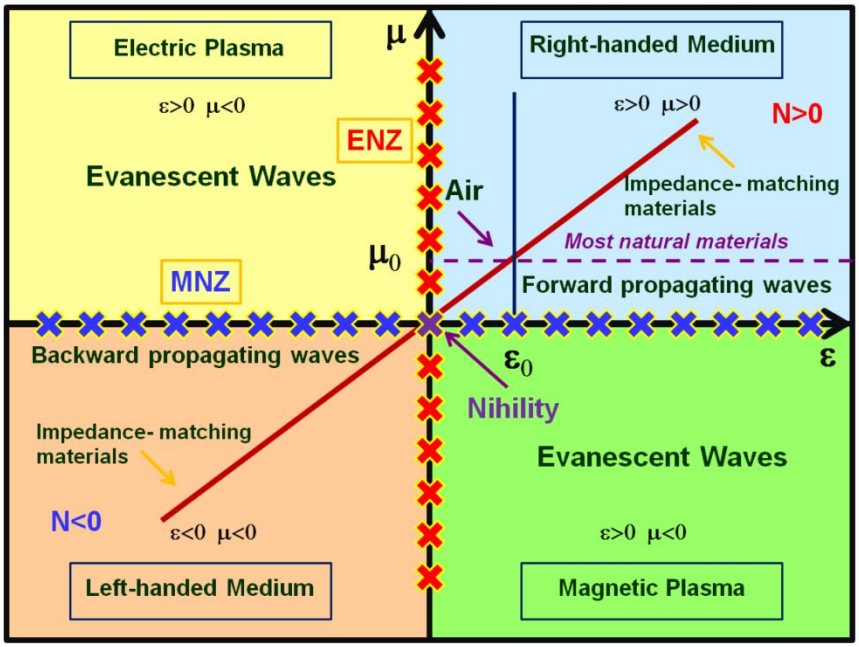

Figure 1-3 All possible properties of isotropic materials in the $\varepsilon - \mu$ domain. The two axes correspond to the real parts of permittivity and permeability, respectively.

The third quadrant ($\varepsilon < 0$ and $\mu < 0$) is the well-known left-handed materials (LHM) or Veselago materials, since it was proposed by Veselago [5], supporting the backward propagating waves. A media with both negative material parameters is termed as left-handed (LHM) material since the field vectors **E**, **H** in correlation with the wave vector **k** form a left-handed set of vectors rather than the usual right-hand set. In other words, in a left-handed medium, during forward propagation of a wave, its phase undergoes a negative phase change, leading to subversion of the fundamental physical rules and, consequently, intriguing phenomena such as the reversal of Snell low in the borderline of LHM and RHM, the inversion of Doppler Effect and reversed Cherenkov radiation.

For a long period, beside the term of LHM, negative-refractive index materials (NIM), double negative materials (DNG), backward-wave materials in parallel with the term of metamaterials have been regarded as the same sort of materials. However, metamaterials have much broader scope than LHMs. In the $\varepsilon - \mu$ domain, there are several special lines and points

indicating special material properties, as shown in Figure 1.3. For example, the point $\mu = -\mu_0$ and $\varepsilon = -\varepsilon_0$ represents an anti-air in the LHM region, which will produce a perfect lens; the point $\varepsilon = 0$ and $\mu = 0$ represents a nihility, which can yield a perfect tunneling effect; the line $\mu = \varepsilon$ in both RHM and LHM regions represents impedance-matching materials, which have perfect impedance matching with air, resulting in no reflections. Also, the vicinity of $\mu = 0$ is called as μ-near zero (MNZ) material, and the vicinity of $\varepsilon = 0$ is called as ε-near zero (ENZ) material, which has special properties [9].

1.5 Figure of Merit

As it has been mentioned earlier metamaterials suffer from rather strong dissipation of energy, because the building blocks are constituted by intrinsically lossy elements. The Figure of Merit (FOM) is the parameter which can provide a reflection from the efficiency of a designed metamaterial. The imaginary part of dielectric constant is responsible for absorptive losses and real part is known as dispersive part. Thus, designing a device with lower value of imaginary part is the step toward manufacturing efficient devices. In fact, FOM is a suitable measure for the loss, defined as the ratio of the real part to the imaginary part of the effective refractive index.

$$FOM = -\frac{\mathrm{Re}(n_{eff})}{\mathrm{Im}(n_{eff})} \qquad (1-1)$$

Clearly, potential applications (such as Pendry's perfect lenses) require that the modulus of the real part Re (n_{eff}) < 0 is much larger than the imaginary part Im (n_{eff}) > 0. Noble metal nanoparticles (NPs) as the main ingredient of plasmonic metamaterials exhibit large values of imaginary part in visible frequency range, which make optical metamaterials obstructive for most optical applications. In fact, filling the gap between manufactured prototypes of metamaterials in laboratories and functional devices strongly depends to finding an effective strategy for compensating absorptive losses.

1.6 Fabrication of 3D Optical Metamaterials

Over the past couple of years, advanced fabrication technologies have brought the field of metamaterials into a new stage where, besides lithography-based approaches, new 'bottom-up' fabrication techniques based on nanochemistry and material science strongly influences manufacturing route of metamaterials.

By combining recent progresses in the chemical synthesis of engineered nano-particles with bottom-up manufacturing techniques, the implemented designs on micrometer regime now can be rescaled to nanometer range. The obtained nanostructures can be appropriate to apply as subunits of optical metamaterials. In order to manufacture a functional, three-dimensional bulk metamaterial with valid effective homogeneous behavior, an average density of one to ten active units (nano-resonators) per wavelength is necessary. The individual, direct manipulation of such a huge number of nanostructures seems unrealistic for large-scale applications. On the other hand, self-assembly appears as a common and highly efficient process well known in soft condensed matter physics. It results from the spontaneous organization of individual objects under the effect of complex pair interactions and can lead to well organized two-dimensional or three-dimensional structures of various symmetries. This is why it is currently one of the most promising routes to 3D metamaterials [10].

The following subsections introduce some designs of artificial dielectric and magnetic structures, proper for metamaterial applications which can be fabricated by bottom-up manufacturing technologies.

1.6.1 Artificial Dielectrics Inclusions

Artificial dielectrics, which can be made of dielectric or metallic inclusions, can create relevant values of permittivity in metamaterial operation wavelength. In order to apply artificial dielectrics as subunits of a metamaterial two points need to be considered. First of all, inclusions should be electrically much smaller than the wavelength of incident electromagnetic wave to obtain an effective homogeneous medium. Second, the building blocks of artificial dielectrics obviously must be made by electrically polarizable materials such as small metallic or dielectric spheres [10]. In order to keep valid effective medium theory the size of inclusion should be the scale of tenth of nanometer. For optical applications, noble metals as natural materials are widely available and artificial dielectrics are not needed.

The invention of the optical artificial dielectrics has stimulated the interest of many researchers to suggest different structures (see Figure 1-4) and develop the theory of artificial dielectrics with small dipolar inclusions [11,12], leading to produce materials with permittivity smaller than unity or close to zero for various applications such as cloaks [13] and optical nanocircuits [14]. Artificial materials formed by electrically dense arrays of thin conducting

wires were originally proposed by Rotman. These artificial dielectrics possess effective permittivity smaller than unity, but they are reacting with strong nonlocality in the effective material response (strong spatial dispersion) [15].

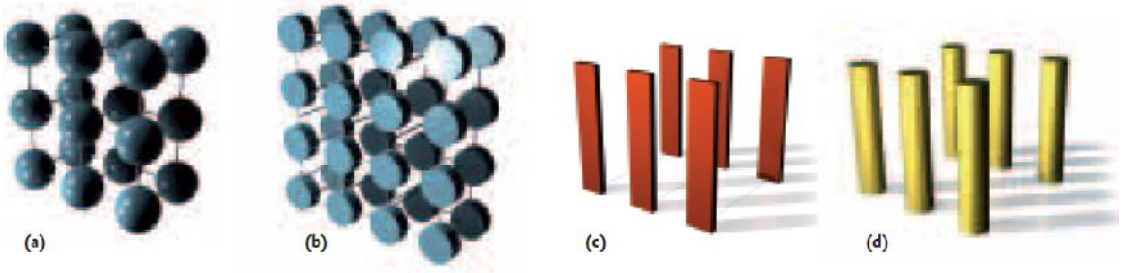

Figure 1-4 Typical geometries of artificial dielectrics for creating negative values of permittivity proposed by Collin [12].

1.6.2 Artificial Magnetic Inclusions

Shapes of inclusions for artificial magnetic materials should be chosen carefully, some points should be in consideration: i) the stronger bi-anisotropy effects would be forbidden due to the geometrical symmetry and ii) among all the second order effects the artificial magnetism would dominate [11]. For microwave applications, this is relatively easy as the dimensions are in the order of a millimeter, but the theory is equally valid for nanostructured metamaterials. The key for a proper design is to choose the shape so that induced currents form loops with a rather uniform distribution of the induced current which then produces a strong magnetic moment [16]. Several typical geometries of split ring resonators are shown in Figure 1-5.

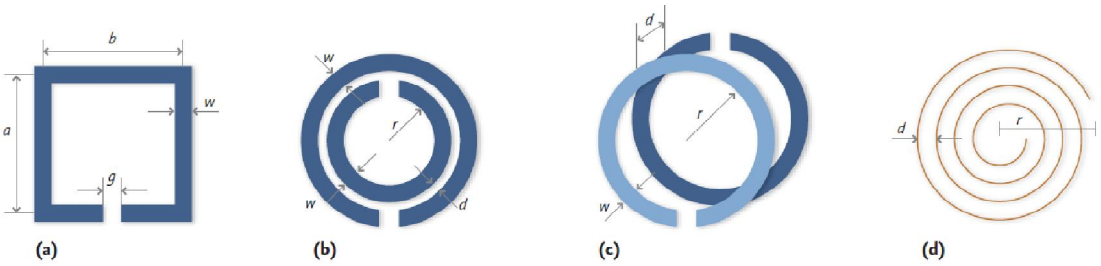

Figure 1-5 Architectures of some proposed structures to realize artificial magnetic materials [16].

At optical frequencies, scientists harnessed approaches to design and fabricate artificial magnetic materials leading to promising structures based on colloidal clusters consisting of plasmonic NPs. Figure 1-6 shows some of those proposed structures, appropriate for obtaining negative permittivity. These geometries have the potential to show magnetic response under conditions of weak spatial dispersion, which would hopefully result in fabricating of metamaterials with permeability different from unity at optical frequencies.

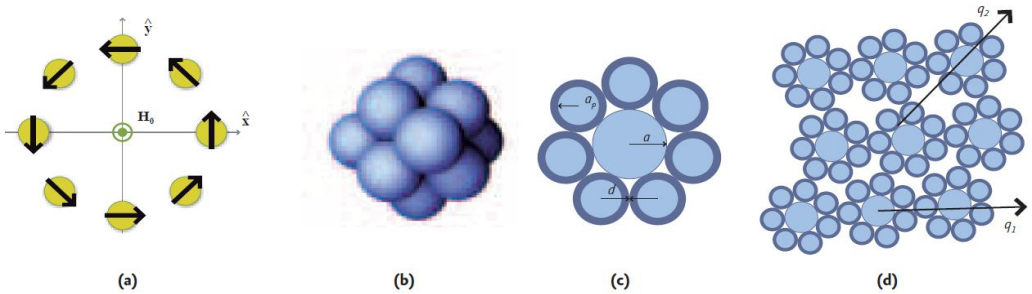

Figure 1-6 Structures of some proposed structures for obtaining optical artificial magnetic by clusters. Structure **(a)** from Alu [17], Structures **(b-d)** from Simovski [18].

Furthermore, theoretical studies accompanied by simulation results show that proper arrangements of plasmonic clusters and as well as embedding semiconductor spheres with strong excitonic oscillation strength in the heart of core-shell NPs arrangements provide the possibility to obtained a controlled electric and magnetic resonances in the visible regime.

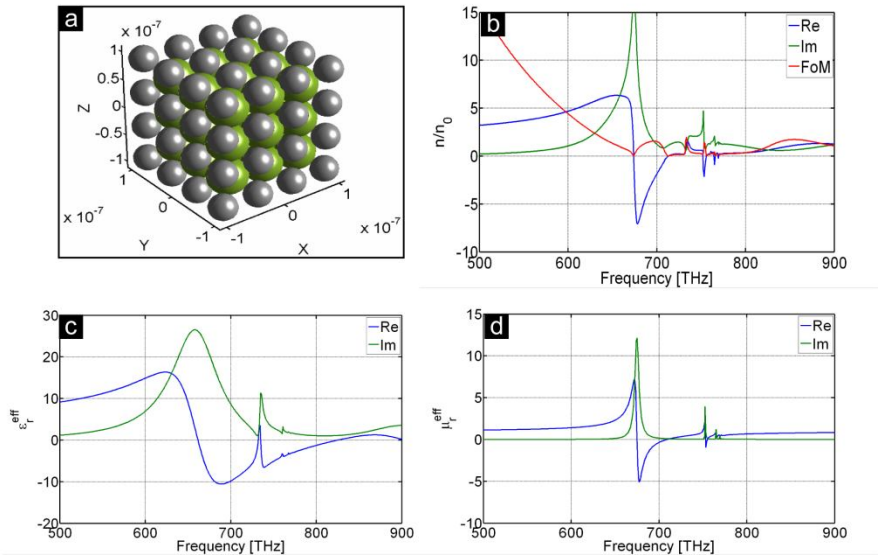

Figure 1-7 Binary bcc lattice composed of alternating layers of excitonic and plasmonic nanoparticles. **(a)** Perspective view of the resulting superlattice with a total filling fraction *f=0.729* **(b)** refractive index **(c)** effective permittivity **(d)** effective permeability of such a collection of coated spheres [19].

Figure 1-7(a) shows a slab of the binary multilayered bcc crystal made by a series of alternating two-dimensional photonic crystal planes of plasmonic (silver) and excitonic (CuCl) spheres with diameter of 40 and 29 nm, respectively. The simulation results show that presence of simultaneous negative values in resonance band of effective permittivity and permeability can lead to negative refractive index. However, as it can be seen from figure 1-7(b), higher negative values of refractive index real part appears with enhanced positive values of imaginary part and this causes lower FOM for designed metamaterial. However, the operational frequency can be chosen near the upper edge of the resonance band where losses are relatively small.

REFERENCES

1. W. Cai, and V. Shalaev, *"Optical Metamaterials"*, Springer, New York, 2010.
2. D.J. Barber, and I.C. Freestone, *Archaeometry*, **1990**, 32, 33.
3. J.C. Bose, *Proc. R. Soc. Lond.*, **1898**, 63,146.
4. W. E. Kock, *Proc. IRE.*, **1946**, 34,828.
5. V.G. Veselago, *Sov. Phys. Usp.*, **1968**, 10, 509.
6. D. R .Smith, W. J. Padilla, D. C. Vier, S. C. Nemat-Nasser, and S. Schultz, *Phys. Rev. Lett.*, **2000**, 84, 4184.
7. J.B. Pendry, A.J. Holden, D.J. Robbins, and W.J. Stewart, *IEEE Trans. Micro. Theory Tech.* **1999**, 47, 2075.
8. J.B. Pendry, *Phys. Rev. Lett*., **2000**, 85, 3966.
9. T. J. Cui, D. R. Smith, and R. Liu, *"Metamaterials, theory, design and applications"*, Springer, New York, 2010.
10. F. de Baas Anne, "*Nanostructured Metamaterials"*, Publications Office of the European Union, Luxembourg, 2010.
11. S.B. Cohn, *J. Applied Phys.*, **1950**, 21, 674.
12. R.E. Collin, "*Field Theory of Guided Waves"*, 2nd. ed., New York, IEEE Press, 1991.
13. 42. J.B. Pendry, D. Schurig, and D.R. Smith, *Science*, **2006**, 312, 1780.
14. N. Engheta, *Science,* **2007**, 317, 1698.
15. W. Rotman, *IRE Trans. Antennas Propag*., **1962**, 82, 95.
16. S.A. Schelkunoff, and H.T. Friis, *"Antennas: Theory and Practice"*, Wiley New York, 1952.
17. A. Alu, A. Salandrino, and N. Engheta, *Opt. Express*, **2006**, 14, 1557.
18. C.R. Simovski, and S.A. Tretyakov, *Phys. Rev. B*, **2009**, 79, 045111.
19. M. Albani, and A. Vallecchi, "*Technical report on the state of the art on the design rules for fabrication possibilities to obtain defined EM properties for the classes of metamaterials"*, Siena (Italy), 2011.

Chapter 2

Optical Properties of Plasmonic Nanostructures

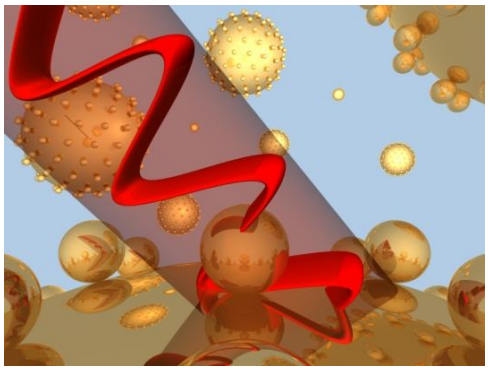

2.1 Introduction

In order to design and synthesize an appropriate nanostructure for plasmonic metamaterials, it is crucial to understand comprehensively how to deal with the optical loss problem of metallic NPs. Therefore, the main aim of this chapter is to provide fundamental information about optical characteristics of NPs, which can be useful to improve the functionality of plasmonic nanostructures. The first part of the chapter explains the origin of negative real part for dielectric constant of NPs that makes them appropriate candidate to apply as building blocks for plasmonic metamaterials. In the next part, after describing Mie theory for core and core-shell NPs, the dielectric constant of metallic NPs have been investigated by Drude model and Johnson & Christy data. Then, a brief introduction for Maxwell-Garnet theory and Kramers-Kronig Relations has been provided. Finally the chapter is accomplished by exploring tunable parameters that can influence the optical behavior of NPs.

2.2 Localized Surface Plasmon Resonances

The size transition of noble metals (Au, Ag, and Cu) from bulk to atomic scale exhibits a particular wide range of interesting material behavior. As the size or shape of the nanoparticle

changes, the observed color also changes. The red color of gold NPs and yellow color of silver NPs originate from collective oscillation of the conduction electrons with respect to the positive metallic lattice in resonance with the electric component of incident electromagnetic (EM) field, known as the plasmon resonance. This coherent delocalization of the free electrons induces an electric dipole in the metal particle. Figure 2-1(a) shows a model for the interaction of light with free electrons of a metal particle.

According to this matter that an imposed electromagnetic wave on a metal surface only penetrates for a certain depth (<50 nm for Ag and Au), thus just the electrons on the surface can be driven most significantly, thereby their collective oscillations are termed as surface plasmon resonance (SPR) [1-4]. Plasmon resonances of NPs in a size smaller than incident wavelength create the opportunity to confine the electromagnetic field of the light in a nanoscale volume. For this reason, such plasmon oscillations are termed as Localized Surface Plasmon Resonances (LSPRs).

In contrast with SPRs, the other type of plasmonic signals well known as surface plasmon polaritons (SPPs) relevant to localized SPs, are the propagating surface waves parallel to the interface between two media possessing permittivities with opposite signs, such as a metal and a dielectric [5]. SPPs strongly influence the optical responses at the micro and nanoscale and have to be accounted for in modern nanotechnology. In both cases of SPRs and SPPs oscillations are excited by light, exhibiting enhanced near-field amplitude at the resonance wavelength (Figure 2-1(b)).

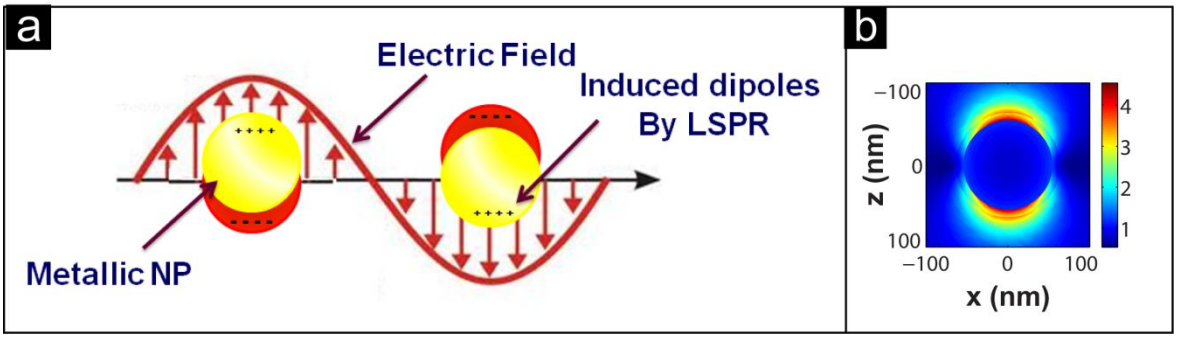

Figure 2-1 (a) Origin of surface plasmon resonances due to coherent interaction of the electrons in the conduction band with electric component f the electromagnetic field **(b)** Simulated Enhanced plasmon field around NP as result of Localized SPR.

2.3 Local field Enhancement in NPs

As a result of SPR in metal NPs, enhanced electromagnetic fields are generated that affect the local environment. These electromagnetic fields are significantly stronger than

observed from the bulk material. The fields determined by the geometry of NPs, can influence the photoluminescence of fluorescent molecules, Raman signal of a molecule on the surface and the scattering of light.

Excitation of bulk plasmons by photons is not allowed, since for a given wavelength a photon in free space has a wave vector that is always smaller than the corresponding plasmon, and the momentum conservation required for their coupling cannot be fulfilled [4]. In fact, when particle size is comparable to the resonant electromagnetic wavelength, the electric field distribution along the particle is non uniform, electron polarization is no more coherent in each point of the particles and multipolar plasmon oscillations are excited [6]. In contrary, when particle size is small compared to the resonant electromagnetic wavelength, the electric field distribution along the particle is uniform, electron cloud polarization is coherent in each point of the particle and dipolar plasmon oscillations are excited. Hence, enhanced confined field is occurred only in such small NPs, in which the particle size is much smaller than the wavelength of incident light.

The potential for achieving interesting optical effects using these strongly confined photons is tremendous [7,8]. The large enhancement of scattered and absorbed light by NP, along with Surface Enhanced Raman Scattering (SERS) from adsorbed molecules can be mentioned as some of those remarkable optical affects. Figure 2-2 summarizes the major optical processes that occur on the interaction of light with gold nanoparticles.

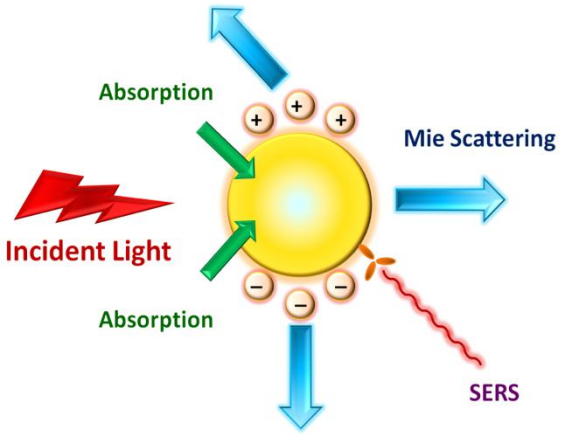

Figure 2-2 Important optical processes resulted from the interaction of light with a gold nanoparticle: light absorption, Mie scattering, surface-enhanced electromagnetic field and surface-enhanced Raman scattering from adsorbed molecules.

In fact, light scattering results from the plasmon oscillations decays by radiating their energy [9]. On the other hand, the oscillating electrons suffer from collisions with other electrons

and as well as collisions with the lattice phonons, the nanoparticle surface, defects, and surface ligands are considered as the additional damping processes. These nonradiative pathways result in the generation of heat, and constitute light absorption by the particle [10]. In addition, the SERS mechanism results in an increase in the Raman scattering of the adsorbed molecules [11].

2.4 Mie Theory

The interactions of light with spherical metal particles can be described by Mie theory, that Gustav Mie solved Maxwell's equations for the case of a spherical particle under irradiation of a plane wave [12]. Mie found that optical absorption, light scattering and extinction of a metal sphere depend on its volume and bulk dielectric functions [4,13]. In contrary with Rayleigh scattering theory which is only applicable to small spherical particles made of a dielectric (non-absorbing) material, Mie theory express a generic solution to extract scattering and it can be applied to spherical particles of any size and composed of an absorbing or non-absorbing material [14]. Therefore, Mie theory is the most useful approach for describing the optical properties of metal-dielectric core-shell nanospheres.

If we consider a single homogenous isolated sphere of radius r and propagation constant k embedded in infinite, homogeneous medium with photon wave vector k_h which is illuminated by a plane wave with electric and magnetic components, the extinction cross-section (C_{ext}) of such a sphere can be obtained as a series of multipole oscillations, if the proper boundary conditions for electromagnetic fields at the interface between the metallic NP and its surrounding medium have specified [4]. In the following equations, multipole series of spherical harmonics are identified by the multipolar order n. For instance, n equal to 1 corresponds to dipolar sphere excitation and n equal to 2 correspond to quadrupolar oscillation and so on. By dividing by the geometrical cross-section of the particle to the physical cross sectional area (πr^2), the expressions of the associated efficiencies are obtained. The following infinite series state the Mie model expressions for extinction (Q_{ext}) and scattering efficiencies (Q_{sca}) of a single NP [14,15].

$$Q_{ext} = \frac{2}{|x|^2} \sum_{n=1}^{\infty} (2n+1)\,\mathrm{Re}[a_n + b_n] \qquad (2-1)$$

$$Q_{sca} = \frac{2}{|x|^2} \sum_{n=1}^{\infty} (2n+1)[|a_n|^2 + |b_n|^2] \qquad (2-2)$$

$$Q_{abs} = Q_{ext} - Q_{sca} \qquad (2-3)$$

$$a_n = \frac{m.\psi_n(mx).\psi_n'(x) - \psi_n'(mx).\psi_n(x)}{m.\psi_n(mx).\xi_n'(x) - \psi_n'(mx).\xi_n(x)} \qquad (2-4)$$

$$b_n = \frac{\psi_n(mx).\psi_n'(x) - m\psi_n'(mx).\psi_n(x)}{\psi_n(mx).\xi_n'(x) - m\psi_n'(mx).\xi_n(x)} \qquad (2-5)$$

$$m = \frac{k}{k_h} = \frac{n}{n_h} \qquad (2-6)$$

$$x = |k_h| R \qquad (2-7)$$

In these equations x denotes the so called size parameter, m is the relative refractive index, where n is the complex refraction index of the sphere and n_h is the real refraction index of the non absorbing surrounding medium. The functions of ψ_n and ξ_n are the spherical Riccati–Bessel functions [16,17] and the primes indicate differentiation with respect to the argument. In the multipole series expansion of the scattered field, the terms a_n is proportional to the coefficients of the transverse magnetic (TM) modes, associated with surface plasmon polariton resonances, while transverse electric (TE) solutions corresponding to the b_n coefficients which are associated with eddy currents arising from magnetic resonances. In particular, the scattered magnetic dipole field is proportional to b_1, whereas the scattered electric dipole field is proportional to a_1.

The size parameter x determines if the sphere is in dynamic (multipolar: $R \sim \lambda$) or in quasi-static regime (dipolar: $R << \lambda$ then $x << 1$) [4]. In dynamic regime, due to significant phase-changes of the driving field over the particle volume, the precise electrodynamics approach (in above equations) is required. But in quasi-static approximation, due to the small size of nanoparticle with respect to wavelength, all the electrons confined in a nanoparticle sense the same electric field at a given time t, the electric field of light is assumed as independent of the position and constant. Consequently, only dipole mode contribution to the extinction cross-section is considered whereas higher multipole orders contributions in the electrodynamic calculation can be ignored. In fact, in order to relate the scattering of a small obstacle to the bulk permittivity and permeability, only the terms of a_1 and b_1 of the scattered field are required instead of finding the effective permittivity and effective permeability, respectively. Under such a condition, the polarizability of a spherical particle of volume $V=(4/3)\,\pi r^3$ is given by the Clausius-Mossotti relation [15].

$$\alpha = 4\varepsilon_0 \pi r^3 \frac{\varepsilon - \varepsilon_h}{\varepsilon + 2\varepsilon_h} \qquad (2-8)$$

where ε_0 is the permittivity of vacuum, ε_h is the dielectric constant of the host medium and r is the metal sphere radius. ε stands for the dielectric function of the metal which is complex and frequency and size dependent and can expressed as $\varepsilon(\omega,r)=\varepsilon_r(\omega,r)+i\varepsilon_i(\omega,r)$, where ε_r is the real part of the dielectric function and ε_i is the imaginary part. To extract the dielectric constant as a function of known parameters, size corrected Drude model can be applied, which will be discussed in the next section. The extinction and scattering cross-sections, C_{ext} and C_{sca} are given in the terms of the dipolar polarizability as [15]

$$C_{ext} = k\,\mathrm{Im}(\alpha) \qquad (2-9)$$

$$C_{sca} = \frac{k^4}{6\pi}\left|\alpha^2\right| \qquad (2-10)$$

By neglecting the scattering cross-section for small NPs, the most popular expression of extinction cross-section, mainly dominated by absorption is given as [4, 14]

$$C_{ext} = \frac{24\pi^2 r^3 \varepsilon_h^{3/2}}{\lambda}\frac{\varepsilon_i(\omega,r)}{(\varepsilon_r(\omega,r)+2\varepsilon_h)^2+\varepsilon_i^{\,2}(\omega,r)} \qquad (2-11)$$

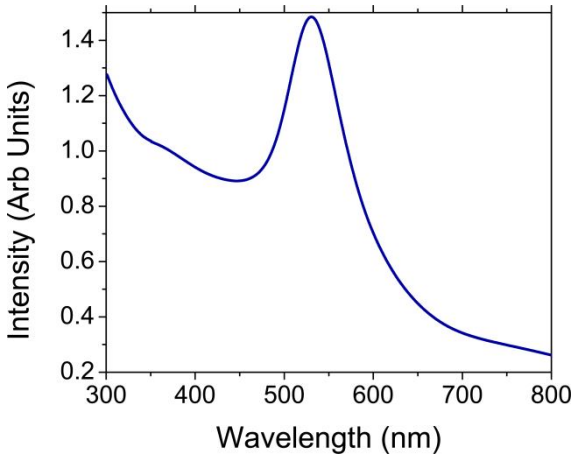

Figure 2-3 Extinction cross section of bare gold sphere nanoparticle with diameter of 14 nm dissolved in Chlorophorm with plasmon peak in visible band.

As an example of extinction cross section, Figure 2-3 shows the surface plasmon band (SPB) of colloidal solutions of gold spherical nanoparticles obtained by laser ablation in common solvents. From equation (2-11), we see that polarizability and consequently extinction cross section (equation (2-12)) have a strong resonance when the following condition is satisfied.

$$\varepsilon_r = -2\varepsilon_h \qquad (2-12)$$

It is assumed here that ε_i is small and weakly dependent on frequency [18]. Taking into account ε_h has a positive value, for satisfaction of equation (2-12), the real part ε_r requires to be

negative, which is possible for noble metals at particular visible frequency, famous to plasmon resonance frequency (ω_p). The plasmon frequency of a bulk metal is given as:

$$\omega_p = (\frac{Ne^2}{\varepsilon_0 m_e})^{\frac{1}{2}} \qquad (2-13)$$

where ε_0 is the dielectric constant of vacuum, N is the total electron density of the bulk metal, e and m_e are the charge and the effective mass of a free electron, respectively. For a spherical NP made of a metal with bulk dielectric function ε_∞ located in a medium ε_h, the frequency at which the resonance condition is satisfied is usually referred as the Fröhlich frequency (ω_F).

$$\omega_F = \frac{\omega_p}{\sqrt{\varepsilon_\infty + \frac{1+L}{L}\varepsilon_h}} \qquad (2-14)$$

where L is the oscillation mode. L is equal to one for dipole oscillation (small NPs) and two for quadrapole oscillation and so on. This equation is extracted by substituting the expression of the real part of metal dielectric constant in resonance condition expressed in equation (2-12).

2.5 Resonances of core-shell nanoparticles

The extinction coefficients (2-1) and (2-2) cannot be applied to core-shell spheres. The appropriate expressions, which are extracted from the Mie solution for the scattering by a coated sphere, can be written as following expression.

$$C_{ext} = \frac{2\pi}{k_h^2}\sum_{n=1}^{\infty}(2n+1)\,\mathrm{Re}\left(a_n + b_n\right) \qquad (2-15)$$

here a_n and b_n are giving by the following expressions:

$$a_n = \frac{\psi_n(x_2)\left[\psi'_n(m_2x_2) + \xi'_n(m_2x_2)A_n\right] - m_2\psi'_n(x_2)\left[\psi_n(m_2x_2) + \xi_n(m_2x_2)A_n\right]}{\xi_n(x_2)\left[\psi'_n(m_2x_2) + \xi'_n(m_2x_2)A_n\right] - m_2\xi'_n(x_2)\left[\psi_n(m_2x_2) + \xi_n(m_2x_2)A_n\right]} \qquad (2-16)$$

$$b_n = \frac{m_2\psi_n(x_2)\left[\psi'_n(m_2x_2) + \xi'_n(m_2x_2)B_n\right] - \psi'_n(x_2)\left[\psi_n(m_2x_2) + \xi_n(m_2x_2)B_n\right]}{m_2\xi_n(x_2)\left[\psi'_n(m_2x_2) + \xi'_n(m_2x_2)B_n\right] - \xi'_n(x_2)\left[\psi_n(m_2x_2) + \xi_n(m_2x_2)B_n\right]} \qquad (2-17)$$

where

$$A_n = \frac{m_1\psi_n(m_1x_1)\psi'_n(m_2x_1) - m_2\psi_n(m_2x_1)\psi'_n(m_1x_1)}{m_2\xi_n(m_2x_1)\psi'_n(m_1x_1) - m_1\psi_n(m_1x_1)\xi'_n(m_2x_1)} \qquad (2-18)$$

$$B_n = \frac{m_2\psi_n(m_1x_1)\psi'_n(m_2x_1) - m_1\psi_n(m_2x_1)\psi'_n(m_1x_1)}{m_1\xi_n(m_2x_1)\psi'_n(m_1x_1) - m_2\psi_n(m_1x_1)\xi'_n(m_2x_1)} \qquad (2-19)$$

$x_1=k_h r_c$ and $x_2=k_h d$ are the size parameters for a coated sphere with diameter of r_c and shell thickness of d. Also, $m_1=k_r/k_h$ and $m_2=k_s/k_h$ are the relative refractive indices of core and shell with wave vectors of k_r and k_s, respectively. The polarizability of a single shell metal nanosphere in dipolar approximation can be expressed as:

$$\alpha = \frac{4\pi}{3}(r+d)^3 \frac{(\varepsilon_s-\varepsilon_h)(\varepsilon+2\varepsilon_h)+(\frac{r}{r+d})^3(\varepsilon-\varepsilon_s)(\varepsilon_h+2\varepsilon_s)}{(\varepsilon_s+2\varepsilon_h)(\varepsilon+2\varepsilon_s)-(\frac{r}{r+d})^3(\varepsilon-\varepsilon_s)(\varepsilon_h-2\varepsilon_s)} \qquad (2-20)$$

By substituting the obtained equation of polarizability in following formula, simply we can extract the extinction cross section of a core-shell NP.

$$C_{ext} = 4\pi k_h \,\mathrm{Im}[\alpha] \qquad (2-21)$$

2.6 Dielectric Constant of Metal Nanoparticles

The optical properties of noble metals are determined mainly by two facts: (i) the conduction electrons can move freely within the bulk of material. (ii) The inter-band excitations can take place if the energy of the incoming photons exceeds the band gap energy of the respective metal. In 1900, Drude successfully applied the kinetic theory of gases to explain the electrical and thermal conduction of metals with three assumptions [4,19]: (1) the interactions of an electron with another electrons and with ions are neglected between collisions. (2) Electron-electron scattering is neglected. (3) Electrons experience a collision probability per unit time of $1/\tau$, where τ is the interval time between two adjacent collisions.

According to Drude model, the motion of a whole electron cloud is the summation of the motion of the individual electrons. Thus, due to the large electron density and delocalization, all the free electrons in a metal consequently coherently oscillate in phase under a time dependent electrical field, which gives the well-known bulk plasmon resonance in the plasmon frequency [19]. Maxwell's equations can be used to represent the interaction of an electromagnetic wave with a metal NP and they link the electric field **E**, the electric polarization **P** to the electric displacement **D** and also, link the magnetization **M,** the magnetic field **H** to magnetic induction **B**; ε_0 is the permittivity of free space, μ_0 is the vacuum permeability and ε_∞ stands for the background dielectric constant of the bulk medium.

$$\boldsymbol{D} = \varepsilon_0 \boldsymbol{E} + \boldsymbol{P} = \varepsilon_0 \varepsilon_\infty \boldsymbol{E} \qquad (2-22)$$

$$\boldsymbol{B} = \mu_0(\boldsymbol{M} + \boldsymbol{H}) \qquad (2-23)$$

Using the mentioned equation and assuming an isotropic medium, the dielectric constant can be expressed as,

$$\varepsilon_\infty = 1 + \frac{\boldsymbol{P}}{\varepsilon_0 \boldsymbol{E}} \qquad (2-24)$$

By applying the Drude model for the free-electron gas, the displacement *x* of an electron in the presence an electric field and the macroscopic polarization **P** can be obtained by solving the motion equation of the electrons under the influence of an external field.

$$m_e \frac{\partial^2 x}{\partial t^2} + m_e \Gamma_{bulk} \frac{\partial x}{\partial t} = eE_0 e^{(-i\omega t)} \qquad (2-25)$$

The second term of first side of the differential equation is a viscous friction due to different factors such as free electron inelastic collisions but also electron phonon coupling, defects, impurities, *etc.*[4]. Γ_{bulk} is the corresponding collision frequency, also known as the bulk metal damping constant. The notation of ω_d can be used for this parameter, as well. The second side of the motion equation is the force due to the electric field. Compared to that of the electric field, the force exerted on the electrons by the magnetic field is negligible. Solving the differential equation of (2-25) by applying the relation of (2-24) yields,

$$\varepsilon_{Drude}(\omega) = \varepsilon_\infty - \frac{\omega_p^2}{\omega^2 + \Gamma_{bulk}^2} + i\frac{\omega_p^2 \Gamma_{bulk}}{\omega(\omega^2 + \Gamma_{bulk}^2)} \qquad (2-26)$$

The real part of the expression (2-26) is responsible for group velocity dispersion and imaginary part describes the dissipation of energy associated with the motion of electrons in the metal. For ω larger than plasmon frequency ω_p, the metal becomes transparent and radiation can propagate without absorption.

The experimental model of optical constants of noble metals (copper, silver, and gold) obtained by P. B. Johnson and R. W. Christy through reflection and transmission measurements is an acceptable reference for evaluating the accuracy of Drude model [20]. In Figure 2-4, the real and the imaginary parts of dielectric function of gold simulated by Drude model are compared with Johnson & Chrisity data.

As it is evident from these graphs, Drude model demonstrates a good prediction for negative real part of permittivity of gold in wavelength higher than 450 nm, but unfortunately this model doesn't have an acceptable calculation for the imaginary part in visible range of

frequency. Deviation of Drude model from experimental data mostly comes from this fact that this model is based on free electron theory and the effect of bound electrons is not considered. Consequently, the resonance frequency ω_0 from the standard Lorentz model is zero and it has not appeared in above analysis.

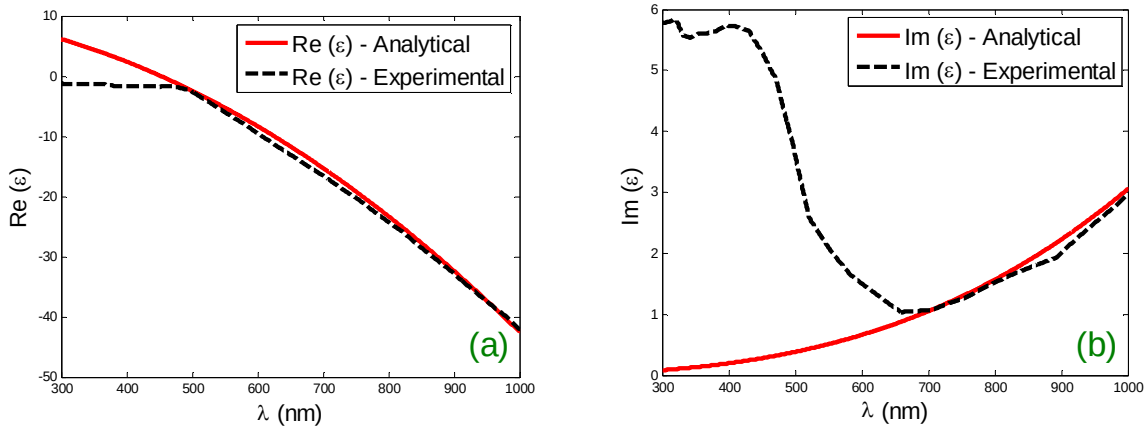

Figure 2-4 (**a**) Real and (**b**) imaginary part of the dielectric constant for gold according to the Drude free electron model (solid lines) and Johnson&Christy data (dashed lines) (ω_p=13.8×10^{15} s^{-1}, Γ = 1.075×10^{14} s^{-1}).

2.7 Size Dependent Correction on Drude Model

The appeared term of Γ_{bulk} in dielectric function equation is closely related to the resistivity of the metal. In fact, due to presence of this term, the dielectric constant of metal contains an imaginary part. The inverse of Γ_{bulk} defines as mean electron collision time. According to following equation, Γ_{bulk} is related to the electron mean free path l (25 nm for gold and 40 nm for silver) and the Fermi velocity v_f (1.4×10^6 m/s for Au).

$$\Gamma_{bulk} = \frac{v_f}{l} \qquad (2-27)$$

In fact, the term of damping frequency incorporates inelastic collisions of electron-electron, electron-phonon, electron-defect and electron-impurities type. Thus, the damping term usually on the order of hundredths of an electron volt is thus expressed as a sum of the relaxation rates for each of these processes [4,21].

$$\Gamma_{bulk} = \frac{1}{\tau_{e-e}} + \frac{1}{\tau_{e-p}} + \frac{1}{\tau_{e-d}} \qquad (2-28)$$

As a result of the surface effects, for NPs much smaller than the electronic mean free path of the bulk metal, new contributors on scattering process appear, resulting in a huge increase in the rate of scattering from the surface of the NP. Therefore, in order to provide a complete

definition for a size dependent damping frequency, an additional term as radiative damping of electron-surface scattering is added to the bulk damping constant,

$$\Gamma(r) = \Gamma_{bulk} + A\frac{v_f}{r_p} = v_f\left(\frac{1}{l} + A\frac{1}{r_p}\right) \qquad (2-29)$$

where r_p is the size of NP and A incorporates the nature of the surface scattering processes which is 0 for elastic,¾ for diffusive, and 1 for isotropic [22]. This surface scattering term overshadow absorption band of gold and silver NPs smaller than about 2 nm and 1.5 nm, respectively and create a complete damping in surface plasmon band [6,23]. By substituting Γ_{bulk} with $\Gamma(r)$, the size dependent correction for the frequency dependent dielectric constant (equation 2-26) can be expressed by following formula [19]:

$$\varepsilon_{Drude}(\omega, r) = \varepsilon(\omega) + \frac{\omega_p^2}{\omega^2 + i\omega\Gamma_{bulk}} - \frac{\omega_p^2}{\omega^2 + i\omega\left(\Gamma_{bulk} + A\frac{v_f}{r_p}\right)} \qquad (2-30)$$

Evidently, the dielectric response of nanoparticle is isolated in two terms. The first part is equal to the bulk constant and the second term is responsible to consider the size effect on dielectric constant.

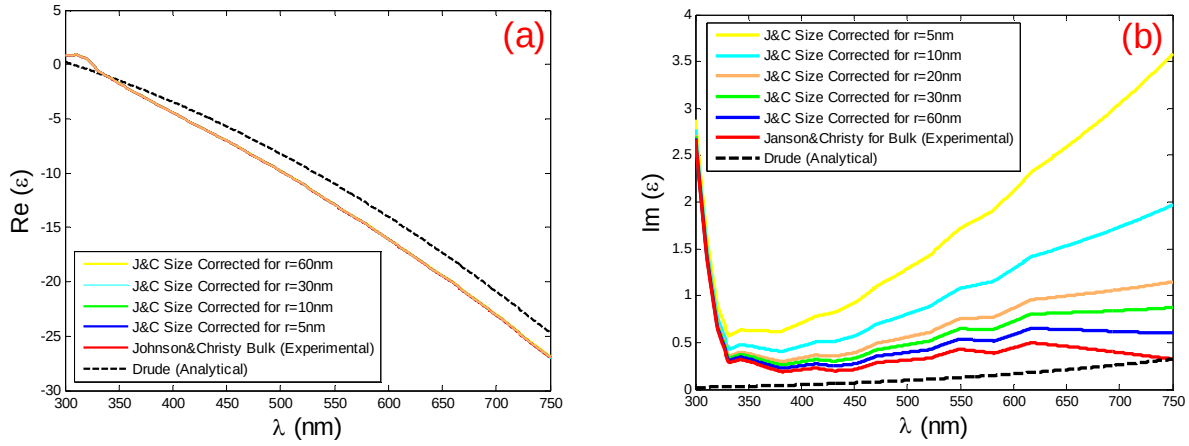

Figure 2-5 (**a**) Real and (**b**) imaginary part of the dielectric constant for silver according to the Drude free electron model (dashed lines) and Johnson & Christy data (solid lines) (ω_p=13.8×10^{15} s^{-1}, Γ = 27.3×10^{12} s^{-1}, l=40 nm, v_f =1.4×10^{16} m/s). The influence of size effect on modification of experimental model has been illustrated.

Consider that introducing size dependent damping frequency is important for obtaining a more reliable prediction of optical losses. Therefore, in order to increase the accuracy of this model for predicting nanospheres dielectric function, the size correction term can be applied on Johnson & Christy experimental data obtained for bulk metals (Figure 2-5(b)).

2.8 Band electron effects on Drude Model

The Drude model for the dielectric function in (2-26) is an elegant and concise treatment for the optical properties of noble metals. However, it has to be modified to reflect reality by taking into account the contribution from bound electrons for high frequency operations.

The induced dipolar charge repartition imposes a new force on the electron cloud. The electrons undergo a restoring force that conflicts with the external electric field. By considering the system equivalent to classical mechanical oscillators, the position, *x*, of an electron placed in the oscillating cloud of a nanoparticle is then governed by following equation, where *K* is the spring constant of the potential that keeps the electron in place and γ symbolizes the damping constant describing mainly radiative damping in the case of bound electrons with effective mass m_e [17].

$$m_e \frac{\partial^2 x}{\partial t} + m_e \gamma \frac{\partial x}{\partial t} + Kx = eE_0 e^{(-i\omega t)} \qquad (2-31)$$

This equation describes the movement of a forced, damped harmonic oscillator. The contribution of bound electrons to the dielectric function can be written in a standard Lorentz form as:

$$\varepsilon_{ib}(\omega) = 1 + \frac{\hat{\omega}_p^2}{\omega_0^2 - \omega^2 - i\gamma\omega}, \qquad (2-32)$$

Here $\hat{\omega}_p$ is introduced in analogy to the plasma frequency in the Drude model related to the density of bound electrons. Also, $\omega_0 = \sqrt{K / m_e}$ denotes the oscillation frequency of a bound electron under an applied electric potential [19]. Therefore the modified dielectric constant in the UV–Vis–NIR regime is composed of two terms: ε_{ib} is the contribution of d–bands electrons and ε_{Drude} is that of s–band conduction electrons.

$$\varepsilon(\omega, r) = \varepsilon' + i\varepsilon'' = \varepsilon_{ib} + \varepsilon_\infty - \frac{\omega_p^2}{\omega^2 + i\Gamma_\infty \omega} \qquad (2-33)$$

The contribution of bound electrons to the dielectric constant of gold has illustrated in Figure 2-6, clear resonant behavior is observed for the imaginary part and a dispersion-like behavior for the real part. The dielectric function of gold is distorted moving towards the positive ε direction, associated with increased loss for blue and green light. Thus, due to the strong absorption of blue and green light by the gold, predominantly yellow light reflected back to the observer.

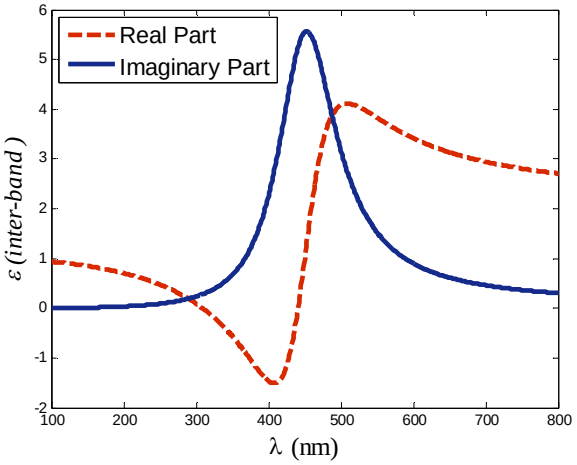

Figure 2-6 Contribution of bound electrons to the permittivity of gold at visible frequencies. The parameters used are $\widehat{\omega}_p = 46\times10^{14}(s^{-1})$, γ = 0.6 eV and $\omega_0=2\pi C/\lambda$, with λ_0=450 nm. The dashed red curve is the real part and the solid blue curve is the imaginary part of the dielectric function due to bound electrons.

Figure 2-7 is a plot of the dielectric constant (real and imaginary parts) of modified Drude model in comparison with Johnson & Christy experimental model for gold. For wavelengths above 650 nm the behavior clearly follows the Drude theory, while for wavelength below 650 nm obviously interband transitions become significant. One can try to model the shape of the curves by adding up the free-electron (equation 2-26) and the interband absorption contributions (equation 2-33) to the complex dielectric function (squares) and indeed, this much better reproduces the experimental data.

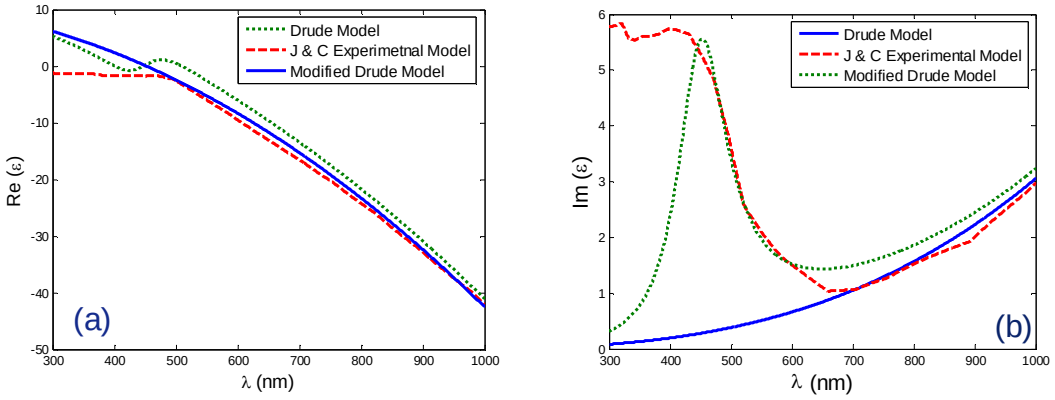

Figure 2-7 (**a**) real and (**b**) imaginary parts of dielectric function of gold: Experimental values from Johnson & Christy data (red dashed curves), Drude model (blue solid line) and modified Drude model (green dotted line). The parameters used are ω_p=13.8×10^{15} s^{-1}, Γ=1.075×10^{14} s^{-1}, γ=0.6 eV, λ_0=450 nm and $\widehat{\omega}_p = 46\times10^{14}s^{-1}$.

The observed negative permittivity of noble metal NPs in visible range of frequency can bring this idea in mind to use them as building blocks of plasmonic metamaterials. Additional

advantages such as simple preparation techniques for a wide range of sizes and shapes and easy surface conjugation to a variety of ligands, make them a promising candidate for optical metamaterial applications.

2.9 Maxwell-Garnett Theory

Historically, the "effective medium theory", one the first approaches for describing interactions between light and nanostructures has been published in the very beginning of the 20th century, by Maxwell–Garnett [24,25]. The developed model gives the expression of the dielectric constant of nanocomposite materials composed by a host medium (dielectric constant ε_m) containing randomly dispersed small metallic spheres [4]. The size of the spheres is small compared to the wavelength and the material under consideration has a spatial extension larger than the wavelength. The spheres are considered as small Hertzian doublets that provide the polarisability of the medium. Maxwell-garnett approach can be useful to explain the overall dielectric properties of a material when randomly dispersed metal NPs are present in high concentration, in which the plasmon absorption of each single metallic NP is affected by other particles present in the surrounding matrix. Applying Maxwell equations and the expression of the electric field caused by a sphere, the effective dielectric constant ε_{eff} of the nanocomposite matrix, according to the so-called Clausius-Mossotti formula can be derived by the following expression [26,27]:

$$\frac{\varepsilon_{eff} - \varepsilon_h}{\varepsilon_{eff} + 2\varepsilon_h} = f \frac{\varepsilon_{np} - \varepsilon_h}{\varepsilon_{np} + 2\varepsilon_h} \qquad (2-34)$$

where ε_{np} and ε_h are the dielectric constants of NPs and the host matrix, respectively. $f=nV$ is the fill fraction of particles, a dimensionless quantity signifying the volume fraction of the inclusions in the mixture, where V is the volume of the sphere and n is the number density of inclusions. Note that because only the volume fraction and the permittivities appear in the mixing rule, the spheres are not required to have the same size and shape if only all of them are small compared to the wavelength of the propagating light. Perhaps the most common mixing rule is the Maxwell Garnett formula written explicitly for the effective permittivity.

$$\varepsilon_{eff} = \varepsilon_h + 3f\varepsilon_h \frac{\varepsilon_{np} - \varepsilon_h}{\varepsilon_{np} + 2\varepsilon_h - f(\varepsilon_{np} - \varepsilon_h)} \qquad (2-35)$$

This formula is in wide use in very diverse fields of application. The beauty of the Maxwell Garnett formula is its simple appearance combined with its broad applicability. It satisfies the limiting processes for vanishing inclusion phase ($f \to 0$) the effective dielectric constant approaches to permittivity of host medium ε_h and for vanishing background ($f \to 1$), ε_{eff} moves toward the dielectric constant of nanoparticles (ε_{np}).

2.10 Kramers-Kronig Relations

The real and imaginary parts of the complex optical functions such as surface impedance dielectric function or the index of refraction are not wholly independent but both are connected by a special form of the Hilbert transforms. The relations that describe the existence of a fundamental connection between the real (dissipative) and imaginary (absorptive) parts are termed Kramers-Kronig relations and also referred to as dispersion relations [28].

Actually, measuring the real and imaginary part of the susceptibility requires different experimental set-ups and instruments such as spectroscopic ellipsometry. But, applying Kramers-Kronig relations which provide the possibility to perform the so-called inversion of optical data, in which information on dispersive phenomena, can be obtained by measurements of absorptive phenomena over the whole spectrum or vice versa. [29,30].

The conceptual foundations of such general properties lie upon the basic physical principle of causality [31]. This principle expresses that the polarization response of a medium to an electric excitation cannot precede its cause. Therefore, such response can be explicitly calculated by taking the convolution in the time domain only over past events. The following Kramers-Kronig relations demonstrate the correlation between the real and imaginary parts of the susceptibility function $x(\omega)$.

$$\mathrm{Re}[x(\omega)] = -\frac{2}{\pi} PV \int_0^{\infty} \frac{\mathrm{Im}[x(\omega')]\omega'}{\omega'^2 - \omega^2} d\omega' \qquad (2-36)$$

$$\mathrm{Im}[x(\omega)] = -\frac{2\omega}{\pi} PV \int_0^{\infty} \frac{\mathrm{Re}[x(\omega')]\omega'}{\omega'^2 - \omega^2} d\omega' \qquad (2-37)$$

Here the function of $x(\omega)$ refers to the susceptibility of the material and *PV* stands for the principal value part, which means that in the integration, the singular point $\omega' = \omega$ is symmetrically excluded. These relations, connected to the Hilbert transform, are useful in the analysis of the dispersive properties of materials.

2.11 Tunability of the Absorption Band of Nanoparticles

The position, the shape and the intensity of the surface plasmon band strongly depends on various factors such as the composition of metal, size and shape/geometry, as well as the composition of the surrounding medium or environment, monodispersity of the NPs and the electronic interactions between the stabilizing ligands with NPs [1]. Variation in these parameters allows tunability of the plasmon resonance frequency, the intensity of the plasmonic enhancement, and as well as the bandwidth of the plasmon band. In this part we investigate how the properties of the SPB of NPs can be modified under the influence these parameters.

2.11.1 Size Effect

The Mie theory predicts a size dependence of the intensity of the plasmon band (equation (2-11)). The bandwidth of SPB is also affected by size of NP, but through intrinsic effects, which means that the size parameter can modify the expression of the dielectric constant of the metal through ω_d, the size-dependent damping frequency (equation 2-29). As a result of higher values for damping frequency, particles smaller than 10 nm diameter have a resonance that is significantly broadened in inverse proportion to the nanoparticle size r_p [32]. Figure 2-8 shows the extinction spectra for gold NPs of different sizes calculated using Mie theory. As it is evidenced, the broadening of surface plasmon band for 5 and 10 nm NPs is more pronounced respect to larger ones with size less than 50 nm. However, these results show that larger NPs are also subject to broadening of the plasmon resonance bandwidth due to dominant contribution of scattering in extinction of light field.

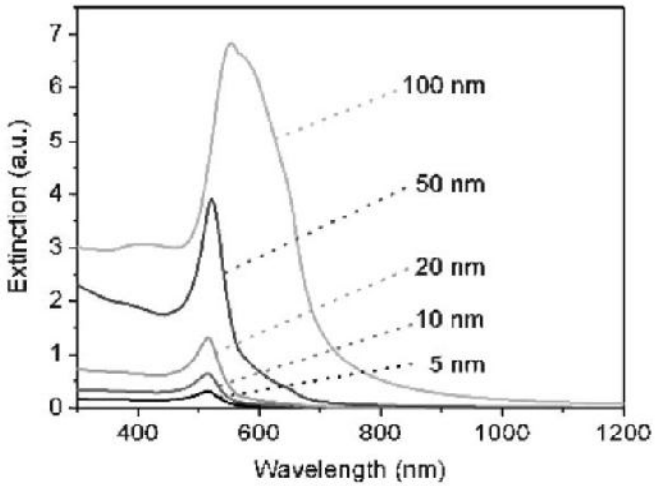

Figure 2-8 Extinction spectra (Q_{ext}) calculated using Mie theory for gold nanospheres with diameters varying from 5 nm to 100 nm [33].

On the other hand, as it has mentioned before, once the particle size is comparable to the incident light wavelength, the particle no longer experiences a uniform electromagnetic field. As a result of this phase retardation a red shift of the dipole resonance occurs. Qualitatively, larger the metal nanoparticle is, the higher its surface plasmon absorption wavelength. In addition, the effects of phase retardation in larger size NPs are responsible for the excitation of higher order multipoles in the plasmon resonance, which are blue shifted with respect to the main dipole resonance of the particle [1].

2.11.2 Metal Composition Effect

Electromagnetic characteristic of any material can be different from the other one, and this is not an exception for noble metals. According to the expression of extinction cross section in equation (2-11) both the intensity and position of plasmon band of a spherical NP are related to dielectric constant of applied noble metal. Moreover, the expression of Fröhlich frequency in equation (2-14) reveals the strong dependence of resonance frequency to metal composition, in which increasing of this parameter results in red shift in the wavelength position of plasmon band. As an evidence for this fact, Figure 2-9 illustrates how the surface plasmon absorption band of NPs can be influenced by constituent metal.

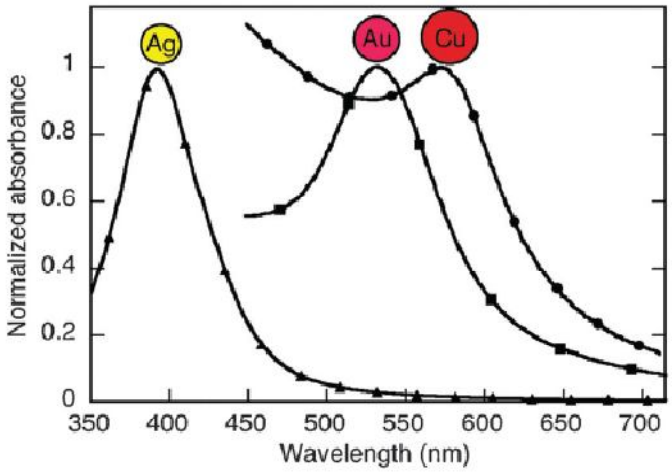

Figure2-9 Surface plasmon absorption band of Au, Ag and Cu nanoparticles [34].

2.11.3 Surrounding Medium Effect

The expression of extinction cross-section for small NPs provided in equation (2-11) clearly shows that the host medium plays a predominant role in determining both the plasmon

peak position and intensity. Typically by increasing the dielectric constant of surrounding medium the intensity of absorbance band diminishes.

The refractive index of the medium surrounding the metal particles can influence the frequency position of surface plasmon bands. Assuming that an oscillating weighted spring represents the electric field of the SP and a high dielectric medium stands as a viscous medium like oil. The oscillation frequency of mass-spring system decrease in a vacuum will be higher than in the oil. Fröhlich equation justifies this fact and further expresses the remarkable dependence of the resonance frequency on the dielectric environment: the resonance shifts to higher wavelength as ε_h is increased.

For instance, transferring NPs from water or ethanol to a transparent oxide matrix induces a remarkable shift on plasmon band of dissolved gold NPs [35]. This fact has been illustrated in Figure 2-10 nicely, in which the color (plasmon peak position) of NPs solution change with respect to variation of solvent refractive index.

Figure 2-10 plasmon peak position variation induced by changing the solvent refractive index. Refractive indices of the solutions at the absorption band maximum are 1.336, 1.407, 1.481, 1.525 and 1.583, respectively [36].

2.11.4 Shape Effects

As a response to the induced polarization in NP, the bound electrons undergo a restoring force which conflicts with the external electric field. The magnitude of such force depends on the shape of the electron cloud and the polarization of the light. Quantitatively, for any general shape the polarizability is given as [7]:

$$\alpha = \frac{\varepsilon_0 V}{L_{dp}} \left(\frac{\varepsilon - \varepsilon_h}{\varepsilon + \frac{1 - L_{dp}}{L_{dp}} \varepsilon_h} \right) \qquad (2-38)$$

L_{dp} is a depolarization factor, which depends on the shape. For a sphere, which is isotropic in all three dimensions, L_{dp}=1/3, which reduces equation (2-38) to the expression of polarizability in equation (2-8). The plasmon resonance condition which summarizes the effect of the nanoparticle shape (through L_{dp}) on the surface plasmon resonance frequency is extracted from equation (2-38) as following [7]:

$$\varepsilon = -(\frac{1-L_{dp}}{L_{dp}})\varepsilon_h \qquad (2-39)$$

By considering L_{dp}=1/3 for a spherical nanoparticles the resonance situation in equation (2-12) can be reconstructed again.

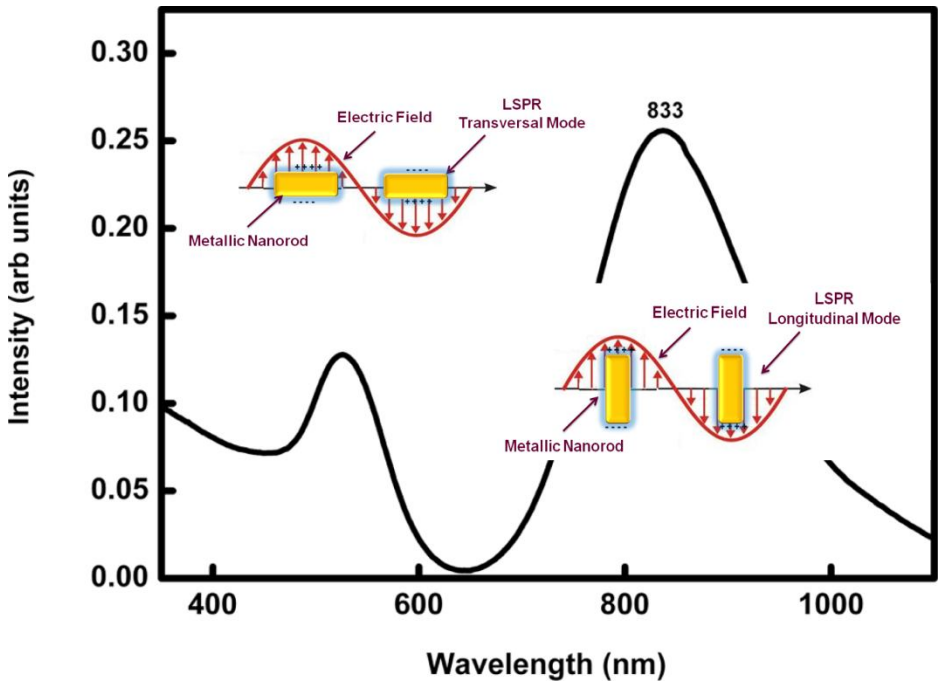

Figure 2-11 Scheme which explains the presence of two peaks of Transverse and Longitudinal in the absorption spectra of a nanorod structure.

As per the theory developed by Gans [37] spherical particles have three values for depolarization factor, corresponding to each of the three axes A, B, C. Since for a cylindrical shape A > B = C, there are two unique modes of electron oscillation giving rise to two SPR modes [38,39]. The short-wavelength SPR mode is due to electron oscillation along the spheroid short-axis, corresponding to $L_{B=C}$. The second mode arises from electron oscillation along the spheroid long-axis, corresponding to L_A. The presence of these two modes can be ascribed by electron oscillations across and along the long axis of the nanorod, respectively and therefore termed transverse and longitudinal modes accordingly (Figure 2-11).

In fact for nanorods, the boundary conditions in Mie theory have to be modified in order to describe their plasmonic properties. Unfortunately, it is not possible to obtain analytic expressions for particles with an arbitrary shape [1].

2.11.5 Aggregation effect

Aggregation of nanoparticles modifies the characteristics of plasmonic systems and creates a new plasmon absorbance position along with a decrease in the intensity of the plasmon absorbance, which leads to a pronounced color transition from red to purple [40]. The observed red shift on resonance wavelength of aggregated NPs originates from plasmonic couplings between attached particles. For an instance, as it illustrated in figure 2-12, the plasmon absorbance position of gold NPs with the size changing from 12 to14 nm dissolved in water appears near 527 nm. But, as a result of the aggregation process a broad plasmon band, with a reduced intensity comes out with a peak position around 575 nm.

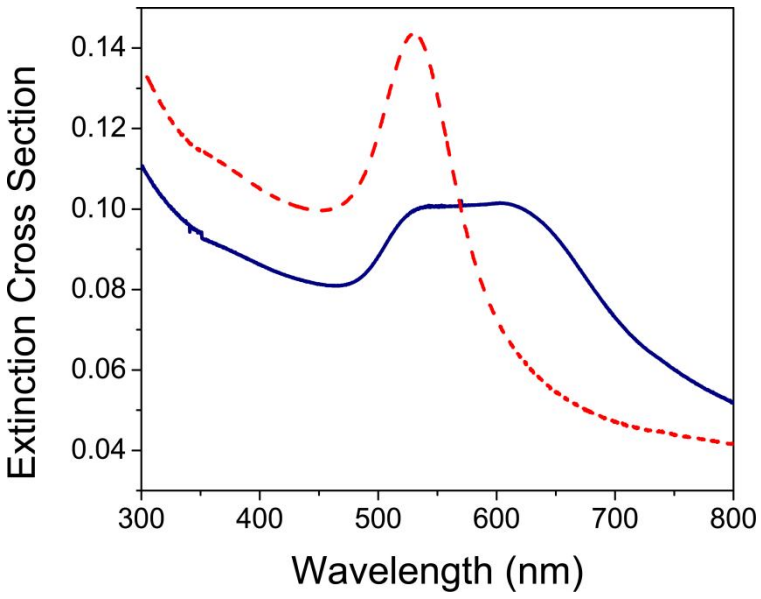

Figure 2-12 Experimental extinction cross section spectra of mono-dispersive (dashed red curve) and aggregated (blue solid curve) aqueous gold NPs with diameter of 12 nm.

REFERENCES

1. A. Moores, and F. Goettmann, *New J. Chem*., **2006**, 30, 1121.
2. J. M. Pitark, V. M. Silkin, E. V. Chulkov, and P. M. Echenique, J. *Optics A-Pure App. Op*., **2005**, 7, S73.
3. P. Mulvaney, *Langmuir*, **1996**, 12, 788.
4. N. Mirlin, "*Surface phonon polaritons in dielectrics and semiconductors"*, North-Holland Publishing Company, Amsterdam, 1982.
5. U. Kreibig, and M. Vollmer, "*Optical Properties of Metal Clusters"*. Springer, New York, 1995.
6. Y. Xia, and N. J. Halas, *MRS Bulletin*, **2005**, 30, 338.
7. K. L. Kelly, E. Coronado, L. L. Zhao, and G. C. Schatz, *J. Phys. Chem. B*, **2003**, 107, 668.
8. P. K. Jain, K. S. Lee, I. H. El-Sayed, and M. A. El-Sayed, *J. Phys. Chem.*, **2006**, 110, 7238.
9. C. Sonnichsen *et al., Phys. Rev. Lett.*, **2002**, 88, 077402.
10. S. Link, and M.A. El-Sayed, *Annu. Rev. Phys. Chem.*, **2003**, 54, 331.
11. X. Huang, P. K. Jain, I. H. El-Sayed, and M. A. El-Sayed, *Nanomedicine*, **2007**, 2, 681.
12. M. Gustav, *Ann. Phys.*, **1908**, 25, 377.
13. H. Haberland, "*Clusters of Atoms and Molecules"*, Springer-Verlag, Berlin, New York, 1994.
14. H. C. van de Hulst, "*Light Scattering by Small Particles"*, Dover Publications, New York, 1981.
15. G. F. Bohren, "*Absorption and Scattering of Light by Small Particle"*, Wiley, New York, 1998.
16. U. Kreibig, and C. Fragstein, *Z. Phys.*, **1969**, 224, 307.
17. C. Kittel, "*Introduction to Solid State Physics"*, Wiley, New York, 1996.
18. S. Link, and M. A. El-Sayed, *Int. Rev. Phys. Chem.*, **2000**, 19, 409.
19. N. W. Ashcroft, and N. D. Mermin, "*Solid State Physics"*, HOLT, Rinehart and Winston, New York, 1976.
20. P. B. Johnson, and R. W. Christy, *Phys. Rev. B*, **1972**, 6, 4370.
21. S. Link, Z. L. Wang, and M. A. El-Sayed, *J. Phys. Chem. B*, **1999**, 103, 3529.
22. T. Okamoto, "*Near-field optics and surface plasmon polaritons"*, vol. 81 of Topics in Applied Physics, Springer, Newyork, 2001.
23. M. C. Daniel, and D. Astruc, *Chem. Rev.*, **2004**, 104, 293.
24. J. C. Maxwell-Garnett, *Philos. Trans. R. Soc. A*, **1904**, 203, 385.

25. J. C. Maxwell-Garnett, *Philos. Trans. R. Soc. A*, **1905**, 205, 237.

26. W. T. Doyle, *Phys. Rev. B*, **1989**, 39, 9852.

27. R. Ruppin, *Opt. Commun.*, **2000**, 182, 273.

28. R. Kronig, *J. Opt. Soc. Amer.*, **1926**, 12, 547.

29. D. E. Aspnes, "*The accurate determination of optical properties by ellipsometry*", in Handbook of Optical Constants of Solids, E. D. Palik, ed., Academic Press, New York, 1985.

30. K. E. Peiponen, E. M. Vartiainen, and T. Asakura, "*Dispersion, Complex Analysis and Optical Spectroscopy*", Springer, Heidelberg, 1999.

31. P. W. Milonni, *J. Phys. B, At. Mol. Opt. Phys*., **2002**, 35, R3.

32. S. Link, and M. A. El-Sayed, *J. Phys. Chem. B*, **1999**, 103, 4212.

33. G. C. Prog. Papavassiliou, *Solid State Chem.,* **1980**, 12, 185.

34. J. C. Scaiano *et al*., *Appl. Chem.*, **2011**, 83, 913.

35. F. Goettmann, A. Moores, C. Boissiere, P. Le Floch and C. Sanchez, *Small*, **2005**, 1, 636.

36. S. Underwood, and P. Mulvaney, *Langmuir*, **1994**, 10, 3427.

37. R. Gans, *Ann. Phys.* **1912**, 37, 881.

38. S. Link, M. B. Mohamed, and M. A. El-Sayed, *J. Phys. Chem. B*, **1999**, 103, 3073

39. J. Erratum, *Phys. Chem. B*, **2005**, 109, 10531.

40. S. Solomon, *et al*., *J. Chem. Educ.*, **2007**, 84, 322.

Chapter 3

Overview on Fluorescence Spectroscopy

3.1 Introduction

The absorptive properties of plasmonic nanostructures operating at optical frequencies drastically influence the FOM of a metal NPs based metamaterial. Hence, in order to improve the performance of the plasmonic metamaterials the optical losses of NPs must be mitigated. In this thesis, the proposed solution and applied technique is to bring gain materials such as organic dye molecules or quantum dots in close vicinity of absorptive NPs. Nonradiative energy transfer processes between active materials and plasmonic NPs creates the opportunity for optical loss compensation.

The objective that this chapter traces is to create a background for optical properties of gain materials and fluorescence spectroscopy techniques which are used to characterize them. The discussion starts by introducing Jablonski diagram which explains corresponding processes, resulted from the interaction of light with a chromophore. In the second part of this chapter, the optical properties of the fluorescent materials used for energy transfer purposes are explored.

Finally, this chapter is completed by investigation of static and dynamic techniques of fluorescence spectroscopy.

3.2 Photoluminescence Process and Jablonski Diagrams

Photoluminescence (PL) is the process which a chromophore acquires the required energy for emitting photon by absorbing the coming photons of light sources [1]. This process can be categorized in two types: fluorescence and phosphorescence, depending on whether the transition to the ground state is spin-allowed or spin-forbidden, respectively.

In order to understand the complex processes of PL, the energy levels in a molecule must be defined. These levels can be classified in energy terms in the following order rotational, vibrational and electronic. The energy of rotational levels is less than vibrational ones while electronic levels possess much higher energy than the others. The difference between each of these transitions typically is an order of magnitude. Rotational transitions occur at lower energies in the microwave region, with energies typically of 10^{-3} eV. Vibrational transitions occur in the near infra-red region, requiring energies more than 10^{-1} eV. Finally, electronic transitions by acquiring energies higher than 1 eV can occur in the ultraviolet and visible region of the electromagnetic spectrum [2].

The energy levels of a chromophore and its relaxation process via radiative and nonradiative pathways can be illustrated by the Jablonski diagrams [3]. These diagrams are used in a variety of forms to illustrate processes that can occur in excited states. These diagrams are named as honor of Professor Alexander Jablonski, who is regarded as the father of fluorescence spectroscopy [4]. Figure 3-1 demonstrates an example of Jablonski diagram for explaining excitation and relaxation processes of a fluorescent molecule. In this diagram, electronic states for an organic molecule are showed by the letter S for singlet states and the letter T for triplet states. A singlet state is one in which all of the electrons in the molecule have their spins paired. Triplet states are those in which one set of electron having unpaired spin [5]. The vibrational ground states of each electronic state are indicated with thick lines, the higher vibrational represented with groups of horizontal thinner lines. The radiative processes which include fluorescence and phosphorescence are referred by straight lines, while the nonradiative ones by dashed arrows. In the following subsections, all the processes are explained when a chromophore undergoes the irradiation of light

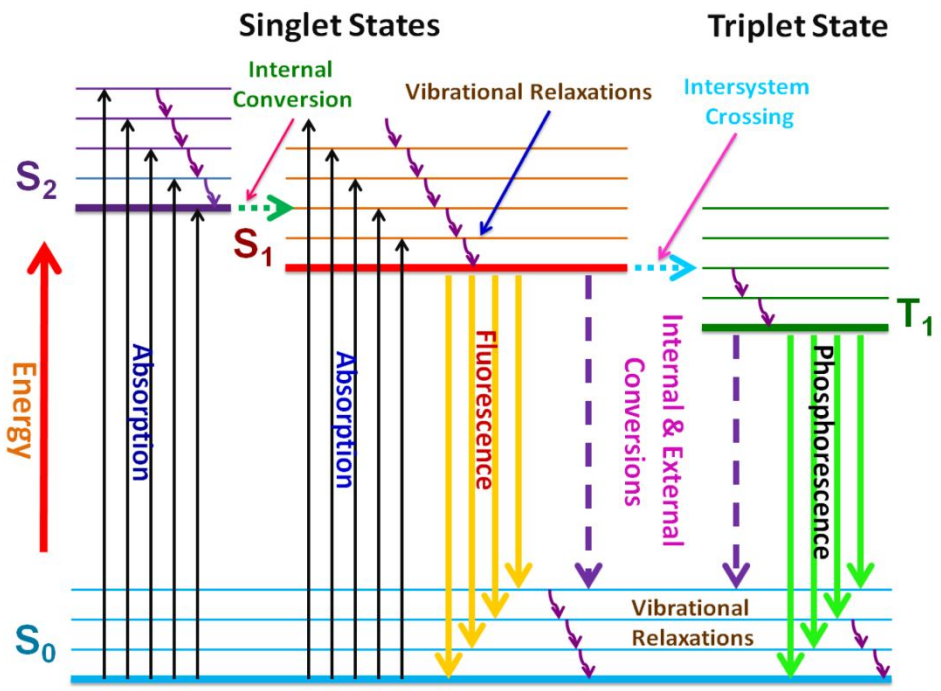

Figure 3-1 Jablonski diagram showing the de-excitation pathways of a molecule including fluorescent and phosphorescent Components.

3.2.1 Absorption and Fluorescence Processes

Each of excited and ground states has different levels of the energy. The energy of each state can be describe by $E=hv$, where v denotes frequency of photon and h is the Planck constant. The gap energy between excited state and ground state is described by

$$E_{gap} = E_1 - E_0 = hv_1 - hv_0 \qquad (3-1)$$

where E_0 is the energy of the ground state and E_1 is the energy of meta-stable state or energy of emission signal. A fluorophore molecule can absorb a photon with energy equal or greater than the energy difference between the ground and excited state (E_{gap}), while the photons will lower energies will be transmitted. The energy of E_{gap} for thermal population of S_1 energy level at room temperature is too much, and this is the reason why light must be applied to induce fluorescence [5].

As a result of the light absorption by a molecule, one of its electrons from the occupied orbital is promoted to an unoccupied orbital or in the other word the valence electron is transferred to the excited electron. As a result of this process, this electron is promoted to a higher electronic orbital, thus putting the molecule into the excited state. This transition period between states is very fast, of the order of 10^{-15} s. Absorption of light by a molecule can be described according to principles explained by the Lambert-Beers Law [6].

The excited electrons release rapidly their energy to the lowest level of singlet by two methods of vibrational relaxations and in the case of populating higher excited singlet states (S_2) by internal conversion, both toward the lowest singlet level of an excited state (S_1). Depopulation of meta-stable state S_1 which is accompanied by emitting a photon is referred as fluorescence or simply emission. For fluorescence processes, the period of time between absorption and emission is extremely short. In this case electron stays in the S_1 excited state typically for 10^{-8}s and returns to the ground state S_0 very quickly, on the order of 10^{-15} s.

It is clear from Jablonski diagram that due to the presence of rotational and vibrational relaxation the energy of the emission is typically lower than the energy of the absorption. Therefore, fluorescence generally occurs at lower energies or longer wavelengths respect to absorption. As it illustrated in Figure 3-2, the difference in energy (or wavelength) between the absorbed photon and the emitted photon is often referred as the Stokes shift.

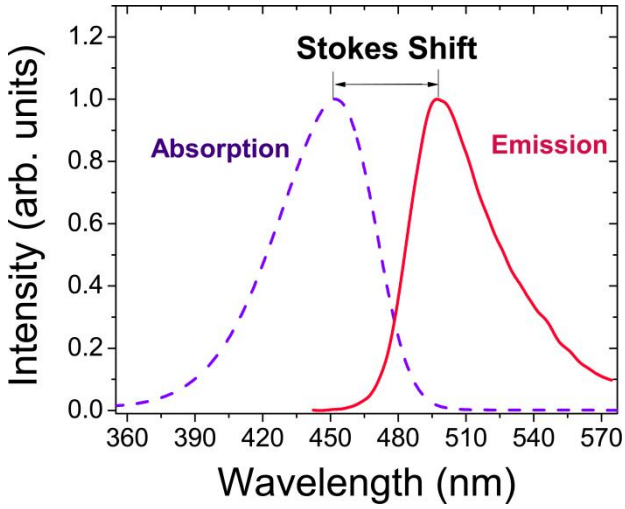

Figure 3-2 Stokes shift between absorption (blue dashed curve) and emission spectra (red solid curve) of Coumarine 334 dye molecules dissolved in ethanol.

The entire fluorescence process is cyclical. Therefore, the same fluorophore can be repeatedly excited and detected. Unless the fluorophore irreversibly being destroyed in the excited state. Such an important phenomenon is known as photobleaching, which can occur under irradiation of an excitation source with higher values of intensity [7].

3.2.2 Internal and External Conversion

In addition to radiative processes, one also encounters radiationless processes where molecules in an excited singlet state may come back to the ground state without photon emitting, converting all the excitation energy into heat. If the excited-state fluorophore is deactivated upon

contact with some other molecule in solution, collisional quenching occurs. Collisional deactivations of excited molecules which lead to nonradiative relaxation are termed as external conversion.

The internal conversion is the other radiationless process, which includes both direct vibrational coupling between the ground and excited electronic states (vibronic level overlap) and also quantum mechanical tunneling (no direct vibronic overlap but small energy gap). In addition, as it is illustrated in Figure 1-3, if a molecule is excited to a higher singlet state such as S_2, relaxation of the excited molecule to the zeroth vibrational level of the S_1 state is the case of internal conversion, as well. Consider that this process can be happened, if the overlap between lowest vibrational level of S_2 with higher vibrational levels of the S_1 state are existed.

3.2.3 Phosphorescence and Intersystem Crossing

Populating of triplet states by direct absorption from the ground state is insignificant. In many molecules, transitions between lowest singlet and triplet states act as more efficient processes for population of triplet states. This vibrational coupling occurs, if the energy states of the singlet state overlap those of the triplet state. This phenomenon is a nonradiative process with a lifetime of 10^{-9} s. The spin and therefore energy of the electron which undergo intersystem crossing changes and therefore they relax into a triplet state (T_1). Transition from this triplet state to the singlet ground state which is accompanied by the photon emission is called Phosphorescence. Because this is a classically forbidden transition, the triplet state has a long lifetime. Hence the rate of phosphorescence is slow and it happens in time range of 10^{-3}s up to even a few seconds or as long as minutes [5]. Since triplet states are in lower energy respect to singlet states, the phosphorescence signal of fluorophore always appears in higher wavelength respect to the fluorescence.

Furthermore, the molecules which have populated the lowest vibrational level of triplet state undergo the nonradiative internal and external conversion process for returning to ground state (Figure 3-1). Indeed, these radiationless transitions between the lowest triplet state and the ground state is more enhanced than between lowest singlet state and ground state, because of two factors. First the energy difference between the triplet state and the ground state is smaller than the difference between the lowest singlet state and the ground state. Second, and more important, the life time of a triplet state is much longer than that of an excited singlet state and therefore loss of excitation energy by collisional transfer is generally enhanced.

3.3 Fluorescent Materials

Fluorescent materials (Chromophores) have the possibility to absorb photons of impinged excitation light and re-emit light in a wavelength of visible light spectrum, but different from the energy of the excitation light. Researchers have explored different applications of these materials in chemical sensing, solar cells, LEDs, biosensors, diode lasers or as fluorescence probes in fluorescence spectroscopy. Nevertheless, as it is showed in this thesis, there is possibility for applying the fluorescent materials as an alternative for compensating the absorptive loss of plasmonic NPs. Since these materials are supposed to transfer the energy to lossy nanostructures, the term of gain materials or active materials are exploited to refer them. Two main groups of gain materials are applied in this research study: organic fluorophores and semiconductor quantum dots. In the following subsections the optical properties of both materials are investigated and advantage and shortcoming of them are explored.

3.3.1 Organic Dyes Molecules

Fluorophores or simply fluorescent dye molecules are small organic chemical compounds which can emit light in visible range. These emissive molecules typically contain several combined aromatic groups, or planar or cyclic molecules with several π bonds as responsible for photon absorption and emission.

The possibility to find a fluorophore with a large quantity of stock shift, high values of quantum yield, desire shape and position of emission and absorption band make them popular for energy transfer purposes. Moreover, development of well controlled synthesis methods for incorporation of dye molecules in close proximity of plasmonic structures, make them a promising alternative for mitigating NPs absorptive losses. Figure 3-3 illustrates the emission spectra of different dye molecules dispersed in ethanol. The prepared solutions are pumped at 355 nm with a pulsed laser. Since emission always happens from the lowest excited level, so the applied excitation wavelength does not affect significantly the shape of the emission spectrum. However, the emission intensity changes respect to the amplitude of the excitation light and concentration of the fluorophore in solution.

Fluorescent dye molecules beside all mentioned perfect characteristics, contain some drawbacks such as typically narrow absorption bands, low chemical and optical stability, and fast fluorescence emission of the dyes (<8 ns), which in a system with short-lived fluorescence

background results in diminution of the signal-to-noise ratio [8]. However, QDs can cover perfectly the negative aspects of dye molecules.

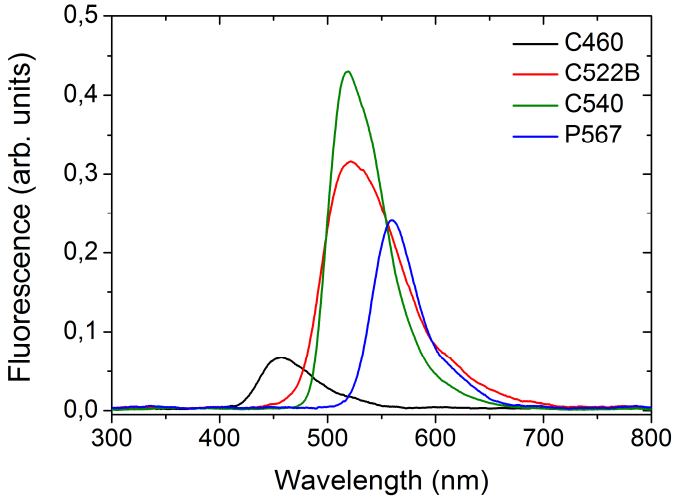

Figure 3-3 Fluorescence spectra of different dye molecules dissolved in ethanol pumped by a pulse laser at 355 nm.

3.3.2 Fluorescent Quantum Dots

Quantum dots (QDs) are semiconductor based fluorescent nano-crystals (NCs), which can demonstrate unique electronic and optical properties. The exceptional properties of QDs which are distinct from those of bulk materials, originate from the electron confinement phenomena due to small sizes of QDs (typically 2-10 nm). As a result of these "geometrical" restrictions, electrons feel the presence of the particle boundaries and respond to changes in particle size by adjusting their energy. This phenomenon is known as the quantum-size effect, which results in discrete atomic-like states with energies that are determined by the QD radius [8]. As the size of a QD increases, the band gap between energy states decreases and consequently, NC emits in higher wavelength (see Figure 3-4).

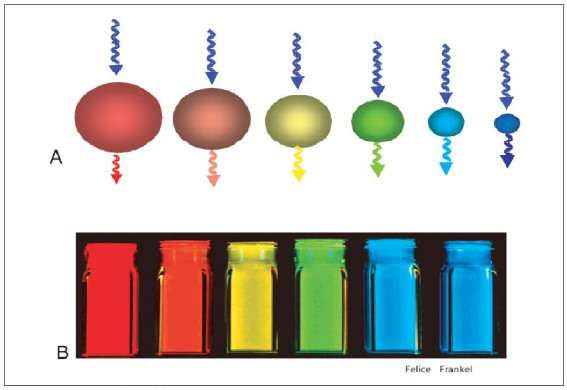

Figure 3-4 Solutions of CdSe QDs of different radii, pumped with blue laser, emit different colors due to the quantum size effect. The QD of 12 nm has a lower energy gap and emits in the red, whereas a dot of radius 2 nm has a larger band gap and emits a blue color [9].

In general, in order to increase charge carrier confinement, QDs are coated with higher band gap materials. CdSe/ZnS and CdTe/ZnS are two examples for such kind of NCs. In fact, the presence of semiconductor shell can improve the emission property of the resulting core–shell QDs and also photo-stability of the structure under irradiation of energetic sources [10,11].

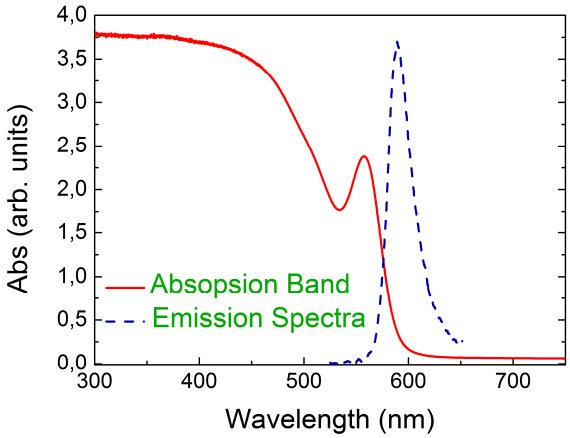

Figure 3-5 Absorption and emission spectra of 3 nm radii CdSe@ZnS QDs dissolved in ethanol.

All tremendous properties of QDs such as high fluorescence quantum yields, Size-tunable photoluminescence, proper fluorescence decay time, high chemical and optical stabilities, extremely broad excitation spectrums and intense absorption band with narrow emission spectrum that span the visible spectrum (evidenced from Figure 3-5) make them brilliant candidates for emission quenching and enhancement intentions. QDs offer several advantages over organic dyes, but they have their own slew of problems that must be addressed. QDs can suffer from surface defects which can result in blinking of the quantum dots and deteriorates the quantum yield of the dots [12]. However, this weakness can be lessened by coating a shell around the core. The exhibited aggregation can be considered as another drawback of QDs which can influence drastically their intrinsic optical properties [13]. Nonradiative Auger recombination is another problem that originates from transferring the e-h recombination energy to a third particle (an electron or a hole), resulting in their re-excitation to a higher energy state, instead of releasing that energy as a photon. Such effect through reducing the radiative decay channels, results in shortening of the lifetime and quantum efficiency of the NCs [11].

3.4 Fluorescence Spectroscopy

Fluorescence spectroscopy is a method to study radiative and nonradiative processes which occur for an excited chromophore. In order to represent experimental evidences for

proposed theories which describe the processes in nano-composite systems, fluorescence spectroscopy plays a crucial role. Steady state experiments accompanied by dynamic fluorescence spectroscopy (time-resolved measurements) are two techniques to accomplish fluorescence spectroscopy on an emissive sample. In the next two subsections these two methods briefly are investigated.

3.4.1 Steady-State Fluorescence Spectroscopy

The emission signal of a chromophore dispersed in a solution or solid host matrial can be acquired by pumping the material in a wavelength of its absorption spectrum. Both continuous and pulsed lasers can perform as a pump to create population inversion in meta-stable state of a chromophore, leading to emission process. Radiated photons can be acquired by an appropriate spectrometer. The spectrometer should be enough precise and with enough wide operation bandwidth to be able to detect scattered photons of the emissive material. Since this method is based on measuring the radiative energy dissipation of the excited electrons (molecules), it cannot provide any information of nonradiative processes which take place in excitation process of a gain material. However, this technique can be used to study various energy transfer processes, occurred in different conjugate systems (e.g. dye-dye, dye-QDs, QDs-NPs) by observing quenching or enhancement in their photoluminescence respect to intrinsic PL of emissive material.

3.4.2 Time-Resolved Fluorescence Spectroscopy

Time-resolved spectroscopy data can be more informative than the results of the steady-state experiments. In fact, according to the particular characteristics of dynamic fluorescence spectroscopy, by missing the information provided by these experiments, demonstrating convincing definition for the observed phenomena in composite systems is unfeasible. To make clear this point, consider a mixture of two fluorophores, each with a distinct lifetime although with quite strongly overlapped emission spectra. Because of the mentioned emission overlap, usually, from the steady state data the emission of one molecule from the other one is indistinguishable. However, the time-resolved data may reveal two decay times, which can be used to resolve the emission spectra and relative intensities of two different emissive molecules. Now as another example, suppose a sample consisted of a donor and quencher molecules, and

the steady-state measurements indicates the donor is 50% quenched by the acceptor. The observed 50% donor quenching can be 100% due to quenching of 50% of whole fluorophores or 50% quenching of all donors, or some combination of these two limiting possibilities. In fact, the steady-state data cannot distinguish between these extreme cases, while very different donor intensity decays would be observed for each case [4].

In addition, the time-resolved donor decays are highly informative about donor-to-acceptor distances, while such kind of precise information cannot be extracted from steady-state data.

3.4.2.1 Fluorophore Decay Time

Suppose excitation light pulse creates an initial population n_0 of excited state of a fluorophore. Depopulation of excited state occurs with total decays rate of $k_t = k_r + k_{nr}$ according to the following expression.

$$\frac{dn(t)}{dt} = (k_r + k_{nr})n(t) \qquad (3-2)$$

where $n(t)$ is the number of excited molecules at time t following excitation, k_r is the radiative decay rate, and k_{nr} is the nonradiative decay rate. For QDs nonradiative pathways are often attributed to defects in the core crystalline structure and/or surface states.

Because emission is a random process, so each excited fluorophore molecule has the same probability of emitting in a given period of time. This results in an exponential decay of the populated excited state,

$$n(t) = n_0 e^{(-\frac{t}{\tau})} \qquad (3-3)$$

The equation (3-2) can be written in term of intensity, since in fluorescence spectroscopy, the thing that is detected is not the number of the photons, but rather fluorescence intensity, which is proportional to $n(t)$. Fluorescence intensity begins to decrease when the excitation stops. Hence,

$$I(t) = I_0 e^{(-\frac{t}{\tau})} \qquad (3-4)$$

where I_0 is the intensity at time 0 and the τ is the lifetime of the fluorophore which is defined as the inverse of the sum of the decay rates which depopulate the excited state.

$$\tau = \frac{1}{k_r + k_{nr}} \qquad (3-5)$$

Also, lifetime is the average amount of time a fluorophore remains in excited state prior to relaxation and is characteristic of the fluorophore. This value is obtained by averaging *t* over the intensity decay of the fluorophore.

$$< t >= \frac{\int_0^\infty tI(t)}{\int_0^\infty I(t)} dt = \frac{\int_0^\infty te^{(-\frac{t}{\tau})}}{\int_0^\infty e^{(-\frac{t}{\tau})}} dt \qquad (3-6)$$

For single exponential decays solving the integrals of numerator and denominator leads to τ^2 and τ, respectively and consequently average time will be equal to lifetime of fluorophore. Experimentally, two methods of time-resolved fluorescence are popular: time-domain and frequency-domain methods.

In time-domain or pulse fluorometry, as it shown in Figure (3-6) the fluorophore is excited with an infinitely sharp (δ-function) pulse of light, preferably much shorter than the decay time τ of the sample. After acquiring emitting photons of excited sample, the fluorescence lifetime can be determined from the slope of a plot of log *I*(*t*) versus *t* (Figure 3-6(b)) or from the time at which the intensity decreases to 1/*e* of the intensity at *t* = 0 (Figure 3-6(b)), but more commonly by fitting the data to assumed decay models. The time-domain technology has become smaller, less expensive, and more reliable, which make this method more popular [4].

Lifetime can also be determined within the frequency domain or phase modulation method. In this case the sample is excited by using an intensity modulated light source. The emission of excited fluorophore is forced to respond at the same modulation frequency, but due to the lifetime the emission will be delayed in time relative to the excitation. In addition, due to the lifetime of the fluorophore a decrease in the peak-to-peak height of the emission relative to that of the modulated excitation is occurred. Phase angle and the modulation value between excitation and emission signals can be used to calculate lifetime [4].

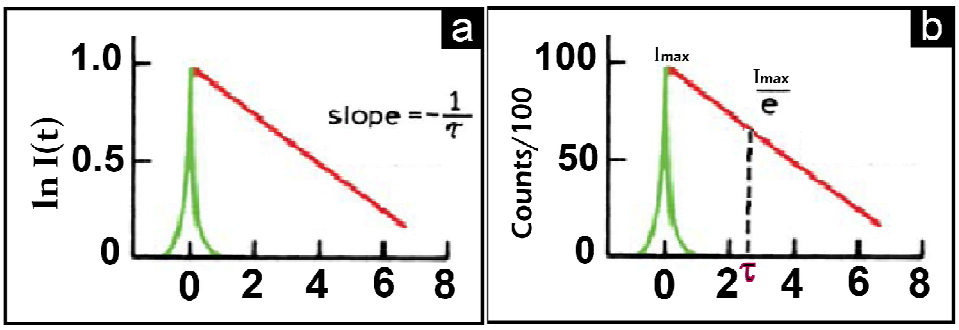

Figure 3-6 Scheme of pulse fluorometry or time-domain lifetime measurement in two methods: **(a)** Slope of ln I(t) and **(b)** time at I_{max}/e. The green signal represents impulse excitation pulse.

3.4.2.2 Extraction of Lifetime by Fitting of Acquired Data

As it represented in Figure 3-6(b), the acquired data are presented as photon counts, because most such measurements are performed by single photon counting method. Also, the linear plot of the log intensity versus time in Figure 3-6(b) could be an example for a single exponential decay time. It is important to consider excitation pulse practically cannot be an ideal impulse function. In this case the instrument response function (IRF), which depends on the shape of the excitation pulse and detection of that by the instrument, needs to be taken into account in data analyzing process.

Analysis of the time domain data is accomplished mostly by nonlinear least squares [14,15]. In this method the lifetime is extracted as a result of best fit between the measured data and the data calculated for the assumed lifetime. Generally, the deviation between the measured and calculated data is shown accompanied by measured lifetime data, which provides a reflection from accuracy of applied fit. For a good fit the deviations are random, indicating the only source of difference is the random error in the data [4].

Interpretation of the data for single exponential decays is quite simple. However, most samples display more than one decay time. For instance the mixture of two different fluorophores with diverse lifetimes experiences a bi-exponential decaying or for those donor molecules presented in different distances of the acceptor, a multi-exponential decay would be observed because some donors will be partially quenched by the acceptor and some of the donors do not. In such cases, the intensity decay will be fit with a multi-exponential function:

$$I(t) = \sum_{i=1}^{n} \alpha_i exp(-t / \tau_i) \qquad (3-7)$$

Where τ_i are the decay times and α_i represent the amplitudes of different components at $t = 0$. The goal of the intensity decay measurements is to recover the decay times (τ_i) and amplitudes (α_i) from the $I(t)$ measurements. For multi-exponential decays, the average time that fluorophore spent in meta-stable state by considering equation (3-7) is extracted from the following relation,

$$< t >= \frac{\sum_{i=1}^{n} \alpha_i \tau_i^2}{\sum_{i=1}^{n} \alpha_i \tau_i} \qquad (3-8)$$

In multi-exponential the point that should not be neglected is the values of α_i amplitudes and τ_I are correlated. This means that, one can vary the lifetime to compensate for the amplitude,

or vice versa. As a result of correlation between α_i and τ_I finding the actual values for these parameters faces with difficulty [4]. This is an inescapable problem that just can be moderated by obtaining high signal-to-noise in the time-resolved experiment and doing a precise data analyzing.

3.5 Chromophore Quantum Yield

Another property exhibited by the fluorophore is the fluorescence quantum yield or quantum efficiency, which is the ratio of the number of luminescence molecules to the total number of excited molecules.

$$\Phi = \frac{\text{Number of photons emitted}}{\text{Number of photons absorbed}} \qquad (3-9)$$

In fact, the quantum yield is a measure of the efficiency of emission in competition with the other processes. Thus, this parameter can also be described by using the ratio of the radiative decay rate k_r respect to the total de-excitation rate ($k_r + k_{nr}$) of the electron.

$$\Phi = \frac{k_r}{k_r + k_{nr}} \qquad (3-10)$$

It is better to remind that radiative decay rate is related to photon emission through fluorescence and phosphorescence, while nonradiative decay rate is correlated with sum of non-emissive decay channels such as through internal conversions (k_{ic}), external conversions (k_{ec}), intersystem crossing (k_i), vibrational and rotational relaxations (k_{vib}), photochemical decomposition (k_{pc}) and resonance energy transfer through near field dipole-dipole interactions (k_{RET}). In the other words [9],

$$k_{nr} = k_{ec} + k_{ic} + k_i + k_{vib} + k_{pc} + k_{RET} \qquad (3-11)$$

The quantum yield can lie between 0 and 1, but in practice due to the presence of the mentioned nonradiative processes, it is always lower than unity. By proper combination of equation (3-5) and (3-10) one can calculate the radiative and nonradiative decay times according to following relations.

$$k_r = \frac{\Phi}{\tau} \qquad (3-12)$$

$$k_{nr} = \frac{1-\Phi}{\tau} \qquad (3-13)$$

REFERENCES

1. G. Shenk, "*Absorption of Light and Ultraviolet Radiation: fluorescence and phosphorescence emission"*, Allyn and Bacon, Inc, Boston, 1973.
2. Aoibheann Bird B.Sc. (Hons), "*Fluorescence Resonance Energy Transfer (FRET) Systems for Biomedical Sensor Applications*", PhD thesis, 2010.
3. A. Jablonski, *Z. Phys.*, **1935**, 94, 38.
4. J. R. Lakowicz, "*Principles of Fluorescence Spectroscopy"*, 3rd ed., Springer, New York, 2006.
5. D. Wild, "*The Immunoassay handbook"*, Elsevier Ltd. 2005.
6. C. Zhu, and P. R. Griffiths, *Appl. Spectrosc*., **1998**, 52, 1403.
7. W. G. J. H. M. van Sark, *et al*., *J. Phys. Chem. B,* **2001**, 35, 8281.
8. E. Ippen, C. Shank and A. Dienes, *IEEE. j. Quan. Elect.* **1971**, 7,178.
9. A. Watson, X. Wu and M. Bruchez, *Biotechnology*, **2003**, 34, 296.
10. D. Gerion *et al*. *J. Phys. Chem. B,* **2001**, 105, 8861.
11. V. I. Klimov, *Science*, **2003**, 214.
12. Michalet *et al*., *Science*, **2005**, 307, 538.
13. Weng *et al*., *Curr. med. chem.*, **2006**, 13, 897.
14. P.R. Bevington, D.K. Robinson, "*Data reduction and error analysis for the physical sciences"*, 2nd ed. McGraw-Hill, New York. 1992.
15. J.R. Taylor, "*An introduction to error analysis: the study of uncertainties in physical measurements*", University Science Books, Sausalito, CA. 1982.

Chapter 4

Energy Transfer Processes in Hybrid Systems

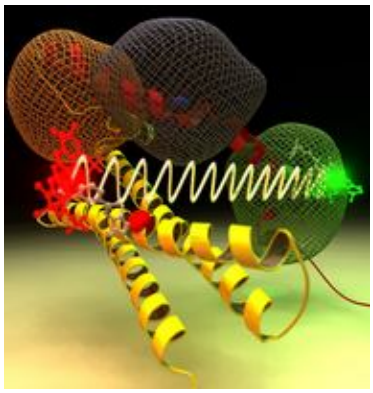

4.1 Introduction

In prior chapters the optical properties of plasmonic NPs and fluorescent materials including dye molecules and QDs have been explored. The provided information makes the mind ready to think about designing proper gain-plasmon hybrid systems and identify different optical processes that can occur among components of these systems. A photo-induced electronic excitation of a chromophore, presented in the close vicinity of a emissive or non-emissive quencher, leads to energy transfer from excited active molecules to another entity, either by emitting a photon (Radiative re-absorption), by non-radiative channels (Förster type), or by electron-exchange (Dexter type).

In this regard, Förster Resonance Energy Transfer (FRET) which is the energy transfer process between a pair of fluorescent molecules (dyes, QDs or combination of both) can be considered as the principle near field interaction process. In fact, the other energy transfer mechanisms can be explained by understanding FRET process.

However, when the acceptor is changed with a metallic NP, the energy transfer processes for such a composite system will differ respect to FRET case. This arises from different optical properties of metallic nanostructures respect to organic or non-organic acceptors. Moreover,

according to the size of NPs, energy transfer from an active material to metallic NPs can be different. One set applies Förster like dipole-dipole interaction model, among NPs with bigger size and fluorescent materials, labeled as DMPET (Dipole to Metal Particle Energy Transfer). While the second set is based on the approximating a chromophore-NP pair with a point dipole which interacts with an infinite surface. Such a mechanism of the coupling between small NPs with weak plasmon band and active materials is referred as NSET (Nanometal or Nanoparticle surface energy transfer) process.

The first part of this chapter dedicated for FRET mechanism and different experimental techniques to evaluate this process. The second part deals with the optical characteristic of the NSET model. The third part of this chapter focuses mainly on the optical properties of DMPET process and the application of this process for mitigating the absorptive losses of plasmonic NPs. In the fourth part, the mechanisms beyond fluorescence enhancement in a hybrid system are investigated. The final part of this chapter is dedicated on a brief introduction on Dexter type energy transfer process.

4.2 Förster Resonance Energy Transfer (FRET)

From the point of view of electromagnetism, a radiating molecule can be conveniently described as an oscillating point *dipole* with angular frequency ω and dipole momentum vector **P**. The electric field pattern of such a dipole located in a homogeneous medium can be derived by solving Maxwell's equations for a homogeneous medium with the oscillating dipole acting as a current source. Analytically, it can be shown that there is a possibility for near field communication between two linear dipoles of fluorescent materials which are placed in close proximity of each other [1-3].The mechanism of such kind of couplings can be described by Förster Resonance Energy Transfer (FRET), which is a radiationless dipole-dipole interaction between two chromophores, by which an initially excited fluorophore relaxes to the ground state by transferring its energy to a nearby molecule in a nonradiative way [4]. A pair of chromophores (dye-dye, QD-QD or QD-dye pairs) that interact in such a manner that FRET occurs is often referred to as a donor-acceptor pair.

Typically donor emits at shorter wavelengths with respect to acceptors in which its emission spectrum overlaps with the absorption band of the acceptor. Such overlap is illustrated in Figure 4-1. In this process, the total energy of donor (D) is not emitted as a photon; neither is

absorbed as a photon by the acceptor (A), but is transferred by nonradiative pathways to the acceptor [1].This process has named Förster RET after German scientist *Theodor Förster*. In order to FRET between a pair of donor-acceptor occurs it is not necessary the acceptor to be fluorescent. In fact the case of non-emissive acceptors, the term of RET (Resonance Energy Transfer) is preferred. However, if also the acceptor would be a fluorescent material, the term of FRET can refer to 'Fluorescence' Resonance Energy Transfer to imply that both coupled molecules (either dye molecules or QDs) are fluorescent [1].

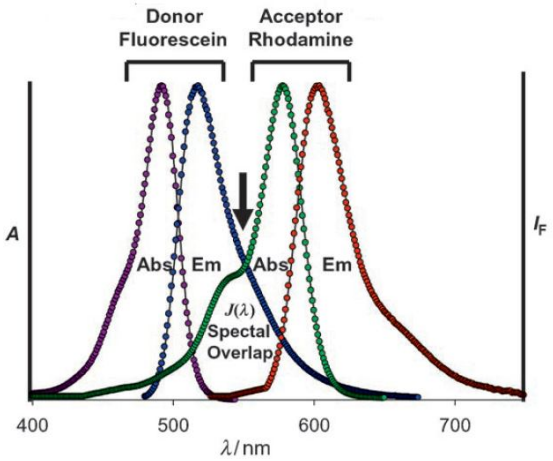

Figure 4-1 The spectral overlap $J(\lambda)$ among emission band (Em) of donor (fluorescein) and absorption band of acceptor (rhodamine) at 500–600 nm. Fluorescein can be efficiently excited at 480 nm and emits at around 520 nm, which results in significant FRET emission of the Rhodamine at above 600 nm. A stands for normalized absorption and IF refers to normalized fluorescence [5].

The symbolic scheme of two coupled pendulums in Figure 4-2 gives the best explanation for occurrence of intermolecular near field coupling in FRET process. If two pendulums have a spring connection between their rods when one of them is stimulate to swing (the donor molecule absorbs an excitation photon) the other will begin to swing (the fluorescent acceptor molecule emits a photon). Here the spring can be considered as the emissionless energy transfer among two coupled molecules.

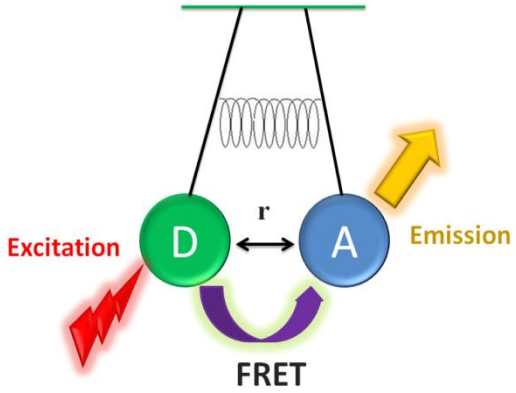

Figure 4-2 Scheme of the FRET process explained by the classical metaphor for FRET process.

The FRET process can be properly illustrated by modified Jablonski diagram (Figure 4-3) as an additional deactivation pathway available for excited donor molecules. Upon excitation, donor molecules promote to the excited state. As it was mentioned formerly, the excited molecules choose both radiative and nonradiative channels to release their energies. But in the case of a donor-acceptor pair, most of the excited molecules relax to the ground state by transferring their energy in nonradiative way to the proximal acceptor molecules. Consequently, the transfer of energy leads to a reduction in the initial donor's fluorescence intensity and to a shortening of its excited lifetime state. Moreover, the relayed energy over the fluorescent acceptor releases radiatively, resulting in the enhancement of its emission. For the case of non-emissive acceptors, the transferred energy dissipates via nonradiative channels.

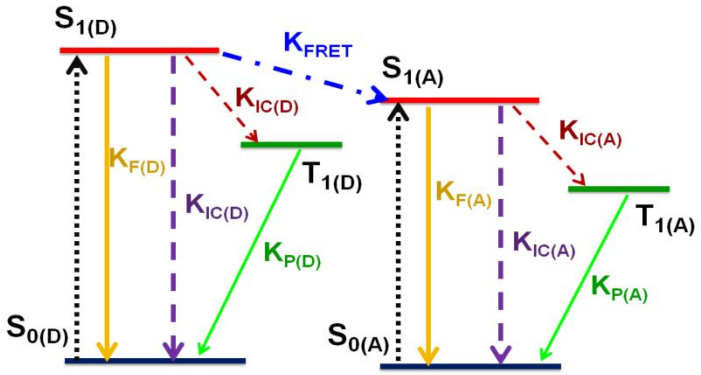

Figure 4-3 Jablonski diagram with fluorescence resonance energy transfer (FRET) among donor (D) and acceptor (A) molecules. S_1, S_0, T_1 refer to the singlet and triplet states; k_{FRET} for energy transfer: k_{IC} for nonradiative internal conversion, k_{ISC} for intersystem-crossing and k_P for phosphorescence and k_f for fluorescence.

4.2.1 Conditions to Obtain the Most Efficient FRET Process

In FRET process, the dipole-dipole interaction occurs without any molecular collision over greater than interatomic distances. The length scale for the distance over which FRET can happen is typically 0.5 to 10 nm. For this reason energy transfer rate has been used as a "spectroscopic ruler" for measurements of distance between molecules such as sites or proteins [6,7]. In fact, the rate of transferred energy significantly is affected by the following factors:

- Spectral overlap among donor emission and acceptor absorption spectra
- Separation distance between donor and acceptor molecules
- Quantum yield of donor
- Absorption coefficient of acceptor
- Orientations of the donor and acceptor transition dipoles
- Concentration of donor molecules

Regarding concentration of donor molecules, there is a point that must be considered. In reality, the efficiency of FRET process could be improved by optimizing the concentration of applied fluorophore, however it should be considered that higher concentrations of donor molecules can cause dimerization effect [8]. Such phenomena can yield in transferring energy from donor monomers towards the formed dimers (known as homo-FRET) and even among donor dimers and acceptor monomers consequently, preventing energy transfer between the monomers of donor and acceptor components. Obviously, higher values of acceptor concentration will cause to the presence of a new FRET process between acceptor monomers and dimers, as well. This effect will have two main issues: Firstly, intrinsic acceptors photoluminescence will be quenched. Consequently, the enhancement of their PL cannot be as high as the acceptors with lower concentration. Secondly, similar to the case of donors with high concentration, too much concentration of the acceptors will prevent the occurrence of the FRET process among donors and acceptors.

4.2.2 The Rate of Energy transfer in FRET Process

The subsequent mathematic expressions of FRET process can reveal the influence of the mentioned parameters in the rate of transferred energy from donor chromophores to the acceptor quenchers.

It should be considered that the most important condition that needs to be met in order to FRET to occur is the donor and acceptor particles must be in close proximity to one another. Indeed, there is a strong correlation between the rate of energy transfer process and donor-acceptor separation distance. Quantum mechanics dictates that the rate of energy transfer varies with the inverse sixth power of the separation distance of donor-acceptor pair. This fact is expressed in the following equation,

$$K_{FERT}(r) = \frac{1}{\tau_D}\left(\frac{R_{0(FRET)}}{r}\right)^6 \qquad (4-1)$$

In this expression, τ_d denotes lifetime of unquenched donor and r is referred to intermolecular distance. Also, $R_{0(FRET)}$ known as the Förster Radius, is the distance at which the FRET efficiency is 50% [4] and is typically is in the range of 2-6 nm.

$$R_{0(FRET)} = 0.211[k^2.n^{-4}.\Phi_D.J(\lambda)]^{\frac{1}{6}}[\mathring{A}] \qquad (4-2)$$

where Φ_D is the quantum yield of a donor in the absence of the acceptor and n is the refractive index of the medium. The parameter of k^2 is the orientation factor which describes the influence of the orientation of the donor's dipole relative to that of the acceptor. The orientation factor can vary from 0 (when the dipoles are perpendicular) to 4 (for collinear transition dipoles). Thus, the approximate parallel transition dipole orientations of donor and acceptor can enhance Förster distance. In general, k^2 is assumed to be 2/3, which is the value for random orientation of donors and acceptors dipoles [9]. Furthermore, $J(\lambda)$ symbolizes the overlap integral, measuring the degree of the spectral overlap between the donor emission and excitation spectrum of the acceptor. The closer these two spectra are one from the other, the better is the transfer.

$$J(\lambda) = \frac{\int_0^\infty F_D(\lambda)\varepsilon_A(\lambda)\lambda^4 d\lambda}{\int_0^\infty F_D(\lambda) d\lambda} \; [M^{-1}Cm^3] \qquad (4-3)$$

here F_D is the fluorescence spectrum of the Donor in the absence of the acceptor, in which the presence of its overall integral in the denominator of $J(\lambda)$ ensures that F_D is normalized. Moreover, $\varepsilon_A(\lambda)$ is the product of the normalized acceptor absorption spectrum with acceptor extinction coefficient ε_A. These spectra, as well as the ε_A, are in general provided by the fluorophore manufacturer. It is important to realize that the overlap integral is not simply the overlapping area under the two spectra, but that the term λ^4 takes into account at which wavelength this overlap occurs.

4.2.3 Energy Transfer Efficiency in FRET Process

The variable of choice to measure the probability of FRET is the efficiency of energy transfer E_{FRET}. The efficiency of transferred energy is the ratio of the absorbed photons by the donor that are transferred to the acceptor non-radiatively to the total amount of the excited acceptors. This can be expressed in terms of rates as following,

$$E_{FRET}(r) = \frac{transferred\ excitation\ to\ the\ acceptor}{excited\ donors} = \frac{k_{FERT}}{k_r + k_{nr0} + k_{FERT}} \qquad (4-4)$$

k_r is the radiative decay rate of the donor in the presence of the acceptor and k_{nr0} is the intrinsic nonradiative decay rate of the donor (in the absence of the acceptor). Since generally the nonradiative pathways of the gain material are not affected by the interactions with proximal molecules and the most significant affect introduces by energy transfer term K_{FRET}, so in equation (4-4) we can consider $k_{nr}=k_{nr0}$ [10]. In above expression, for negligible modifications,

the radiative decay rate of donor in the presence of the acceptor can be considered as same as k_{r0} [1]. In this case, in equation (4-4) the sum of radiative and nonradiative donor decay rates can be rewritten in terms of intrinsic lifetime of donor.

$$E_{FERT}(r) = \frac{k_{FERT}(r)}{\frac{1}{\tau_D} + k_{FERT}(r)} \qquad (4-5)$$

Substitution of the expression of $k_{FRET}(r)$ from (4-1) in equation (4-5) yields,

$$E_{FERT}(r) = \frac{R_{0(FRET)}^6}{R_{0(FRET)}^6 + r^6} = \frac{1}{1 + (\frac{r}{R_{0(FRET)}})^6} \qquad (4-6)$$

As illustrated in Figure 4-4, similar to the rate of energy transfer, the efficiency of this process alters with the inverse of the sixth power of both separation donor-acceptor inter-distance r and Förster distance $R_{0(FRET)}$. For instance, if inter-particle distance be 0.5 $R_{0(FRET)}$ the energy of D will be transmitted to proximal A with the efficiency of 98.5%, while increasing the intermolecular distance just to 2 $R_{0(FRET)}$ will reduce drastically the efficiency of this process (E_{FRET}=1.56%).

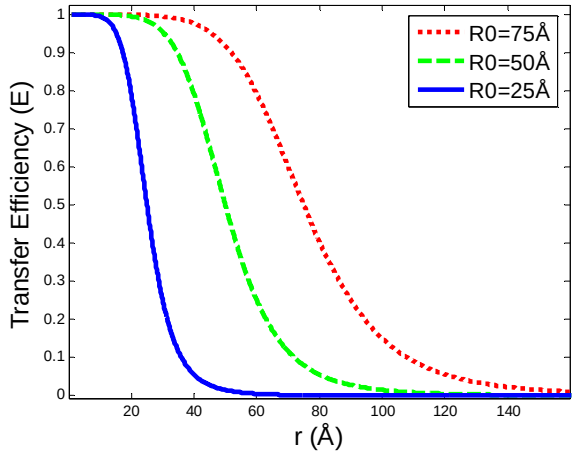

Figure 4-4 Dependence of the FRET efficiency on the distance between the donor and the acceptor. Numbers represent theoretical R_0 values of 25, 50, and 75 Å.

Someone can exploit steady-state measurements for quantifying experimentally the value of E_{FRET}. In fact, by measuring the fluorescence intensity of the donor, in the absence (F_D) and the presence (F_{DA}) of the acceptor and applying them in following equation we can have,

$$E_{FERT}(r) = 1 - \frac{F_{DA}}{F_D} \qquad (4-7)$$

Microscopes are designed to either measure fluorescence intensities at discrete wavelengths corresponding to the donor and acceptor emission peaks or by gathering emission spectra when the donor is excited. Moreover, by using time-resolved fluorescence spectroscopy measurements the parameter of E_{FRET} can be extracted even more precisely by,

$$E_{FERT}(r) = 1 - \frac{\tau_{DA}}{\tau_D} \qquad (4-8)$$

The following equation, which has been acquired by merging two equations of (4-5) & (4-8), can be helpful to extract the rate of energy transfer (K_{FRET}) by applying the experimental data obtained from time-resolved spectroscopy and quantum yield measurement.

$$k_{FERT}(r) = \frac{1-\Phi_{DA}}{\tau_{DA}} - \frac{1-\Phi_D}{\tau_D} \qquad (4-9)$$

It is worth to mention that if in a case we would be able to estimate $k_r=k_{r0}$, then in above equation, the two terms related to quantum yields can be neglected. So we can rewrite equation (4-9) as below expression.

$$k_{FERT}(r) = \frac{1}{\tau_{DA}} - \frac{1}{\tau_D} \qquad (4-10)$$

Strong shortening of donor lifetime in the presence of the acceptor (τ_{DA}) is the signature of an efficient FRET process between donor-acceptor pairs. By acquiring experimentally the value of energy transfer rate and calculating Förster distance (R_0) through equation (4-2) and by applying their values in equation (4-6), one can evaluate the intermolecular distance among a donor-acceptor pair.

We need to consider that these equations are derived from assumptions involving a single donor and a single acceptor separated by a fixed distance. However, theory is completely different for mixture of donors and acceptors dissolved in solution, either for donors and acceptors dispersed randomly in a host medium. More complicated expressions are required in these cases and such expressions are generally derived by averaging the energy transfer rate over the assumed spatial distribution of donor and acceptor molecules [11-13].

4.2.4 Different techniques to measure FRET

The theory developed in the previous section highlights the various aspects of FRET measurements. Respect to the observed physical phenomenon in FRET, this process can be

experimentally measured in numerous methods, including steady-state techniques by monitoring reduction in donor emission and enhancement in acceptor PL, time-resolved spectroscopy by demonstrating a decreased donor lifetime, and as well as quantum efficiency measurement, which can be considered as the most efficient employed technique for quantifying FRET. The mentioned static and dynamic methods for measure FRET are suffering from lacked spatial information. The combination of such techniques with confocal scanning microscopy has permitted to extend the measurements to the second, third or fourth dimension, where the lifetimes are measured on a single voxel (3D pixel) basis to generate an efficiency map [14].

4.3 Nanoparticle Surface Energy Transfer (NSET) Process

It has been mentioned already in chapter 2 that spherical NPs with sizes much smaller than electronic mean free path (below 3 nm), due to strong surface scattering effects, the dielectric function of such NPs is modified, which yields in diminishing of their plasmon band [15]. In addition, since these small clusters have a large surface-to-volume ratio, the conduction electrons are very likely to be found near the nanometal (NM) surface [16]. In such a case, NMs behave as a single point dipole and more accurately they can be described as fragments of metal surfaces, rather than fragments of bulk metal crystals.

On the other hand, the lack of SPR band at NM size notifies that the coherent behavior of electrons is diminished. However, this does not revoke the ability of NP to accept transferred energy to its surface but implies the lack of participation of the plasmon oscillations or enhanced rates of energy transfer presented over the plasmon bandwidth [17]. The emission quenching of gain material in close proximity of NPs is a signature of transferring energy from donor molecules to NM acceptors. The quenching of the fluorophore intensity must be related to a mechanism which involves only the dipole of the donor and surface modes of NP. Such a mechanism is explained by NSET model. In contrast to FRET process, NSET does not require a resonant electronic transition. The physical origin for SET is attributed to the interaction of the dipole-induced electric field of the donor with the free conduction electrons of NPs, localized on the surface of metal [18,19]. These conduction electrons behave like a Fermi gas and will interact most strongly with the oscillating dipoles if they travel near and perpendicular to the metal surface. Consequently, the dipole does not interact with a discrete resonance electronic transition as in case of FRET but with a continuum of electronic levels of a metallic system

providing greater degree of coupling. This is a surprising result, since this suggests that a metal cluster similar in size of gain material acts like a metal surface with respect to the dye dipole [20]. Several theoretical and experimental studies have been published on energy transfer from a dye to a metal surface [21-30].

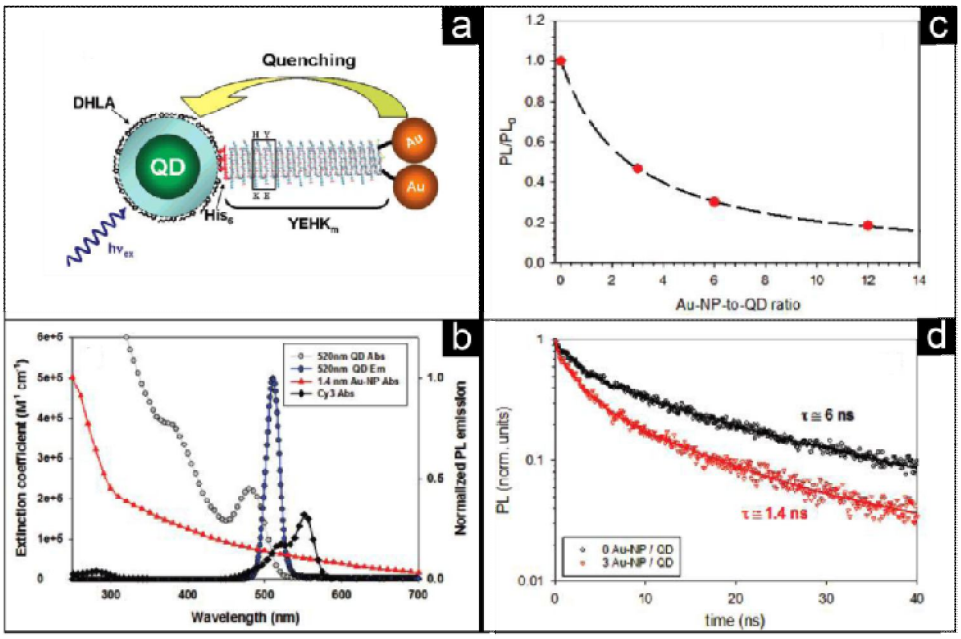

Figure 4-5 (a) Schematic representation of the QD-peptide-Au-NP bioconjugates. **(b)** Extinction coefficient spectra of 520 nm emitting QDs, 1.4 nm Au-NPs and Cy3 dye. **(c)** Plot of normalized PL loss (PL/PL_0) as a function of the number of Au-NP per QD **(d)** Plot of time-resolved fluorescence for 520 nm QDs versus elapsed time in the absence and in the presence of Au-NP per QD conjugate [24].

Figure 4-5 shows an experimental example of NSET process between CdSe-ZnS QDs and Au-NP acceptors with the size of 1.4 nm arrayed around the QD surface, where the center-to-center separation distance was varied over a broad range of values (50-200 Å) [24]. As it is evidence from Figure 4-5(b), the plasmon band for 1.4 nm NMs has completely vanished. However, in spite of the absence of SP band, the presence of adjacent NMs leads to the PL quenching of QDs and even this process is more predominant for higher number of NM quenchers (Figure 4-5(c)). Furthermore, the results of time-resolved fluorescence measurements (showed in part d of this figure) confirm the existence of nonradiative energy transfer process within gain-NM conjugates.

4.3.1 The Rate of Energy Transfer in NSET Process

In order to NSET process happens there is no need for coincidence of resonance bands i.e. an overlap of the emission band of gain elements with that of the resonance band of NPs, like

FRET process. Furthermore, in contrast to the conventional FRET, there is no dipole orientation factor that can forbid energy transfer in NSET process. Indeed, because of the diminished plasmon band, induced dipoles in NMs like those ones of emissive chromophores do not exist. Since the mechanism of NSET is completely different from FRET, hence energy transfer rate in both of these processes have different dependence on distance between donor and acceptor.

The nonradiative dissipation of transferred energy on NP surface via heat is analogous to the theoretical treatment developed by Chance, Prock and Silbey [27], and Persson and Lang [28] for bulk metals. According to Persson and Lang's model, the rate of energy transfer is calculated by using a Fermi Golden Rule calculation for an excited state molecule depopulating with the simultaneous scattering of an electron in the nearly metal above the Fermi level [28].

$$k_{NSET}(r) = \frac{1}{\tau_D}\left(\frac{d_{0(NSET)}}{d}\right)^4 \qquad (4-11)$$

In this equation, τ_D is the decay time of the donor in absence of the NP, d is the distance between donor and NP and $d_{0(NSET)}$ is the distance at which the transfer rate k_{NSET} is equal to the decay rate of the donor in absence of the acceptor.

As it is evident from equation (4-11), the rate of energy transfer in NSET process is correlated with the inverse fourth power of the separation distance of gain-plasmon pair. The Gersten-Nitzan models [29,30] which have been applied for modeling fluorophore dipoles interactions with the plasmon bands of gold NPs seem to have fallen short in describing the distance dependence of NSET process. The physical definition of this process can be understood from Fermi golden Rule approach which relates the energy transfer (k_{et}) to the product of interaction elements of donor (F_D) and the acceptor (F_A) as

$$k_{et} \cong F_D.F_A \qquad (4-12)$$

The interaction elements of donor and acceptor can be considered as a sole function of their geometric arrangement, in which F ~ $1/d^3$ for single dipoles, F ~ 1/d for a 2D dipole array and F= *constant* for a 3D dipole array. These imply that the power of the distance factor decreases as the dimension increases [20]. The rate constant for FRET process follows $1/d^6$ dependence, since

$$k_{FRET} \cong F_D.F_A \cong \frac{1}{R^3}.\frac{1}{R^3} = \frac{1}{R^6} \qquad (4-13)$$

while the rate constant for NSET which consists of a single dipole and a metal surface can be easily derived from this approach.

$$k_{NSET} \cong \ F_D.F_A \cong \frac{1}{d^3}.\frac{1}{d} = \frac{1}{d^4} \qquad (4-14)$$

As the $1/d^4$ dependence has been theoretically predicted by Chance, Prock and Silbey [27], according their model, the NSET distance length d_0 can be calculated, as well.

$$d_{0(NSET)} = \ (0.225\frac{c^3\Phi_D}{\omega^2\omega_f k_f})^{1/4} \qquad (4-15)$$

Respect to mentioned formula, $d_{0(NSET)}$ is the function of the donor quantum efficiency (Φ_D), the frequency of the donor electronic transition (ω), and the Fermi frequency (ω_f), and Fermi wavevector of the metal (k_f).

4.3.2 Energy Transfer Efficiency in NSET Process

The quantum efficiency of energy transfer in NSET process can be written as following equation,

$$E_{NSET}(r) = \frac{d_{0(NSET)}^4}{d_{0(NSET)}^4 + r^4} = \frac{1}{1+(\frac{r}{d_{0(NSET)}})^4} \qquad (4-16)$$

In order to experimentally acquire the parameters of k_{NSET} and E_{NSET}, the expressions (4-7), (4-8) and (4-10) can be applied here, as well.

Equation (4-16) shows a different distance dependence expression respect to dipole-dipole RET process. Thus, the nature of the energy transfer mechanism can be identified by comparing the slope of fitted plot of the measured energy transfer efficiency versus separation donor-acceptor distance respect to theoretically extracted curves of different energy transfer mechanisms. Such an evaluation of energy transfer process has been executed for a system consisting of fluorescein moiety dye molecules attached to one end of ds-DNA and 1.4 nm Au-NMs at the other end. The comparison of the experimental data, with the theoretical energy transfer curves for a pure dipole–dipole (FRET) and dipole–surface (SET) energy transfer process is illustrated in Figure 4-6, which reveals precisely the ($1/R^4$) dependence as predicted for a dipole interacting with the metal surface [20]. In fact, Föorster resonance energy transfer (FRET) technique is restricted to an upper limit of separation of only 80 Å and the energy transfer becoming too weak beyond this distance. But the modification of distance dependence from $1/R^6$ for FRET to $1/R^4$ for NSET process extends the usable distances for the measurement and energy transfer process.

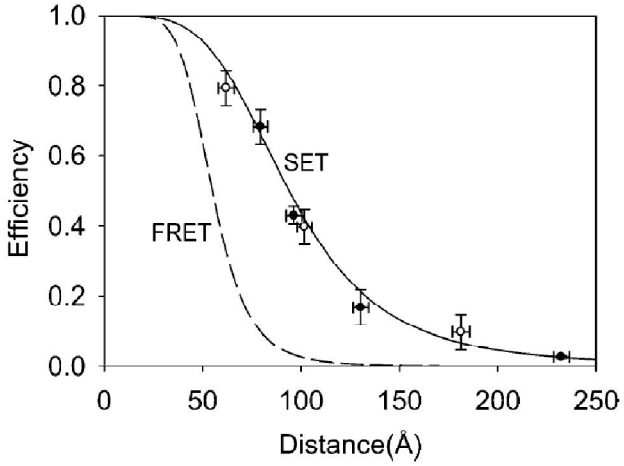

Figure 4-6 Energy transfer efficiency plotted versus separation distance between fluorescein moiety and Au (NM). Filled circles (b) represent DNA lengths of 62 Å, 96.4 Å, 130.4 Å, and 232.4 Å. The measured efficiencies of these strands with the addition of M.EcoRI are represented by the open circles (O). The dashed line is the theoretical FRET efficiency, while the solid line is the theoretical SET efficiency [20].

4.4 Dipole to Metal Particle Energy Transfer (DMPET)

In a gain-plasmon hybrid system, the electric dipoles of emissive donor can couple to plasmon modes of a metallic NP and consequently, the optical properties of fluorescent material can be influenced by the enhanced EM field around metal nanoparticle. The theoretical and experimental studies prove that the near field communication between resonant dipoles of active materials and induced dipoles of plasmonic NPs can transfer energy of gain material nonradiatively to absorptive NPs [29-33]. Such a resonance interaction among components of a plasmon-gain hybrid system is called DMPET (Dipole-Metal Particle Energy Transfer) [29-31].

4.4.1 Jablonski Diagram for Metal-Quenched Fluorescence

Jablonski diagram can be applied for describing the resonant energy transfer process from a fluorescent molecule over a proximal plasmonic NP. First of all, excitation energy source such as a laser or lamp promotes chromophores to the excited state, which yields in population inversion of fluorophore meta-stable state. In parallel, the plasmonic NP absorbs the incoming light, resulting in the enhancement of their plasmonic local fields and excitation of bipolar modes of NP. As we know, de-excitation process of fluorophores could be performed either by radiative (spontaneous emission) or by nonradiative channels. However, for a fluorophore placed in close vicinity of a metallic NP, nonradiative relaxing channels significantly enhance through RET process from chromophores to absorptive NPs. As a result of this process, intrinsic emission of fluorescent materials either QDs or organic dyes strongly can be quenched. Obviously, as

equation (4-17) shows that both parameters of fluorescence lifetime and quantum yield of donor molecules will be modified, as well. The new lifetime of donor molecule is expressed by

$$\tau_{DA} = \frac{1}{k_r + k_{nr0} + k_{DMPET}} \qquad (4-17)$$

where k_r is the quenched donor emission. Also, the term of k_{DMPET} represents the presence of nonradiative energy transfer from donors to plasmonic acceptors. The sum of energy transfer rate with k_{nr0} denotes total nonnative decay rate of a single fluorescent molecule (k_t) in the presence of metal acceptor. Take it into account that since the enhancement of nonradiative rate is outweighed respect to dropping of radiative rate, hence, radiative lifetime of the donor is shortened. Respect to the relation of quantum yield with lifetime and radiative rate, we can write,

$$\Phi_{DA} = \frac{k_r}{k_r + k_{nr0} + k_{DMPET}} = k_r \times \tau_{DA} \qquad (4-18)$$

Since both terms of k_r and τ_{DA} have been decreased, the reduction of gain material quantum yield is expected. Briefly, we can write those sentences in the following expression.

$$k_{rad} \downarrow \quad k_{nr} \uparrow\uparrow \quad \Rightarrow \quad \tau_{D-A} \downarrow \ , \ \Phi_{D-A} \downarrow \ , \ PL \downarrow$$

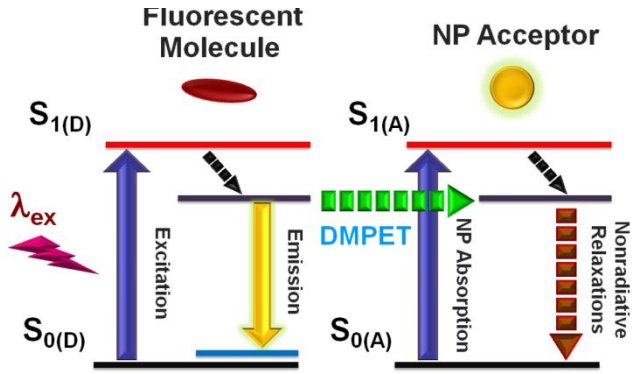

Figure 4-7 Jablonski diagram for demonstration of DMPET process in a gain-plasmon hybrid system.

The nonradiative relaxations term which has been illustrated in Figure 4-7 includes thermal energy dissipation through Joule effect (*i.e.*, electron-phonon coupling) and plasmonic state relaxation of excited electrons.

4.4.2 Optical Loss Mitigation in Plasmonic systems by DMPET Process

Nonradiative energy transfer from active materials to plasmonic NPs not only as an additional pathway for releasing the energy of excited gain molecules involves collective excitation (plasmon) of compressible electron gas in the nanoparticle. Someone can exploit this interesting process to mitigate the absorptive loss of plasmonic systems. In fact, the absorptive

losses could be compensated with inclusion of active gain media, able to transfer energy on propagating SPPs and localized SPRs in metal nanostructures using stimulated emission. In this regard, several theoretical [349-36] and experimental studies [37-40] have demonstrated how nonradiative RET process from gain materials to plasmonic nanostructures can mitigate NPs absorptive losses. Thus, the transferred energy from donor on absorptive NPs does not dissipate completely thermally through electron-phonon coupling, but also it can be relevant for decreasing the radiation damping of NPs in terms of reduction in the imaginary part of the dielectric permittivity.

This point should be remind that the negative permittivity of plasmonic NPs in visible range which makes them as a promising alternative for constructing the subunits of optical metamaterials, originates from absorptive nature of metallic NPs. Hence the intention of introducing gain to plasmonic NPs is not completely eliminating the absorptive behavior of NPs. However, it should be moderated sufficiently to make NPs enough appropriate for optical applications, in particular to apply as building blocks of plasmonic metamaterials. Indeed, transferring energy is the cost that we must pay to reduce the optical loss of NPs, but also keep alive the plasmonic resonances.

4.4.3 The Rate of Energy Transfer in DMPET Process

The study of the energy transfer between gain material and nanoparticle can be executed in two different approaches. First, the full Coulombic interaction between donor and acceptor can be used in the Fermi Golden Rule to calculate the rate of energy transfer. Second, the interaction within the dipole approximation can be considered, where the Coulombic interaction is approximated by the dipole interactions among the charge distributions of the fluorophore and the NP [41]. Since the mechanism of energy transfer in DMPET is kind of similar to FRET process (both exploit dipole-dipole interactions), hence energy transfer rate in DMPET model has the dependence on donor-acceptor separation gap respect to FRET model. The following equation is expressing the rate of energy transfer in DMPET process, where λ_{PL} is the maximum emission wavelength of gain material [31,42].

$$k_{DMPET}(r) = \frac{1}{\tau_D}\left(\frac{R_{0(DMPET)}}{r}\right)^6 \left(1 + \frac{1}{6}(2\pi nr / \lambda_{PL})^2 + \frac{1}{6}(2\pi nr / \lambda_{PL})^4\right) \qquad (4-19)$$

Here $R_{0(DMPET)}$ is the distance at which the transfer rate k_{DMPET} is equal with the decay rate of the donor in absence of the plasmonic acceptor. This parameter can be calculated by the classical Förster separation distance value expressed in equation (4-2).

The effects of DMPET treatment have been revealed by inserting additional "correction terms" of $(r/\lambda_{PL})^2$ and $(r/\lambda_{PL})^4$ in the quenching efficiency expression (4-6), predicted by the Förster dipole-dipole model [42]. However, since separation distances considered for an efficient energy transfer lies in the range of 1 to 40 nm, which are always smaller than λ_{PL} (400-800 nm), even for the largest effective interparticle distances, the effect of correction terms to Förster calculation becomes poor (≤10%). Therefore, at small interparticle distances the anticipated energy transfer efficiency is equivalent to the Förster model (equation (4-6)).

4.4.4 Energy Transfer Efficiency in DMPET Process

The quantum efficiency of energy transfer in DMPET model has been extracted as following equation [42].

$$E_{DMPET}(r) = \frac{1}{1+(\frac{r}{R_{0(DMPET)}})^6[1+\frac{1}{6}(2\pi nr/\lambda_{PL})^2+\frac{1}{6}(2\pi nr/\lambda_{PL})^4]^{-1}} \qquad (4-20)$$

Also in this case only at large separation distances, the higher order corrections terms are expected. For shorter distances, the expression of decay rate reduces to the equation (4-6).

Indeed, DMPET model exhibits a $1/R^6$ distance dependence which is different from NSET process. For experimental treatments, both decay rate and efficiency of DMPET process can be obtained through steady-state fluorescence measurements or time-resolved spectroscopy by using expressions (4-7), (4-8) and (4-10).

4.4.5 Effective Parameters on Mitigating NPs Losses by DMPET Process

The path to mitigate the optical losses of plasmonic NPs is crossing through achieving an efficient energy transfer process from gain to plasmonic NPs. Since DMPET process follows the Fermi Golden Rule, therefore it has constraints with respect to the: (i) spectral relationship between emission spectrum of gain material and plasmon band of metal NPs, (ii) interparticle distance, (iii) geometry and shape of metal nanostructures, (iv) orientation of the gain material dipole moments relative to the nanoparticle surface normal, (v) concentration and (iv) quantum

yield of gain elements [40,41]. In following subsection, the effects of these parameters in RET process and consequently in loss compensation efficiency will be investigated.

4.4.5.1 Donor-Acceptor Spectral Overlap

In DMPET process, similar to FRET model, sufficient spectral overlap between donor emission and acceptor absorption spectra is a crucial condition for attaining the RET process. Figure 4-8 represents an example of proper spectral overlap between the emission spectra of donor Coumarin 334 molecules with plasmon band of 12 nm gold NPs.

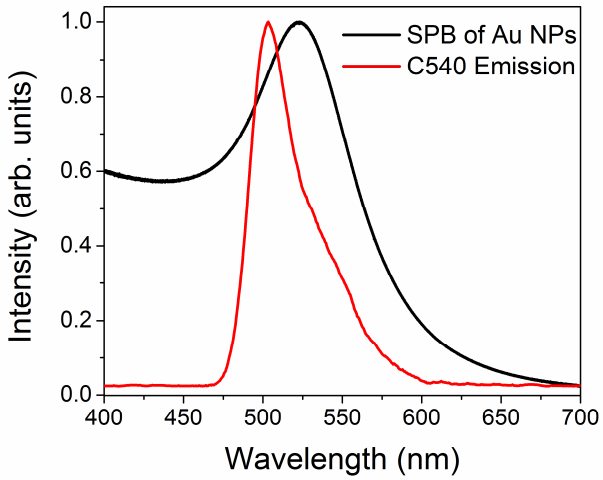

Figure 4-8 Spectral overlap between C540 dye emission spectrum with SPB of 12 nm gold NPs.

Concerning the necessity for donor emission-acceptor absorption spectral overlap, there is a delicate difference regarding quenching mechanism between DMPET and FRET processes. In FRET process, for occurrence of a resonance coupling, donor emission must be in higher energy levels respect to acceptor absorption band, whereas in DMPET process regardless of the red shift or blue shift of emission spectrum of the gain material respect to the maximum wavelength of the plasmonic extinction band, only the existence of a sufficient spectral overlap among these two spectra is necessary. The validity of the mentioned fact is demonstrated in the experimental results part of this thesis [43]. Accordingly, our experimental result reveals another difference between DMPET and FRET processes. In FRET process, this overlap must be presented to create the possibility for inter-band transitions through dipole-dipole interactions, while in DMPET process, the spectral overlap besides the providing the opportunity for such transitions, represents another energy transfer contributor, which is the interaction between LSP modes of NP and electrical dipoles of the excited donor molecule, resulting in a significant quenching of donor emission.

For larger NPs, in which the "quadrupolar" surface mode becomes manifest in lower wavelength of visible spectra, its effect on RET process needs to be considered. But normally the emission spectra of the donor doesn't have an effective crosstalk with absorption spectra of NPs for L=2 mode, so the rate of energy transfer over this mode can be ignored [41].

Recently Bo Peng *et al.* [40] have reported that the incorporation of gain material at a controlled distance from gold NPs, by means of silica spacers, allows controlling and optimizing the nonradiative resonant energy transfer processes between gain medium and plasmonic gold NPs. From the obtained emission and fluorescence lifetime measurements, they concluded that both the spectral overlap and coupling distance are key factors for optimizing gain-plasmon interplays.

4.4.5.2 Interparticle Distance

In order to provide an opportunity for energy transfer from excited dipoles of a gain element over the absorption band of a NP, appropriate donor-acceptor separation distance is essential. Interestingly, DMPET can be occurred in the range of 1 to 40 nm donor-acceptor separation distance for NPs with diameters of 5 to 40 nm [44]. This is a particular feature of plasmonic NPs as energy quenchers that they can quench fluorescence over longer distances than conventional chromophores. This fact can be explained by taking into account that the energy transfer rate from a chromophore to a small NP surface follows the R^{-4} distance dependence [45]. While for dipole-dipole interactions, such dependence is R^{-6} [29]. Therefore, energy transfer rate towards a NP that is in the middle between these two limiting cases will track R^{-n} distance dependence, where n is between 4 and 6 [41].

Moreover, due to the high absorption cross-section of metallic NPs the Förster radius of a gain-plasmon conjugate would be longer than for a pair of donor-acceptor consisted of active materials. This arises from this fact that the absorption spectrum of the acceptor ($\varepsilon_A(\lambda)$) in the overlap integral is not normalized.

$$R_0^6 \sim \int_0^\infty I_D(\lambda)\,\varepsilon_A(\lambda)\lambda^4 d\lambda \qquad (4-21)$$

However, as equation (4-20) represents the efficiency of DMPET process drastically drops for longer interparticle distances. Figure 4-9 reveals the mentioned correlation between the rate of RET with gain-NP interparticle distance.

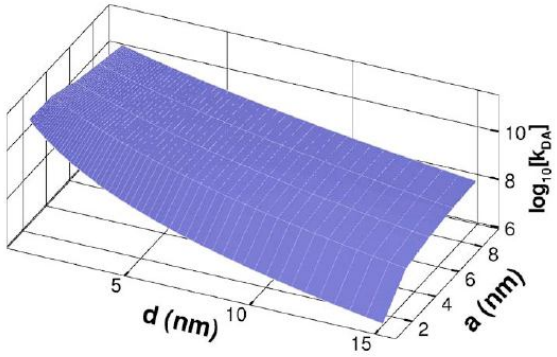

Figure 4-9 Energy transfer rate as a function of the core radius "*a*" of a NP and inter-particle distance "*d*" [41].

4.4.5.3 Geometry and Shape of Metal Nanostructures

Simply, the geometry and size of the nanostructures affect the shape and position of the plasmon band, resulting in modification of spectral overlap among nanostructures plasmon band with emission spectrum of gain materials. As it has been explained broadly, typically small spherical NPs cannot support the surface plasmons and subsequently they exhibit not so much intensive absorption band. Accordingly, as it represented in Figure 4-9, in a conjugates of gain-metal quencher included small NPs, it is not possible to expect a strong resonance coupling between excited donors and plasmon modes of metal NP for loss compensation purposes.

4.4.5.4 Dipoles Moments Orientation Factor

The relative dipole angular orientation of a chromophore's molecule with respect to the induced dipole of NP determines whether the rate of energy transfer is increased or decreased [46]. If dipoles of two chromophores are oriented perpendicular to each other ($\theta = 0°$ for one dye and $\theta = 90°$ for the other) then there is no energy transfer among them. On the contrary, when the chromophores dipoles are parallel to each other, the rate of energy transfer is either maximum for both dipoles at $\theta = 0°$ or a quarter of maximum value of K_{et}, when both are at 90° [41].

However, due to the symmetric shape of the spherical NPs for a pair of chromophore-NP the orientation dependence is different from that in a pair of two active components. Furthermore, as it showed in Figure 4-10, in contrast to the conventional FRET, energy transfer from active materials to plasmonic quenchers can take place as the chromophore is rotated along the NP surface from the perpendicular to the parallel orientation. More to that point, at large separation distances the ratio of the largest rate of energy transfer to the smallest value of that approaches 4. This means that on the contrary of the FRET model, the orientation factor takes

values from 1 to 4 depending on the chromophore-NP orientation [51]. Interestingly, as it is evident from Figure 4-10, the orientation dependence becomes weaker as the interparticle distance decreases.

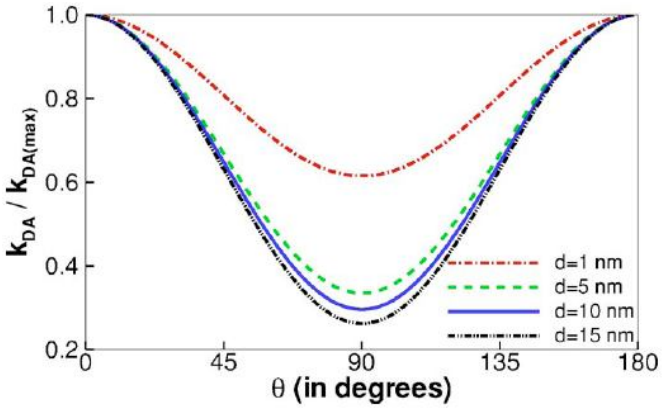

Figure 4-10 Dependence of the rate of energy transfer on the orientation of the dye dipole moment with respect to the surface of the NP, calculated using the full Coulombic interaction [51].

It is reported that the energy transfer rate of DMPET process is correlated with the intrinsic radiative rate K_{r0} of the chromophores, because both processes depend on the dipole orientation [51]. A direct proportionality between K_{r0} and the energy transfer rate K_{DMPET} is found for both radial (⊥) and tangential (||) dipole orientations [29,47].

$$\mathrm{R}_{et,\perp} = -\frac{K_{r0}}{\left|1-\Delta_{\perp}\right|}\left(\frac{3c^3\varepsilon_m}{2\omega^3 r^3}\right)\times$$
$$\sum_{n=1}^{\infty}(2n+1)\frac{(n+1)^2}{n}\,\mathrm{Im}\left[\frac{1}{\varepsilon+(1+1/n)\varepsilon_m}\right]\left(\frac{r}{r+d}\right)^{2n+4} \qquad (4-22)$$

$$\mathrm{R}_{et,\parallel} = -\frac{K_{r0}}{\left|1-\Delta_{\parallel}\right|}\left(\frac{3c^3\varepsilon_m}{2\omega^3 r^3}\right)\times$$
$$\sum_{n=1}^{\infty}(n+1)(2n+1)\,\mathrm{Im}\left[\frac{1}{\varepsilon+(1+1/n)\varepsilon_m}\right]\left(\frac{r}{r+d}\right)^{2n+4} \qquad (4-23)$$

Here, $\Delta_{\perp}$ and $\Delta_{\parallel}$ indicate the so-called image enhancement factors [47], ω is the angular frequency of the incident light wave, c is the speed of light, ε and ε_m are the dielectric constants of the metal NP and the host medium, respectively. The symbol of r is the particle radius, and d denotes the distance between the chromophore and the NP surface. It is worth to mention that the direct proportionality between, K_{r0} and RET was also found by Förster for a purely organic donor-acceptor pair [48].

4.4.5.5 Concentration of Active Material

In order to mitigate effectively the optical loss of NPs, the ratio between plasmonic absorptive NPs and active elements should be chosen in a proper manner. Respect to size, shape and molar concentration of plasmonic quencher, the right value of the gain material concentration should be proposed. In the next chapter, the procedure of calculating right value for gain material concentration for a dispersion of NPs-fluorophores will be demonstrated.

4.4.5.6 Quantum Yield of Gain Elements

As it clear from Förster distance equation, quantum efficiency of donor can influence the interparticle distance for obtaining an effective RET in a gain-plasmon composite. In fact, higher values of the quantum yield can improve the efficiency of DMPET process for longer separation distances. We can arrive to the same point from the other treatment. Suppose that someone chooses a material with low values of quantum yield for optical loss compensation purposes. Such a material cannot exhibit an intensive fluorescence signal, since nonradiative relaxation pathways even in the absence of any quencher are already significantly powerful. In such a case, energy transfer process cannot treat as an additional channel for nonradiative relaxation of excited molecules and for that reason an efficient loss mitigation process is not expected. Regardless of the fact that for an efficient fluorescence quenching process the gain material with higher values of donor quantum yield is suggested, for metal enhanced emission purposes, an active material with lower values of this parameter must be considered.

4.5 Plasmon-Enhanced Fluorescence of Chromophores

As it discussed in prior parts, DMPET and NSET are the models which are describing the interaction of chromophores with proximal NPs, in two different size regimes. In spite of the difference of these two processes regarding nonradiative energy transfer method, interestingly, the plasmonic NPs which are involved in DMPET process, can exhibit either quenching or enhancement of donor emission. This particular future of DMPET process arises due to the enhanced local field of plasmonic NPs. Therefore, respect to the quencher characteristics in NSET and as well as in FRET, such donor emission enhancement is not expected. Plasmonic NPs influence the emission of chromophores in several ways. The PL signal from a chromophore (R_{PL}) close to a NP can be described as

$$R_{PL}(\hat{\mathrm{d}},\mathbf{R}) = R_{\mathrm{ex}}(\hat{\mathrm{d}},\mathbf{R}).\Phi_D(\hat{\mathrm{d}},\mathbf{R}), \qquad (4-24)$$

where R_{ex} is the enhancement factor and Φ_D is the quantum efficiency of the gain material [49, 50]. $\hat{\mathrm{d}}$ is the unit vector in the direction of the chromophore transition oscillating dipole d and **R** is the radius vector of the chromophore in relation to the center of the NP. Both parameters of R_{ex} and Φ_D can be influenced in the presence of the NP local field. In addition, the excitation rate (absorption rate) of proximal fluorophore can be increased by the EM field around the metal NPs. If the absorption of a chromophore would be far from saturation (i.e. in the linear range), the excitation rate (in the absence of NP), k_{ex}, is directly proportional to the square of the intensity of the incident Electric field $\mathbf{E}_{inc}(\mathbf{R})$ and molar absorptivity of the chromophore $\varepsilon(\lambda)$.

$$k_{ex} \propto \varepsilon(\lambda)\left|\mathrm{d}.\mathbf{E}_{inc}(\mathbf{R})\right|^2, \qquad (4-25)$$

When the chromophore is placed nearby the proximity of a metal nanostructure by the chain of organic groups [51, 52] or at a metal-dielectric interface [53], the excitation enhancement factor of the electric field (R_{ex}) can be defined as the ratio of excitation rates of the chromophore in presence and in the absence of NP.

$$\mathrm{R}_{\mathrm{ex}}(\mathrm{d},\mathbf{R}) = \frac{\left|\mathrm{d}.\mathbf{E}_{loc}(\mathbf{R})\right|^2}{\left|\mathrm{d}.\mathbf{E}_{inc}(\mathbf{R})\right|^2} \qquad (4-26)$$

where $\mathbf{E}_{loc}(\mathbf{R})$ is the electromagnetic field amplitude of chromophore generated by the metal nanoparticle. The incident excitation field $\mathbf{E}_{\mathrm{inc}}(\mathbf{R})$ induces a dipole moment of $\mathrm{P}_{NP}=4\pi\alpha\mathbf{E}_{\mathrm{inc}}(\mathbf{R})$ in the NP, where α is the electrostatic polarizability of the NP. This leads to an enhancement in the local field around the NP and consequently around active material. In fact, due to this phenomenon in such a case, NPs can be labeled as nano-antennas or resonant dipole antennas [54-56]. The enhanced local field around the NP can be defined as,

$$\mathbf{E}_{loc}(\mathbf{R}) = \mathbf{E}_{inc}(\mathbf{R}) + \mathbf{E}_{sca}(\mathrm{P}_{NP},\mathbf{R}) \qquad (4-27)$$

where an additional scattered field $\mathbf{E}_{\mathrm{sca}}(\mathrm{P}_{\mathrm{NP}},\mathbf{R})$ due to the induced dipole in NP appears. Thus, the enhancement of the absorption rate would also lead to increased fluorescence emission intensity without modifying the excited state lifetime and quantum yield [57]. Moreover, when three vectors of **R**, P_{NP} and d are co-linear, the enhancement of excitation is maximal [50].

The second parameter in equation (4-24) is the quantum efficiency of the gain element. The quantum yield and decay time of active material can be rewritten with a new notification as,

$$\Phi_D(\hat{\mathrm{d}},\mathbf{R}) = \frac{\Gamma_r(\hat{\mathrm{d}},\mathbf{R})}{\Gamma_r(\hat{\mathrm{d}},\mathbf{R}) + \Gamma_{nr}(\hat{\mathrm{d}},\mathbf{R})} \qquad (4-28)$$

$$\tau_D(\hat{\mathrm{d}},\mathbf{R}) = \frac{1}{\Gamma_r(\hat{\mathrm{d}},\mathbf{R}) + \Gamma_{nr}(\hat{\mathrm{d}},\mathbf{R})} \qquad (4-29)$$

where Γ_r and Γ_{nr} are the radiative and non-radiative decay rates of the fluorescent material. Due to the enhanced local field of NP, both radiative and non-radiative decay rates are modified, resulting in the change in quantum yield and lifetime of chromophore.

$$\Phi_{DA}(\hat{\mathrm{d}},\mathbf{R}) = \frac{\Gamma'_r(\hat{\mathrm{d}},\mathbf{R})}{\Gamma'_r(\hat{\mathrm{d}},\mathbf{R}) + \Gamma'_{nr}(\hat{\mathrm{d}},\mathbf{R})} \qquad (4-30)$$

$$\tau_{DA}(\hat{\mathrm{d}},\mathbf{R}) = \frac{1}{\Gamma'_r(\hat{\mathrm{d}},\mathbf{R}) + \Gamma'_{nr}(\hat{\mathrm{d}},\mathbf{R})} \qquad (4-31)$$

The notation of prime on parameters of above equations indicates the influence of NP on mentioned processes. Nonradiative rate of chromophore in the presence of metallic NP is defined as the sum of the intrinsic nonradiative decay rate Γ_{nr} with energy transfer rate Γ_{et}.

The relative dipole moment orientation of a chromophore with respect to the induced dipole of NP determines whether the radiative rate is enhanced or diminished [29]. Figure 4-11 represents schemes of the relative orientation of interacting dipole moments, resulting in modification of the radiative decay rate.

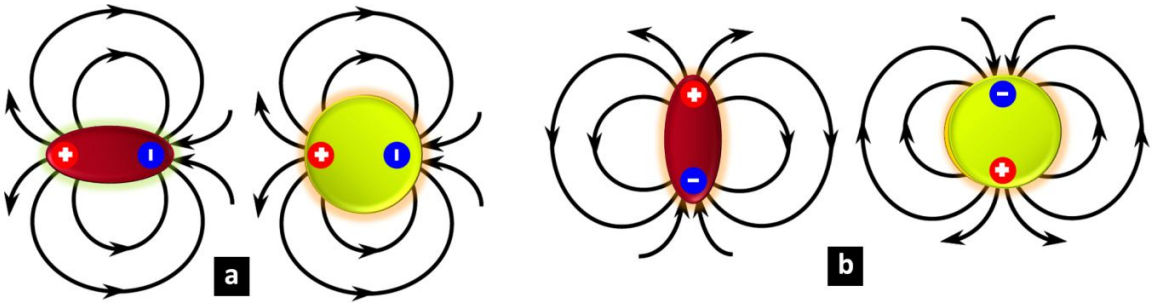

Figure 4-11 Radialy (perpendicular) [Constructive interferences] **(a)** and tangentially (parallel) [destructive interferences] **(b)** orientation of chromophore dipole moment respect to surface of spherical NP leads to the enhancement or to the reduction of the radiative decay rate of the gain materials, respectively.

In the case of tangential (parallel) orientation of chromophore dipole moment to the surface of the NP, since dipoles of donor and plasmonic acceptor radiate out of phase, hence interferences of their EM fields are destructively [46,58]. Consequently, the total dipole moment will decrease, which results in reduction of absorption rate and therefore decreasing of the radiative decay rate (Figure 4-11a). In addition, as a result of RET on NP the nonradiative rate increases. Consider that the increase of RET rate is a dominate effect respect to the quenching of

the radiative rate. Thus, both effects likewise lead to luminescence quenching, shortening of life time and decreasing quantum efficiency of donor.

In contrast, if the chromophore transition dipole is orientated radially (perpendicular) toward NP surface, due to the constrictive fields interferences of the chromophore dipole with plasmonic dipole, total dipole moment will increase [56,59]. This leads to the improvement of absorption rate, resulting in the enhancement of radiative decay rate (Figure 4-11b). Take into account, even in this case due to the presence of the energy transfer, the nonradiative rate will be increased. However, because radiative decay rate enhancement is the dominating effect, luminescence will be enhanced [60].

4.5.1 Jablonski Diagram and Physical Definitions of Metal-Enhanced Fluorescence

As it has been discussed in prior section, the presence of NP nearby an active material can lead to PL enhancement. In fact, the term of fluorescence enhancement is defined as any process whereby a larger number of photons can be emitted by a single molecule. The graphical illustration for the excitation and emission processes of a chromophore in Jablonski diagram can help reader to understand how by engineering both the excitation and emission processes fluorescence enhancement can be mediated.

Figure 4-12 illustrates how the locally enhanced electric field of NP provides an additional term for excitation rate, resulting in an enhanced absorption rate. Mathematically and schematically, it has been demonstrated in previous section that the absorption rate of a chromophore can be influenced upon to (i) the enhanced near field by nano-antennas, (ii) the capability of the molecule to absorb light (absorptivity) and (iii) the orientation of the molecule to the excitation electric field. However, enhanced excitation may result in saturation and eventual photobleaching of the molecule. On the other hand, shortening of the lifetime due to emission enhancement, leads to improving the photostability of the active molecule, since the chromophore will spend less time in the excited state and therefore be less susceptible to photobleaching [61].

It is well-known that the modification of a local field environment of the chromophore by plasmonic NPs leads to the presence of nonradiative decay channel $k_{nr,m}$. In the fluorescence enhancement regime, field interactions result in a new radiative channel which is demonstrated as denoted as $k_{r,m}$ in Figure 4-12. Beside the definition of SPR effect for the presence of $k_{r,m}$

radiative channel, Dulkeith *et al.* have interpreted such phenomenon by the process in which excited *d*-band holes recombine nonradiatively with *sp*-band electrons, emitting particle plasmons. These plasmons subsequently radiate, giving rise to the photoluminescence observed in different experimental studies [62].

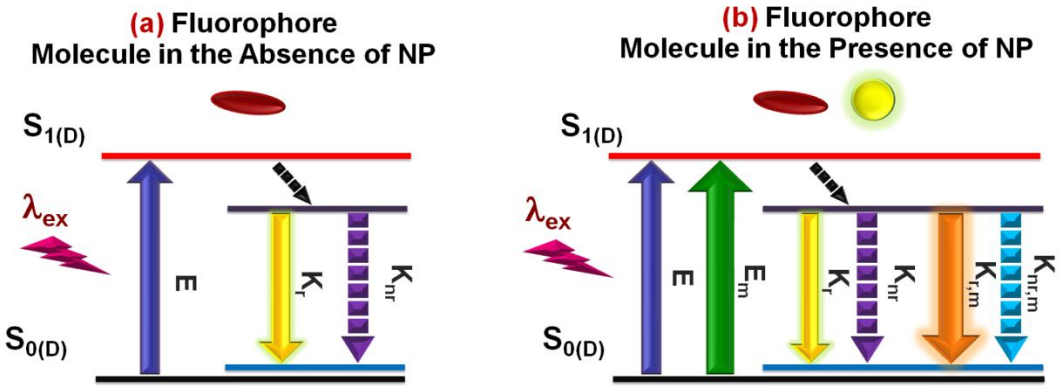

Figure 4-12 Simplified Jablonski diagram for illustrating the excitation enhancement process due to local enhanced field of NPs and the emission enhancement processes due to creation of a new decay channels, described by decay rates $k_{r,m}$ and $k_{nr,m}$.

As result of these additional terms, variation in emission properties of a fluorescent material such as the quantum yield and the fluorescence life time is expected.

$$\Phi_{C,M} = \frac{k_{r,0} + k_{r,m}}{k_{r,0} + k_{nr,0} + k_{r,m} + k_{nr,m}} \qquad (4-32)$$

$$\tau_{C,M} = \frac{1}{k_{r,0} + k_{nr,0} + k_{r,m} + k_{nr,m}} \qquad (4-33)$$

In mentioned equations, the notification of C-M stands for chromophore-metal. It is clear from these equations that the lifetime of chromophore is shorter than its intrinsic lifetime. An enhanced fluorescence emission can be attained if the modified quantum efficiency is larger than the initial quantum efficiency of a chromophore [1].

Evidently the enhancement of quantum efficiency for an acceptor molecule occurs, if enhancement of total radiative decay rate is overweighed respect to the modification of the total nonradiative decay rate. On the other words,

$$k_{r,0} + k_{r,m} = k_r \uparrow\uparrow \quad , \quad k_{nr,0} + k_{nr,m} = k_{nr} \uparrow \quad \Rightarrow \quad \tau_{C,M} \downarrow \ \& \ \Phi_{C,M} \uparrow \quad PL \uparrow .$$

The emission enhancement strongly depends on the quantum efficiency of the chromophore. An active material with a low quantum yield has a nonradiative decay rate much larger than the radiative rate ($k_{nr,0} >> k_{r,0}$). Quantum efficiency of such a material in the presence of a plasmonic NP can be significantly enhanced. This can occur because nonradiative DMPET

pathways are much weaker than introduced new radiative channel ($k_{nr,m} << k_{r,m}$) and additionally the induced chromophore emission by NP is much stronger than the intrinsic one ($k_{r,m} >> k_{r,0}$) [63]. Therefore, the fluorescence emission cannot be enhanced significantly for a dye that has a high quantum yield. The only expected effect can be the shortening of the fluorescence lifetime, resulting in an improvement in the photo-stability of the chromophore [64].

More to the point, as equation (4-27) expresses this fact that the coupling efficiency of the fluorescence emission to the far field can be improved through NP scattering [65-67]. Broadly speaking, metal NPs whose extinction cross section is dominated by plasmonic absorption tend toward quenching of the chromophore fluorescence whereas those whose extinction is dominated by scattering cross section can enhance the overall external quantum efficiency [68]. The experimental observations of Viste *et al*. confirm this fact that emission of chromophore-gold NPs array can be either enhanced or quenched, respect to size of NPs. As Figure 4-13 shows that the emission of QDs in close proximity of NPs with 80 nm of size is quenched whereas for sizes bigger than 100 nm, PL efficiency of QDs is enhanced [68]. Consider that changing the size and shape of nanostructures can modify their plasmon band spectral coincidence with emission spectrum of chromophore, which can affect the emission enhancement process. The enhancement rate can be at maximum point when the absorption peak wavelength of the chromophore overlaps with the resonance wavelength of the NP [69].

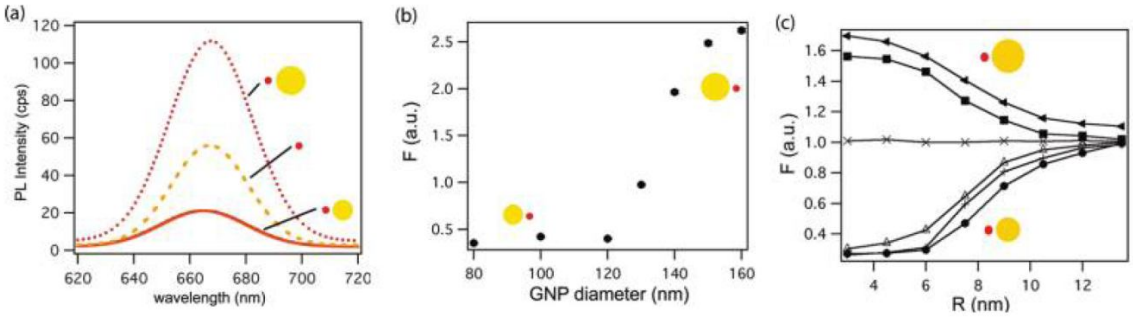

Figure 4-13 (a) PL spectrum measured in the vicinity of Au NP of 80 nm (line), without NP (dash), and in the vicinity of Au NP of 140 nm (dots), respectively. **(b)** Modification factor of photoluminescence F as a function of the NPs diameter **(c)** Modification factor of F as a function of the gap between Au NP and the QDs for a diameter of NP of about 80 nm (black circle), 100 nm (+), 120 nm (triangle up), 130 nm (X), 140 nm (black square), and 160 nm (black triangle left) [67].

In addition, the experimental study of the same group evidences the effect of interparticle distance in the emission efficiency of both photoluminescence enfacement and quenching regimes (Figure 4-13(c)). On the other hand, the experimental studies of Peng *et al.* show that for gold core-silica shell NPs dispersed into water solutions, in particular thicknesses of silica shell

between gold core and Rhodamine 6G (R6G) dye molecules, emission quenching occurs (below 7.6 nm), while for silica interparticle distances longer than 7.6 nm fluorescence enhancement takes place and arrives to the maximum intensity at 21.9 nm of silica spacer [40].

4.5.2 Gersten-Nitzan Model

A full understanding of the chromophore-NP interactions requires the inquiry of both radiative and nonradiative decay rates, which can be extracted experimentally by steady-state PL spectroscopy and theoretically by using some models [29]. In particular, J. Gersten and A. Nitzan developed an electrostatic theoretical model to describe interactions of a fluorescent molecule with a metal nanoparticle. This model has developed for a spherical NP with a diameter much smaller than the wavelength of light. The whole system is considered electrostatically, hence retardation effects are neglected. The parameters such as size and dielectric constant of NP, interparticle distance, permittivity of host medium and dipole moment orientation can be considered by the model. Since fluorophore in solution has no defined dipole orientation, hence a random orientation to the NP surface would consist of 2/3 of the pure tangential and 1/3 of the pure radial contributions from the corresponding radiative and non-radiative rates.

Figures 4-14(a) and (b) show the distance dependencies of the radiative and nonradiative energy transfer rates for tangential and radial orientations for a Cy5 dye with 1390 ps decay time near a 6 nm gold NP which are attached by ssDNA groups [58]. Calculations are made for the relevant distance range which the dye-NP conjugates are made in this work. Furthermore, the orientation of the Cy5 transition dipoles is assumed to be tangential (dash dotted line) or radial (dotted line) to the surface of Au NP.

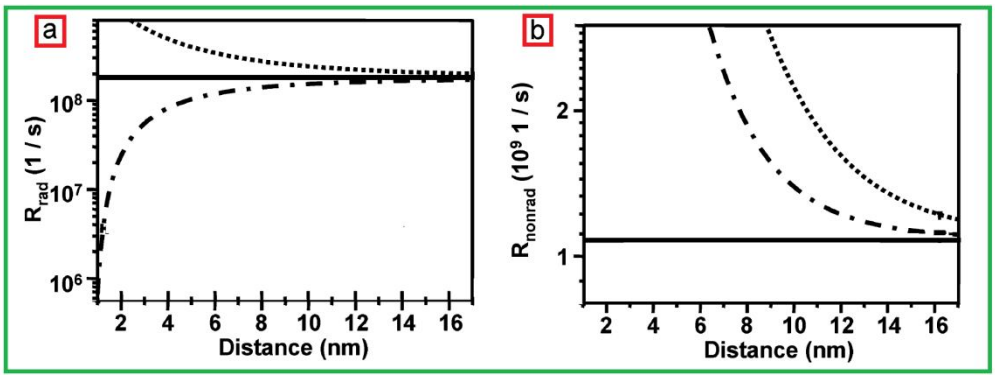

Figure 4-14 (a) Radiative rate and **(b)** nonradiative rate of Cy5 molecules as a function of their distance to the gold nanoparticle surface. The solid lines are the radiative and nonradiative rates and quantum efficiencies with negligible influence of the Au NPs. Calculated radiative and nonradiative rates and the resulting quantum efficiencies are shown for molecular dipole orientations that are radial (dotted lines) or tangential (dash dotted lines) to the NP surface [58].

As Figure 4-14(a) shows in perpendicular orientation, the radiative decay rate can be enhanced for shorter interparticle distances. While in tangential orientation, k_r for all dye-NP distances lies below intrinsic radiative decay rate of fluorophore (k_{r0}). By comparing the experimental results with calculated radiative decay rate, we can conclude which is the dominant orientation of chromophore dipoles respect to NPs surface. Figure 4-14(b) reflects the proof for the existence of energy transfer process in chromophore-plasmon composite, in spite of the orientation of active material toward NP surface. The results show that at very short distances below 5 nm energy transfer dominates and fluorescence efficiency diminishes.

4.6 Dexter and Radiative Re-absorption Energy Transfer Methods

If the fluorescent material is in subnanometric distance apart from metal NP (typically less than 10 Å), energy transfer is mediated through Dexter-type energy transfer. In this type of energy transfer which was first theoretically described by Dexter [70], the orbital wave functions of the two entities start overlapping, allowing for electron exchange. The energy transfer rate in this case has the following distance dependence

$$k_{et,Dexter} \sim Je^{-2R/l}, \qquad (4-34)$$

where J is the spectral coincidence between the normalized donor emission and acceptor absorption spectra $J = \int_0^\infty F_D(\lambda)\varepsilon_A(\lambda)\lambda^4 d\lambda$, R is the donor-acceptor distance and l is the typical penetration depth of the wave function in the environment. To avoid the Dexter-type transfer, the distance between donor and acceptor should be more than 10 Å.

Furthermore, the radiative re-absorption is an energy transfer method where a real photon emitted by a donor is absorbed by an acceptor. The energy transfer rate varies as power of 4 or 6 with distance inverse for non-radiative energy transfer processes whereas as (R^{-2}) for radiative energy transfer. The radiative re-absorptions can be ignored by considering very dilute samples.

REFERENCES

1. J. R. Lakowicz. "*Principles of fluorescence spectroscopy*". Kluwer Academic/Plenum Publishers, New York, 1999.
2. G. Ramos-Ortiz, Y. Oki, B. Domercq, and B. Kippelen, *Phys. Chem. Chem. Phys.*, **2002**, 4, 4109.
3. L. Medintz, *et al.*, *P. Natil. Acad. Sci. USA.*, **2004**, 101, 9612.
4. T. Förster, *Ann. Physics*, **1948**, 2, 55. [Translated by R. S. Knox].
5. C. S. Lim, J. N. Miller, J.W. Bridges, *Anal. Chem. Acta*, **1980**, 114, 183.
6. L. Stryer, *Annu. Rev. Biochem.*, **1978**, 47, 819.
7. I.Z. Steinberg, *Annu. Rev. Biochem.*, **1971**, 40, 83.
8. J. Weber, *Z. Physik*, **1973**, 258, 277.
9. A. R. Clapp, *et al.*, *J. Am. Chem. Soc.*, **2004**, 126, 301.
10. T. L. Jennings, M. P. Singh, and G. F. Strouse, *J. Am. Chem. Soc.*, **2006**, 128, 5462.
11. B. K-K. Fung and L. Stryer, *Biochemistry US*, **1978**, 17, 5241.
12. A. Yekta, J. Duhamel, and M.A. Winnik, *Chem. Phys. Lett.*, **1995**, 235, 119.
13. O.J. Rolinski, and D.J.S. Birch, *J. Chem. Phys.*, **2000**, 112, 8923.
14. P. J. Verveer, A. Squire, and P. I. Bastiaens, *Biophys. J.*, **2000**, 78, 2127.
15. S. L. Logunov, T. S. Ahmadi, M. A. El-Sayed, J. T. Khoury, and R. L. Whetten, *J. Phys. Chem. B*, **1997**, 101, 3713.
16. U. Kreibig, and M. Vollmer, "*Optical Properties of Metal Clusters*", Springer-Verlag: New York, 1995.
17. R. Ruppin, *J. Chem. Phys.*, **1982**, 76, 1681.
18. S. Saraswat, *et al.*, *J. Phys. Chem.*, **2011**, 115, 17587.
19. J. Zheng, C. W. Zhang, and R. M. Dickson, *Phys. Rev. Lett.*, **2004**, 93, 077421.
20. C. S. Yun, *et al.*, *J. Am. Chem. Soc.*, **2005**, 127, 3115.
21. T. L. Jennings, J. C. Schlatterer, M. P. Singh, N. L. Greenbaum, and G. F. Strouse. *Nano Lett.*, **2006**, 6, 1318.
22. Ming Li, *et al.*, *J. Phys. Chem. Lett.*, **2011**, 2, 2125.
23. T. Sen, S. Sadhu, and A. Patra, *Appl. Phys. Lett.*, **2007**, 91, 0431040.
24. T. Pons, *et al.*, *Nano Lett.*, **2007**, 7, 3157.

25. J. Griffin, *et al*., *Chem. Eur. J*., **2009**, 15, 342.

26. M. Prabha Singh, and G. F. Strouse, *J. Am. Chem. Soc.*, **2010**, 132, 9383.

27. R. Chance, and A. Prock, R. Silbey, *Adv. Chem. Phys.*, **1978**, 60, 1.

28. B. N. J. Persson, and N. D. Lang, *Phys. Rev. B*, **1982**, 26, 5409.

29. J. Gersten, and A. Nitzan, *J. Chem. Phys.*, **1981**, 75, 1139.

30. J. Gersten, and A. Nitzan, *Surf. Sci*. **1985**, 158, 165.

31. E. Dulkeith et al., *Phys. Rev. Lett.*, **2002**, 89, 203002,

32. P. C. Das, A. Puri, *Phys. Rev. B*, **2002**, 65, 155416.

33. D. A. Weitz, S. Garoff, J. I. Gersten, and A. Nitzan, *J. Chem. Phys.*, **1983**, 78, 5324.

34. S. Campione, and F. Capolino, *Nanotechnology*, **2012**, 23, 1.

35. S. Campione, M. Albani, and F. Capolino, *Opt. Mater. Express*, **2011**, 1, 1077.

36. M. A. Noginov, *et al., Opt. Express*, **2008**, 16, 1385.

37. C. Garcia, V. Coello, Z. Han, I. P. Radko, and S. I. Bozhevolnyi, *Opt. Express*, **2012**, 20, 7771.

38. D. A. Bobb, *et al*., *Appl. Phys. Lett.*, **2009**, 95, 1511021.

39. M. A. Noginov, G. Zhu, M. Bahoura, J. Adegoke, and C. E. Small, *Opt. Lett*., **2006**, 31, 3022.

40. B. Peng, *et al*., *ACS Nano*, **2012**, 6, 6250.

41. S. Bhowmick, S. Saini, V. B. Shenoy, and B. Bagchi, *J. Chem. Phys.*, **2006**, 125, 181102.

42. R. Carminati, J. J. Greffet, C. Henkel, and J.M. Vigoureux, *Opt. Commun.*, **2006**, 261, 368.

43. A. De Luca, M. Ferrie, S. Ravaine, M. La Deda, M. Infusino, A. R Rashed, A. Veltri, A. Aradian, N. Scaramuzzaa, and G. Strangi, *J. Mater. Chem.* **2012**, 22, 8846.

44. J. Seelig, *et al*., *Nano Lett.*, **2007**, 7, 685.

45. R. Rossetti, and L. E. Brus. *J. Chem. Phys*., **1982**, 76, 1146.

46. T. Soller, M. Ringler, M. Wunderlich, T. A. Klar, and J. Feldmann, *Nano Lett*., **2007**, 7, 1941.

47. E. Dulkeith, "*Optische Charakterisiserung von Hybridsystemen aus Gold Nanopartikeln und Farbstoffmolekülen"*, Ph.D. Thesis, 2004.

48. T. Förster, *Z. Naturforsch*., **1949**, 4a, 321.

49. M. Thomas, J. J. Greffet, R. Carminati, and J. R. Arias-Gonzalez. *Appl. Phys. Lett.*, **2004**, 85, 3863.

50. S. Kuhn, G. Mori, M. Agio, and V. Sandoghdar. *Mol. Phys*., **2008**, 106, 893.

51. O. Stranik. "*Plasmonic enhancement of fluorescence for biomedical diagnostics"*, PhD thesis, 2007.

52. J. R. Lakowicz, *et al*., **2008**, 133, 1308.

53. T. Neumann, M. L. Johansson, D. Kambhampati, and W. Knoll., *Adv. Funct. Mater*., **2002**, 12, 575.

54. Y. Chen, *et al*., *Appl. Phys. Lett.*, **2008**, 93, 053106.

55. P. J. Schuck, D. P. Fromm, A. Sundaramurthy, G. S. Kino, and W. E. Moerner, *Phys. Rev. Lett.*, **2005**, 94, 017402.

56. S. Kuhn, U. Hakanson, L. Rogobete, and V. Sandoghdar, *Rev. Lett.*, **2006**, 97, 017402.

57. F. R. Aussenegg, A. Leitner, M. E. Lippitsch, H. Reinisch, and M. Riegler. *Surface science*, **1987**, 189, 935.

58. E. Dulkeith, *et al*., *Nano Lett.*, **2005**, 5, 585.

59. P. Anger, P. Bharadwaj, and L. Novotny. *Phys. Rev. Lett.*, **2006**, 96, 017402.

60. S. Mayilo, "*Exploiting Energy Transfer in Hybrid Metal and Semiconductor Nanoparticle Systems for Biosensing and Energy Harvesting*", PhD Thesis, 2009.

61. J. R. Lakowicz, *Anal. Biochem.*, **2001**, 298, 1.

62. E. Dulkeith, T. Niedereichholz, T. A. Klar, and J. Feldmann, *Phys. Rev. B*, **2004**, 70, 205424.

63. M. Trnavsky, "*Surface plasmon-coupled emission for applications in biomedical diagnostics*", PhD Thesis, 2009.

64. K. Vasilev, F. D. Stefani, V. Jacobsen, W. Knoll, and M. Kreiter. *J. Chem. Phys.*, **2004**, 120, 6701.

65. F. Tam, G. P. Goodrich, B. R. Johnson, and N. J. Halas. *Nano Lett.*, **2007**, 7, 496.

66. J. H. Song, T. Atay, S. Shi, H. Urabe, and A. V. Nurmikko, *Nano Lett.*, **2005**, 5, 1557.

67. P. Viste, *et al*,. *ACS Nano*, **2010**, 4, 759.

68. J. Lakowicz, *Anal. Biochem.*, **2005**, 337, 171.

69. R. Bardhan, N. K. Grady, J. R. Cole, A. Joshi, and N. J. Halas, *ACS Nano*, **2009**, 3, 744.

70. D. L. Dexter, *J. Chem. Phys.*, **1953**, 2, 836.

Chapter 5

Experimental Instruments and Setups

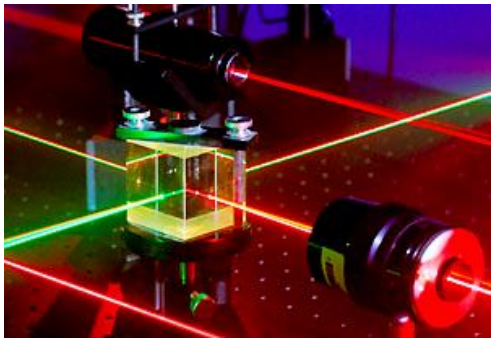

5.1 Introduction

In order to obtain a systematic characterization of designed and fabricated samples, the employing of proper and accurate experimental setups in essential. According to the properties of the samples and the expected information from the experimental analysis, the type of the nneded optical setup or instruments and essential alignments of the associated equipments are determined. In this research study, comprehensive experimental investigations on all the samples ranged from nano-scale to macro-scale has been accomplished. These experimental studies are consisted of acquiring extinction cross section, optical absorption, emission, fluorescence decay time, quantum efficiency, and optical transmission and Rayleigh scattering signals. Varieties of instruments and optical setups including light sources and detectors have been employed to provide experimental evidences, which were essential for completing this research study.

This chapter gives a brief introduction and explanation to the applied experimental setups and instruments of the work, consisting of: (i) the applied spectrophotometer and the sort of the experiments that have been done by this machine, (ii) the exploited spectrofluorometer for

acquiring fluorescence lifetime and quantum yield of prepared samples, (iii) pump-probe setup and involved equipments in this optical arrangement, (iv) advanced optical arrangement, consisted of ultrafast fluorescence lifetime spectrometer and broadband pump-probe setup, and (v) the employed electron microscopes to acquire the accurate images of different samples.

5.2 Application and Specifics of the Applied Spectrophotometer

The optical properties such as absorption, transmittance and diffusion (scattering) of various dispersion and bulk samples are acquired by mean of Cary5E UV-Vis-NIR spectrophotometer manufactured by Varian. This Spectrophotometer covers the wavelength range of 175 nm (ultraviolet or UV) to 3300 nm (near infrared or NIR) with an accuracy of 0.1 nm in the UV-Vis range and 0.4 nm in the NIR range. Figure 5-1 illustrates a scheme for the optical components of a Cary500 spectrophotometer.

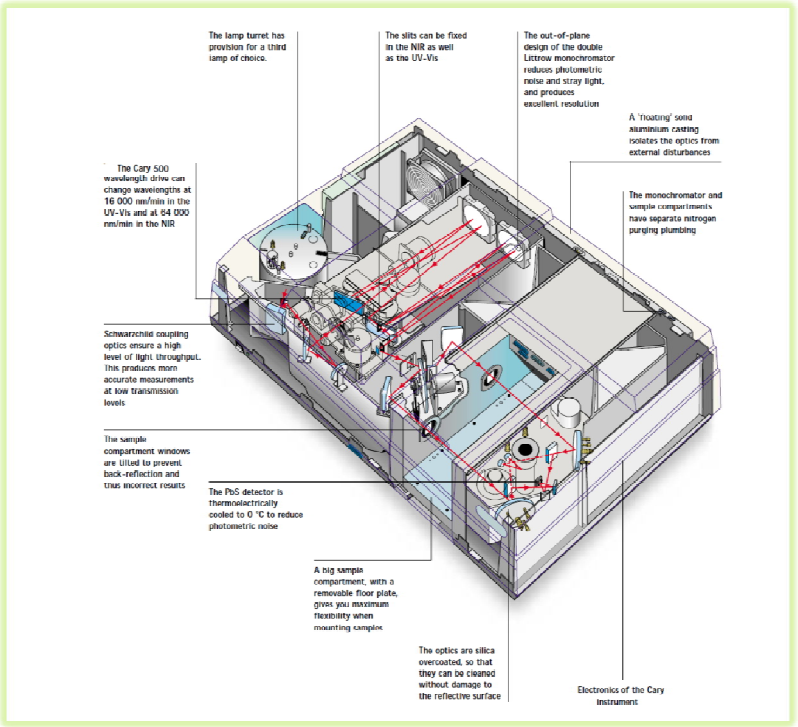

Figure 5-1 Scheme for the optical parts of Cary5E UV-Vis-NIR spectrophotometer.

This instrument uses a double beam, double out-of-plane Littrow monochromator and dual double-sided gratings. Light sources are a deuterium lamp (185 – 350 nm), xenon lamp (350 – 850 nm) and quartz-halogen lamp (850 – 3300 nm). Detection in the UV-Vis range is with a high performance R928 photomultiplier tube and in the NIR with a low noise, electrothermally-controlled PbS photocell. Spectral bandwidths from 0.01 - 5.00 nm (UV-Vis)

and 0.04 - 20.0 nm (NIR) are presented. Signal averaging is available from 0.033 to 999 seconds and scan rates up to 2000 nm/min (UV-Vis) and 8000 nm/min (NIR). The spectrophotometer is centrally controlled by means of user friendly software from PC.

5.2.1 Absorbance and Transmittance Measurements

In spectroscopy, according to the Bear-Lambert- Bouguer law [1], the absorbance *A* of the sample is defined as,

$$A(\lambda) = -\log(\frac{I_T(\lambda)}{I_0}) = -\log(T(\lambda)) \qquad (5-1)$$

where $I_T(\lambda)$ is the intensity of transmitted light through the sample at a specified wavelength λ and I_0 is the intensity of the light before it enters the sample or simply incident light intensity. Beside measuring the transmittance parameter (*T*), which varies logarithmically with thickness and concentration of the sample, the spectrophotometer can provide the absorbance spectrum of the sample which is proportional to the thickness of the sample (*d*) and the molar concentration of the absorbing species in the sample (*c*); this is illustrated in Figure 5-2.

$$A(\lambda) = -\varepsilon cl = -\alpha l \qquad (5-2)$$

here ε and α are defined as molar concentration and optical absorption coefficient of the sample, respectively. Indeed, the spectrophotometer gives an experimental value of the absorbance using transmittance values for non-scattering samples. The procedure for measuring the pure absorbance of scattering samples is defined in the next part.

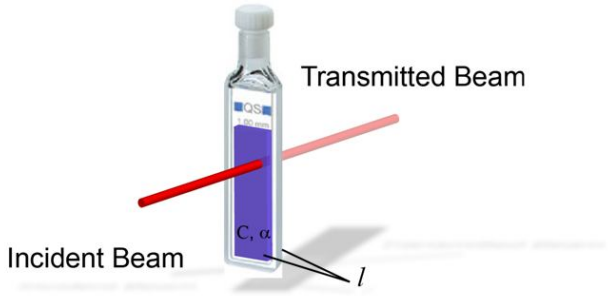

Figure 5-2 Scheme of Beer-Lambert absorption of a beam of light as it travels through a cuvette of width *l* for an undiffused system.

5.2.2 Absorbance Measurement of Diffusive Samples

Most of the samples that have been studied in this thesis are diffusive. In order to extract the absorbance of such samples, the integrated sphere needs to be installed in spectrophotometer, which is a simple device that spatially integrates the radiant flux. It consists of a large hollow

globe with diameter of 102 mm which has its inner surface covered with a diffuse reflectance coating of pure calcium carbonate. The exciting light passes through the entrance port, and the emission reaches to the detector via the exit port. The sample can be placed at the centre of the sphere or side mounted on the sphere wall. Figure 5-3 shows this accessory of Cary5E with inside optical components.

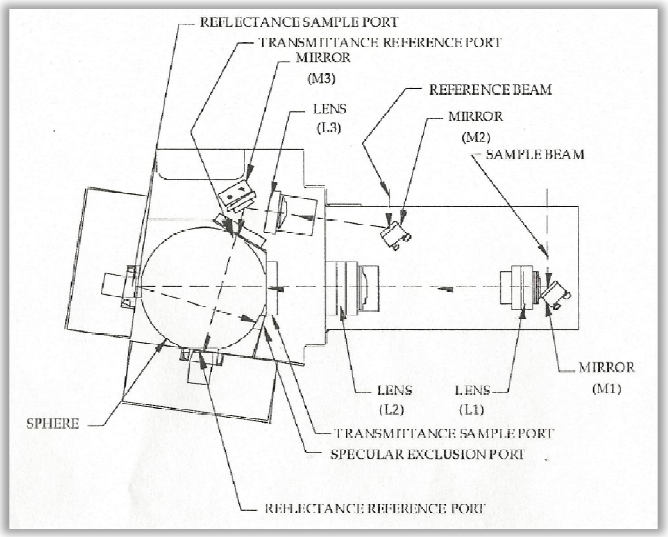

Figure 5-3 the integrated sphere of the Cary 5E spectrophotometer.

In fact, for scattering samples, there are three primary types of transmittance measurements: *total transmittance* (T_t), *diffuse transmittance* (T_d) (forward scattering) and *regular transmittance* (T_r). Figure 5-4 demonstrates various types of the transmittance that can be acquired for a scattering sample.

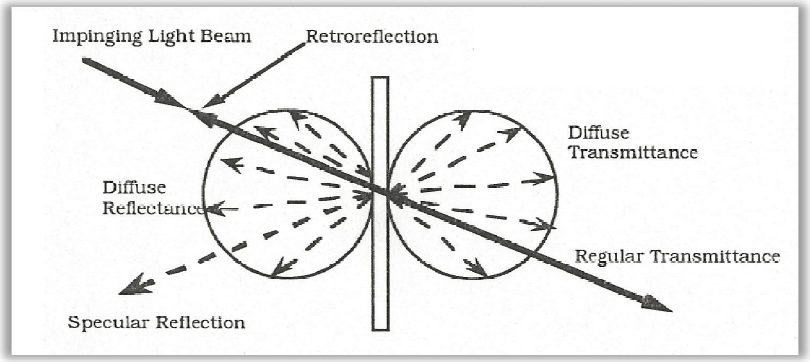

Figure 5-4 Diagram of the Reflectance and transmittance components of a scattering sample.

For sample exhibiting a high degree of scattering, the transmittance-measurement procedure described in prior section, does not provide a measurement of *total transmittance*. Instead, the result displayed by the instrument will be an instrument-specific value which is

known as *regular transmittance*, defined as the ratio of the transmitted light respect to the incident light. In the other words, according to the scheme of Figure 5-2 we have,

$$T_r = \frac{I_T}{I_0} \qquad (5-3)$$

In this case, the value resulting from the following formula is the extinction cross section of the sample.

$$C_{ext} = \log(-T_r) \qquad (5-4)$$

Total Transmittance of the sample is defined as the sum of *diffused transmittance* (T_d) and *regular transmittance* (T_r).

$$T_t = T_r + T_d \qquad (5-5)$$

Diffuse transmittance or simply scattering is referred to the transmittance in which flux is scattered in many directions by diffusion at front surface of sample, while regular transmittance is the ratio of the undiffused transmitted light respect to the incident light. Note that two parameters of regular transmittance and regular transmittance factor are slightly different.

Total reflectance of the sample is defined as the sum of diffused reflectance (R_d) and specular reflectance (R_s).

$$R_t = R_s + R_d \qquad (5-6)$$

Diffuse reflectance or back scattering is referred to the reflection in which flux is scattered in many directions by diffusion at rear surface of the sample, whereas specular reflection is the reflection without diffusion, in accordance with laws of optical reflection, as in a mirror. Now by applying Bear-Lambert law, it is possible to extract absorption cross section (absorbance) of the sample.

$$A = -\log[(T_t + R_t)/100] \qquad (5-7)$$

This expression means that undiffused and unreflected fractions of the incident light are absorbed by the given sample.

In order to extract experimentally the value of total transmittance, the sample should be inserted at the *transmittance sample port* of the integrated sphere (see Figure 5-3). In addition, in order to focus the beam on sample surface, the lens L1 should be moved back along its base plate as close to mirror M1 as possible and the lens L2 should be shifted toward sphere as far as it goes. After applying zero, base line corrections, the resulting measurement will be the *total*

transmittance of the sample. In addition, with the aim of acquiring total reflection, according to Figure 5-3 the given sample must be placed in *reflectance sample port*. The position of two mirrors of L1 and L2 exactly should be reversed respect to the total transmission measurement (these two mirror should be placed as close to each other as possible) for creating new focus point on sample surface. Obviously in this case, due the manipulation of the instrument optical objects, zero baseline correction procedure must be repeated.

5.2.3 Forward and Backward Scattering Measurements

In order to acquire Forward scattering (T_d) parameter, the position of the sample and lenses (M1&M2) must be adjusted similar to the total transmittance measurement, except the standard positioned at the reflection sample port should be replaced by a beam trapper. In this way, the undiffused portion of the flux transmitted by the sample is excluded from measurement. Note that by measuring total transmittance and diffuse transmittance factors, and applying their values in equation (5-5), the component of regular transmittance can be extracted. Hence, the extinction cross section of the diffused sample can be calculated by means of the integrated sphere, as well.

Furthermore, the parameter of the backward scattering (R_d) can be measured by integrated sphere. The arrangement of the focusing lenses and sample position must be set as it should be done in total reflectance experiment. Except for excluding the specular component of reflected beam from the experiment, the removable plug adjacent to the sample transmittance port needs to be replaced by a beam trap. This plug is corresponds to an 8° angle of reflection (i. e. specular reflection).

5.3 Steady-State and dynamic fluorescence spectroscopy

5.3.1 Emission

Steady-state emission spectra were recorded on a HORIBA Jobin-Yvon Fluorolog-3 FL3-211 spectrometer (Figure 5-5) equipped with a 450W xenon arc lamp (**L**), double-grating excitation ($\mathbf{M_{ex}}$) and single-grating emission ($\mathbf{M_{em}}$) monochromators (2.1 nm/mm dispersion; 1200 grooves/mm), and a Hamamatsu R928 photomultiplier tube (**PM**) or a TBX-04-D single-photon-counting detector ($\mathbf{D_{TCSPC}}$) or a InGaAs liquid nitrogen-cooled solid-state detector

($\mathbf{D_{InGaAs}}$). Emission and excitation spectra were corrected for source intensity (lamp and grating) and emission spectral response (detector and grating) by standard correction curves.

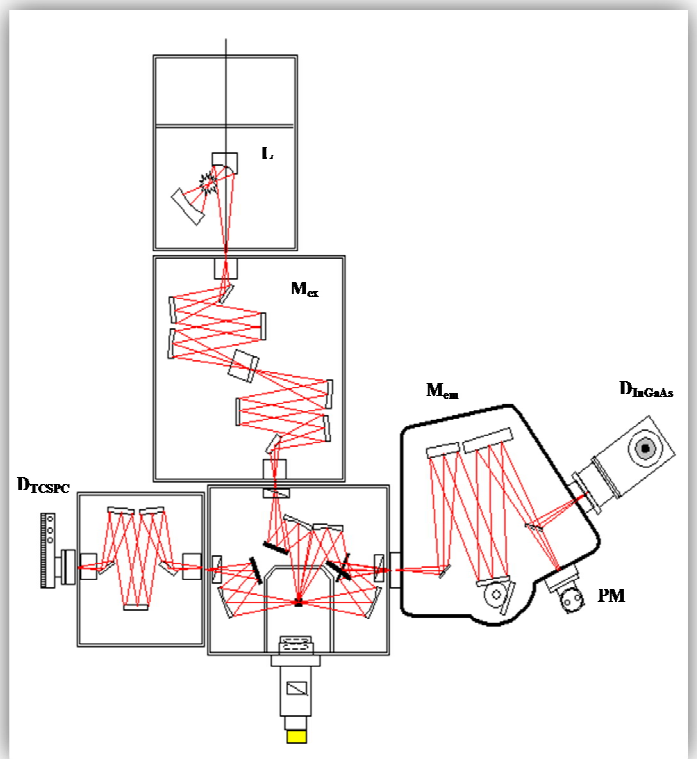

Figure 5-5 FluoroLog3-2iHR1-TCSPC-IGA, optical configuration.

5.3.2 Time-Correlated Single Photon Counting Technique

Since the principle operation of acquiring the fluorescence lifetime in time-domain for both HORIBA Jobin-Yvon spectrofluoromoter and Edinburgh FLS980 Series fluorescence lifetime spectrometer is based on the Time-correlated single-photon counting (TCSPC) data, therefore before describing the characteristics of the mentioned instruments, this method of lifetime measurement is described.

Time-correlated single-photon counting (TCSPC) is a digital technique, in which counting of time-correlated photons is related to excitation pulse [2]. To collect TCSPC data the sample is excited periodically with a fast source. Excitation frequency is determined respect to the optical behavior of the sample. This provides the possibility to extend the data collection over multiple cycles and reconstruct the decay profile from single photon events collected over many cycles. The expected exponential shape of lifetime waveform would be observed if many fluorophores are excited and numerous photons are detected. However, for acquiring TCSPC

data, due to conditions of measurement, less than one photon is detected per laser pulse. In fact, typically in every 100 excitation pulses just one photon is detected. This drawback comes from the dead time of electronics that they are not enough fast to measure multiple photons per pulse. The principle of TCSPC used in both spectrofluorometers can be understood by provided scheme in Figure 5-6 [2]. The experiment starts with exciting the sample by repetitive pulses of a light source such as laser or flash-lamp. Simultaneously, the light source sends a signal to a constant function discriminator (CFD), which accurately measures the arrival time of the pulse. The output signal of CFD block is applied to time-to-amplitude converter (TAC) block, in order to trigger a voltage ramp, which can increase linearly with time on the nanosecond timescale. A second channel identifies the pulse from the single detected photon. As a single photon sensitive detector a Photomultiplier Tube (PMT), Micro Channel Plate (MCP) or a Single Photon Avalanche Diode (SPAD) can be used. As the emission pulse is arrived to CFD, this block sends a signal to TAC to stop the voltage ramp. Now TAC provides an output pulse which the difference between start and stop points of that, is proportional to time delay between the excitation and emission signals. The output signal of TAC is amplified by a programmable gain amplifier (PGA). Finally a multichannel analyzer converts the output signal of PGA to a numerical value by using an analog-to-digital converter (ADC). The electronic circuits embedded in window discriminator (WD) block are responsible to minimize false readings of signal by restricting the acquired signal to determined range of voltages. The obtained digital signal is stored as a single event with the measured time delay. In order to complete the decay histogram this process needs to be repeated with a pulsed-light source, until one has collected more than 10000 counts in the peak channel [2,3].

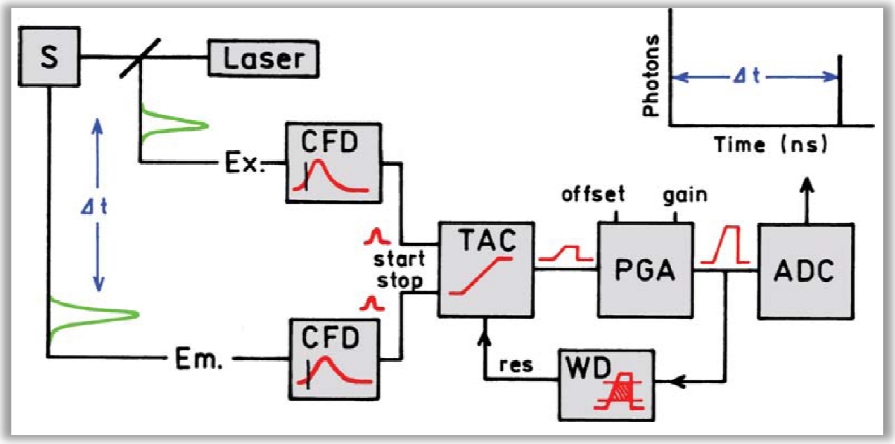

Figure 5-6 Electronic schematic for TCSPC [2].

5.3.2.1 Fluorescence Lifetimes

Time-resolved measurements were performed using the TCSPC option on the Fluorolog 3. Excitation sources respect to the type of the sample (Table 5-1) were mounted directly on the sample chamber at 90° to a single-grating emission monochromator (2.1 nm/mm dispersion; 1200grooves/mm) and collected with a TBX-04-D single-photon-counting detector. The photons collected at the detector are correlated by a TAC to the excitation pulse.

Source	λ_{em}	Duration	Power	Repetition rate
Nanoled	265 nm	1.2 ns	0.2 pJ	1 MHz
Laser Nanoled	379 nm	750 ps	63 pJ	1 MHz
Nanoled	461 nm	1.3 ns		1 MHz

Table 5-1 Equipped excitation sources of the spectrofluorometer.

Signals were collected using an IBH Data Station Hub photon counting module, and data analysis was performed using the commercially available DAS6 software (HORIBA Jobin Yvon IBH). The fitting procedure of the emission intensity decays $I(t)$ according to equation (3-7) uses a multi-exponential model according to the expression. Quality of fit was assessed by minimizing the reduced Chi squared function (χ^2) and visual inspection of the weighted residuals. When using the multi-exponential decay law it is often valuable to determine the average lifetime ($< \tau >$), which is given by the equation (3-8).

5.3.3 Emission Quantum Yield Measurement

According to the method proposed in 1997 by de Mello *et al.* [4], the emission quantum yields (Φ) of the solid samples were obtained by means of a 102 mm diameter integrating sphere coated with Spectralon and with the sample mounted at the centre, in the optical path of the spectrofluorimeter (Figure 5-7).

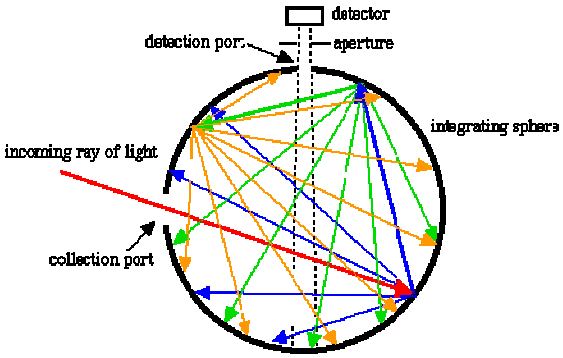

Figure 5-7 Scattering of the incident laser beam from the inner wall of an integrated sphere.

This method employs a 450 W xenon lamp coupled with a double-grating monochromator for selecting wavelengths as an excitation source and the detection system consists of a grating spectrometer with a CCD detector. In this technique in order to determine the absolute luminescence quantum yield of the sample, three experiments are needed to be done in which each experiment records full spectrum.

1. The first experiment provides a sharp high energy peak corresponds to the detection of the laser excitation, L_a, where the laser beam directly hits the inner wall of the empty sphere.

2. In the second experiment, the sample is positioned inside the sphere, but not in the laser beam pathway. In such a situation, the detected signal is composed by the scattered laser light L_b and the light emitted by the sample E_b, after absorbing of the scattered excitation light. E_b has a broader profile with respect to L_a and L_b and due the emission from sample it appears in higher wavelengths. Since the fraction μ of the laser light scattered from the sphere wall is absorbed by the sample, thus the intensity of L_a is lower than the total laser excitation light L_a. We can write,

$$L_b = L_a(1-\mu) \qquad (5-8)$$

3. In the third experiment the laser beam directly hits the sample surface and a fraction A of excitation light is absorbed. The unabsorbed fraction $(1 - A)$ is either transmitted or reflected and scattered inside the sphere. μ is a fraction of this scattered light which is then reabsorbed by the sample. This results in the detection of a more quenched laser excitation signal respect to its initial intensity. The area under the laser profile is proportional to the amount of unabsorbed light. This value for the detected excitation light spectrum L_c can be expressed by the following equation:

$$L_c = L_b(1-\mu)(1-A) \qquad (5-9)$$

Combining equations (5-8) and (5-9) yields an expression for the absorption coefficient A [5].

$$A = (1-\frac{L_c}{L_b}) \qquad (5-10)$$

The measured emission profile in this experiment has higher intensity than E_b due to the presence of two contributions: (a) the first one is arises by absorbing the scattered excitation light, given by $(1-A)E_b$; and (b) the second component is as a result of the direct absorption of the excitation laser light, which is given by $\Phi A L_a$.

$$E_c = E_b(1-A) + \Phi A L_a \qquad (5-11)$$

Here Φ is the absolute photoluminescence efficiency which can be obtained by rearranging equation (5-11).

$$\Phi = \frac{E_c - E_b(1-A)}{AL_a} \qquad (5-12)$$

The experimental uncertainties were 1 nm for the band maxima for the luminescence spectra and 5% for emission quantum yield.

However, since the prepared bulk composites sample of Au NPs and QDs dispersed in PDMS host are low emissive and high diffusive, hence the mentioned method of measuring quantum yield should be adopted for such samples. In this method, there is no need to perform the first mentioned experiment to acquire laser excitation profile. Instead of that, the reference sample is mounted inside integrated sphere in front of the detector, but not in direct pathway of excitation beam of xenon lamp. However, a reflecting baffle is used within the sphere, in order to shield the detector from direct sample emission rays. The operation wavelength of xenon lamp has been selected at maximum point of excitation band of the sample. The spectra profile of L_a and E_a related to the reference sample can be obtained by this experiment.

The second experiment is performed on a main sample. Also in this case the sample should not be placed in direct pathway of excitation beam. This experiment provides the data regarding the scattered light profile L_c of source light and fluorescence spectrum E_c of main sample. By modifying the equation (5-9) and (5-11) as following expressions, the absorption coefficient and quantum yield of sample can be calculated.

$$A = (1 - \frac{L_c}{L_a}) \qquad (5-13)$$

$$\Phi = \frac{E_c - E_a(1-A)}{AL_a} \qquad (5-14)$$

5.4 Pump-Probe Rayleigh Experimental Setup

In order to provide convincing evidences for optical loss mitigation in designed gain-plasmon composite systems, two vital experiments of optical transmission and Rayleigh scattering must be performed based on a pump-probe setup. The scheme of this setup is illustrated in Figure 5-8. In this setup, the sample S is optically lamp-pumped with 4ns pulses of the third harmonic of a Q-switched Nd:YAG laser, Brio manufactured by Quantel. This laser can generate the fundamental wavelength of Nd:YAG at 1064 nm or its harmonics (532 nm, 355 nm,

266 nm). This is achieved by specific modules (2ω, 3ω, 4ω) easily plugged onto the optical head with no alignment required. The harmonic generator is made with different kinds of the crystals, depending of the oscillator type and requested wavelength. However, in this research work, the third harmonic (λ = 355 nm) of this laser is applied and the second generated harmonic (λ = 532 nm) is eliminated by a proper filter, placed in laser beam path. This pulses are produced with repetition rate of the laser is 20 Hz. The energy of the output laser beam can be controlled by a half wave plate, indicate by symbol of VA in Figure 5-8.

Beside the Q-switched pump, another pulsed laser which generates pulses at 532 nm can be employed as a pump. The repetition rate of this laser can be varied by a control volume up to 20 Hz. In addition, in order to adjust the energy of emitted pulses an electromechanical half-wave plate, controlled by software designed in LabVIEW environment, is mounted in laser beam.

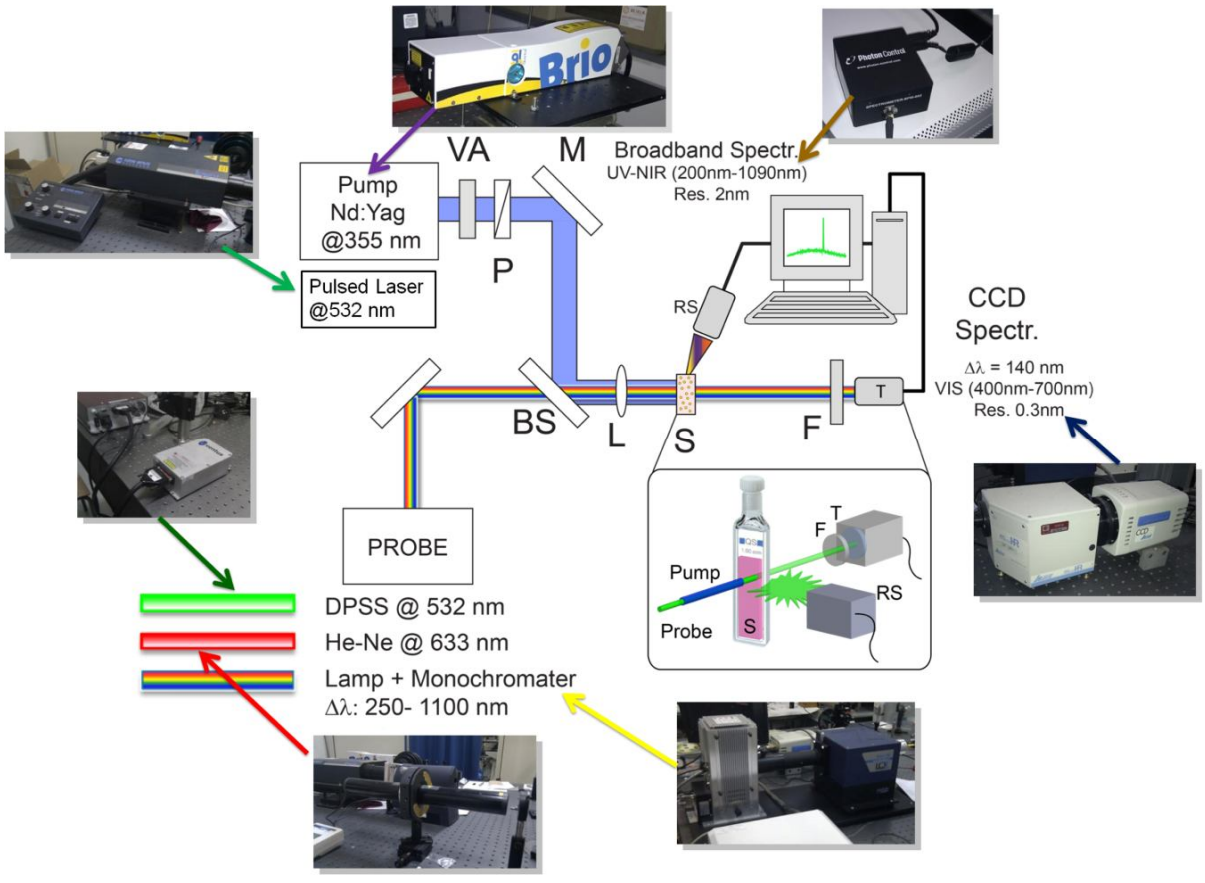

Figure 5-8 Pump–probe Rayleigh experimental set-up. VA: variable attenuator, P: polarizer, M: mirror, BS: beam splitter, L: lens, S: sample, F: filter, RS: Rayleigh scattering detector, T: transmission detector, DPSS: diode pumped solid state laser CW.

According to the properties of the synthesized hybrid samples, different types of probe beam are applied. In fact, the probe wavelength was chosen in the proximity of the overlapping region between dye fluorescence and plasmon band maxima, where localized surface plasmon modes are expected. In particular, the continuous wave diode-pumped solid-state laser at 532 nm manufactured by Laser Quantum is used as a probe beam. This laser provides the possibility to adjust the intensity of the output beam. However, during the experiment it operates with a fixed low power which is focused within the excitation region of the sample. In addition, a xenon based lamp with a monochromator by LOT-Oriel Group, which can produce a spectrum of light ranged from 250 nm to 1100 nm with 1 nm wavelength resolution. During the experiment, the power of the lamp is fixed and the generated light beam is focused within the pumped region of the sample. Furthermore, this setup is equipped by Helium-Neon gas laser, operating at 633 nm. The output beam intensity is tunable by a half-wave plate, positioned in beam path.

The probe light emitted, scattered, or transmitted by samples can be collected by means of two types of detectors: (a) A high-resolution spectrometer, fabricated by HORIBA Jobin-Yvon MicroHR Symphony. This spectrometer features a 140 mm focal length, a 400 nm to 700 nm wavelength range and 0.3 nm wavelength resolution, with adjustable slits, a high precision counter, and an interchangeable kinematic grating mount. (b) A broadband compact spectrometer (SPM-002-ET Hamamatsu S9840 Back-Thinned CCD), manufactured by Photon-Control. This spectrometer operates in UN-NIR light spectra, ranged from 200 nm to 1090 nm with wavelength resolution of 2 nm, which can connect directly to a laptop or desktop PC through USB port.

The position of the employed spectrometer is determined depending on the particular experiment. The fiber is positioned at the angle of 70° relative to the beam propagation direction for scattering (90° for fluorescence) experiment, within several millimeters from the sample. In the case of Rayleigh scattering measurement the pump beam is focused onto the sample by means of a spherical lens L (f=100 nm), yielding a beam waist of about 100 μm at the focus position. Transmission signals are acquired far from the sample, on the same pump beam direction and with a high neutral filter in front of the fiber head, in order to prevent any possible signal different from the probe one (high stable power). A pin-hole and a notch filter (F in Figure 5-8) provide the best conditions to avoid stray light and any other undesired contribution to the transmitted light.

5.5 Broadband Pump-probe & Ultrafast Dynamic Spectroscopy Setup

Ultrafast spectroscopy has been used to perform broadband pump-probe measurements, to investigate, at the same time, scattering and transmission enhancement on a broad wave-length range. The used system consists in an ultra-fast spectroscopic pump-probe setup. A Ti:Sapphire pulsed laser (red beam in Figure 5-8, rep. rate = 80 MHz, pulse width = 140 fs, by Coherent Inc.), tunable in the 680 nm-1080 nm range, represents the core of a customized set-up that presents at least two possible investigations lines: first line includes a Pulse Picker used to decrease the repetition rate in the range between 4 and 5 M Hz, in order to be synchronized with a multi pronged spectrofluorimeter able to perform both steady state measurements (by means of a Xenon lamp and multiple gratings, by Edinburgh) and time correlated single photon counting investigations. In the same line a Second Harmonic Generation (SHG) module in used to decrease the excitation wavelength in the range 340 nm-540 nm (blue beam). All the above mentioned investigations are performed inside the spectrometer chamber (sample position S1). Second investigation line (dashed white on red beam in fig. 6) includes all the components used to perform broadband pump-probe analysis, both in transmission and scattering configuration (D1 and D2). An infrared light beam (from 750 nm to 900 nm) is sent to a 30:70 beam splitter without passing thorough the pulse picker; 70 percentage of the beam is duplicated in frequency and used to excite sample in position S2 (outside of the chamber); at the same time, the remaining 30% is used to generate super continuum light from a nonlinear photonic crystal fiber, to obtain a probe beam with a broadband distribution (500 nm-1300 nm), phase matched with the primary pulsed beam.

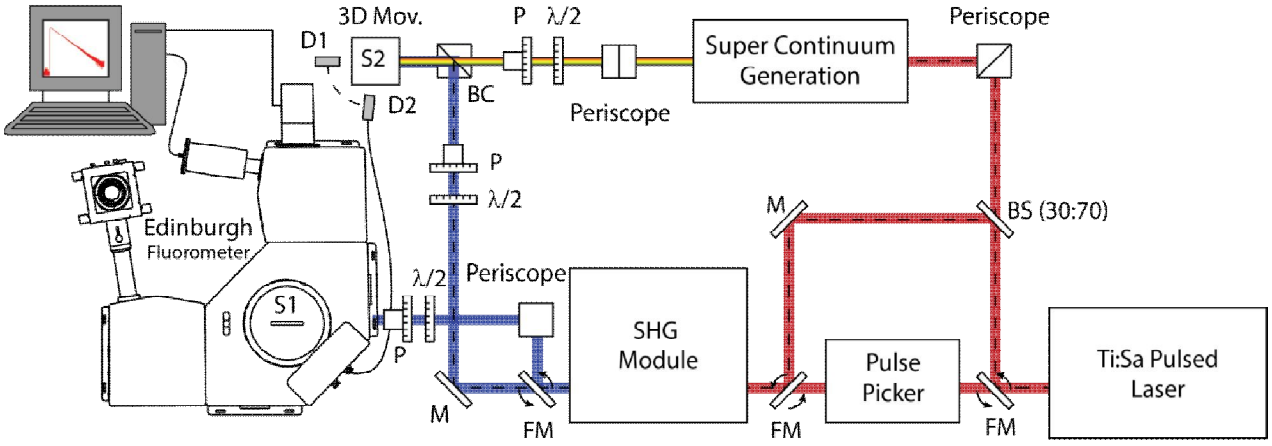

Figure 5-9 Scheme of the ultrafast spectroscopy setup to perform broadband pump-probe Rayleigh experiments and time-resolved fluorescence measurements.

Pump and probe beams are coupled by means of a beam coupler (BC) and co-launched on the 3D holder sample (S2). A larger beam waist is chosen for pump beam with respect the probe one, in order to be sure to investigate an area really shined by pump light. Transmitted (D1) and scattered (D2) light are collected with a multimode fiber and sent inside the spectrometer chamber in order to be spectroscopically analyzed by means of a CCD camera (by Andor). A multi channel plate, synchronized with the incoming pulses, is instead used to acquire the fluorescence decay lifetime in the proper temporal range. Broadband half wave plates ($\lambda/2$) and high damage threshold polarizers (P) are used to control the pump and probe power. Three periscopes (PE) have been used to have each time an in-plane beam at different heights.

5.6 Electron Microscopy Characterization Instruments

In the whole spatial stages of this research study ranged from nano-scale to macro-scale, electron microscopy images have been acquired to be assure concerning the desire geometrical considerations and other quality parameters of chemically synthesized samples.

For NPs used to prepare gain-assisted system in nano-scale range, Transmission Electron Microscopy (TEM) was carried out with a JEOL JEM 1010 transmission electron microscope operating at an acceleration voltage of 100kV. The particles size and shell thickness distributions were determined from TEM images using at least 100 particles. Fluorescence confocal microscope images were acquired on the prepared system by a Leica TCS SP2, aimed to study the dye-NP aggregation size and separation distance dependence in a resonant energy transfer process. In addition, the Scanning Electron Microscopy (SEM) images are acquired by Environment Quanta FEG 400 manufactured by Philips.

For prepared gain-functionalized systems, multimeric samples (both in nano-scale size range) and also for meso-scaled nanoshell system, TEM observations were performed with a Hitachi H-600 microscope operating at 75 kV, where particles were cast on a glass substrate by leaving a drop of a diluted suspension evaporating. Moreover, TEM investigations were carried out on macro-scaled bulk samples by using a JEOL JEM1011 microscope, operating at an accelerating voltage of 100 kV and equipped with a W electron source.

REFERENCES

1. C. Zhu, and P. R. Griffiths, *Appl. Spectrosc*., 1998, 52, 1403.

2. J. R. Lakowicz, "Principles of Fluorescence Spectroscopy", 3rd ed., Springer, New York, 2006.

3. W. Becker, *et al*., *Rev Sci Instrum*., 1999, 70, 1835.

4. J. C. de Mello, H. F. Wittmann, and R. H. Friend, *Adv. Mater*., 1997, 9, 230.

5. L. Palsson, and A. P. Monkman, *Adv. Mater*., 2002, 14, 757.

Chapter 6

Optical Loss Mitigation in Nano-scaled Hybrid Systems

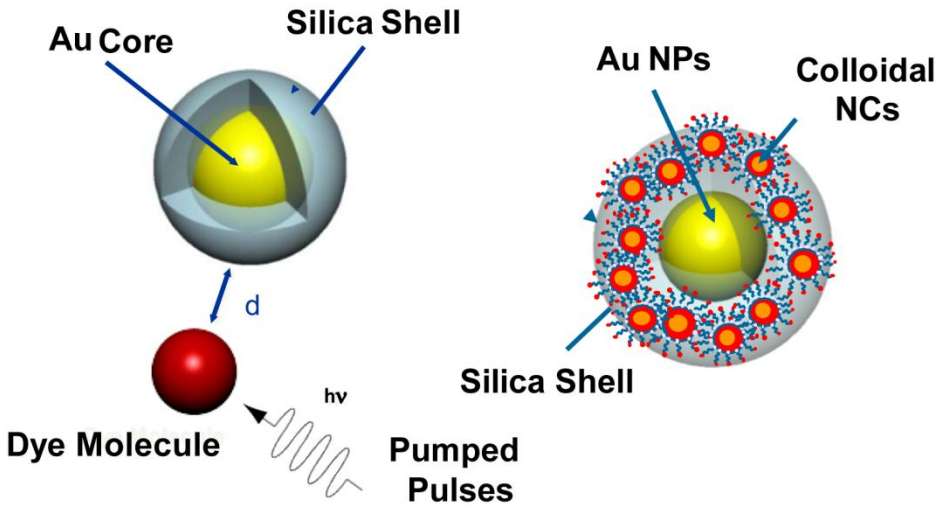

6.1 Introduction

As it has discussed before, plasmonic sub-wavelength structures can be employed as the unit cells of optical metamaterials, due to their interesting behavior of the dielectric permittivity in visible frequencies. This main interest arises from a distinctive feature of plasmonic subunits known as LSPR which makes them capable to confine and strongly enhance the incident electromagnetic field. However, these metal based nanostructures suffer a strong radiation damping which strongly limits their functional applications. In chapter four, it has been represented that how the presence of the active materials in close proximity of metallic NPs can mediate RET in gain-plasmon composites. On the other hand, theoretical studies have shown that

bringing gain to plasmonic structures can reduce the radiation damping in terms of reduction in the imaginary part of the dielectric permittivity.

In this chapter, mitigation of optical losses of plasmonic NPs in nano-scaled hybrid systems experimentally has been reported. In this regard, three different composite systems are investigated: (i) gain-assisted system, (ii) gain functionalized system, (iii) grafted dye multimeric systems. The gain-assisted system is composted of the gain materials such as dye molecules or semiconductor QDs which have been dissolved in solution with plasmonic NPs. Gain-functionalized system, as a step forward towards the goal of the research, is the system in which gain materials are encapsulated within silica shell of core-shell NPs. Finally, the third system is multimeric dye functionalized nanostructures, which has been fabricated by attaching monomeric NPs in a controlled chemical approach to each other, in order to provide the possibility to exploit plasmon hybridization effect within arranged NPs. It is worth to notify that all three systems have been dispersed in ethanol solution.

In all the mention nano-scaled systems, first of all photo-physical characterizations have been performed to extract the plasmon band of NPs and emission spectrum of gain materials. Then, steady-state fluorescence spectroscopy and time-resolved data have been acquired to provide evidences for the occurrence of DMPET process and finally, pump-probe Rayleigh scattering measurements have been performed to create a clear image of optical loss mitigation of plasmonic NPs applied in nano-scale spatial range.

The attained excellent results of the optical loss compensation in nano-scales structures flourish the dare to execute this strategy in meso-scaled systems in order to mitigate their plasmonic losses.

6.2 Structure 1:

Optical Loss Mitigation in Gain-Assisted Systems

As a first step of studying optical loss mitigation in gain-plasmon hybrid structures, nano-scaled gain-assisted (G_A) system is investigated. In this system, fluorescent guest elements (laser dyes or nanocrystals of QDs) are dissolved in the dispersion of bare or core-shell NPs (Figure 6-1(a)), while in a gain-functionalized (G_F) system, as it has showed in Figure 6-1(b), gain materials are encapsulated within silica shell, surrounding plasmonic NPs. The study of this system provides the opportunity to optimize compatibility, spectral overlap and concentration of gain elements towards an efficient nonradiative energy transfer process for optical loss mitigation purposes in practical systems.

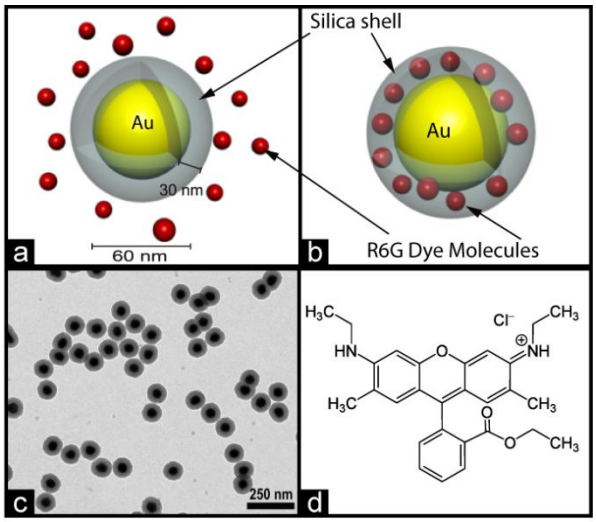

Figure 6-1 The schemes of the **(a)** gain-assisted system in which R6G dye molecules have been dissolved in the ethanol solution of gold core-silica shell NPs; **(b)** gain-functionalized system, in which R6G has been encapsulated within the silica shell. **(c)** TEM image of the gold core/silica shell NPs**. (d)** Chemical formula of R6G dye molecules.

More in detail, the applied core-shell nanoparticles in this gain-assisted system are consisted of a gold core with diameter of 60 nm and a silica shell with 30 nm thickness, which are dispersed in ethanol. The monodispersity and well-controlled shape and size of the mentioned NPs are evidenced in the TEM image illustrated in Figure 6-1(c). The adequate concentration of Rhodamine 6G (R6G) organic dye molecules are added to gold NPs solution to turn out the desire G_A system. The chemical formula of this type of dye molecules is showed in Figure 6-2(d). Despite of not enough large stock shift (~ 40 nm), the tremendous optical properties of R6G dye molecules such as remarkably high photostability, high fluorescence quantum yield (0.95), high absorptivity reasonable range of decay time (~5.5ns) and its

compatible lasing range with respect to the plasmon band of used Au NPs make it as a suitable candidate to create a G_A system [1].

6.2.1 Steady-State Fluorescence Measurements

Figure 6-2 shows the absorption spectrum of R6G dye molecules and the spectral overlap among plasmon band of core-shell NPs and emission spectrum of active dye molecules when it is optically excited by Q-switched laser pulses at 355 nm.

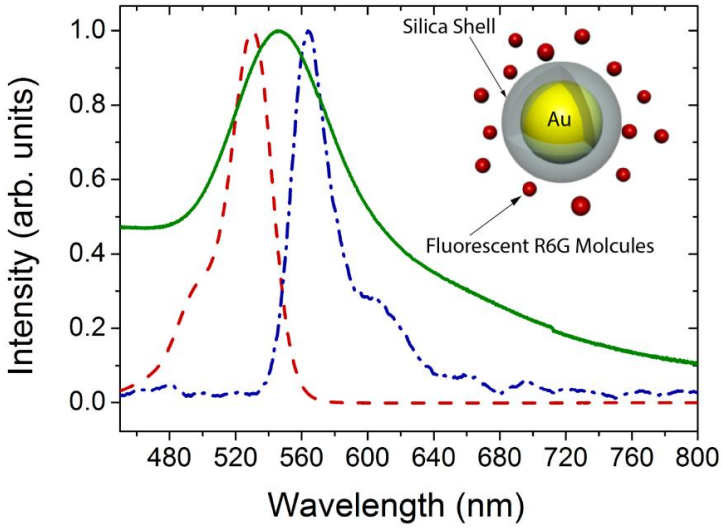

Figure 6-2 Absorption (red dashed line) and emission (blue dash-dotdot line) spectra of Rhodamine 6G dye in ethanol and plasmon bands of gain-"assisted" gold nanoparticles (green solid line).

The presence of this overlap is a necessary situation for occurrence of RET process among active dye molecules and absorptive plasmonic NPs. As this figure shows that the dye has an absorption maximum approximately at 530 nm and its lasing range is located within 550 to 585 nm with a maximum at 563 nm.

It is well-known that relevant modifications of the fluorescence of dye molecules placed in close proximity to metal nanoparticles (NPs) are due to mutual interactions with nanoparticle surface plasmons including resonant energy transfer [2]. As reported by Dulkeith, as a result of remarkable enhancement of nonradiative decay rate respect to modification of radiative decay rate a drastic quenching of dye fluorescence is expected [3]. In order to make evidence this phenomenon in our prepared gain-assisted system, emission of R6G dye molecules in both cases of pure ethanol-based solution and mixed with plasmonic quenchers has been acquired by optically pumping with large spotted pulse trains of a tripled Nd:YAG laser (λ = 355 nm) at the same pump energy value (see section 5.4 for setup details). Figure 6-3 shows the fluorescence

quenching observed in the Au@SiO2/R6G system with respect to pure R6G dye molecules with the same concentration (0.01wt%) in ethanol solution.

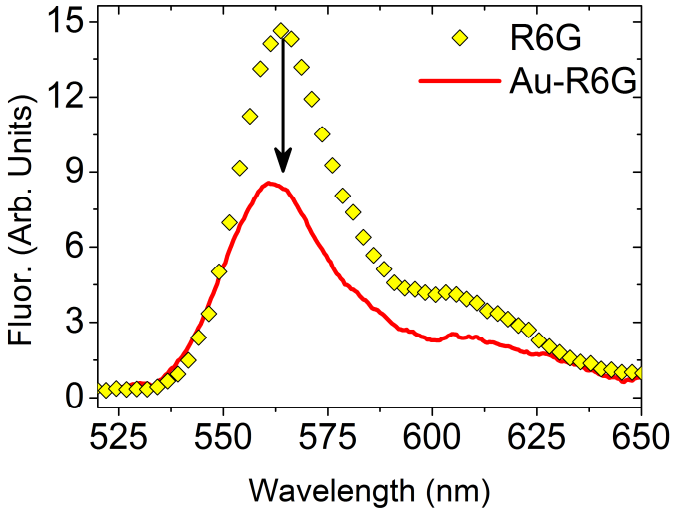

Figure 6-3 Fluorescence quenching observed in G_A system (solid red line) with respect to the R6G ethanol-based solution (blue dashed-dotted line) under the same pump energy value.

This doubt may arise in mind that the observed quenching in dye emission is simply originated from the absorptive nature of metallic NPs which are presented in dye solution. Hence, in order to provide a convincing proof that the observed phenomenon can be related also to the near field coupling between dye dipoles and induced plasmonic dipoles, the maximum fluorescence emission of dissolved dye molecules in the presence and the absence of the plasmonic quenchers as a function of pump energy (λ=355 nm) was acquired. The results of this experiment which has been performed by pump-probe Rayleigh experimental setup (explained in section 5.4), has been plotted in Figure 6-4. The applied linear fit for the obtained results cites the different rate of emission enhancement with respect to the increased pump energy.

This phenomenon can be as a result of resonant nonradiative energy transfer process occurring from active molecules to metallic NPs present in the surrounding volume which causes the decrease of quantum yield and consequently the radiative rate.

Indeed, performing steady-state fluorescence spectroscopy over such hybrid systems only can reveal fundamental indications of excitation energy transfer processes. These observations are necessary but not sufficient to demonstrate the occurrence of DMPET toward mitigation of absorptive losses of NPs. Hence, time-resolved fluorescence spectroscopy along with pump-probe experiments has been carried out on prepared gain-assisted system to perform a systematic analysis of gain-induced optical loss modifications.

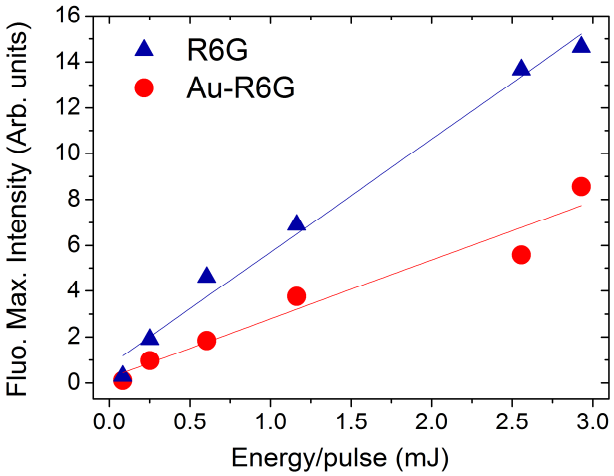

Figure 6-4 Fluorescence emission maxima of the gain-assisted sample (red circles) with respect to the R6G ethanol-based solution (black triangles) as a function of pump energy (λ = 355 nm).

6.2.2 Time-resolved Fluorescence Spectroscopy

Decay time of a fluorescent molecule is determined with respect to the both parameters of radiative and nonradiative decay rates. As it has been discussed before, modification of the lifetime of a dye molecule in close proximity of a plasmonic quencher can be due to the enhancement of the nonradiative decay rate and reduction or increase of the radiative decay rate. Thus the results of this experiment can be considered as complimentary evidences for the claimed concept according to the observed quenching of dye molecules in gain-assisted system.

Figure 6-5(a) reports the TCSPC data at 560 nm for G_A and G_F systems with respect to the pure R6G dye solution when irradiated with a 265 nm NanoLed pulsed laser diode (see section 5.3.2 for setup details). The time-resolved fluorescence intensity decay of the ethanol solution of pure R6G molecules is fitted as a single exponential function in Figure 6-5 (red dots and yellow line fit), giving a time constant of $\tau_D = k_D^{-1}$ =5.4 ns ($\chi 2$ = 0.978). However, from the TCSPC data of G_A system (blue dots and cyan line fit), two components can be identified in the decay dynamics. The presence of these two components are illustrated in Figure 6-5(b) fast decay time of τ_{A1}~190 ps ($\chi 2$ = 0.978) is accompanied by a long-living emission of τ_{A2}~6 ns where the first decay time is attributed to the fraction of dissolved dye molecules in ethanol that experience the nonradiative resonant energy transfer process; the long-living decay kinetics can be assimilated to the fluorescence decay for pure R6G dye molecules. In fact, this decay component is related to the fraction of unbound dye molecules (the largest fraction) present in solution but that are not coupled to plasmonic NPs. The combination of time-resolved data with

steady-state measurement results imply these facts that (i) quantum yield of fluorescent dye molecules in the presence of the gold NPs has been reduced, (ii) as a result of RET nonradiative decay rate of participated dye molecules has been enhanced dramatically, in which overweighed respect to whether enhancement or quenching of radiative decay rate, (iii) only a small fraction of dissolved dye molecules which are presented in surrounding area of core-shell NPs participates in emission quenching process.

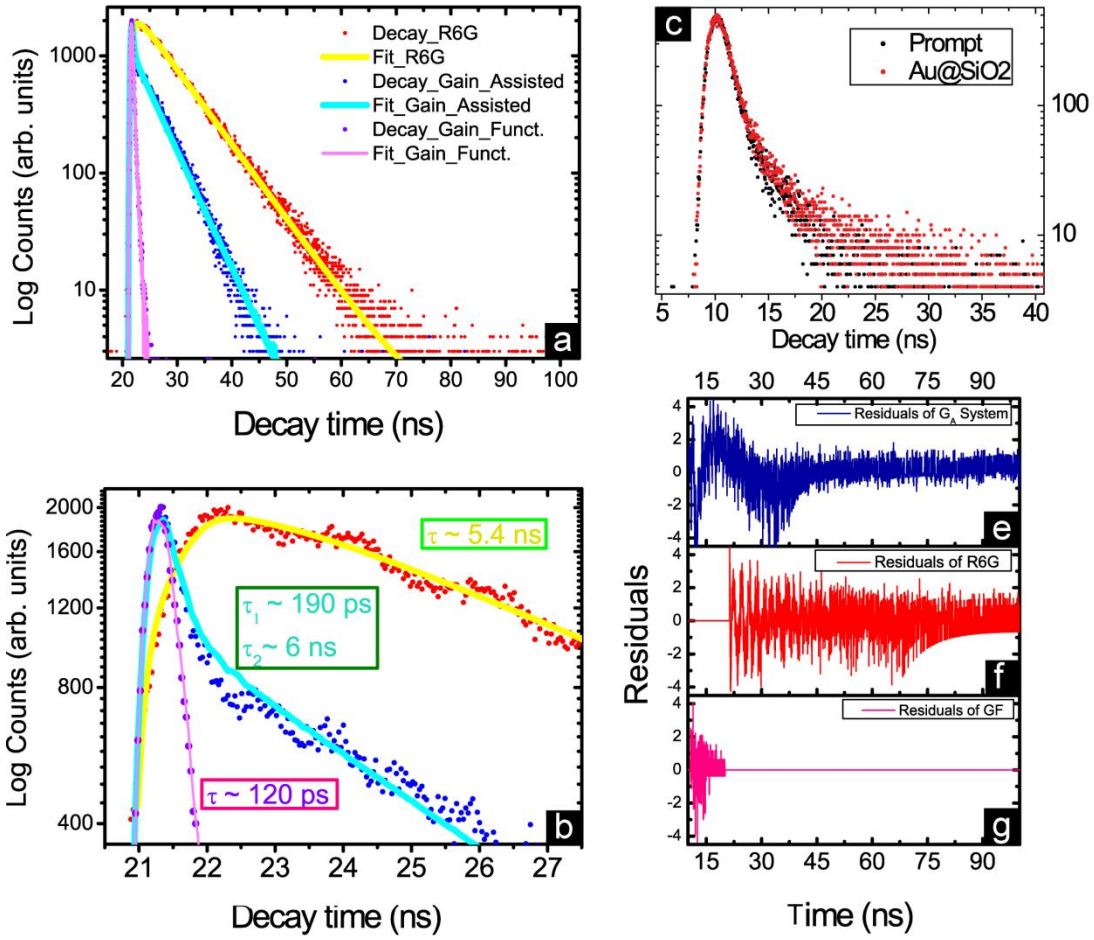

Figure 6-5 (a) Time-resolved fluorescence intensity decays: G_A and G_F systems are compared to pure R6G dye solution. Emission decay of pure R6G characterized by a single time constant τ_D = 5.4 ns (red dots). Yellow line is the result of single exponential fit. However, in the decay dynamics of the G_A system two components of fast living and short living emission are identified (blue dots). A single short-living emission is identified for G_F, clearly indicating a strong dye-NP coupling (pink dots) **(b)** Zoom image of the time-resolved fluorescence decays. The double decay time in the case of the G_A system is more evident. **(c)** TCSPC data collected from a solution containing the Au@SiO2 particles only; results obtained in the same experimental conditions as used for the G_F system confirm that the origin of short decay is due to the dye-NP coupling. **(d)**, **(f)** and **(g)** contain residuals for the R6G dye molecules, G_A and G_F systems decay fits, respectively.

If R6G dye molecules are encapsulated within silica shell, without any modification in material parameters and geometry of core-shell NPs, emission decay rate of the new produced system (gain-functionalized) would be different from gain-assisted system. Remarkably, the

obtained TCSPC data of the G_F system (pink dots) shows only a short-living intensity emission decay rate, fitted as a single-exponential with a time constant τ_F~120 ps ($\chi 2$ = 1.058). Accordingly, this decay time can be attributed to the integrated fluorescent molecules resonantly coupled to the plasmonic field of gold core. As it is evident from decay time curve, in the case of G_F system the long living emission due to the unbounded R6G molecules has not presented. Thus, the identification of a single-exponential decay of the short-living encapsulated dye emission indicates a complete and effective dye-NP coupling, which is manifested as a significant reduction of the dye fluorescence. As compared to the gain-assisted system, this approach allows a fine control of key parameters such as chromophore-metal core inter-particle distances and the concentration of active elements, providing the ability for an efficient resonant coupling between resonant field of chromophores and induced dipoles of plasmonic nanostructures, hopefully toward loss compensation targets.

In order to determine the possible interferences of silica-gold particles in the observed RET process, TCSPC data has been collected from a solution containing the Au@SiO2 particles only in the same experimental conditions as used for the prepared composite systems. The obtained results for the mentioned solution are clearly different, confirming that the origin of the short decays in studied gain-plasmon hybrid systems are due to the near field coupling among active and passive components of both mentioned systems (Figure 6-5(c)). All of these results elucidate the nonradiative RET rate as a consequence of coupling for gain-assisted and in particular for gain-functionalized system. The residuals of performed decay fits on collected TCSPC data of R6G, G_A and G_P systems are illustrated in Figure 6-5(e), (f) and (g), respectively.

6.2.3 Pump-Probe Rayleigh Experimental Experiments

The steady-state observations accompanied by time-resolved spectroscopy results provide persuasive confirmations for nonradiative energy transfer from R6G dye molecules over core-shell NPs. However, in order to demonstrate the outcome of this process as absorptive loss mitigation of gold core NPs the other experimental evidences must be presented by using pump-probe Rayleigh scattering setup. The details of the setup have been expressed in section 5.4 of chapter 5. The capacity of these experiments to provide information regarding the performance of the system in direction of optical loss compensation is correlated to the bear-Lambert law. According to this law, when a beam strikes on a sample surface, a fraction of incident light is

absorbed while the remained portion is scattered (forward or backward) or transmitted. Hence, in a particular energy of the impinging light which can be able to excite plasmon modes and promote resonant coupling process, if both components of the scattered and transmitted light are enhanced simultaneously, the absorption must be modified towards lower values, due to the constant value of the incident wave intensity. Such an observation can be interpreted as the mitigation of the absorptive losses of the system, by supplying gain over it.

$$A\downarrow + Sc\uparrow + Tr\uparrow = I_0 \ (cte) \qquad (6-1)$$

Thus, with the intention of demonstrating the absorptive power of the material is affected by excitation energy transfer process, the optical transmittance and Rayleigh scattering of the sample need to be evaluated.

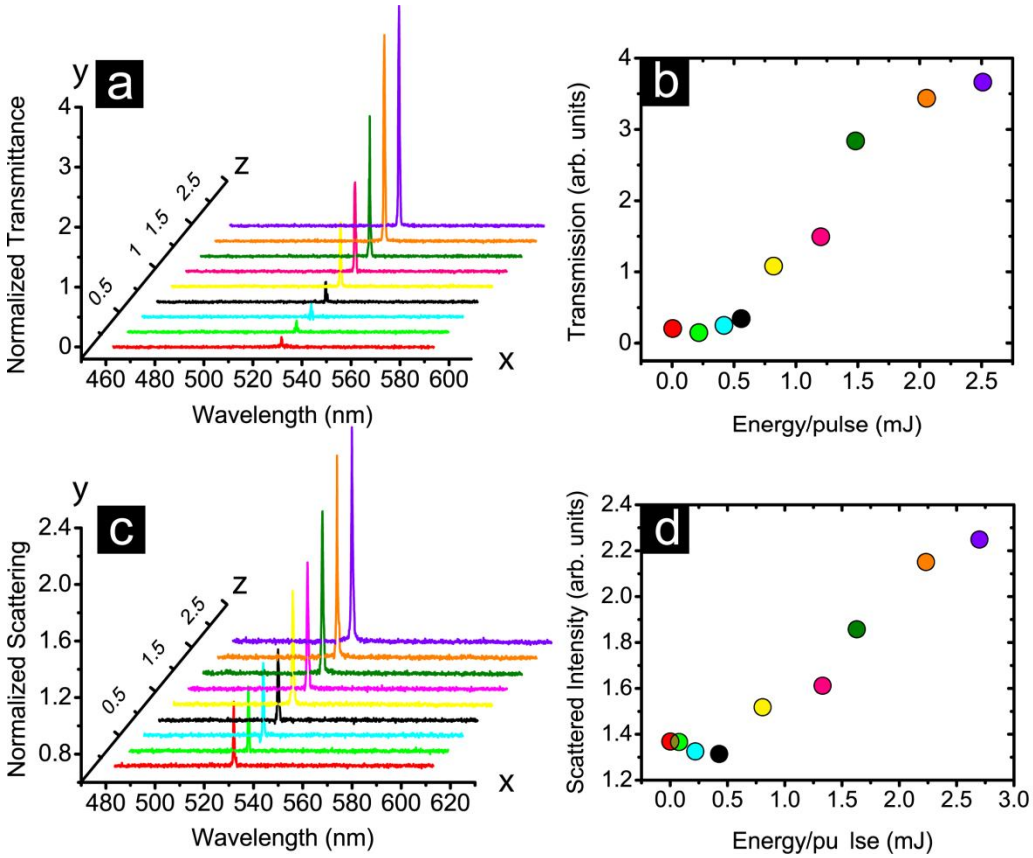

Figure 6-6 Scattering and transmission enhancement signals of gain-assisted hybrid system. **(a)** Normalized transmitted probe beam at 532 nm of G_A system versus wavelength (x-axis) and excitation energy (z -axis). **(b)** Optical transmission increasing of a probe beam as a function of pump energy **(c)** Normalized Rayleigh scattering signal of probe beam versus wavelength (x-axis) and excitation energy (z -axis). **(d)** Enhancement of SP evidenced by an increasing of normalized Rayleigh scattering signal of probe beam as function of pump energy (355 nm). Comparable threshold values for both transmission and scattering signals have been observed in this sample.

The optical transmittance of the sample at far field of probe light waves after passing the excited area with different level of gain is evaluated respect to the introduced pump energy

(λ=355 nm). Figure 6-6 (a) illustrates how the normalized transmission peaks of the probe signal (x-axis) at 532 nm as a function of excitation energy (z-axis) is enhanced, evidencing a clear gain-induced increase of the whole system transparency. Such enhancements are more evidenced in Figure 6-6(b). The increase of the systems transparency signifies the reduction in the absorptivity of the plasmonic hybrid system.

In addition, the enhancement of Rayleigh scattering signal as a function of impinging excitation energy is demonstrated in Figure 6-6(c) and (d). The presence of the enhanced scattered beam is considered as a signature for the enhancement of the plasmonic local field surrounding the nanoparticle. Hence, a pump-probe Rayleigh scattering experiment enables observation of the enhancement of the SP resonance due to the gain material present in the solution. As it is evidenced from Figure 6-6, after providing the energy above about 0.5mj/pulse simultaneous enhancement of transmittance and Rayleigh scattering signals are occurred. The super linear increase of the both scattered and transmitted signal above a certain threshold value of gain imply this fact that the optical absorption of the composite system can be reduced, only if enough gain material is excited by impinging pump beam. This subject is correlated with the concentration of the active molecules, in which for achieving an effective resonant near field coupling towards loss compensation approaches, enough value of chromophore concentration needs to be provided.

In the next section it will be explained how the normalized scattering and transmitted signals are extracted from the results of the pump-probe experiments.

6.2.4 Experimental Considerations

In both performed pump-probe experiments, the prepared solution is excited by a pulsed laser, operating at 355 nm and the consequence of pumping is observed by probing sample by means of a collinear launch of a probe beam. Principally, the probe beam wavelength must be selected in a region of the spectrum in which the system demonstrates the best coupling. For the prepared gain-assisted system, the wavelength of 532 nm which can be supplied by a solid-state continuous wave laser is applied as the probe beam.

As it is illustrated in Figure 6-7, the scattered probe light which has been acquired by means of the optical fiber of a high-resolution spectrometer, was superimposed in the spectrum as a relatively narrow line centered at 532 nm, over the much broader emission band relative to

the dye fluorescence. Since in parallel with increasing of the impinging energy the dye fluorescence signal is amplified, thus, in order to extract the pure enhancement of the scattered signal, the contribution of such raising in signal intensity must to be considered.

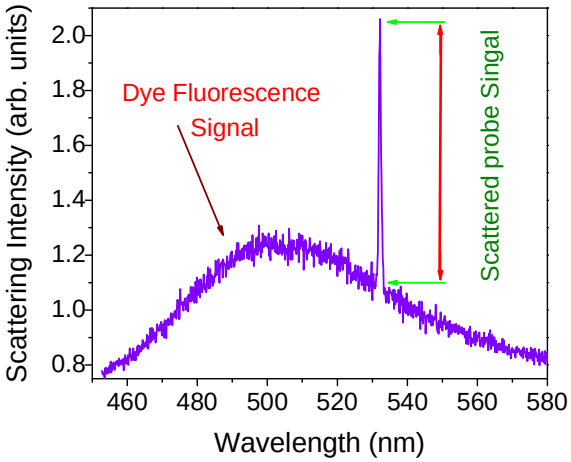

Figure 6-7 The scattering and emission components of the signal measured in pump-probe Rayleigh scattering experiment

Thus in order to determine the exact enhancement of the scattered signal ($I_{Enh.Sca}$) from G_A sample three experiments needs to be performed for every point of the applied pump energy: (i) The first experiment measures the spectrum of the background signal ($I_{Background}$) by probing the sample in the absence of the excitation pump beam. In this case, the emission of the fluorescent dye as a result of probe light is considered. (ii) The second experiment evaluates the emission spectrum of dissolved dye in solution as a result of pumping by pulsed laser $I_{Flue(pump)}$. (iii) Finally, in the third stage, the sample is pumped and is probed by collinear beam of 532 nm CW laser. The observed signal contains both components of scattering and dye photoluminescence. Hence, by applying the obtained values from the mentioned experiments in the following expression, the influence of the excited emissions by either pump or probe are excluded and exact enhancement rate of the scattered signal is concluded.

$$I_{Enh.Sca} = I_{Sca(pump-probe)} - I_{Flue(pump)} - I_{Background} \qquad (6-2)$$

The normalized value of the Rayleigh scattering signal is offered by this equation:

$$I_{Norm.Sca} = \frac{I_{Enh.Sca}}{I_{Flue(pump)} + I_{Background}} \qquad (6-3)$$

In optical transmittance experiment, by using pinhole and notch filters any stray lights and undesired contributions are ruled out, which provides this opportunity for measuring only

transmitted probe beam wavelength. Moreover, by placing the detector enough far from the sample, the contribution of the light emission and scattering can be eliminated. In every step of the acquiring data, the background signal by removing the exposure of pump signal ($T_{no.pump}$) was acquired to be sure that the optical properties of the system was not modified as a result of pumping with energetic pulses of the ND: YAG laser. The normalized optical transmission can be calculated by the following equation, in which T_{pump} denotes the measured optical transmittance of the probe beam passed through the sample in the presence of the pump signal.

$$T_{Norm} = \frac{T_{pump} - T_{no.pump}}{T_{no.pump}} \qquad (6-5)$$

6.2.5 Sample Preparation Process

Before providing the information regarding the NPs sensitization process, the preparation procedure of the gain-assisted system is explained. As it has been mentioned before, in order to obtain an efficient plasmonic loss compensation results, the proper concentration of the gain material needs to be introduced for the absorptive NPs. In this regard, the value of 10 is considered for the ratio of the gain material molar concentration (MC_{gain}) respect to NPs molar concentration (MC_{NP}). These words can be stated by following mathematical expression.

$$\frac{MC_{gain}}{MC_{NP}} = 10 \qquad (6-6)$$

Molar concentration is defined as the number of the presented moles in unit volume of the solution. Thus, the equation (6-6) can be written as the ratio of the gain and NP moles.

$$\frac{M_{gain}}{M_{NP}} = 10 \qquad (6-7)$$

By considering a determined volume of the NPs ethanol based solution (for example 100 μl), respect to the concentration of the NPs in that solution, the mass of gold in that volume can be calculated (the mass of shell surrounding NPs is neglected). The concentration of NPs in prepared solution is reported by chemist collaborator as 0.38 *g/l*.

$$m_{NP} = C_{NP} \times V_{NP,solvent} = 0.38(g/l) \times 100\mu l = 0.038\ mg \qquad (6-8)$$

The mass of one mole of a material is described as molar mass of that material. This parameter for gold is equal with 196.966 *g/mol*. Hence, the number of moles of NP in 100 μl solution can be calculated as,

$$M_{NP} = \frac{m_{NP}}{(Molar\ Mass)_{NP}} = \frac{0.038(mg)}{196.966(g/mol)} = 1.929\times10^{-7}\ \ mol \qquad (6-9)$$

Now, by embedding the obtained value from equation (6-9) in equation (6-7) the number of the moles of the gain material can be obtained in final solution (1.929×10^{-6} *mol*).

The molar mass of chromophore is provided by the manufacturing company (479.02 *g/mol*). Thus, the mass of dye molecules in calculated number of moles is obtained simply as:

$$m_{gain} = Mo_{gain} \times (Molar\ Mass)_{gain} \qquad (6-10)$$
$$= 1.929\times10^{-6}(mol)\times 479.02(g/mol) = \boxed{9.24\times10^{-1} mg}$$

This amount of R6G dye molecules where can be measured by balance will be used to prepare the final sample. By considering the supposed weight concentration of the final sample (for this case 0.01 wt%), total mass of solvent (ethanol) to prepare the solution can be achieved.

$$\frac{m_{gain}}{m_{gain} + m_{total.solvent}} = 0.01\% \qquad (6-11)$$
$$m_{total.solvent} = \frac{(1-0.0001)\times 9.24\times10^{-4}(g)}{0.0001} = 9.239g$$

Now by excluding the weight of NPs solvent from total mass of ethanol, the mass of the ethanol that needs to be used for sample preparation can be calculated as,

$$m_{total.solvent} = m_{solvent} + m_{NPs,solvenet} \qquad (6-12)$$
$$m_{solvent} = 9.239(g) - (100\mu l \times 0.789(g/ml)) = \boxed{9.1601 g}$$

In above calculation, the number of 0.789 *g/ml* stands for ethanol density. It is worth to mention that the mass of dissolved NPs in 100 μl of ethanolic solution is neglected.

The concentration of gain material in final prepared sample needs to be considered for the preparation of reference sample, which is the solution of dye molecules in ethanol.

$$C_{gain,\,final} = \frac{m_{gain}}{V_{total.solvent}} \qquad (6-13)$$

The following equation provides the value of solvent volume corresponding to calculated mass.

$$V_{total.solvent} = \frac{m_{total.solvent}}{\rho_{solvent}} = \frac{9.24(g)}{0.789(g/ml)} = 11.711 ml \qquad (6-14)$$

By inserting this value in equation (6-13) the concentration of final sample is calculated as 0.0789 *g/l*.

6.2.6 Confocal Microscope Characterizations

Fluorescence laser scan confocal microscope images were acquired on the prepared system Au@SiO2/R6G (shown in Figure 6-8), aimed to study the dye-NP aggregation size and separation distance dependence in a resonant energy transfer process. These images, combined with SEM and TEM observations of the same area, demonstrated that some metal aggregates appear in the solution, and that the dye is present in close proximity to these aggregates. This important observation confirms the possibility to activate Dipole-Metal Particle Energy Transfer mediated by Coulombic interactions, even if the dye is dissolved in solution, toward the mesoscale building blocks of metamaterials.

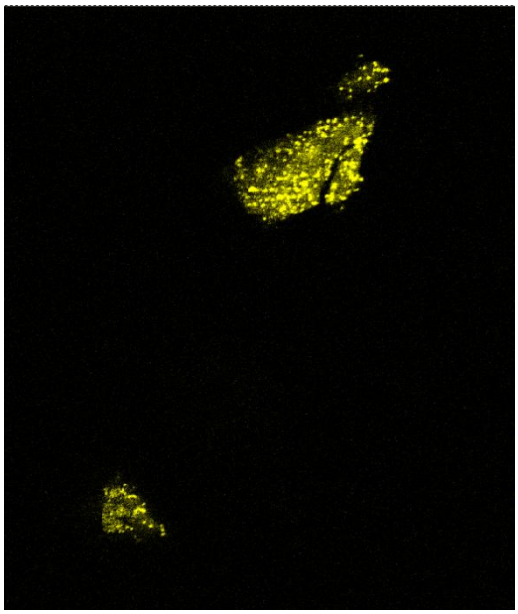

Figure 6-8 Fluorescence confocal microscope images were acquired on the prepared system Au@SiO2/R6G.

6.2.7 Silica Coated Gold Core NPs Synthesis Procedure

Au spherical particles with an average diameter of 58 ± 3 nm were prepared by chemist collaborator, following the method developed by Rodríguez-Fernández *et al*. [4] Briefly, 2.5 ml of ascorbic acid (0.5 mM) was added to 500 ml of an aqueous solution containing $HAuC_{l4}$ (0.25 mM) and CTAB (0.015 M) at 35 °C. Subsequently, the seed solution (15 nm citrate Au seeds, [Au] = 3.97×10^{-6} M) was added and allowed to react for one hour.

The Au nanoparticles were coated with silica using the method reported in reference 5. The 58 nm gold NPs were first functionalized with mPEG-SH and transferred to ethanol. This was carried out by dropwise addition of an aqueous solution containing 1.06×10^{-6} mol of mPEG-

SH to 5 ml of assynthesized Au spheres (0.5 mM). After 30 min, the mixture was centrifuged (3300 rpm, 30 min) three times to remove excess mPEG-SH and redispersed in 3 ml of ethanol. The modified particles were then mixed with TEOS and ammonia in the following final concentrations: [Au]=0.4 mM, [H2O]=10.55 M, [NH3] =0.2 M, [TEOS]=0.8 mM. The thickness of silica shell after this first growth step was around 19 nm. Before a second growth step, the sample was centrifuged (3100 rpm for 30 min) to remove any free silica nuclei. Eventually, the silica shell was overgrown up to 30 nm by adjusting the concentration of silica precursors as indicated above.

The encapsulation of fluorophore probes was carried out by simply adding the dye (diluted in ethanol) dropwise under gentle stirring immediately prior to TEOS addition [5]. The concentration of Rhodamine 6G in the reaction mixture was around 6 μM. The final system is represented by Au@(SiO2 + R6G), with R6G dye encapsulated into the silica shell [6].

6.3 Structure 2:

Optical Loss Mitigation in Gain Functionalized Core-shell NPs

In prior section the optical behavior of gain-assisted system for compensating the absorptive losses of plasmonic NPs has been investigated. In addition, it has been demonstrated that by functionalizing the gain elements within silica core, the rate of energy transfer process can be dramatically enhanced. That issue can provide the possibility for producing more efficient loss mitigated hybrid systems.

In this section, two types of gain-functionalized dye-NP hybrid system are studied. The DMPET process among active embedded dye molecules in silica shell and absorptive plasmonic NPs by using steady-state fluorescence experiments and time resolved spectroscopy in both systems is explored. Such energy transfer process involves simultaneous de-excitation of dye molecules and excitation of plasmon NPs resulting in a huge enhancement of the local excitation field and as well as a modification of the radiative and nonradiative decay rates of the fluorophores. Moreover, the issue of this process for mitigating the absorptive losses of NPs by using pump-probe experiments is studied. The induced optical transparency accompanied by a considerable enhancement of the Rayleigh scattering intensity as a function of the gain is presented.

The geometry and material parameters of both systems are considered as the same. The only dissimilarity comes from type of the gain material which has been encapsulated in silica shell of plasmonic nanospheres. This difference drastically influences the fluorescence lifetime behaviors for the investigated systems, as evidenced by the partial or absolute (a few thousand counts) absence of an emission signal.

6.3.1 Steady-state Fluorescence Investigations

Gain functionalized (G_F) metal nanoparticles with the same aspect ratio consist of a gold core with diameter of about 12 nm coated by means of a silica shell with thickness of 12 nm containing organic dye molecules. Two photo-stable organic dyes of Coumarin500 and DCM were chemically encapsulated into the shell, creating two functionalized systems: Au@SiO2/C500 (G_F – C500) and Au@SiO2/DCM (G_F – DCM). The size of the metal core and the thickness of the silica shell were both measured by statistical analysis of TEM images. The

scheme of these two systems accompanied by an example of acquired TEM images of active NPs and chemical formula of applied dye molecules are illustrated in Figure 6-9.

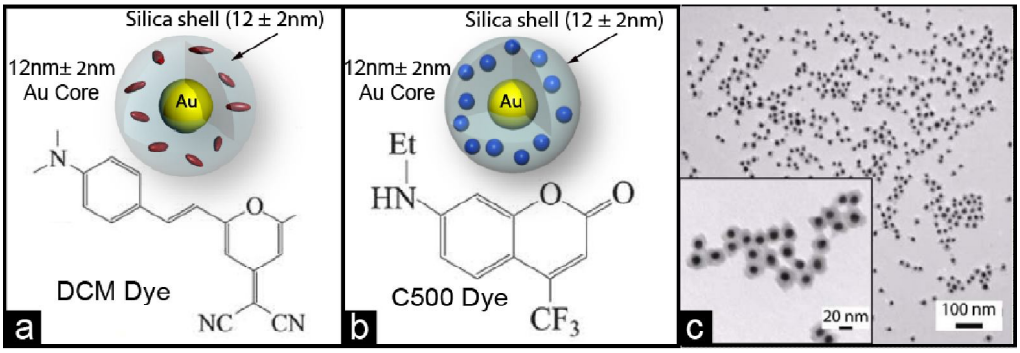

Figure 6-9 Scheme of gain-functionalized NPs accompanied with chemical formula of applied dye molecules **(a)** DCM, **(b)** C500, **(c)** TEM image of core-shell NPs with the same aspect ratio.

The plasmon bands of silica coated nanospheres with maximum intensities at 532 nm have been measured by spectrophotometer (black lines in Figure 6-10). These two systems were optically excited by laser pulses at 355 nm, a wavelength far from the maximum of the NP extinction band. The acquired results showing a completely different gain curve overlapping with the plasmon band of gold NPs for two synthesized systems. This difference is evidenced from Figure 6-10, presenting a maximum at 500 nm (C500) and 630 nm (DCM). For such emission bands, a spectral position blue shifted with respect to the plasmon band for C500, whereas it is red shifted for DCM. The presence of such spectral overlap between emission spectra of incorporated dye molecules and plasmon band of core-shell NPs provide the possibility for occurrence of DMPET process.

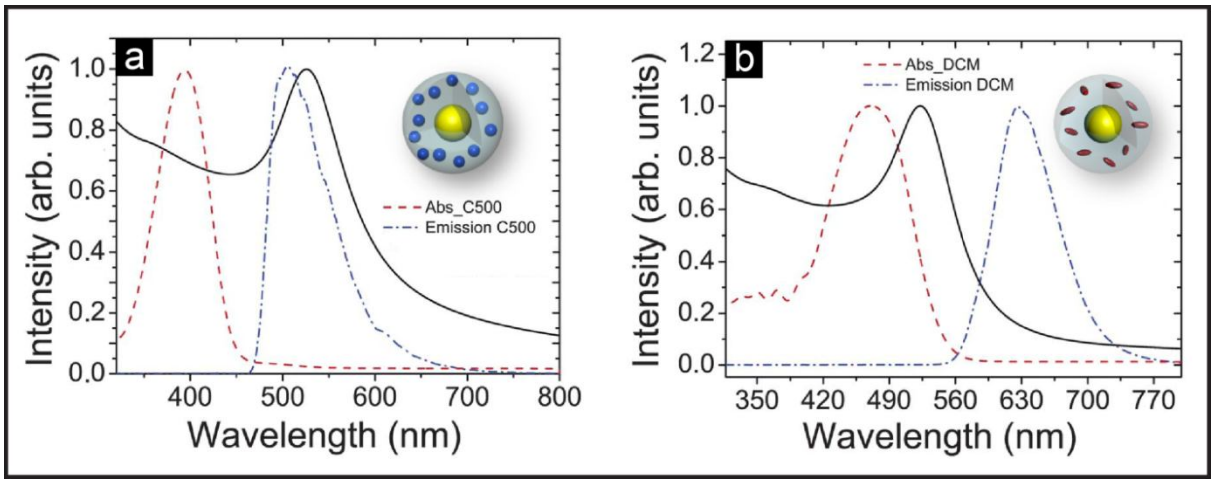

Figure 6-10 (a) Absorption (red dash) and emission (blue dash dot) spectra of C500 dye dissolved in ethanol and plasmon band (black line) of G_F-C500 gold nanoparticles. **(b)** Absorption (red dash) and emission (blue dash dot) spectra of DCM dye dissolved in ethanol and plasmon band (black line) of G_F-DCM gold nanoparticles.

In fact, it is motivating to investigate the effect of such different spectral overlap over RET process. In the next sections, the observations on performed time-resolved fluorescence spectroscopy on two systems, along with comparative analysis of gain induced optical loss modifications (pump–probe experiments) are demonstrated.

6.3.2 Time-resolved Fluorescence Spectroscopy

In first part of this chapter, the presence of resonance energy transfer process from encapsulated R6G dye molecules in silica shells over gold cores of NPs, by applying time-resolved spectroscopy is explored. Also, in the case of these two samples, in order to do a systematic investigation of gain induced optical loss modifications, fluorescence decay time measurements have been carried out over both systems.

As a result of short separation distance between encapsulated dye molecules and absorptive surface of nanoparticles and by considering the presence of the coincidence between the spectrums of components of the hybrid system, a strong coupling within both systems is expected. Figure 6-11 represents the results of time-resolved spectroscopy performed over both gain-functionalized systems. The luminescence is recorded in TCSPC method at 498 nm for G_F – C500 and at 626 nm for G_F – DCM with respect to the pure C500 and DCM dye solutions, when irradiated with a 265 nm or 379 nm NanoLed pulsed laser-diode, respectively. The detail of the applied spectrofluoromoter has been presented in section 5.3.2 of chapter 5. The observed quenching behavior in the lifetime of encapsulated gain materials respect to their intrinsic decay times confirms the occurrence of RET process in both systems.

The time-resolved fluorescence intensity decay of the ethanol solution of pure C500 molecules has been fitted as a single exponential function in Figure 6-11(a) (purple dots and yellow line fit), giving a time constant of τ_{fluo}(C500)=5.42 ± 0.01 ns (χ^2 = 0.997). The same measurement made on the DCM solution gave a time constant of τ_{fluo}(DCM)=1.682 ± 0.005 ns (χ^2 = 0.995). From the TCSPC data of the G_F – DCM system (pink dots and green line fits), two components can be identified in the decay dynamics, but only one component for the G_F-C500 system. Indeed, a fast decay is accompanied by a long-living emission (see Table 6-1 for details). The first decay time is attributed to the fraction of encapsulated dye molecules in the silica shell that experience the resonant energy transfer process more efficiently, while the long-living emission is related to that portion of dye molecules presented in the silica shell that are not

coupled to plasmonic nanoparticles as strong as the first portion. In fact, the long living emission more looks like the fluorescence decay of pure dye molecules in ethanol. The bi-exponential fitting of intensity emission decays for this system yields two time constants. The short-living time constant is τ_1=0.508 ns in which is ten folds is lower than that of the pure dye solution (see Table 1), whereas the long-living decay time is equal with τ_1= 2.78 ns is in the same range.

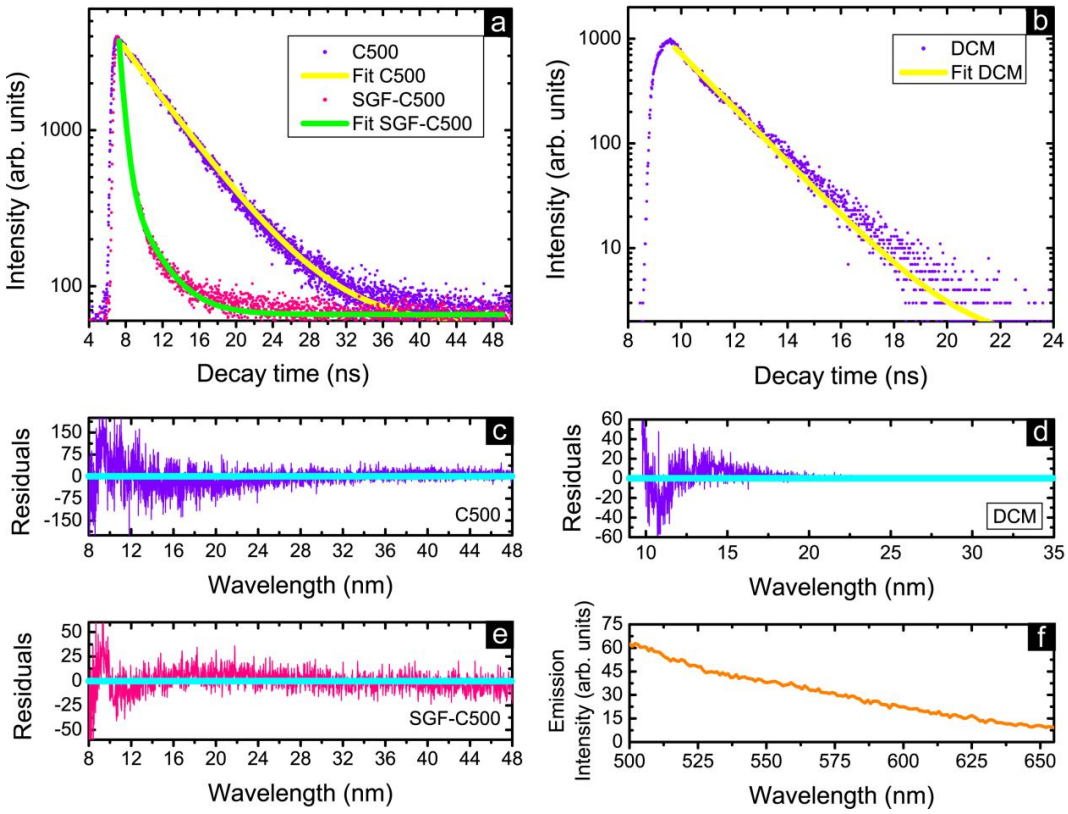

Figure 6-11 Time-resolved fluorescence intensity decays: **(a)** G_F - C500 and **(b)** G_F - DCM systems are compared to pure dye solutions of C500 and DCM, respectively. The long-living emission of pure C500 is characterized by a time constant τ_{fluo}(C500) =5.42 ns (purple dots and yellow fit). Two components are identified in the decay dynamics of the G_F - C500 system: τ_1(C500)= 2.78 ns and τ_2(C500)=0.5 ns (pink dots and green fit). **(c)** and **(e)** represent the residuals obtained for the C500 and G_F–C500 decay fits, respectively. Spectrum (*b*) contains only the decay of DCM dye, because of an absence of an emission signal in the G_F–DCM system. **(d)** and **(f)** contain residuals for the DCM decay fit and the very low emission acquired for the G_F–DCM system (excitation 379 nm, cut-off 450 nm), respectively.

Sample	$\lambda_{excitation}$(nm)	$\lambda_{emission}$(nm)	χ^2	τ_1(ns)	τ_2(ns)
C500-Ethanol	265	498	0.997	5.42±0.01	
G_F - C500	265	498	0.998	2.78±0.05	0.508±0.003
DCM-Ethanol	379	626	0.995	1.682±0.005	
G_F - DCM	379	626	-----	no emission	no emission

Table 6-1 Time resolved fluorescence decay times accompanied by excitation and emission wavelength reports for G_F - C500 and G_F - DCM systems with respect to the pure dye solutions.

The identification of two exponential decays indicates all of the encapsulated C500 molecules in silica shell of nanoparticles are not participated in energy transfer process in the same rate. However, the presence of a reduced decay time is attributed to a significant increase of the nonradiative decay rate due to the fraction of encapsulated dye molecules into the silica shell that experiences the resonant energy transfer process. This fact influences nonradiative energy transfer rate as a consequence of near field coupling for G_F – C500 system, representing a clear demonstration that a portion of embedded gain is introduced to absorptive NPs. Residuals for the pure dye solution and G_F – C500 system are reported in Figure 6-11(c) and (e).

On the contrary, as evidenced by the absence of data for the G_F -DCM system in Figure 6-11(b), any significant emission (see Figure 6-11(f)) at 626 nm for this sample has been observed. Such a phenomenon can be explained by two possibilities: First, the electronics of the spectrofluorometer were not enough fast to acquire extremely fast fluorescence decays of corresponding sample. Second, as a result of a strong dye–NP coupling, DCM dye molecules presented in the silica shell surrounding gold cores experienced complete fluorescence quenching.

Figure 6-11(d) shows residuals for the DCM dye solution, whereas Figure 6-11(f) represents the signal acquired as fluorescence emission (excitation 379 nm, cut-off 450 nm to avoid multiple wavelength generation) of the G_F -DCM system (a few thousand counts, that can be considered zero). Such a remarkable enhancement of nonradiative resonant energy transfer have been predicated by Gersten and Nitzan [7] and it has been clarified experimentally by Dulkeith *et al.* [2], for a donor fluorescent molecule which is maintained in the vicinity of a metal nanoparticle, resulting in a gain to plasmon couplings effects.

6.3.3 Pump-Probe Broad-band Transmission Measurements

In order to evaluate photophysical properties of gain functionalized hybrid systems by applying a proper pump-probe setup optical transparency and Rayleigh scattering measurements are carried out. However, before performing these experiments, a broadband transmission experiments have been performed, with the intention of finding a proper probing wavelength. The frequency-tripled output of a Q-switched pulsed laser (λ=355 nm) is used as the optical excitation source and the samples are probed by a xenon based lamp with a monochromator with a fixed power, which is focused within the pumped region of the sample. The detail information

about applied setup to perform these experiments has been expressed in section 5.4 of chapter 5. By applying such configuration of pump-probe setup, the transmitted lamp light can be acquired at different wavelength in the presence and absence of the pumped pulses of excitation laser.

By plotting maximum intensity of transmitted light at every wavelength of probe beam, the extinction cross sections of both samples are acquired in the passive (without excited gain) and active (with excited gain) cases. The results of this experiment reflect the modifications of absorptive power induced by energy transfer during dye excitation. The plotted difference of the transmitted signal ($\Delta T = T_p - T_{wp}$, orange dots) in the presence (T_p) and in the absence of the pump beam (T_p) as a function of probe wavelength is illustrated for G_F – C500 and G_F – DCM systems in Figure 6-12 (a) and (b), respectively. In addition, in order to identify the overlapping region in corresponding figures the blue shifted fluorescence spectrum of C500 and red shifted emission spectrum of DCM dye molecules (green lines) with respect to extinction band of core-shell nanospheres (blue lines) are demonstrated.

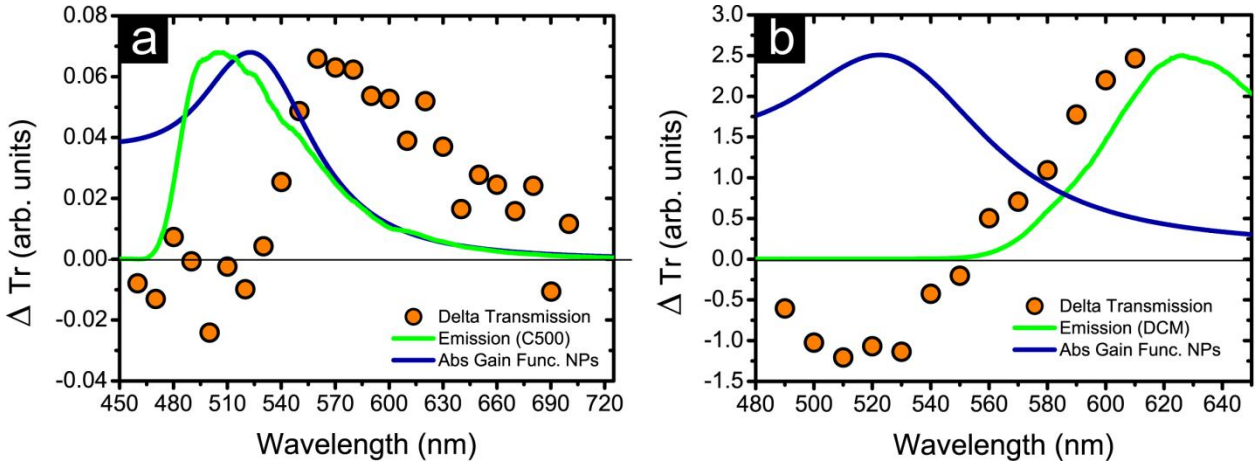

Figure 6-12 Broadband differential transmission measurements of the two hybrid G_F systems: **(a)** G_F - C500 and **(b)** G_F – DCM. $\Delta T = T_p - T_{wp}$, where T_p is the transmittance of probe beam with pump, and T_{wp} is that without pump as a function of wavelength. The extinction band of core-shell NPs are showed with blue lines and green spectrums demonstrate the emission of corresponding gain materials.

As it is represented in Figure 6-12(a), for G_F – C500 NPs the difference ΔT assumes negative values in the wavelength range 460 – 530 nm, whereas after 530 nm, ΔT starts to became positive ($T_p > T_{wp}$). The same sort of the experiments have been performed over G_F – DCM system, in which plasmonic NPs of this system experiences extinction band more blue-shifted and with a smaller overlapping area with respect to the dye emission curve (green curve in Figure 6-12(b)). In this case, ΔT over the wavelength range of 480–550 nm is negative, but beyond the wavelength of 530 nm it starts to cover positive values. Such increasing attitude

exactly is correspondence with the rise of the DCM emission curve, where spectral overlapping starts to become non-zero. Such positive value of transmission difference is interpreted by the occurrence of the DMPET process, among the gain–plasmon elements of both hybrid systems.

As it is evidenced from these results, regardless of the blue shift or red shift of the emission peak wavelength with respect to the maximum wavelength of extinction band of NPs, resonant energy transfer process occurs in the wavelength higher than the plasmon band. In order to interpret such effect, it should be taken into account that the plasmon frequencies ω_l for the pertinent localized surface modes depend on the size of the nanoparticle and they are related to plasma frequency by following equation.

$$\omega_l = \omega_p \sqrt{\frac{l+1}{2l+1}} \qquad (6-15)$$

here l being the orbital quantum number and ω_p is the plasmon frequency of gold at 6.7×10^{14} s^{-1} correspondent to λ=450 nm, as evidenced by experimental studies and theoretical predictions. This clearly implies that frequencies of the surface modes are lower than ω_p (ω_l / ω_p = 0.8 for 12 nm NP core size [8]), and that the l=1 surface plasmon modes are presented around 550 nm, which is red-shifted about 20 nm with respect to the measured maximum of the plasmon band. These considerations show that, for gold nanoparticles in the range of 5–10 nm radius, the ‘‘dipolar’’ mode (l=1) is the predominant accepting mode for energy transfer with a dye emitting in the visible range from 500–600 nm. Other surface plasmon modes (l=2, located around 580 nm) might be involved in the resonant energy transfer process in case the emission band of the encapsulated fluorophores overlaps these modes. Therefore, the dye–Au NP resonance band for effective energy transfer which can lead to a high coupling between two species is separately always red-shifted with respect to the plasmon band maximum (relative to the l=0, bulk mode).

Figure 6-13 represents the retrieved data from the demonstrated results in Figure 6-12 utilized to reconstruct the extinction band for both hybrid systems of G_F – C500 and G_F – DCM in the absence (purple dots) and presence (red dots) of gain (pump beam on) calculated as

$$A = -\log(\frac{I_T}{I_0}) \qquad (6-16)$$

where A stands for the absorbance of the core shell NPs. Take into account that because of the small size of the NPs, the scattering cross section can be neglected against absorption cross section. I_T is the transmitted intensity and I_0 is the incident intensity on the sample.

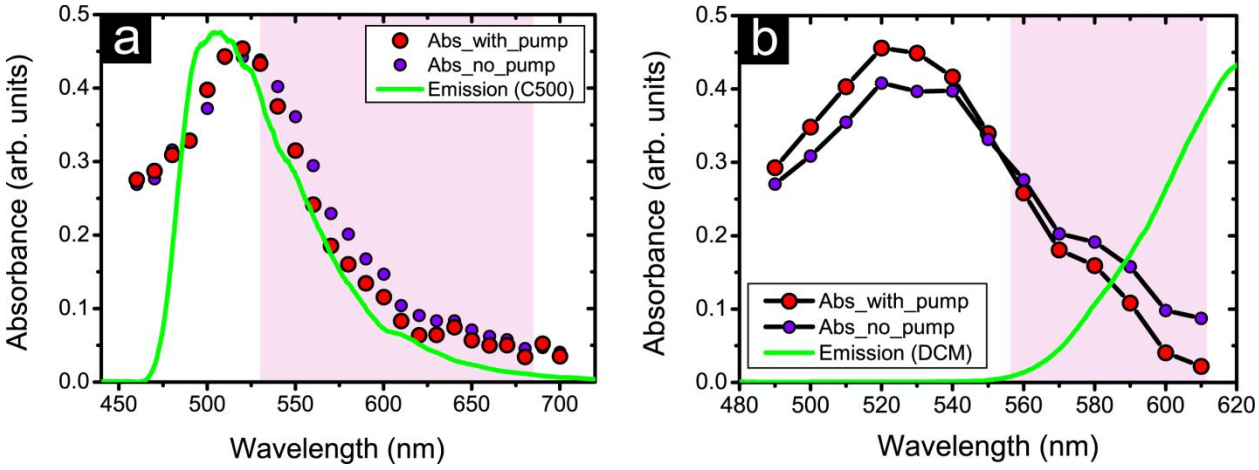

Figure 6-13 (a) and **(b)** represent the retrieved data from demonstrated data in Figure 6-12 (a) and (b) utilized to reconstruct the extinction band for both hybrid systems in the absence (purple dots) and presence (red dots) of gain (pump beam on) calculated as Abs = – log (I_T/I_0). The pink colored bands show the wavelengths of the enhanced optical transparency.

As it is clear from Figure 6-13(a) as a result of the RET process, the absorptivity of the plasmonic NPs in the range that is colored with pink band is decreased, which is an evidence for the enhancement of the optical transparency in that range. However, in the wavelengths lower than this band (460 – 530 nm) the absorption of the NPs under pump irradiation is even more than the non-excited case. These observations are even better evidenced by the extinction bands of G_F – DCM system reported in Figure 6-13(b). The extracted curves from ΔT measurements data which are related to the absorption bands of this composite system in the presence (red dots) and in the absence of the pump beam (purple dots in Figure 6-13(b)) clearly show how in wavelength range of 490–550 nm, whole excited system experienced higher values of the absorption in comparison with non-excited situation. However, this reduction of the optical transparency (increasing the imaginary part of the system permittivity) is compensated by the modification of the curve in the range between 550–610 nm (pink area in Figure 6-13(b)), where absorption is reduced by supplying gain to the system as evidenced by lower values for extinction curve with respect to those obtained in the absence of an exciting optical field. Such a correlation between reduction of absorption in a band of extinction cross section (above a particular wavelength) and increase of the same quantity in a complementary wavelength band (blow of that wavelength), are confirmed by these experimental clarifications. This phenomenon can be elucidated via Kramers-Kronig dispersion relations where by showing a relationship between modification of the real part respect to the changes in imaginary part account the

coupling between gain and plasmonic nanoparticles upon verifying the causal nature of the response of materials.

Furthermore, the obtained results show that in wavelength range where dye emission and SP modes overlaps the excited localized surface plasmon modes interact in resonance with the dipoles of gain material. Thus, the spectral region related to the transmission enhancement of the plasmon-gain system is labeled as resonance regime (pink bands in figure 6-13(a) & (b)). While in opposite the off-resonance regime is the range of probe wavelength in which as a result of the non-resonant gain-plasmon interactions the optical absorptivity of the system is increased. Such optical behavior has been observed in a gain-functionalized system studied by G. Strangi *et al.* [9]. The investigated hybrid system is constituted of 30 nm gold cores surrounded by 30 nm silica shells doped by C500 dye molecules. The optical transmission measurements were performed in several wavelengths selected from spectral overlap range of dye molecules and plasmonic NPs reveal the presence of off-resonance (460–520 nm) and resonance 520–580 nm) regimes. The results show that the probe wavelengths lying in the off-resonance band do not experience any increase in the transmission as function of the gain. On the contrary, the light waves characterized by wavelengths belonging to the resonance band, where dye emission and SPB overlaps, present a considerable enhancement as the excitation energy is resonantly transferred (Figure 6-14).

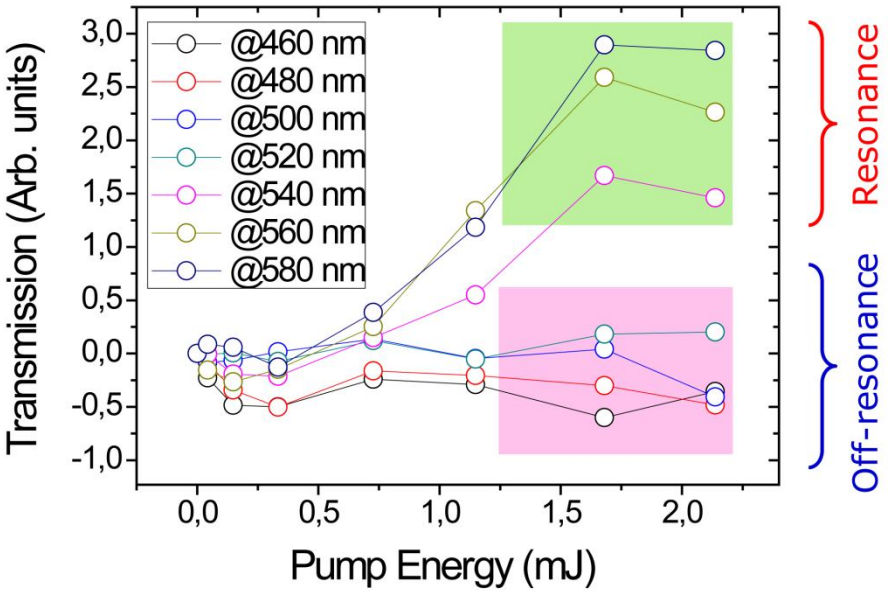

Figure 6-14 Selective optical transmission measurements by using off-resonance (460–520 nm) and resonant probe wavelengths (540–580 nm), as excitation energy is increased.

Thus, the presented observations experimentally confirm this fact that if the emission band of shell encapsulated efficient fluorophores is properly overlapped to localized SPB of adequate NPs, nonradiative resonant energy transfer occurs within the dye functionalized NP, resulting in the modifications of the imaginary part of the permittivity $\varepsilon_{im}(\omega)$.

Respect to achieved broadband transmission results, the probe wavelength was chosen in the proximity of the overlapping region between dye fluorescence and plasmon band maxima, where localized surface plasmon modes are excited. The probe light emitted, scattered or transmitted by fabricated systems (λ = 532 nm or λ = 600 nm) was collected by an optical fiber, in a position depending on the type the experiment (for more information see chapter 5, section 5-4).

6.3.4 Pump-Probe Rayleigh Experimental Measurements

In order to perform a comparative analysis of gain induced optical loss modifications, Rayleigh scattering and optical transient absorption spectroscopy have been carried out on the two systems, by using pump-probe setup. Indeed, simultaneous enhancement of the measured Rayleigh scattering and transient absorptivity is the signature of the gain-induced optical transparency of the system, as a result of excitation energy transfer process. Thus, modifications of the Rayleigh scattering and transmitted intensity of a constant probe beam at λ_{pr}=532 nm for G_F – C500 and λ_{pr}=600 nm for G_F – DCM have been monitored as a function of the pump energy for both systems (λ_{ex}=355 nm).

It is well-known that the enhanced local field around NPs can cause a strong Rayleigh scattering. The scattering of a nanosphere synthesized with an active shell can be enhanced, as the field surrounding NP is enhanced as a result of DMPET process. However, a singularity in NP local field is expected if a critical value of the excitation energy is provided to promote enough amounts of the gain molecules to the meta-stable state and in parallel excite NP surface plasmon modes. In this situation, the transferred energy can compensate the absorptive losses of NPs.

The presence of such threshold gain value above which systems show non-linear behavior was already discussed by Lawandy [10]. This fact can be observed in Rayleigh scattering experiment by lunching collinearly a probe beam in a small portion of the sample volume excited by a wider pump spot at λ=355 nm at various excitation rates.

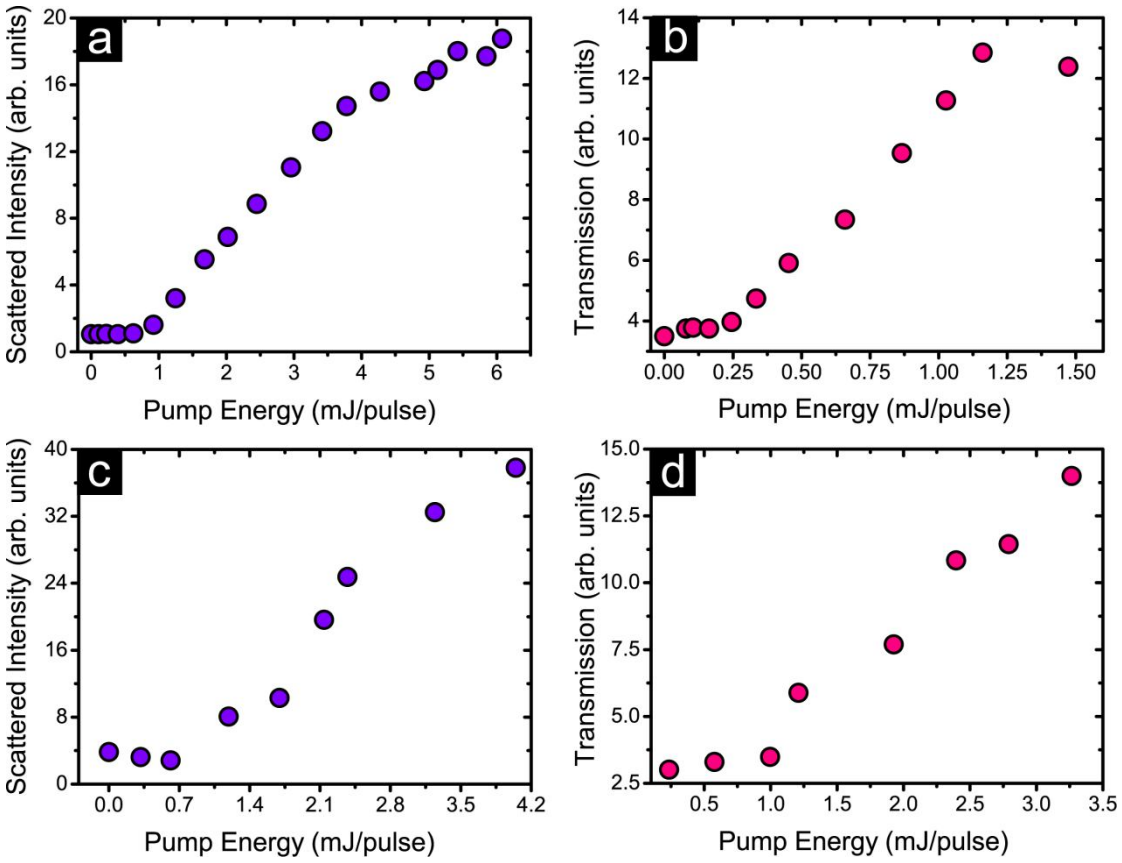

Figure 6-15 Comparison of scattering and transmission enhancement signals between the (a and b) G_F - C500 and (c and d) G_F - DCM systems. Enhancement of SP is evidenced by an increase of the normalized Rayleigh scattering signal of a probe beam **(a)** λ = 532 nm for G_F - C500 and **(c)** λ = 600 nm for G_F - DCM as a function of pump energy (λ = 355 nm). Normalized enhanced transmission of a probe beam as a function of pump energy acquired for **(b)** G_F - C500 at 532 nm and for (d) G_F - DCM at 600 nm. Comparable threshold values for scattering signals have been observed, whereas a lower transmission threshold for G_F - C500 is observed with respect G_F - DCM.

Figure 6-15 (a) and (c) shows the difference in measured maximum intensity of the elastically scattered beam and the corresponding value in the residual fluorescence emission spectrum for both G_F systems, plotted as a function of the pump energy. The presence of a similar threshold value of the pump energy which needs to be applied to start resonant coupling between excited fluorophores and SP resonances of plasmonic NPs is apparent in these curves.

In addition, Figure 6-15(b) and (d) demonstrate that the transmission peaks of the probe signal at 532 nm for G_F – C500 and 600 nm for G_F – DCM as a function of the excitation energy upper a certain value of the excited gain is enhanced, evidencing a clear gain-induced transparency of the whole system. By using a pin-hole and a notch filter in the pathway of the detector the best conditions to avoid stray light and any other undesired contribution to the transmitted light is provided (see section 5-4). By considering a few percent of the occupied volume ratio (10%) and the volume of a single dye molecule, it is estimated 10^3–10^4 molecules

encapsulated per single nanoparticle in both cases, an amount sufficient to permit an effective nonradiative energy transfer to gold NPs and promote excitation of the surface plasmon modes, by providing an estimated local gain of about 10^4–10^5 cm^{-1}[9]. However, Comparing threshold values for transmittance signals of both systems reveals a lower transmission threshold for G_F - C500 with respect G_F - DCM.

Therefore, based on the performed experimental studies upon these two gain-functionalized systems, the absorptive losses of plasmonic nanostructures can be mitigated selectively within the band where resonant energy transfer by the gain medium towards plasmonic nanoparticles occurs.

6.3.5 Silica Coated Gold Core NPs Synthesis Procedure

12±2 nm gold NPs were synthesized through the reduction of hydrogen tetrachloroaurate (III) ($HAuC_{l4}$) in the presence of sodium citrate ($Na_3C_6H_5O_7.2H_2O$) according to the procedure published by Grabar *et al*. [11] The gold NPs were coated with a 12±2 nm fluorescent silica shell according to the procedure published by Graf *et al.* [12] Briefly, 0.15 g of polyvinylpolypyrrolidone (PVP K15, Mw~10000) in 5ml of water was added to 100ml of the aqueous solution of gold nanoparticles (2.71×10^{15} particles l^{-1}).

The reaction occurred at room temperature in the dark under continuous stirring for 12 hours. PVP-capped gold nanoparticles were collected by centrifugation (16000 rpm for 1 hour) and redispersed in 10 mL of ethanol. 100mL of an ethanolic solution of tetraethylorthosilicate (TEOS, 0.2 mM)) and C500 (7.7×10^{-3} mM) or DCM (10^{-3} mM) were then added to this solution. The reactive medium was stirred in the dark for two hours before the addition of 10ml of ammonia (25% in water). The reaction occurred at room temperature in the dark under continuous stirring for over 24 hours. The core–shell particles were collected and washed through three cycles of centrifugation (16000 rpm for 1hour at room temperature) and re-dispersed in absolute ethanol. At the end of the washing cycles, the fluorescence of the supernatant was measured. No significant signal was detected, indicating that dye leaching to solution did not occur [13].

6.4 Structure 3:

Optical Loss Mitigation in Dye Doped Multimeric Nanostructures

The local field interactions between NPs which can be attached in different styles are explained by plasmon hybridization theory. Respect to this theory, the local field of such nanostructures can be enhanced remarkably as compare to a single nanoparticle. This fact can bring such idea in mind that to fabricate multimeric systems to investigate the efficiency of optical loss mitigation over such hybrid nanostructures. Therefore, in this part the absorptive loss mitigation of multimers of spherical NP consisted of gold-core/silica spacer/silica shell, in which chromophores (Rhodamine B Molecules) have been grafted at the interface between silica spacer and the jacket shell is explored as an another nano-scaled system. Furthermore, corresponding monomeric system have been designed and fabricated, in order to perform a thorough investigation. By controlling the intermediate silica shell thickness from 10 to 30 nm, two series of samples have been synthesized: passive (without dye) and active (functionalized with dye) nanostructures. Thus these samples provide the possibility to study the influences of different gain-metal inter-distances and multimeric structures of NPs on the resonant energy transfer processes.

Experimental evidences such as steady-state and time-resolved fluorescence spectroscopy, accompanied by Rayleigh scattering and optical transmission have been executed on these samples, in order to explore absorptive losses mitigation effects. Simulated local field and extinction cross section of passive and active samples (both monomers and multimers) with different interparticle shell thickness facilitate to interpret the experimentally achieved results in order to provide a convincing definition for the observed optical phenomenon.

6.4.1 Characteristics of Monomeric and Multimeric Samples

In this experimental study, two categories of multi-silica shell NPs have been investigated: passive and active NPs. Passive NPs consisted of a gold-core of 60 nm diameter with a silica shell thickness ranging from 10 to 30 nm, labeled as Mo10 and Mo30, respectively.

Active NPs, addressed as Mo+10 and Mo+30, have been fabricated starting from the silica shell which coats directly the gold nanosphere and acts as a spacer to control the distance between gold cores and the grafted Rhodamine B isothiocyanate (RhB) dye molecules, derivative with ethoxy-silane groups [14]. Then the grafted dye molecules have been covered by

a second 10 nm protective silica shell. Monodispersity and good uniformity in shape and size of monomers can be observed in transmission electron microscope (TEM) images (see Figure6-16(c)). At the same time, multimer samples have been produced by mixtures of monomers, dimers, trimers, quadrimers and heptamers of both passive and active monomers with 10 and 30 nm silica shell thickness. In fact, multimeric nanostructures are controlled aggregations of separated nanospheres.

Here active multimers with different silica shell thickness (10 nm and 30 nm) and corresponding passive ones have been labeled as Mu+10, Mu+30 and Mu10, Mu30, respectively. Figure 6-16(b) and 6-16(d) represent a scheme of synthesized multimers and TEM image of those ones with 10 nm silica shell spacer, respectively. By using well known chemical processes, all series of NPs have been dispersed in ethanol solutions (see Methods for details). Such engineered hybrid systems enable the systematic investigations of the resonance energy transfer between active dye molecules and plasmonic nanostructures with different configurations as a function of the thickness of the spacer shell.

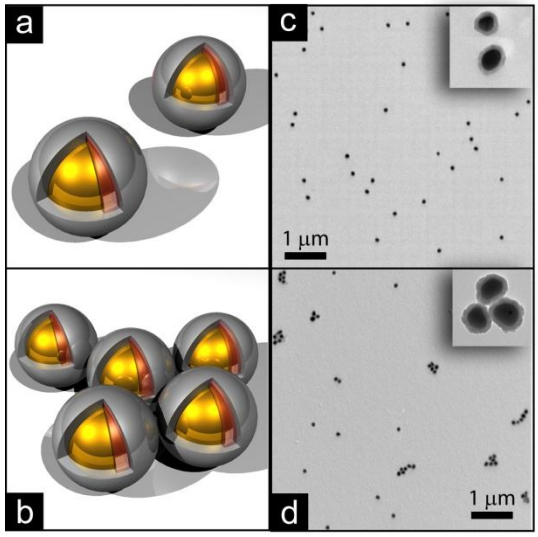

Figure 6-16 Sketches of the active **(a)** monomers and **(b)** multimers; TEM images of **(c)** Mo+10 monomers and **(d)** Mu+10 multimers with core diameter of 60 nm, silica spacer of 10 nm and silica protection shell of 10 nm. Scale bar: 1 micron for monomers and multimers images.

6.4.2 Photophysical Spectroscopy on Monomeric and Multimeric Systems

The study was performed by investigating primarily the photophysical properties of samples, to evaluate the main parameters acting in resonant energy transfer mechanisms. As a first step, the extinction cross section spectra of both series of monomers and multimers have been measured. Figure 6-17 shows the normalized curves of extinction cross section profiles of

both active and passive monomer & multimer systems influenced both by silica shell thickness and presence of dye molecules.

It is well known that the presence of amorphous silica coating around gold NPs influences peak and shape of plasmon band, due to the fact that dielectric constant of silica is higher than that of the solvent, causing a red shift in the plasmon band when silica shell thickness increases [15] (see the simulation results of Figure 6-19 (a) and (b)). This effect has been studied experimentally by Rodrıguez-Fernandez *et al.* [16] for gold NPs with different shell thickness, and those results are consistent with theoretical modeling based on the Boundary Element Method (BEM) [17] for concentric spheres, as well. Evidently, the plasmon fields of both passive monomer and multimer systems have experienced the same behavior, as the shell thickness has been increased from 10 to 30 nm (Figure 6-17(e)).

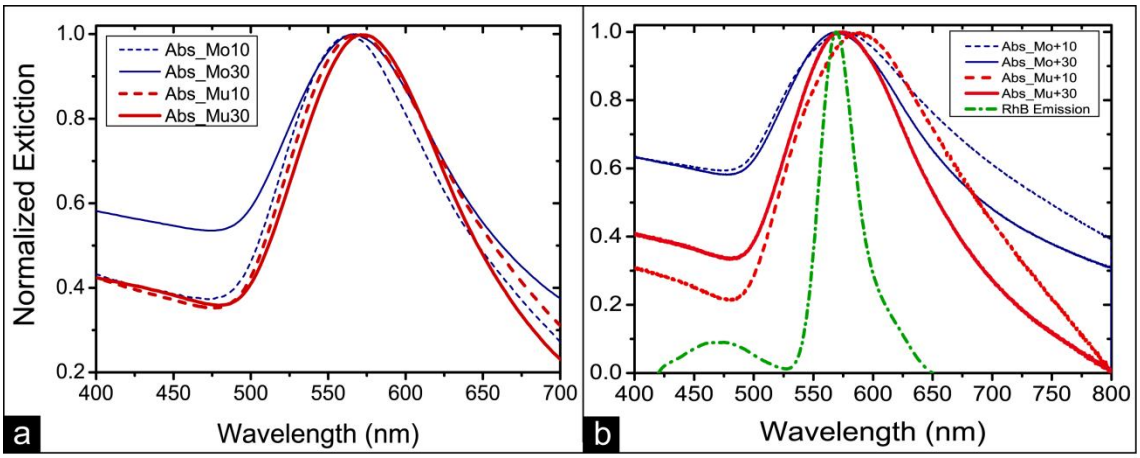

Figure 6-17 Extinction spectra of **(a)** passive and **(b)** active monomers and multimers, including emission spectrum of RhB molecules dispersed in ethanol.

On the contrary, for active monomers and multimers, the plotted results in Figure 6-17(f) show that reduction of silica shell thickness produces a red shift of the plasmon band. In particular, the observed red-shift for multimer samples (from 573 nm to 589 nm) is more pronounced with respect to corresponding monomers (from 568 nm to 575 nm). In the next part, simulation results of extinction cross sections and surrounding electromagnetic fields of both monomeric and multimeric nanostructures are reported, as a support for the experimental observations.

6.4.3 Simulation of the Local Fields and Extinction Cross Sections

In order to study the optical properties of active samples properly, extinction cross section and surrounding local field enhancement of monomeric and multimeric nanostructures

have been simulated by full wave electromagnetic simulation software (COMSOL) based on Finite Element Method (FEM). In simulations, the incident field is a Transverse Electromagnetic (TEM) plane wave with electric field and magnetic fields in Z and Y directions respectively, while wave propagates in X direction. Along with this excitation, electric dipole resonators are formed in Z direction. Gold NPs were modeled as sphere with radius 30 nm with a frequency dependent dielectric function taken from Johnson and Christy [18]. Silica shell was simulated using dielectric properties of silica according to Sellmeier dispersion equation [19].

Before starting to discuss on the obtained results, it is worth to state that simulating the real condition of these complicated systems is really difficult. Since these nanostructures are dispersed in solution and they have size deviation respect to designed structure on paper, therefore defining the real condition of these complex structures with a software is really complicated. However, the simulation results with some acceptable considerations can be reffered to the experimental observations.

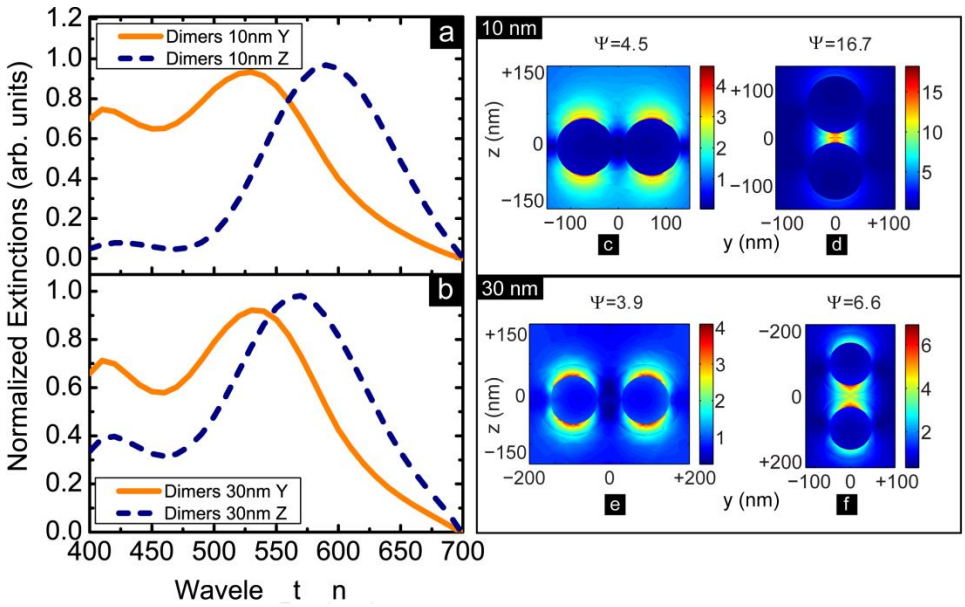

Figure 6-18 Modification of the position and shape of the plasmon band of the dimers with **(a)** 10 nm and **(b)** 30 nm coating shell respect to change their orientation from y-axis towards z-axis. Enhancement of the local field surrounding dimers with shell thickness of **(c)** & **(d)** 10 nm and **(e)** & **(d)** 30 nm by changing their direction from y-axis to z-axis. The parameter of $\Psi = |E/E_i|$ is the absolute value of ratio of the maximum local field surrounded NP (E) to the maximum of incident plane wave (E_i) and the field profiles have been plotted in Y-Z cross section plane.

Figure 6-18 shows how the orientation of a dimer with respect to the polarization angle of the incident light can influence both exctinction cross section spectrum and local field profile of the structure. The modification of the shape and position of plasmon band for dimers regardless of their 10 or 30 nm shell thicknesses is evidenced in Figure 6-18(a) and (b). As it is apparent

from these figures, the intensity of the electromagnetic confined field surrounded NPs is increased by changing the dimer orientation from Y-axis towards Z-axis. Consider that disperesed NPs can have any unintentional movement in solution, in which applying their unpredictable trajectories by software is really difficult. However, these results reveal that maximum local field amplification can be achieved when the polarization angle of the incident light is parallel with dimer longitudinal axis and the probing wavelength would be selected over the resonant wavelength corresponding to peak position of the absorption band. According to these observations, in order to extract the local field profile of the other structures, the electrically polarized beam in Z direction is considered to hit the structure in direction of its longitudinal axes and at the frequency which is the maximum intensity of extinction cross section is observed. Here in these results, Ψ represents the absolute value of ratio of the maximum local field surrounding a NP (E) to the maximum of incident plane wave (E_i)).

The other fact which evident from simulated data in Figure 6-18 is the relation between local field surrounding nanostructures and the position of maximum intensity of their plasmon band. Both dimers which are oriented in Z-axes direction are demonstrated red-shift of plasmon spectrum with respect to those ones directed in parallel with Y-axis. On the other hand, the much enhanced local fields is observed for dimers which are oriented in Z-axes direction. Take into account that the observed red-shift is more pronounced for dimers with 10 nm silica shell thickness with respect to corresponding structures with 30 nm coating shell, in which the local fields of dimers with 10 nm shell thickness are stronger than those ones with 30 nm. These observations demonstrate that the position of the plasmon band is depended to the intensity of the local fields surrounding NPs, in which a more pronounced local field shifts the plasmon band to higher wavelength in visible spectrum [16,20].

The comparison among local enhanced fields of various multimeric nanostructures which are presented in synthesized samples is provided. Figure 6-19 illustrates the simulated data related to the local field of passive monomeric and multimeric system with 10 and 30 nm silica shell thickness. It is evident from these results that modification of the nanoparticle structures from monomeric to the multimeric configuration can drastically influence the confined field around nanostructure. This study points out that the local electric field at the interstice of metal nanoparticles of dimers, trimers and quadrimers several times is higher than for isolated passive particles. Due to the presence of enhanced local electric field within constituent nanoparticles of

multimeric structures, interparticle gap are called hot spots and the effect of local field amplification on nano-scaled volumes is called nanolensing [21]. Such effects can be ascribed by plasmon hybridization model in which plasmon fields of distinct nanoparticles can reciprocally influence each other, depending on particles distance, geometry and relative incident light polarization (as demonstrated in Figure 6-18).

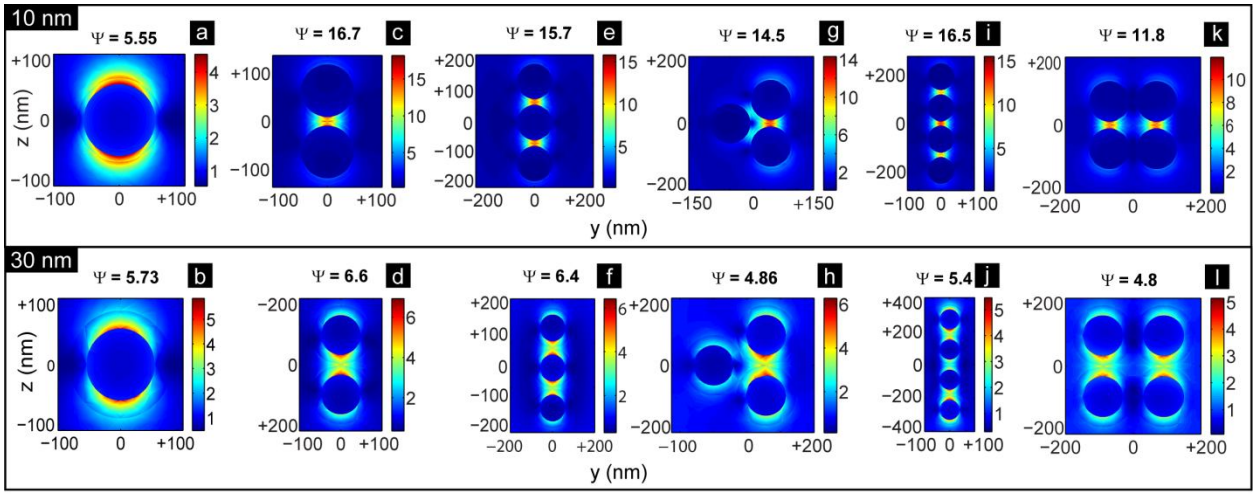

Figure 6-19 Simulated electric local field of passive monomers and multimers with 10 nm silica shell thickness of **(a)** monomers, **(c)** dimers, **(e)** inline trimers **(g)** triangle trimers, **(i)** tetramers, **(k)** inline quadrimers and 30 nm silica shell thickness of **(b)** monomers, **(d)** dimers, **(f)** inline trimers **(h)** triangle trimers, **(j)** quadrimers, **(l)** tetramers. The field profiles have been plotted in Y-Z cross section plane.

According to the reported simulation results in Figure 6-19 (c) and (d) dimeric structures are more efficient structures for amplifying confined local field. In addition these results show that other than dimers, inline chains of several metal nanospheres such as inline trimers (Figure 6-19 (e)) and tetramers (Figure 6-19 (i)) can be applied as very efficient nanolenses. However, by increasing the silica shell thickness which is identical with increasing interparticle distances between NPs of a multimeric structure, the efficiency of the enhanced local field diminishes [22]. Interestingly, by increasing separation gaps within NPs of multimeric structures, the intensity of local field even drops less than local field intensity of a monomer (see Figures 6-19 (h) and (l) and compare their local field intensities with local field of corresponding monomer in Figure 6-19 (b)). Such effect is explained by the presence of more intensive destructive field interactions as compared to the constructive forces.

Furthermore, extinction cross sections and electric local field of active monomeric and multimeric nanostructures are simulated. In order to consider the presence of gain material in simulation program, its electromagnetic properties is modeled by a generic four-level system which is described by the standard semi-classical equivalent model [23]. The approximate active

constitutive relation for a gain medium in the linear regime is expressed by following formula with considering that the relative permeability is one.

$$\varepsilon_g \sim \varepsilon_0 \varepsilon_h + \frac{\sigma_a}{\omega^2 + i\omega\Delta\omega_a - \omega_a^2} \frac{\tau_{21}\Gamma_{pump}}{1+\tau_{21}\Gamma_{pump}} N_0 \qquad (6-16)$$

Where ω_a is atomic transition frequency, $\Delta\omega_a$ is bandwidth of the atomic transition frequency, σ_a shows coupling strength to the external electric field, τ_{21} is non-radiative decay lifetime of fluorophores from metastable energy level, Γ_{pump} pumping rate, N_0 stands for total molecule density and ε_h is the permittivity of the environment surrounded gain elements.

The simulation results for real and imaginary parts of the dielectric function of RhB gain material is presented in Figure 6-20(a) and (b), respectively. The presence of the resonance in real part and negative values in imaginary part of the permittivity are evident. The presence of such negative imaginary part can make clear the idea of the absorptive loss mitigation by means of such active materials. In fact, the positive imaginary part of plasmonic NPs which is responsible for representing the absorptive attitudes can be compensated by the influence of the negative imaginary part of active chromophores. Furthermore, Figure 6-20(c), (d) and (e) display the simulated extinction cross sections of an active monomer, dimer and trimer, respectively regarding different silica shell thickness.

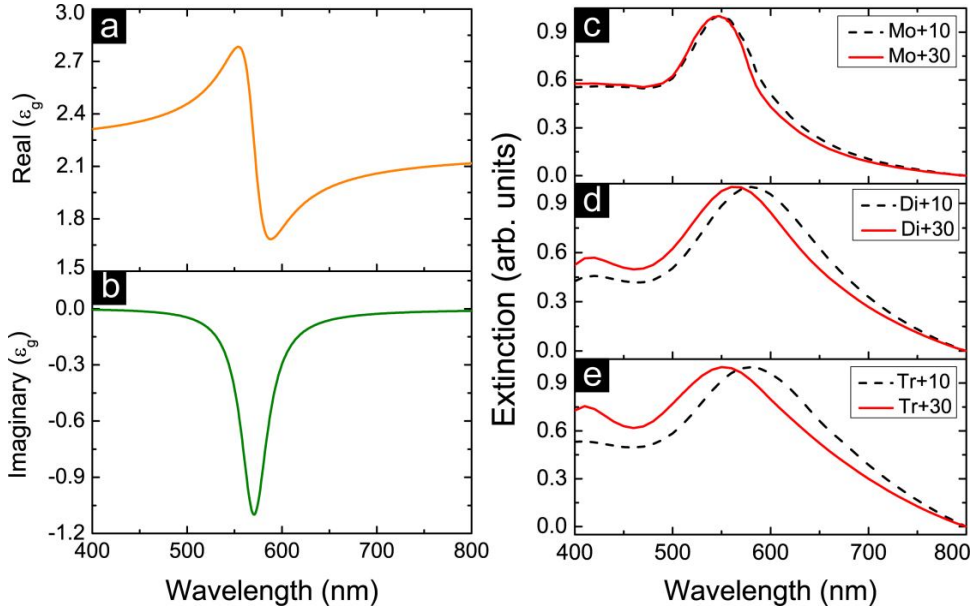

Figure 6-20 Simulated **(a)** real and **(b)** imaginary parts of the dielectric function of Rhodamine B dye molecules with parameter values of $\varepsilon_r = 2.25$, $\omega_a = 526$ THz , $\Delta\omega_a = 31{,}5$ THz , $\sigma_a = 6.55\times e^{-8}$ C^2/kg, $\tau_{21} = 3$ ns, $\Gamma_{pump} = 1.5\times e^{9}$ s^{-1} and $N_0 = 3\times e^{29}$ m^{-3}. Simulated extinction cross sections of active **(c)** monomers **(d)** dimers and **(e)** trimers with 10 nm (black dashed line) and 30 nm (solid red line) silica shell thickness.

Results are in agreement with the observed behavior of the LSP bands obtained in experiments. The simulation results of local field surrounded nanostructures confirms the fact that the position of plasmon bands are dependent to the intensity of NPs near fields, in which more enhanced local fields push the LSP band to upper wavelengths. In addition, our results demonstrate that active monomeric and multimeric systems generate a significant amplification of local fields with respect to passive ones (compare the local fields of an active monomer and multimers in Figures 6-21(c) and (d) with equivalent passive monomers in Figure 6-21(a) and (b)).

In addition, the comparison of active monomers and multimers local fields with 10 nm silica spacer (Figures 6-21(e), (g), (i) and (k)) with corresponding nanostructures with 30 nm silica shell (Figures 6-21(f), (h), (j) and (l)) reveals stronger induced local field in the case of shorter silica gap.

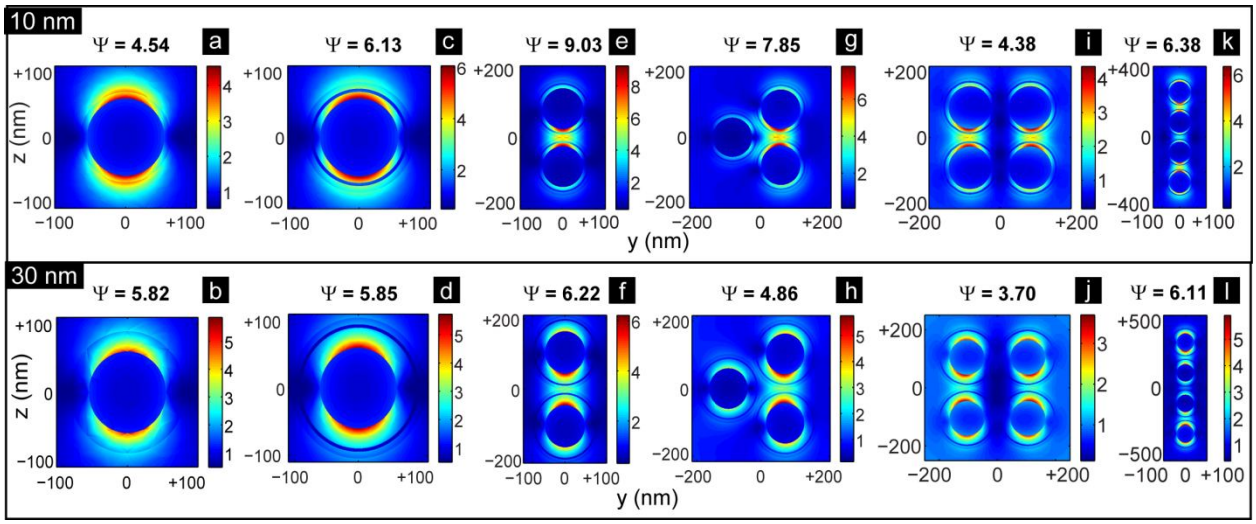

Figure 6-21 Simulation results for local field of monomers and multimers with 10 nm silica shell thickness of **(a)** passive monomers, **(c)** active monomers, **(e)** active dimers, **(g)** active trimers **(i)** active tetramers **(k)** active quadrimers and 30 nm silica shell thickness of **(b)** passive monomers, **(d)** active monomers, **(f)** active dimers, **(h)** active trimers **(j)** active tetramers **(l)** active quadrimers The field profiles have been plotted in Y-Z cross section plane.

In particular, inline multimeric configurations (dimer and quadrimer systems) with a shorter dye-NP separation space result a more promising candidate to comprise extra enhanced near fields, with up to almost 50% enhancement, as a consequence of constructive LSP hybridization within NPs. The obtained results confirm this fact that plasmon hybridization among NPs of a multimeric structure is depended on both interparticle distances and configuration of the nanostructure. As it is evidenced from this figure, for longer separation distances the local field of trimers and tetramers demonstrated in Figure 6-20 (h) and (j),

respectively, are lower than the local field of monomeric structure with corresponding silica shell thickness (see Figure 6-20(b)). This matter again confirms the presence of the destructive interactions beside constructive ones in the structure of a multimer. However, in comparison to the mentioned structures, local field hybridizations within inline multimeric configurations always are in constructive direction, even if separation gaps among NPs are big.

6.4.4 Steady-State Fluorescence Spectroscopy

The emission spectrum of RhB molecules dissolved in ethanol (green dashed curve in Figure 6-17(b)), emphasizes its effective overlap with NP plasmon bands. As evidenced from Figure 3, the peak position of emission spectra of grafted RhB molecules is different from that one showed in Figure 6-17 (b).

In all samples, such a phenomenon can be ascribed due to the combination of mainly two effects: first, the formation of dye excited multimers (excimers), as a result of high density of fluorescent molecules grafted on the inner silica shell [24]. In fact, the creation of excimers can affect the energy levels of dye molecules and consequently induce a more effective intermolecular FRET process, which depends on donor-acceptor distance. Second effect is related to the strong feedback provided by the intense plasmonic field surrounding NPs to the transition dipole moment of excited chromophores, which can induce radiative de-excitation from different metastable states.

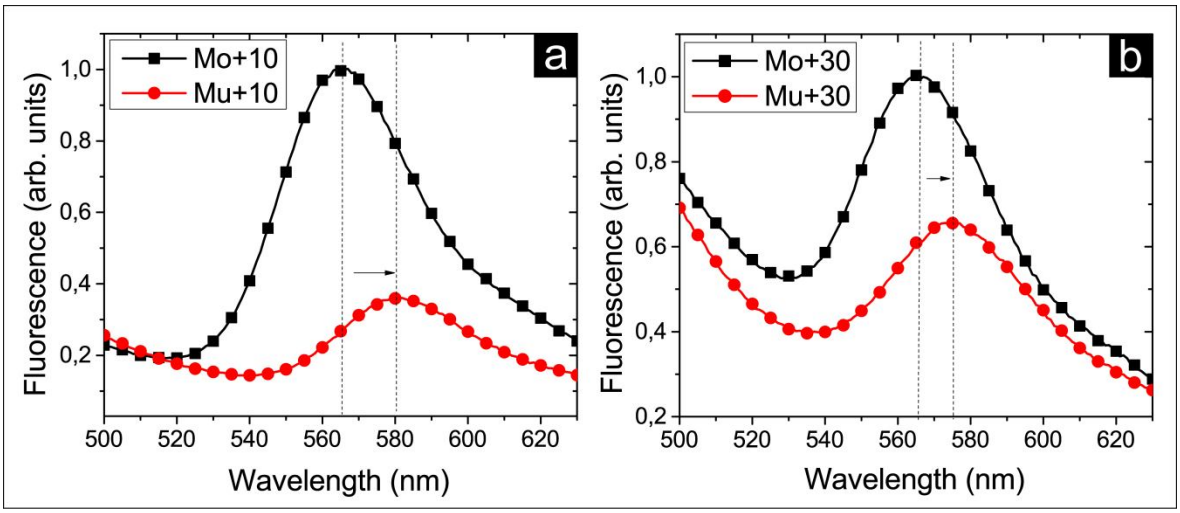

Figure 6-22 Fluorescence quenching observed in multimers with respect to monomers under the same pump energy value. **(a)** Fluorescence emission maxima of Mo+10 sample (black squares) with respect to Mu+10 sample (red circles) **(b)** Fluorescence emission maxima of the Mo+30 sample (black squares) with respect to Mu+30 sample (red circles).

From steady-state photoluminescence (PL) studies, the fluorescence peak corresponding to multimers represent a red shift with respect to monomers (Figure 6-22(b)). Such a phenomenon can be ascribed due to the presence of more efficient coupling between gain medium and the enhanced near fields of metal NPs in multimers structure, creating the probability of resonant transitions from the RhB molecules excited state to a particular vibrational sublevel of the electronic ground state. Moreover, the observed effect is more pronounced in Mu+10 sample (lower silica spacer thickness) with respect to Mu+30. In fact, the thinner is the silica shell, the more effective plasmon hybridization effects are expected, resulting in an enhanced red shift of chromophores emission.

In order to perform a comparative analysis of absorptive losses mitigation as a function of the gain material, we paired the photoluminescence results in both monomers and multimers samples. It is well-known that the presence of gain material in close proximity (a few nanometers) of a metal absorber can cause a quenching of the PL. As it is evidenced from Figure 6-22 PL quenching of RhB dye molecules occurs in both monomers and multimers systems as function of silica spacer thickness. Spontaneous emission spectra of gain materials grafted in Mu+10 sample compared with Mo+10 system show a 2.8 fold lowering (Figure 6-22(a)), while the emission of Mu+30 multimers quenches only 1.5 fold in comparison with Mo+30 monomers, as shown in Figure 6-22(b). The obtained results demonstrate that PL quenching process in multimers is more efficient in comparison to monomers, due to the strong plasmonic dipole interaction within inter-particle gap of adjacent NPs in multimeric structures.

6.4.5 Time-Resolved Fluorescence Spectroscopy

The above presented steady-state measurements are necessary but not sufficient to demonstrate occurrence of nonradiative RET in a metal-gain composite towards mitigation of NPs absorptive losses. Hence, in order to perform a systematic analysis of gain-induced optical loss modifications, time-resolved fluorescence spectroscopy along with transmission and Rayleigh scattering experiments have been carried out on both monomer and multimer systems.

In order to investigate the nonradiative energy transfer rates as a consequence of various coupling strengths in monomers and multimers systems with different spacer shell thicknesses, the fluorescence lifetime has been acquired with respect to pure dye solution. The scheme of the ultrafast time resolved sprectrofluorometer which has been used to acquire TCSPC data from active samples has been shown in Figure 5-9 (see section 5.5 for details of the setup). For an

ethanol solution of RhB molecules, time-resolved PL decay curve (black dots) can be well fitted as a single-exponential function shown in Figure 6-23 (a) and (b), resulting in a lifetime of about τ_D = 3 ns (χ^2 = 1.192), which is consistent with previous studies (fit is not reported into figures). For both monomer and multimer systems, PL decay curves can be fitted neither by a single exponential function nor by a bi-exponential one. In fact, due to dipole-metal interactions of prepared multi-shell systems, a plasmon-induced tri-exponential decay function with three time constants has been used as the best fit.

The presence of a very fast decay time (τ_1) is attributed to a significant decrease of radiative rate due to grafted dye molecules onto the silica shell coupled to the plasmonic gold cores, which experience a strong dipole-metal RET process (Figure 6-24). The intermediate decay time (τ_2) is correlated to dipole-dipole FRET interactions, which happen in two ways such as: direct coupling (*i.e* the coupling between excimers of grafted dye molecules) and indirect coupling (*i.e* the coupling of dye excimers via gold cores) [25]. These two pathways for releasing the energy of optically excited RhB dye molecules are presented in the scheme of Figure 6-24. The long-living emission decay kinetics (τ_3) are due to those dye molecules that do not overcome coupling effect, consisting in a small percentage of unbound dye molecules that may have persisted throughout the synthesis and purification of samples.

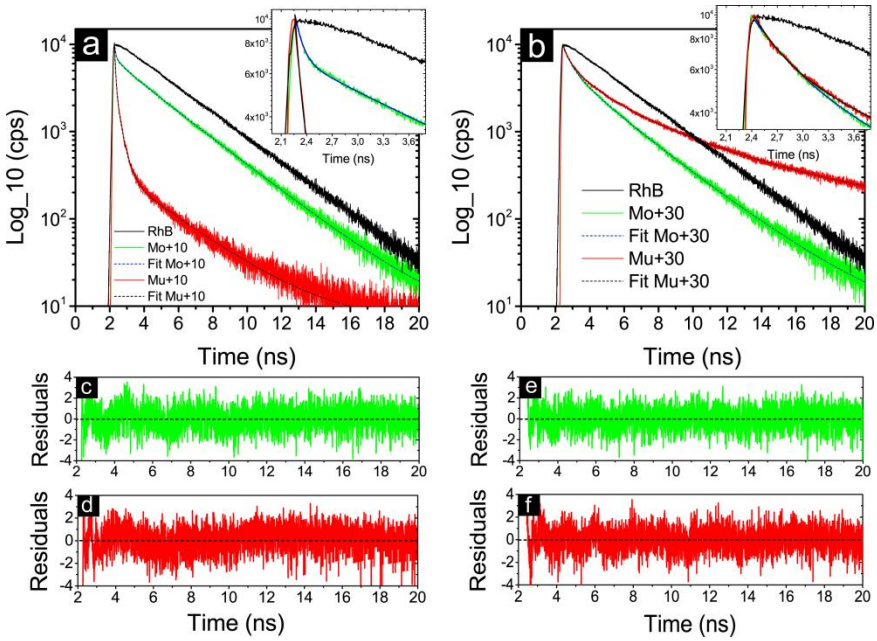

Figure 6-23 Time-resolved fluorescence intensity decays and corresponding residuals of **(a)** monomer (Mo+10) and multimer (Mu+10) systems with 10 nm silica shell thickness. **(b)** monomer (Mo+30) and multimer (Mu+30) systems with 30 nm silica shell thickness. **(c)** and **(d)** contain residuals decay fit of Mo+10 and Mu+10 systems, respectively. Also, **(e)** and **(f)** contain residuals decay fit of Mo+30 and Mu+30 systems, respectively.

Figure 6-23(a) compares the TCSPC data obtained at 572 nm, for grafted dye molecules in Mo+10 and Mu+10 systems with respect to pure RhB dye solution when irradiated with 375 nm ultrafast pulsed laser. From TCSPC data of Mo+10 system (green dots and blue line fit), a fast decay (τ_1~ 88 ps; χ^2 = 1.14) is accompanied by an intermediate decay time (τ_2~ 971 ps) and a long-living emission where the decay kinetics can be assimilated to the fluorescence decay for pure RhB dye molecules (τ_3~ 2.9 ns). Comparative analysis has been performed on decay curve of Mu+10 nanostructures (red dots and black line fit), and three decay times of τ_1 = 70 ps, τ_2 = 332 ps and τ_3~ 3 ns have been extracted for this system (χ^2 = 1.27). The constructive interaction between plasmonic fields of NPs forming multimers causes the strong coupling between grafted donor molecules and plasmonic NPs. This enhanced coupling tends to shorten further the decay time of excited dye molecules in multimers in comparison to corresponding monomers. The obtained results are in agreement with the steady-state fluorescence spectroscopy data, in which multimers showed a higher PL quenching efficiency with respect to the corresponding monomers (Figure 6-22), and also with numerical simulation data in Figure 6-21. Furthermore, besides the nonradiative direct coupling between excimers embedded in a single NP, the nanospheres constituting a multimer structure increases the possibility of nonradiative indirect coupling between dye excimers via gold core, which results in a shortening of τ_2 for the case of Mu+10 respect to Mo+10. The long-living emission decay times τ_3 of both samples are almost the same, which has to be associated to the fluorescence decay time known for RhB dye molecules in solution.

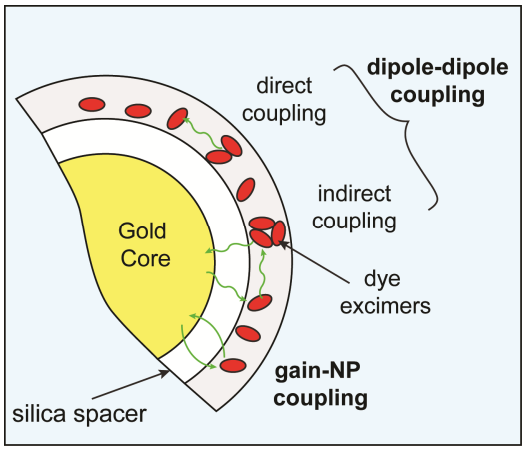

Figure 6-24 The scheme of different coupling configurations between grafted dye molecules and gold cores.

A comparative set of lifetime measurements has been performed on Mo+30 and Mu+30 nanostructures, where chromophores are located 30 nm apart from gold cores. Figure 6-23(b)

illustrates emission transients of these systems. From TCSPC data collected for the Mo+30 sample (green dots and blue line fit) a tri-exponential function was used to fit the emission intensity decay. The evaluated fast decay, intermediate decay and short decay times are 452 ps, 1860 ps and 3.2 ns (χ^2 = 1.07), respectively.

Also, from emission intensity decay of Mu+30 multimers (red dots and black line fit), three decay components have been extracted: τ_1 = 325 ps, τ_2 = 1582 ps and τ_3~5.32 ns (χ^2 = 1.187). The acquired lifetime components of Mo+30 and Mu+30 systems reveal that Mu+30 multimers show reduction in both fast and intermediate lifetimes with respect to Mo+30 monomers, indicating a presence of more effective dye-NP and dye-dye coupling in Mu+30 system. The long-living emission decay time of Mo+30 can be easily compared to the lifetime of pure RhB dye molecules in solution. However, an unexpected behavior has been observed on Mu+30 sample, where the long-living excitonic states show a longer lifetime with respect to the dye solution. Moreover, it is clear that the fast decay times (τ_1) of both Mo+30 and Mu+30 systems are longer than the corresponded decay times of Mo+10 and Mu+10 systems. This indicates that the nonradiative RET occurring between chromophores and metal cores, is drastically affected by their separation space. Additionally, the evaluated longer intermediate decay times (τ_2) infer that the increase of silica shell thickness leads to a reduction of both direct and indirect couplings, irrespective of monomer or multimer systems.

Table 6-2 provides the possibility to compare more conveniently the acquired results of time-resolved spectroscopy for monomeric and multimeric samples in two regimes of silica shell thicknesses.

Sample	$\lambda_{excitation}$(nm)	$\lambda_{emission}$(nm)	χ^2	τ_1 (ps)	τ_2 (ps)	τ_3 (ns)
Mu+10	375	572	1.27	70	332	3
Mo+10	375	572	1.14	88	971	2.9
Mu+30	375	572	1.18	325	1582	5.32
Mo+30	375	572	1.07	452	1860	3.2

Table 6-2 Time-resolved fluorescence decay data, accompanied by excitation and emission wavelength reports for monomeric and multimeric systems with 10 nm and 30 nm interparticle distances.

6.4.6 Pump-Probe Rayleigh Experimental Measurements

In order to complete the systematic analysis of gain induced optical loss modifications, pump–probe experiments have been carried out on both multimer and monomer systems.

According to the Beer–Lambert law, by measuring simultaneously Rayleigh scattering and transient absorption, either in the absence or in the presence of gain, allow us to determine if the extinction curve of the plasmonic system is affected by resonance energy transfer. Thus, modifications of Rayleigh scattering and transmitted intensity of a constant probe beam (CW @ 532 nm) have been monitored as a function of pump energy for all systems (excitation @ 355 nm). As first proposed by Lawandy [10], the localized SP resonance in metallic nanospheres is expected to show a singularity when the surrounding dielectric medium provide a critical value of optical gain. This can be evidenced by an increase of the Rayleigh scattering signal because of the enhancement of the local field surrounding the metal nanoantennas.

Pump–probe Rayleigh scattering experiments were performed by launching collinearly a probe beam in a small portion of the volume excited by a pump beam at λ = 355 nm (see Figure 5-8 and section 5.4 for details of the setup).

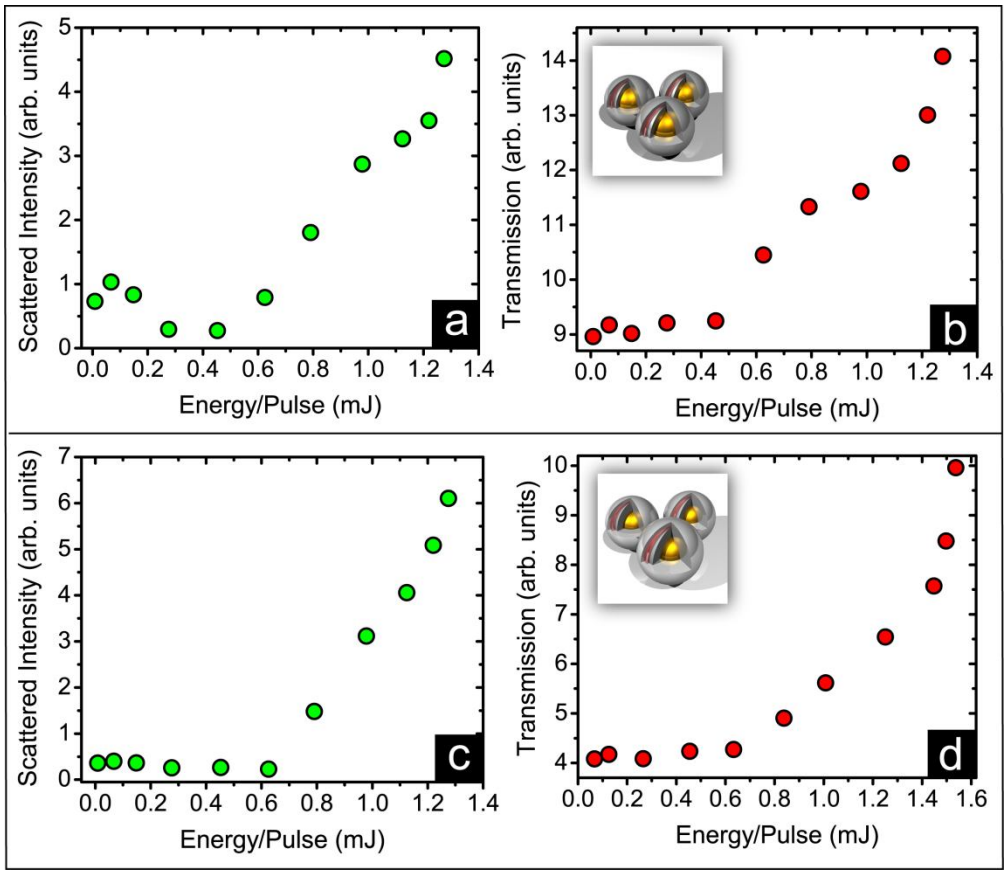

Figure 6-25 Comparison of scattering and transmission enhancement signals between multimers systems with the silica shell thickness of (a,b) 10 nm and (c,d) 30 nm samples. Enhancement of SP evidenced by an increasing of normalized Rayleigh scattering signal of probe beam (532 nm) as a function of pump energy (355 nm) for multimeric systems of **(a)** $Au@SiO_2$ (10 nm)/$RhB@Sio_2$ and **(c)** $Au@SiO_2$ (30 nm)/$RhB@Sio_2$. Normalized transmission enhancement of a probe beam at (532 nm) as a function of pump energy for multimeric systems of **(b)** $Au@SiO_2$ (10 nm)/$RhB@Sio_2$ and **(d)** $Au@SiO_2$ (30 nm)/$RhB@Sio_2$. Different threshold values for both transmission and scattering signals have been observed in the two samples.

Figure 6-25(a) shows the enhancement of Rayleigh scattering signal as a function of excitation energy in Mu+10 multimers. The super linear increase of the scattered signal above a given threshold value of the pump energy is a demonstration of the enhancement of the quality factor of SP resonance mediated by resonant energy transfer processes between active elements and gold cores within the composite NPs [6,9,13]. Thus, the key experiment of this work was performed by measuring the transmittance of the probe beam after traversing the excited volume upon varying the pump rate. Figure 6-25(b) shows the increase of transmission peaks of the probe signal at 532 nm as a function of the excitation energy for Mu+10 system, evidencing a clear gain-induced transparency of the whole system. A critical behavior of the transmission was observed above a given threshold value of about 0.45 mJ/pulse, revealing that a reduction of optical absorption can be induced only if enough gain is provided.

Figure 6-25 (c) and (d) show Rayleigh scattering intensity and transmission of the probe beam at 532 nm, as a function of the pump rate, for Mu+30 sample. The obtained results evidenced that the scattering and transmission of probing light waves, having wavelengths within the resonant band, experienced a considerable enhancement as the gain was increased to a critical value. In fact, a pump energy threshold value of about 0.63mJ/pulse was sufficient to permit an effective RET to gold NPs, promoting excitation of surface plasmon modes.[38] Strikingly, the obtained curves reveal higher threshold values with respect to Mu+10 system. This effect can be explained by considering the inter-distance dependence of the energy transfer rate, owing to NP-dye dipolar interactions according to Dipole to Metal Particle Energy Transfer (DMPT) theory.

A comparative set of experiments, including both Rayleigh scattering and optical transmission has been performed on Mo+10 and Mo+30 monomers. The plotted results of these experiments in Figure 6-26 indicate a striking enhancement in the scattered and transmitted light above the gain threshold, as pump energy increases.

The observed enhancement in scattered and transmitted probe intensity at 532 nm, where the gain curve overlaps the plasmon band, demonstrates that the optical transparency of strongly absorbing monomer nanostructures can be induced by promoting effective resonant energy transfer from active elements to plasmon units, such as was observed for multimer systems. As it is observable from these results, Mo+10 NPs demonstrates lower threshold values (~0.55 mJ/pulse) respect to that of Mo+30 ones ((~0.7 mJ/pulse). Therefore, similar to the case of

multimeric hybrid systems, the importance of shorter NP-gain distances for achieving more efficient absorptive loss mitigation of plasmonic nanostructures is evidenced for single gain doped core-shell NPs, as well.

Take into account that the gain-induced increase of optical transparency of meta-subunits becomes clearer when corroborated by experimental evidences which provide both direct measurements of the physical quantity (transmission) and effects clearly related to the energy transfer process (fluorescence quenching and Rayleigh scattering enhancement).

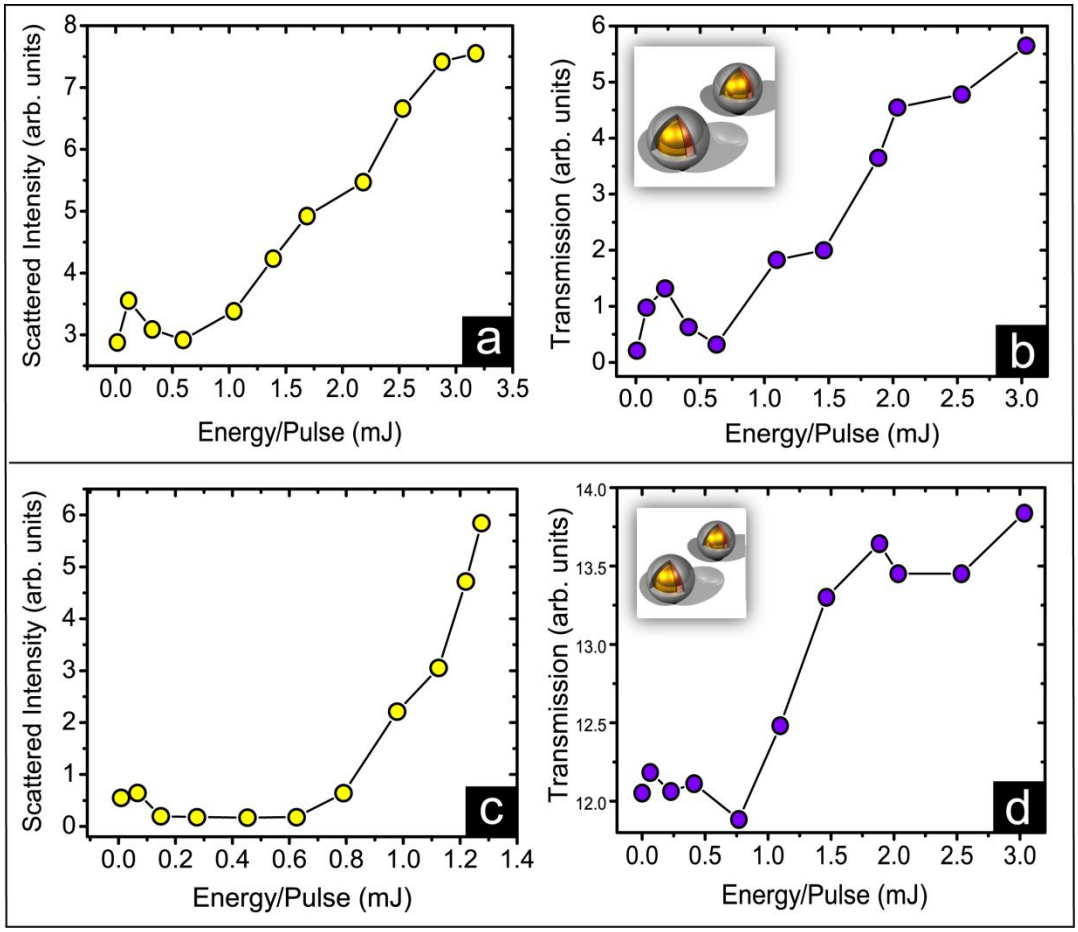

Figure 6-26 Comparison of scattering and transmission enhancement signals between monomer systems with the silica shell thickness of (a,b) 10 nm and (c,d) 30 nm samples. Enhancement of SP evidenced by an increasing of normalized Rayleigh scattering signal of probe beam (532 nm) as a function of pump energy (355 nm) for monomers of **(a)** $Au@SiO_2$ (10 nm)/$RhB@Sio_2$ and **(c)** $Au@SiO_2$ (30 nm)/$RhB@Sio_2$ monomers. Normalized transmission enhancement of a probe beam (532 nm) as a function of pump energy for **(b)** $Au@SiO_2$ (10 nm)/$RhB@Sio_2$ and **(d)** $Au@SiO_2$ (30 nm)/$RhB@Sio_2$ monomers. Different threshold values for both transmission and scattering signals have been observed in the two samples.

The obtained results suggest that by properly bringing gain to strongly absorptive meta-subunits can remarkably modify the imaginary part of the polarizability of these media, resulting in a reduced extinction coefficient at the resonance wavelengths. In particular, upon engineering

multimer nanostructures with proper values of metal-gain distance can be very promising to tailor effective gain assisted plasmon hybridization processes. In the framework of bottom-up systems approach based on plasmonic materials this would represent a relevant step forward towards real applications of plasmonic metamaterials at optical frequencies.

6.4.7 Synthesis Process of Multimeric and Monomeric Nanostructures

Gold NPs with a diameter of (60±5) nm were synthesized by chemist collaborator through the reduction of hydrogen tetrachloroaurate (III) ($HAuCl_4$) in the presence of sodium citrate ($Na_3C_6H_5O_7.2H_2O$) and sodium borohydride ($NaBH_4$) according to the procedure published by Brown *et al*. [26]. Firstly, passive gold nanoparticles (without dye) were coated with a silica shell (monomer) according to the procedure published by Graf *et al*. [27].

The thickness of the shell was controlled by changing the amount of silica precursor (tetraethyl orthosilicate, TEOS). The active nanoparticles (with dye) were obtained from the passive ones by firstly grafting a Rhodamine B derivative with ethoxy-silano group, which was previously prepared by reacting Rhodamine B isothiocyanate (RhB) with aminopropyltriethoxysilane in absolute ethanol, [28] on the silica shell. To do so, an amount corresponding to 15 RhB molecules/nm^2 of silica surface was added in an ammonia (6 % v/v)/ethanol suspension of passive particles. The reactive medium was heated at 70 °C during one hour. The monomers were collected by centrifugation and washed three times with absolute ethanol. A second protective silica shell of 10 nm thickness was then grown by drop wise addition of an ethanolic solution of TEOS [29]. The increase of the concentration of passive and active monomers during the addition of the TEOS solution leads to the formation of multimers that are the mixture of dimers, trimers, quadrimers, heptamers. These mulitmers are formed as a result of collisions between monomer particles and are permanently fixed via the hydrolysis and condensation of TEOS molecules on their surface [30].

REFERENCES

1. J.B. Marling, J.H. Hawley, E.M. Liston, and W.B. Grant, *Appl. Optics*, **1974**, 13, 2317.
2. E. Dulkeith, *et al.*, *Phys. Rev. Lett.*, **2002**, 89, 203002.
3. T. Soller, M. Ringler, M. Wunderlich, T. A. Klar, and J. Feldmann, *Nano Lette*rs, **2007**, 7, 1941.
4. J. Rodríguez-Fernández, J. Perez-Juste, F. J. G. de Abajo, and L. M. Liz-Marzán, *Langmuir*, **2006**, 22, 7007.
5. C. Fernández-Lopez, C. Mateo-Mateo, R. Alvarez-Puebla, J. Perez-Juste, I. Pastoriza-Santos, and L. Liz-Marzán, *Langmuir*, **2009**, 25, 13894.
6. A. De Luca, M. P. Grzelczak, I. Pastoriza-Santos, L.M. Liz-Marzán, M. La Deda, M. Striccoli, and G. Strangi, *ACS Nano*, **2011**, 5, 5823.
7. J. Gersten, and A. Nitzan, *J. Chem. Phys*., **1981**, 75, 1139.
8. J. M. Pitarke, V. M. Silkin, E. V. Chulkov, and P. M. Echenique, *Rep. Prog. Phys.*, **2007**, 70, 1.
9. G. Strangi, A. De Luca, S. Ravaine, M. Ferrie, and R. Bartolino, *Appl. Phys. Lett.*, **2011**, 98, 2519121.
10. N. M. Lawandy, *Appl. Phys. Lett.*, **2004**, 85, 5040.
11. K. C. Grabar, R. G. Freeman, M. B. Hommer, and M. J. Natan, *Anal. Chem.*, **1995**, 67, 735.
12. C. Graf, D. L. J. Vossen, A. Imhof, and A. van Blaaderen, *Langmuir*, **2003**, 19, 6693.
13. A. De Luca, M. Ferrie, S. Ravaine, M. La Deda, M. Infusino, A. R Rashed, A. Veltri, A. Aradian, N. Scaramuzzaa, and G. Strangi, J. Mater. Chem. **2012**, 22, 8846.
14. M. Ferriè, N. Pinna, S. Ravaine, and R. A. L. Vallèe, *Opt. Express*, **2011**, 19, 17697.
15. L. M Liz-Marzan, and M. Giersig, P. Mulvaney, *Langmuir*, **1996**, 12, 4329.
16. J. Rodrıguez-Fernandez, I. Pastoriza-Santos, J. Perez-Juste, F. J. Garcıa de Abajo, and L. M. Liz-Marzan, *J. Phys. Chem. C*, **2007**, 111, 13361.
17. F. J. Garcıa de Abajo, and A. Howie, *Appl. Phys. Rev. B*, **2002**, 65, 1154181.
18. P. B. Johnson, and R. W. Christy, *Phys. Rev. B*, **1972**, 6, 4370.
19. I. H. Malitson, *J. Opt. Soc. Am.*, **1965**, 55, 1205.
20. A. E. Schlather, N. Large, A. S. Urban, P. Nordlander, and N. J. Halas. *Nano let.* **2013**, 13, 3281.
21. P. N. Prasad, "*Nanophotonics*", Wiley, 2004.
22. S. J. Barrow, X. Wei, J. S. Baldauf, A. M. Funston, and P. Mulvaney, *Nat. Commun*., **2012**, 3, 1.
23. A. E. Siegman, "*Lasers*", 3rd ed., University Science Books, Mill Valley, 1986.

24. A. P. Demchenko, "*Advanced Fluorescence Reporters in Chemistry and Biology*", Springer, Berlin, 2011.

25. V. Pustovit, F. Capolino, and A. Aradian, "*Nano-Optics for Enhancing Light-Matter Interactions on a Molecular Scale*", Springer, New York, 2013.

26. K. R, Brown, D. G. Walter, and M. J. Natan, *Chem. of Mater*., **1999**, 12, 306.

27. C. Graf, and A. van Blaaderen, *Langmuir*, **2001**, 18, 524.

28. X. Gao, J. He, L. Deng, and H. Cao, *Opt. Mater.*, **2009**, 31, 1715.

29. S. Kang, S. I. Hong, C. R. Choe, M. Park, S. Rim, and J. Kim, *Polymer*, **2001**, 42, 879.

30. M. Ibisate, Z. Zou, and Y. Xia, *Adv. Funct. Mater.*, **2006**, 16, 1627.

Chapter 7

Optical Loss Mitigation in Meso-scaled Hybrid Systems

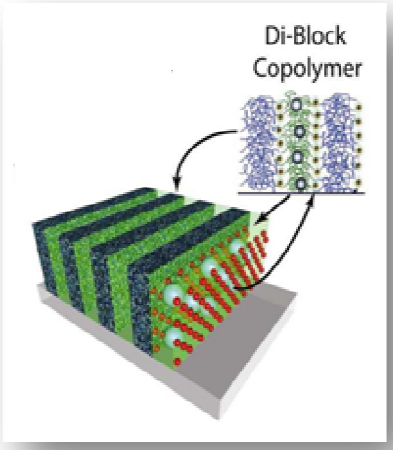

7-1 Introduction

As reported in the previous chapter, gain material interactions with close proximity core-shell nanostructures lead to obtain absorptive losses compensated hybrid systems. In order to follow the determined strategy of this research study, optical loss mitigation process should be investigated in meso-scaled (100-900 nm) plasmonic structures. Such structures can include both dispersion and bulk samples. In a dispersion meso-scaled sample, silica-plasmon composites can be dissolved in solution in order to produce gain-assisted systems by applying an appropriate type and concentration of gain materials. In addition, progress in chemical engineering provides the possibility to incorporate chromophores within the meso-scaled structures, in order to create a proper gain functionalized hybrid system. The concentric nanoshells are an example of such structures which are investigated in this research study. These particles are consisted of gain-

functionalized dielectric core, coated with metallic shell, which are dispersed in a proper solution. In fact, the name of nanoshell for such composite structures arises from the thickness of shell that is in nano scale range. An appropriate design of such structure concerning an optimized ratio of core diameter to metallic shell thickness, and a right alternative of gain material can lead to obtain a more efficient structure for absorptive losses mitigation purposes, by using plasmon hybridization effect.

The investigation of the optical properties of this composite system can direct us towards compensating optical losses in meso-scaled bulk samples, such as periodic layers of gain materials and plasmonic NPs on top of each other. In such structure the near field communications between active and passive layers can provide the opportunity to obtain a loss compensated composite system, leading us towards fabricating lossless bulk samples in macro-scale.

Therefore, in this chapter the possibility of optical losses mitigation in plasmonic nanoshells is explored. The steady-state experiments along with emission intensity decay time measurements can be informative regarding efficiency of DMPET process within hybrid system. Then, in order to provide persuasive evidences for absorptive loss mitigation on synthesized sample, pump-probe scattering experiments should be performed.

7.2 The Structure of Concentric Metallic Nanoshells

A metallic nanoshell is composed of a spherical dielectric core surrounded by a concentric metallic thin shell whose optical resonances are determined by inner and outer radius of metallic shell layer. The diameter of the silica cores for synthesized nanoshells is considered 150 nm and the grown gold shell surrounding dielectric cores has a thickness of 25 nm. The silica core of the synthesized sample is incorporated with RhB dye molecules, in order to compensate the optical losses of plasmonic shell of the structure. Figure 7-1(a) illustrates a scheme of such composite structures and TEM image of the fabricated sample. The inspection on provided TEM images confirm that the prepared nanoshells are synthesized in an acceptable uniformity in shape and size.

Furthermore, in order to evaluate the possible modifications in optical response of embedded dye molecules in silica core of nanoshells, a dye doped silica spheres which are identical respect to the geometry of nanoshells cores (150 nm) were synthesized. By following

relevant chemical processes, both main and reference samples were dispersed in ethanol solutions.

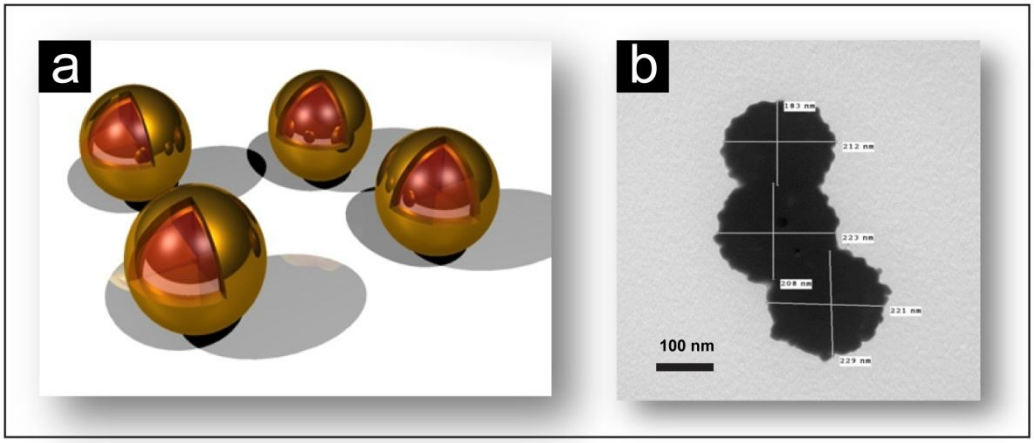

Figure 1-7 (a) Scheme of dye doped silica core spherical nanoshells with metallic shell. **(b)** TEM of the synthesized plasmonic nanoshells consisting of RhB dye doped dielectric cores and metallic shells.

7.3 Geometry Dependent Nanoshell Plasmon Resonances

The most striking feature of a dielectric core with metal shell structure is that by varying the relative dimensions of the core and shell, the optical resonance of such particle can be varied over hundreds of nanometers in wavelength, across the visible and into the infrared region of the spectrum.

In order to experience such effect, the simulation results of SPR spectra of gold nanoshells based on finite-element method are demonstrated in Figure 7-3. The hybrid structures were considered with silica diameter fixed at 150 nm and gold shell thickness is varied from 5 nm to 60 nm. The dielectric function of gold shell is derived from Johnson & Christy data [1]. These simulation results demonstrate the effect of surrounding gold shell on the wavelength position of extinction band, resulting in a red-shift by decreasing shell thickness. In fact, for a nanoshell structure the position of the plasmon resonance peak and the relative contributions of absorption and scattering cross sections to total extinction can be tuned by configuring two structure parameters of inner silica core radius and the thickness of outer metallic shell.

Therefore, contrasting to spherical NP, the adjustment of the core diameter to shell thickness ratio and the overall particle size of concentric nanoshells provide the unique properties in which both intrinsic and extrinsic properties of designed structure can be varied independently.

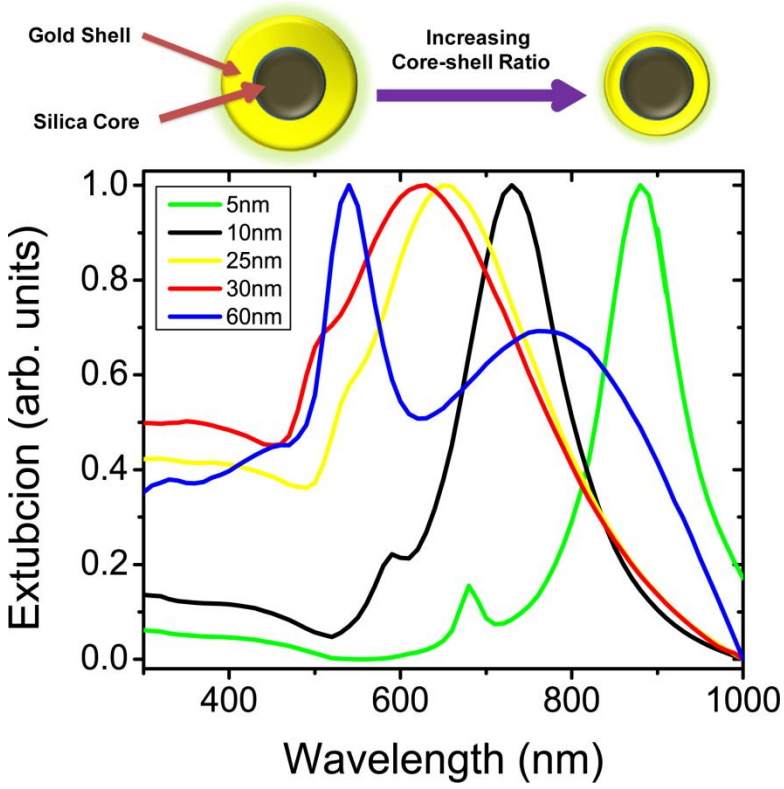

Figure 7-2 The extinction spectra calculated for gold nanoshells supported on silica cores. The diameter of the silica core is fixed at 150 nm while the shell thickness varies from 5 nm to 60 nm.

As it is evident, plasmonic properties of gold nanoshells are extremely sensitive to small variation of plasmonic shell thickness. For example, the SPR peak shifted from 730 nm to 880 nm when the thickness of the shell was merely decreased by 5 nm, i.e., from 10 nm to 5 nm. As expected, the dependence of the position of SPR peak on the shell thickness becomes much weaker when the shells become thicker. This simulation results validate this fact that the SPR peaks of composite spherical nanoshells could be conveniently tuned over a broad range of the electromagnetic spectrum by controlling the ratio of shell thickness to particle diameter [2,3].

As it is evident from Figure 7-2, the nanoshell with shell thickness of 60 nm shows different plasmon spectrum respect to the others. In order to accurately explain the presented peaks in the simulated extinction cross section of such nanoshells it is necessary to move beyond the quasi-static limit. The considered metal shell thickness of 60 nm is beyond the quasi-static approximation which has been described in section 2-4. In this size regime it becomes necessary to consider phase retardation effect in the interaction of incident electromagnetic field with nanoshell particle. Consider that once the nanoshell dimension becomes comparable to the wavelength of incident light, the particle no longer experiences a uniform electromagnetic field.

In fact, due the presence of phase retardation effect higher order multiple modes (n>1 in equation 2-1) are excited. Insertion of higher order multiples in the series expansion of the extinction cross section describe the presence of secondary plasmon peak for bigger size nanoshells. This peak is blue-shifted with respect to the main dipole resonance of the particle.

Moreover, the observed broadening effect of the plasmon resonance and as well as the shift in plasmon peak position of simulated nanoshells with thicker gold shell can be described by accounting phase retardation effects. However, while the particle geometry is fixed at a suitable value such that quadrupole and higher order components of the scattered field can be negligible.

7.4 Plasmon Hybridizations Theory in Nanoshells

As it has been demonstrated in prior section, the plasmon resonant frequencies of a nanoshell can be fine-tuned across the visible and near-infrared regions of the spectrum by tailoring the core-shell dimensions. The geometry-dependent nanoshell plasmon resonances and in general the extinction spectra calculated using Mie theory could be explained in terms of the plasmon hybridization model. In fact, Plasmon hybridization theory is a meso-scaled electromagnetic analogy of molecular orbital theory, which has been developed to theoretically calculate the nanoshell plasmon bands [4,5].

In order to comprehend this theory, consider a thin planar metal layer surrounded by a dielectric medium. Under particular circumstances, the excitation of the surface plasmon of this structure is permitted [6]. Due to the coupling among two boundaries of the mentioned structure, there is possibility to observe splitting of the surface plasmon into two eigenmodes as described by following equation.

$$\omega_{\pm}^2 = \omega_p^2 \frac{1 \pm e^{-kd}}{(\varepsilon_0 + \varepsilon_s) \pm e^{-kd}(\varepsilon_0 - \varepsilon_s)} \qquad (7-1)$$

Here ε_s is frequency dependent, complex dielectric function of shell material and k is the wave-vector of the travelling light. A similar splitting of the plasmon resonances into eigenmodes has been predicted for a spherical nanoshell, resulting from the difference in polarization between the particles of shell and core surfaces [6]. In order to indicate the response of nanoshells to irradiation of electromagnetic field, a fully quantum mechanical model based on a semi-classical approach has been developed, recently [7,8]. For a spherical core-shell particle this approach predicts two divided plasmon oscillation modes consisting of a symmetric and an anti-symmetric

oscillation. Figure 7-3 shows how the presence of these two energy modes of a dielectric-metal structure arising from the core-shell structure. The energies of these two modes are derived by following expression.

$$\omega_{l\pm}^2 = \frac{\omega_B^2}{2}\left[1 \pm \frac{1}{2l+1}\left(1+4l(l+1)\left(\frac{a}{b}\right)^{2l+1}\right)^{1/2}\right] \qquad (7-2)$$

Where ω_B denotes the surface plasmon energy and l refers to the multipolar symmetry of the plasmon mode. Also, a and b indicate the inner radius and the outer radius of the nanoshell structure, respectively. By applying this model, the ω_{l-} is assigned to the lower energy symmetric or "bonding" plasmon mode, while ω_{l+} is assigned to the higher energy anti-symmetric or "anti-bonding" plasmon mode [9]. In fact, equation (7-2) provides the possibility to predict the relative positions of these two modes, in which the anti-symmetric mode is located at higher frequencies with respect to the symmetric mode. This arises due to the higher level of excitation energy needed to oppositely polarize the different surfaces of the metal shell.

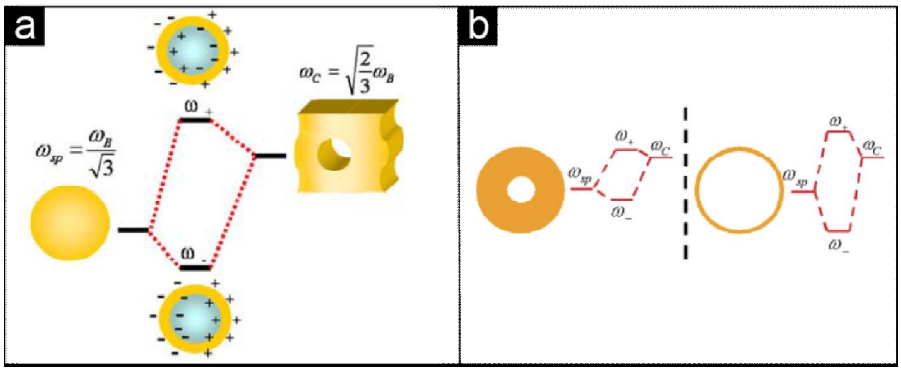

Figure 7-3 (a) Energy level diagram representing plasmon hybridization in metal nanoshells resulting from interaction among sphere and cavity plasmons. The two hybridized plasmon modes are an anti-bonding plasmon (ω_+) and a bonding plasmon resonance (ω_-). **(b)** The sketch of nanoshell plasmon energies dependence on the strength of the interaction between the plasmons of the sphere and cavity shell, determined by the thickness of the metallic shell. (Regenerated from reference [9]).

In sphere-cavity physical model demonstrated in Figure 7-3(a), the electromagnetic excitation at inner and outer surfaces of metallic shell are considered as cavity and sphere plasmons, respectively. The plasmon resonance of the nanoshell particle is the result of the hybridization of the plasmons corresponding to sphere and cavity subunits. The cavity plasmon frequency can be expressed as $\omega_{C,l} = \omega_B[(l + 1)/(2l + 1)]^{1/2}$ and the sphere plasmon has a vibration frequency $\omega_{s,l} = \omega_B [(1)/(2l + 1)]^{1/2}$. Indeed, in a nanoshell the deformation fields associated with the cavity and sphere plasmons introduce surface charges at both the inner and

outer boundaries of the shell (Figure 7-3(a)). These surface charges couple the sphere and cavity modes, resulting in hybridized plasmons [10].

Therefore, the demonstrated geometry-dependent nanoshell plasmon resonances originate from the interaction between the essentially fixed frequency plasmon response of a sphere and that of the cavity. The Strength of the hybridization between the sphere and cavity plasmons of a nanoshell is determined by the difference in their energies $\omega_{C,l}$ and $\omega_{s,l}$ as a function of metallic shell thickness (Figure 7-3(b)). This fact can be experienced by the calculating the plasmon field of a nanoshell, respect to the variation of the metal shell thickness. The simulation results for local electric field profiles of nanoshells with geometries mentioned in section 7.3 are illustrated in Figure 7-4.

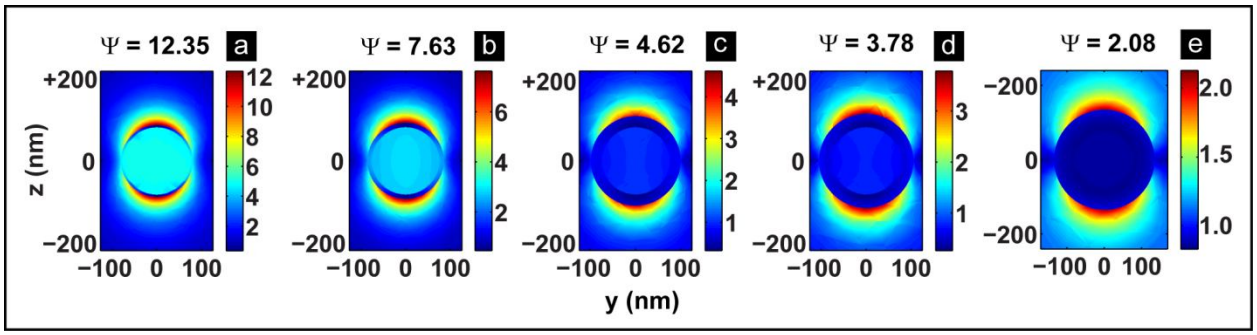

Figure 7-4 Simulation results of the plasmon field of nanoshell particles with diameter of the silica core of 150 nm shell thickness of **(a)** 5 nm, **(b)** 10 nm, **(c)** 25 nm, **(d)** 30 nm and **(e)** 60 nm. The enhancement of the hybridized fields is observed by increasing core radii to shell thickness ratio.

As these results show for thinner metallic shells the plasmonic field surrounding meso-scaled structure is enhanced. In fact, for a higher ratio of core diameter to metallic shell thickness, the strength of plasmon hybridization in nanoshell structure is amplified. Interestingly, the observed behaviors in simulation results of nanoshells are consistent with the obtained simulation results for the hybridized plasmon fields and extinction cross sections of multimeric nanostructures. Similar to the observed effects in nanoshells, stronger plasmon hybridization effects in multimeric nanostructures have pushed the extinction bands peak position to the higher wavelength (see the simulation results demonstrated in section 6.4.3).

7.5 Photophysical Characterizations of Plasmonic Nanoshells

Similar to the investigation procedure which has been treated in nano-scaled samples, a systematic characterization has performed on both main (RhB dye doped core-shell nanoshells) and reference (dye doped silica cores) samples. The assessment process is started with

spectroscopy characterizations in order to extract the extinction band of plasmonic nanoshells. Figure 7-5 illustrates the acquired plasmon band of the prepared meso-scaled structures. Indeed, well optimized ratio of core diameter to metallic shell thickness leads to merely presence of the dipolar mode, which is presented at 540 nm.

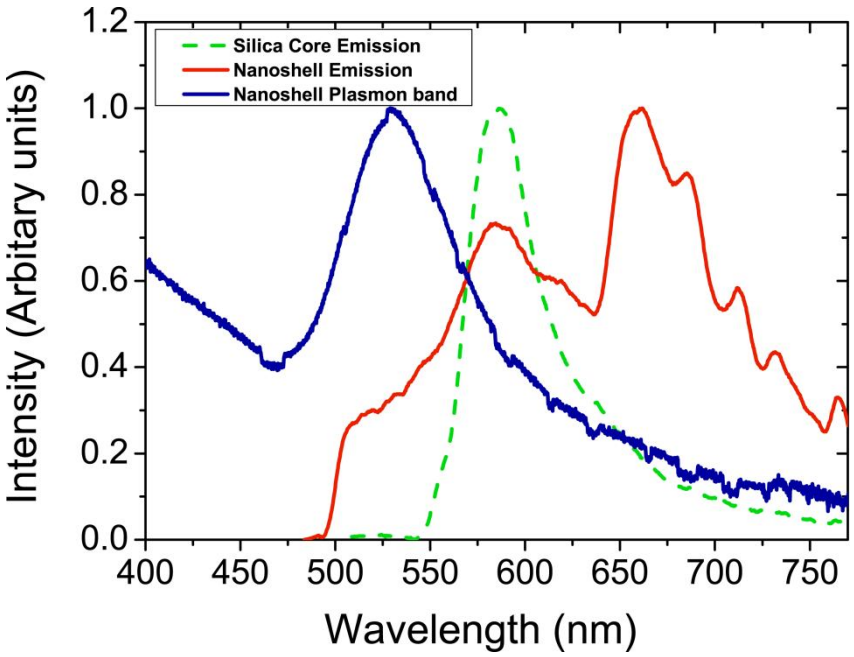

Figure 7-5 Extinction cross section of plasmonic nanoshell (blue dotted curve), emission of RhB dye molecules functionlazied in Silica cores (green dashed curve) and emission of RhB gain embeded in Silica cores of concentric nanoshells (red solid curve).

In addition, the steady-state experiments results concerning the presented dye molecules in both main and reference samples are reported. The normalized emission spectrum of RhB dye molecules encapsulated in silica spheres is demonstrated with green dashed line in Figure 7-5. The excited sample at 400 nm results an emission maximum at 586 nm. The spectral overlap of fluorophore emission with plasmon band of nanoshells satisfies the necessity for the occurrence of resonance energy transfer processes. However, as it showed in Figure 7-6 the obtained spectrum of encapsulated dye molecules in silica core is different from that of RhB dye molecules dissolved in ethanol. Such broadening of emission band of doped fluorophores which cannot be explained by concentration difference [11], indicates that the energy levels of the RhB molecules have been affected by encapsulating in silica spheres and that there is self-quenching by non-radiative energy transfer between active molecules.

Furthermore, the red solid curve in Figure 7-5 is related to photoluminescence of the functionalized fluorophores in cores of plasmonic nanoshells. The pump pulses at 400 nm promote the molecules of gain material to the excited state in the presence of excited hybridized

plasmon modes of metallic layer. The spontaneous emission properties of doped dyes in main sample are completely different from that of the reference sample. Not only the emission peak at 586 nm is quenched and broadened respect to that of doped dye in silica cores, but also the second emission band is appeared, which has strongly red shifted respect to the intrinsic emission band. The presence of this enhanced PL band can be explained according to the presented plasmon hybridization effect which happens between plasmon response of a sphere and that of a cavity. By considering $\omega_B = 6.7\times 10^{14}$ S^{-1} and approximate inner radius a=75 nm and the outer radius b=100 nm of the gold shell, the splitting of the plasmon modes of synthesized nanoshells results a lower energy band at $\omega_{-}\sim 2.6\times 10^{14}$ S^{-1} (λ_{-}=1150 nm) and higher energy band at $\omega_{+}\sim 6.17\times 10^{14}$ S^{-1} (λ_{+}=486 nm). Take into account that the lower energy plasmon mode (λ_{-}=1150 nm) interacts strongly with the incident optical field, while the other mode (λ_{+}) interacts weakly and in the case of gold is further damped by interband transitions at energies above the d-band to Fermi energy optical transitions at approximately 2.3 eV [9].

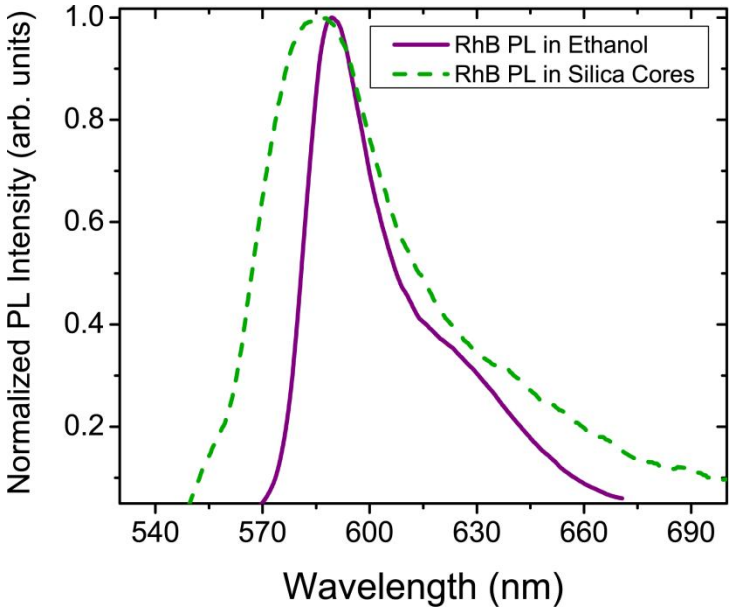

Figure 7-6 Emission spectra of RhB dye molecules dissolved in ethanol solution (purple solid line) dispersed in silica core (green dashed line).

Therefore, the presence of the notified strong lower energy band can lead to modify the quantum energy levels of encapsulated dye molecules in silica core of the nanoshells, resulting in a new enhanced emission band in higher wavelength, respect to the main emission band. The appearance of such emission band grows the motivation to study loss compensation effects over plasmonic gold layer in that wavelength range, as well.

7.6 Time-resolved Fluorescence Spectroscopy Results

As mentioned before, the results of the spontaneous emission decay rates are relavant to recognize the occurrence of different energy transfer processes, in particular DMPET process for absorptive losses mitigation in plasmonic structures. Similar to nano-scaled samples, the assessment of gain material lifetime has been performed. The time-resolved photoluminescence intensity decay rates of embed RhB dye molecules within plasmonic nanoshells silica cores are represented in Figure 7-7. Both systems are excited at a proper dye absorption wavelength of 460 nm with the Ti:Sapphire pulsed laser used in an ultrafast dynamic spectroscopy setup and emission decay rates are acquired at 580nm by means of a multi pronged spectrofluorimeter (see section 5.5 for details of the applied setup).

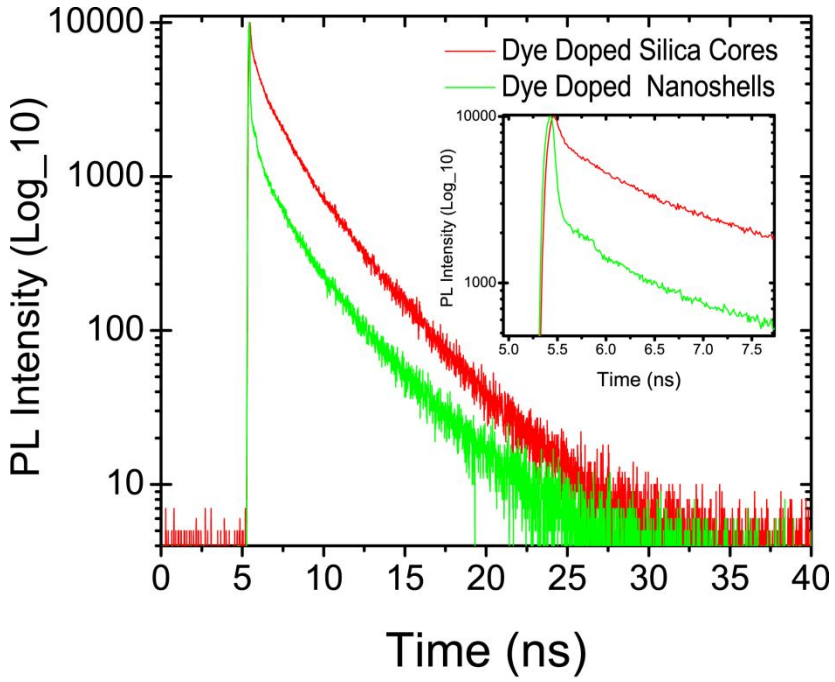

Figure 7-7 Time resolved intensity decay profiles of RhB doped silica cores dispersed in ethanol (red line) and RhB doped plasmonic nanoshells dispersed in ethanol (green line) excited at 480 nm. **Inset:** Zoom image of the time-resolved fluorescence decays in the first 8ns.

A tri-exponential decay function with three time constants has been used to fit the PL intensity decay curves of both reference and main samples as the best option to obtain precise decay times. In fact, in contrast to the time decay profile of RhB in ethanol which has been fitted by a single exponential function (see Figure 6-23), the requirement for applying a tri-exponential decay function for fitting decay curve of RhB molecules in SiO_2 spheres confirm the fact of modification in energy levels of encapsulated molecules. In fact, high density value of dye molecules in silica cores creates the possibility to form fluorophore multimers, resulting an

opportunity for FRET processes between dye monomers and multimers, and as well as among formed multimers with different geometries and sizes [12]. Therefore, the presence of FRET process opens new nonradiative pathways for emission quenching, yielding in lifetime quenching in two different rates of τ_1 = 0.14 ns and τ_1 = 1.28 ns. The last decay time τ_3 is equal with almost 3 ns which is similar to the decay time of pure RhB dye molecules dissolved in ethanol, reported in prior chapter in Figure 6-23. Thus, this part of decay time profile is related to that fraction of single dye molecules which are not participated in FRET process with the others.

In addition, the investigation of the decay time rates of encapsulated dye molecules in nanoshell cores reveal the quenching of their emission decay rates respect to those dyes in the absence of the metal shells. Both decay times of τ_1 and τ_2 have been shortened to values of 0.04 ns and 0.86 ns, respectively, while the decay time τ_3 has remained as like as that of reference sample. The observed 71% quenching of τ_1 and 33% quenching of τ_2 reveals the influence of plasmon resonance field of gold shell on decay times of fluorophore dipoles, which has been resulted due to the presence of DMPET process. Indeed the observed quenching in intrinsic emission band (maximum at 580 nm) of embedded dyes in nanoshells cores validates the mentioned clarification for such phenomena. The presented decay time of $\tau_3 \sim 3$ ns reveals that a portion of dye molecules have not participated either in FRET or DMPET quenching processes.

7.7 Pump-Probe Rayleigh Scattering Experiments

The observed resonant energy transfer process between embedded fluorophores in silica cores of nanoshells and metallic shell can lead to achieve loss compensated meso-scaled plasmonic structures. However, along with time-resolved spectroscopy measurements such issue should be confirmed by investigating the photphysics of gain-functionalized plasmonic nanoshells. For this reason, broadband pump-probe setup has been employed to perform optical transmission and Rayleigh scattering experiments (see chapter 5, section 5.5 for details of setup).

The accessibility of such setup permits to extract the transient absorption and scattering of system in a broadband wavelength range and at various excitation energies, either in the absence or in the presence of gain.

To corroborate our claim concerning gain induced optical transparency in nanoshells the optical transmission measurements were performed by exciting the sample at 400 nm by means of a Ti:Sapphire pulsed laser with repetition rate of 4 MHz and by probing it at various

wavelengths selected from broad band light source. Figure 7-8 shows the acquired normalized optical transmittance of nanoshells at different probe wavelength, changing from 520 nm to 740 nm at fixed power of excitation pump (160 mW). As it is evident from this graph, the optical transmission of plasmonic nanoshells only for particular wavelength range (670 nm – 750 nm) is enhanced. This resonance band where is partially overlapped with the enhanced emission band of embedded dye molecules, is located far from the plasmon absorption band of the particle. On the contrary, the probe wavelengths lying in the off-resonance band, where the SB of gold shell and intrinsic emission band of fluorophores are located, do not experience any increase in the transmission in certain value of gain.

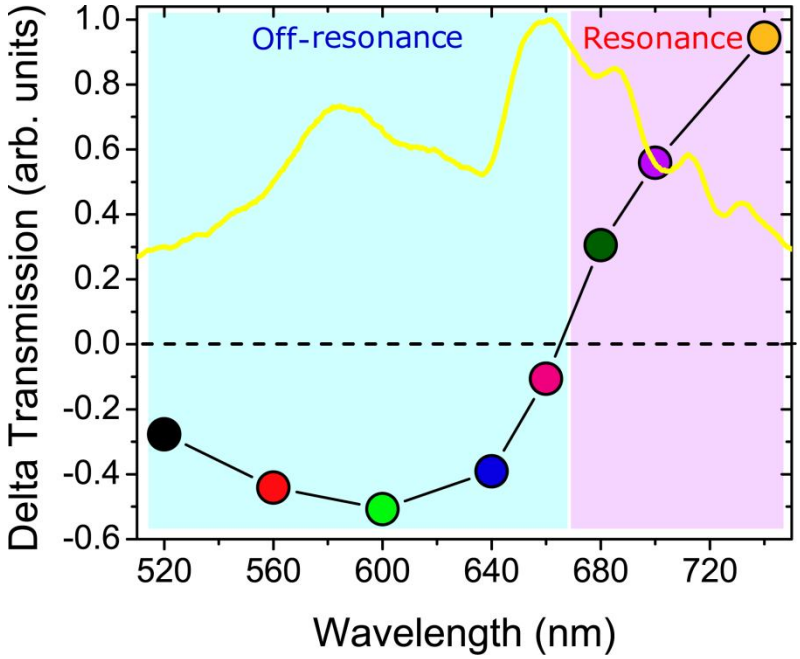

Figure 7-8 Selective optical transmission measurements over off-resonance and resonant probe wavelengths at fixed power of excitation pump.

The observed transmission enhancement and quenching can be ascribed by hybridized plasmon modes. In fact, resonance band is placed close to lower energy symmetric mode (w–), while off-resonance band is located in vicinity of higher energy anti-symmetric mode (w+). Thus, a strong interaction of symmetric plasmon mode with RhB dipoles results in a considerable transmission enhancement for resonance band wavelengths, while weak interaction of anti-symmetric plasmon mode with RhB dipoles yields in transmission quenching for wavelength belonging off-resonance band.

Furthermore, in order to investigate more precisely the observed gain induced optical transparency effect; other transmission measurements are performed in both resonance and off-

resonance regimes as the function of pump power. Figure 7-9 represents how only for a particular value of pump power the optical transparency of nanoshells can be enhanced. These results confirm that in order to overcome the absorptivity of hybrid nanoshells, even for wavelength band close to symmetric plasmon mode certain value of pump energy must be provided. However, for wavelengths which are located in vicinity of asymmetric plasmon mode increasing the power of pump cannot influence the imaginary part of the permittivity of the system.

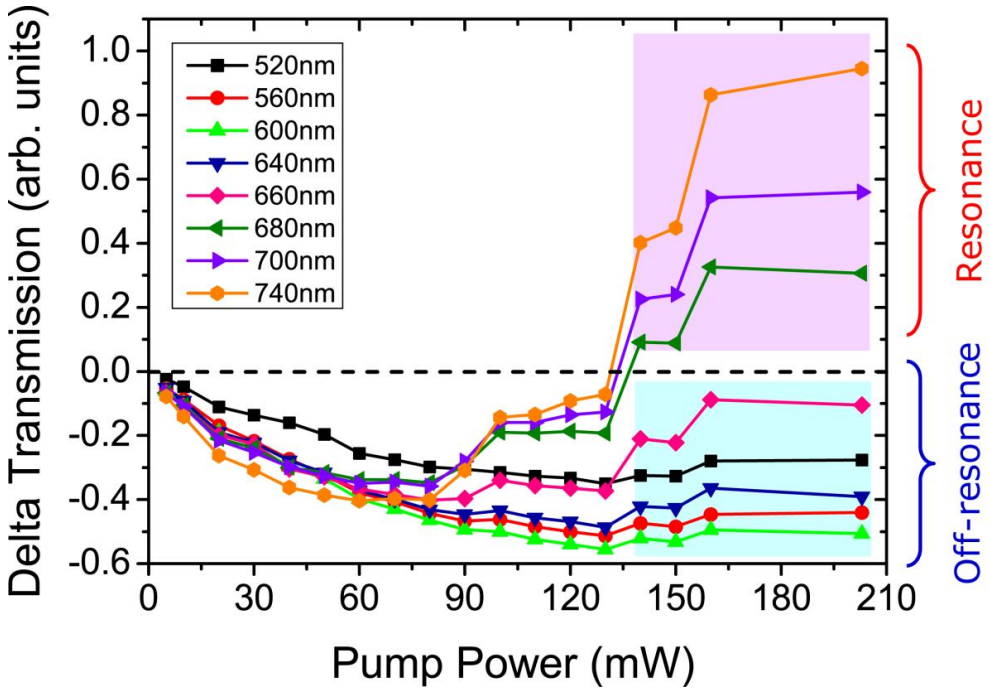

Figure 7-9 Normalized delta transmission for different probe wavelengths as the function of pump power.

In the order to complete the followed systematic investigation of loss compensation in prepared meso-scaled hybrid system, broad band scattering is acquired at both off-resonance and resonance regimes as a function of pump powers at different values. As the plotted results in Figure 7-10 shows that neither by increasing pump power nor by sweeping the wavelengths located at both off-resonance and resonance bands, any considerable modification in normalized scattering have been observed. This phenomenon can be ascribed to big size of meso-scaled particles which the scattered light cannot be considered anymore as Rayleigh scattering. However, the presence of constant values of scattering in particular in resonance band is an evidence of loss mitigation in this range of wavelength. This claim can be explained by following expression.

$$A\downarrow + Sc\,(cte) + Tr\uparrow = I_0\ (cte) \qquad (7-3)$$

Due to the constant intensity of the incident light, in order to satisfy the mentioned relation the enhancement of the transmission can be occurred if only the absorption of nanoshells is diminished.

The study on loss compensation process of gain-plasmon nanoshells revealed the influence of two hybridized plasmon modes to turn out unusual optical behaviors in both steady-state and time-resolved fluorescence spectroscopy results. But, the pump-probe studies have shown that the optical loss of this meso-scaled system can be compensated, as well. However, such optical loss mitigation effects only can be observed in resonance wavelengths band which are located close to symmetric plasmon band of nanoshells.

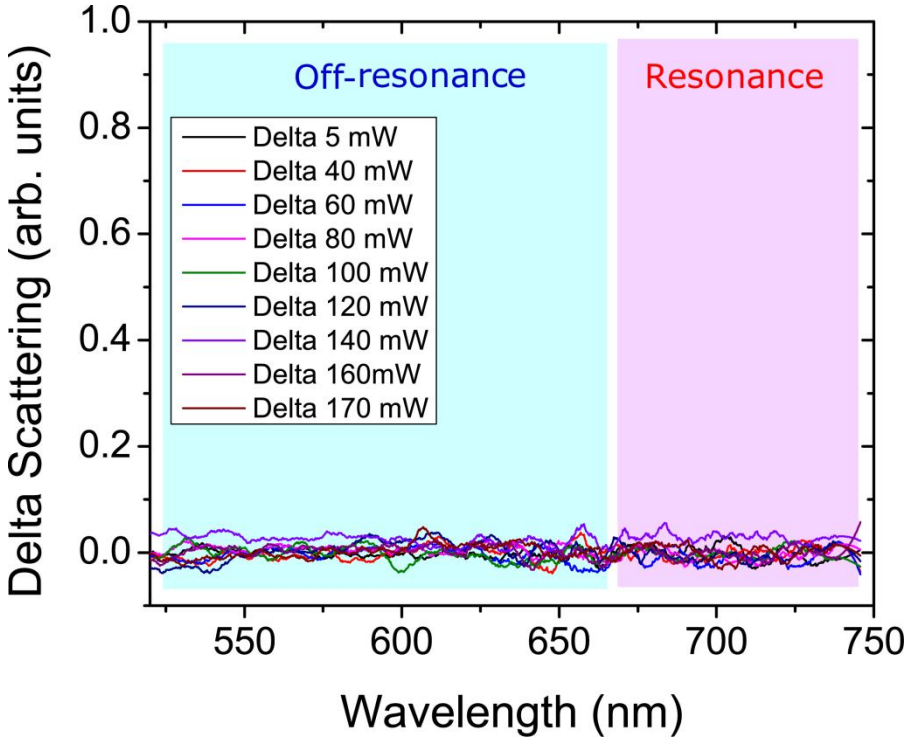

Figure 7-10 Broadband scattering measurements over off-resonance and resonant regimes. The constant values of scattering have been observed in both resonance and off-resonance bands at various amounts of pulsed pump power.

REFERENCES

1. P. B. Johnson, and R. W. Christy, *Phys. Rev. B*, **1972**, 6, 4370.
2. S. J. Oldenburg, R. D. Averitt, S. L. Westcott, and N. J. Halas, *Chem. Phys. Lett.,* **1998**, 288, 243.
3. Hu M, et al., *Chem. Soc. Rev*., **2006**, 35, 1084.
4. Y. Xia, and N. J. Halas, *MRS Bulletin* **2005,** 30, 338.
5. E. Prodan, C. Radloff, N. J. Halas, and P. Nordlander, "A hybridization model for the plasmon response of complex nanostructures," *Science*, **2003**, 302, 419.
6. H. Reather, "*Excitation of Plasmon and Interband Transitions by Electrons"*, Springer, Berlin, 1980.
7. E. Prodan,A. Lee, and P. Nordlander, *Chem. Phys. Lett.*, **2002**, 360, 325.
8. E. Prodan, and P. Nordlander, *Chem. Phys. Lett.***, 2002**, 352, 140.
9. H. Wang, D. W. Brandl, P. Nordlander, Halas, N. J., *Acc. Chem. Res.* **2007,** 40, 53.
10. E.Prodan, and P. Nordlander, *J. Chem. Phys.*, **2004**, 120, 5444.
11. J.Weber, Effect of Concentration on Laser Threshold of Organic Dye Laser, *Z.Physik*, **1973**, 258, 277.
12. E, Ippen, C. Shank, A. Dienes, *IEEE.j.Quan.Elect*., **1971**, 7,178.

Chapter 8

Optical Loss Mitigation in Macro-scaled Hybrid Systems

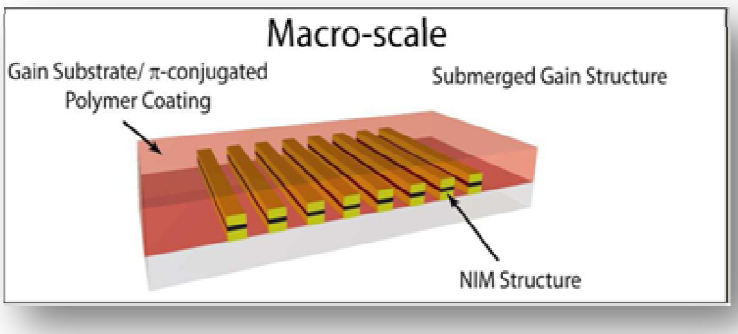

8.1 Introduction

After completing the goal of this research study throughout nano-scaled and meso-scaled gain-plasmon dynamics, the final stage is to investigate absorptive loss mitigation process over macro-scaled structures. In fact, fabrication of such structures which are bulk hybrid systems is a step forward towards achieving functional optical metamaterials. The progress in fabrication technologies such as electron beam lithography and chemical synthesis processes provide this opportunity to fabricate variety of hybrid systems in this spatial stage. The grown mixture of plasmonic nanoparticles and gain materials in macro-scaled channels of microfluidic devices is an appropriate example of macro-scaled hybrid systems. Recently, the progress in nano-chemistry offers versatile routes to design and fabricate engineered bulk composite materials soft in nature, which are relevant both for fundamental understanding and for technological applications. On the other hand, the studies of the interactions between luminescent semiconductor QDs and metal NPs have raised considerable interest due to the variety of

phenomena which have been observed in experimental investigations and theoretical studies. Incorporation of the core-shell QDs as gain material and spherical gold NPs as nano-resonators in a polymer plastic via a nano-chemistry route leads to fabrication of a bulk hybrid material, which exhibits nonconventional electromagnetic properties in the range of visible light.

Among the different organic polymers, polydimethylsiloxane (PDMS), for the first time, has been selected as a suitable host for simultaneous embedding NPs and QDs, due to its chemical inertness, mechanical flexibility, optical transparency in the visible and ultraviolet region, stability, high dielectric constant and breakdown field, and very importantly, a prompt processability, relevant also for integration in standard micro-fabrication processes. The prepared samples provide the possibility to incorporate colloidal emitting QDs into PDMS in close proximity of plasmonic NPs, without changing the pre-polymer mixture composition or processing temperature, by just playing with QD surface chemistry. In fact, only a very few examples can be found in the literature on the incorporation of pre-synthesized colloidal Au NPs or CdSe@ZnS QDs in a PDMS host matrix [1, 2]. Also their presented work reports a first example of a simultaneous dispersion of luminescent QDs and Au NPs in a PDMS host matrix, providing a plastic composite material with peculiar functional properties which can be promptly fabricated in different shapes, including thick films.

In this chapter steady-state fluorescence experiments along with time-resolved spectroscopy results are used to investigate cooperative interactions at a nono-scale level between metallic NPs as nano-resonators and CdSe@ZnS QDs as gain material, based on resonance energy transfer processes. Also, pump-probe experiments have been applied as the methods for studying the behavior of prepared systems in direction of optical loss compensation purposes.

8.2 Optical Characteristics of PDMS based Hybrid Systems

Here for this study, six samples have been prepared. Four samples have been employed as reference samples and the other two have been used as the main samples (Figure 8-1(a)). The first reference sample, which is labeled as sample (A) is simply a PDMS matrix, which can be used to account the physical properties of PDMS host matrix in different experiments. The second and third samples are incorporated gold NPs in PDMS host, but with two different concentrations of 1×10^{-6} M (sample (B)) and 3×10^{-6} M (sample (C)). The fourth reference

sample, labeled as sample (D), has been fabricated by dispersing core–shell CdSe@ZnS QDs in PDMS matrix. The last two samples are used as the main samples ((E) & (F)) in which they are PDMS plastics which contain the mixture of CdSe@ZnS QDs and the Au NPs. The concentration of QDs for both samples has been considered as same as sample (D), while the concentration of plasmonic NPs for sample (E) is equivalent with sample (B) and that of sample (F) is identical to sample (C).

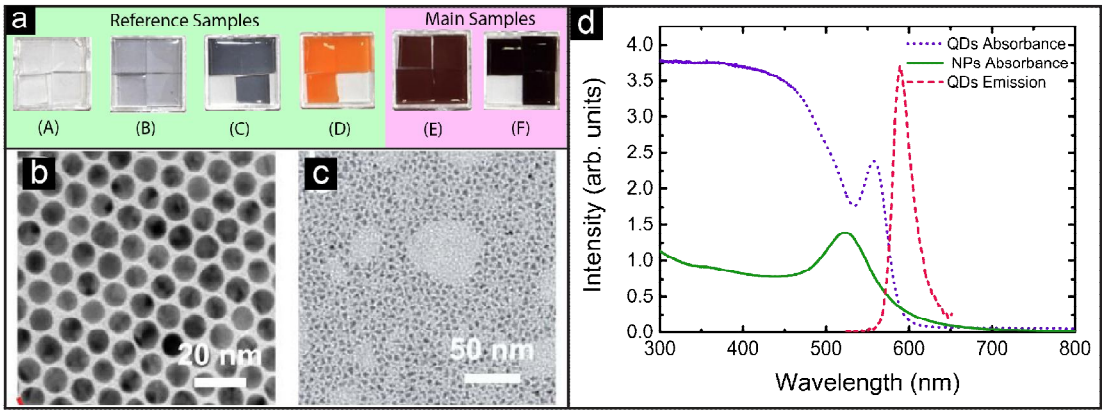

Figure 8-1 (a) Images of the reference and main samples. TEM micrographs of **(b)** Au NPs and **(c)** CdSe@ZnS QDs. **(d)** Absorption spectrum of Au NPs (green solid line), UV-vis absorption (blue dotted line) and PL emission spectrum of QDs (pink dashed line), both in hexane solution.

The prepared Oleylamine (OA) coated Au NPs were characterized by means of TEM analysis, which reveals a narrow NP size distribution with polydispersity of 6.5%. An example of preformed TEM analysis in Figure 8-1(b) shows synthesized gold NPs are spherical in shape and uniform in sizes with average particle size of 11 nm. In Figure 8-1(d) (blue line) the UV-vis absorption spectrum of the Au NPs dispersed in hexane exhibits a surface plasmon absorption band centered at 524 nm. The size of the Au NPs and QDs was suitably selected in order to achieve an effective overlap of the Au NP plasmon adsorption and QD emission signals. In addition, the synthetic and post-preparative procedure was purposely designed for obtaining a homogeneous dispersion of the nano-objects in the host polymer. In addition, the CdSe QDs have been chosen as core-shell nanocrystals, coated with higher band gap materials such as an epitaxial shell of ZnS. The presence of such surrounding shell leads to increase the stability of the NCs and as well as a remarkable charge carriers confinement inside the core, which results in increase in the emission property of the synthesized core–shell QDs [3].

The absorption spectrum of the dissolved CdSe@ZnS QDs in hexane solution with pink solid line is demonstrated in Figure 8-1(d), which illustrates the presence of a first excitonic peak centered at 558 nm, which corresponds to 3 nm sized particles, as theoretically calculated [4].

The calculated size of NCs is confirmed by the TEM micrograph showed in Figure 1-8(c). In addition, the photoluminescence spectrum of the related sample in hexane clearly highlights a narrow emission band centered at 589 nm (red dashed line in Figure 8-1(d)), whose small bandwidth is characteristic of the highly level mono-disperse sample. However, the position of the QDs emission in UV-vis spectrum depends on the concentration of the NCs in solution. Figure 8-2 shows that the peak position of the QDs emission is shifted to higher wavelength with respect to increasing of their concentration in $CHCl_3$ solution, due to the possibility for the formation of QDs multimers. Since the peak position of QDs PL is not red-shifted linearly versus to increase of concentration, hence an exponential function has been used to fit the acquired data. It is worth to mention that similar to optical behavior of organic dye molecules, the modification of chromophore concentration cannot affect the bandwidth of emission spectrum.

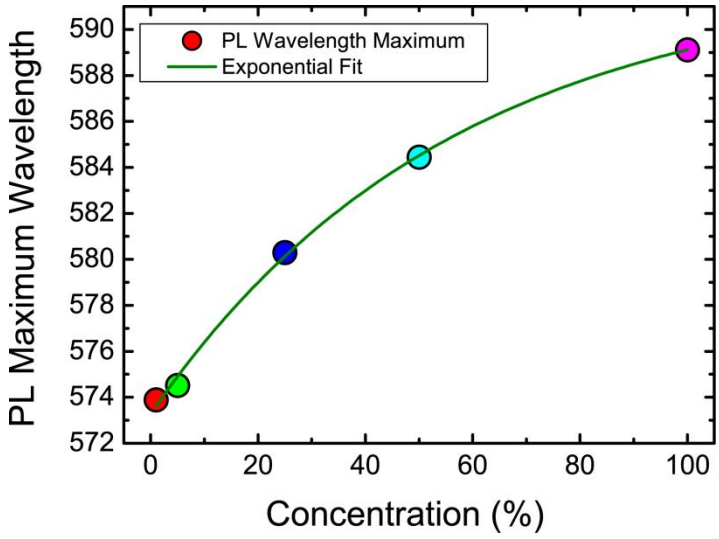

Figure 8-2 Exponentially increase of maximum peak wavelength of QDs emission with respect to their concentration in $CHCl_3$ solution.

8.3 Steady-State Fluorescence Spectroscopic Results

Incorporating of opto-plasmonic nanoresonators and active QDs into a reconfigurable soft matrix provides the possibility to exploit cooperative interactions at nano-scale levels. This fact along with the observed overlap between the PL spectrum of core-shell NCs and SP band of Au NPs are two essential conditions for occurring resonance energy transfer process between QDs and NPs. But in order to provide the convincing evidences concerning a presence of an optical loss mitigated material, such as the other studied systems, performing an organized investigation on optical properties of the fabricated material is essential. In this regard, steady-state spectroscopy needs to be performed on both main samples ((E) &(F)) and as well as on

reference sample of (D), in order to provide supports regarding modification of total photoluminescence of main samples respect to the reference one at the base of resonant coupling processes.

PL measurements of both main samples respect to reference sample (D) were performed by pumping them with a pulsed laser @ 355 nm at fixed pump energy and detecting the spectrum of emission with a broadband precise spectrometer (see chapter 5 section 5.4 for setup details). Figure 8-3 shows how the PL of core-shell QDs with maximum peak at 580 nm is quenched in both mixed samples of (E) and (F) with respect to the PL of the pure QDs in PDMS. However, the observed emission quenching in sample (E) is more significant with respect to that of sample (D) which contains lower concentration of gold nano-resonators.

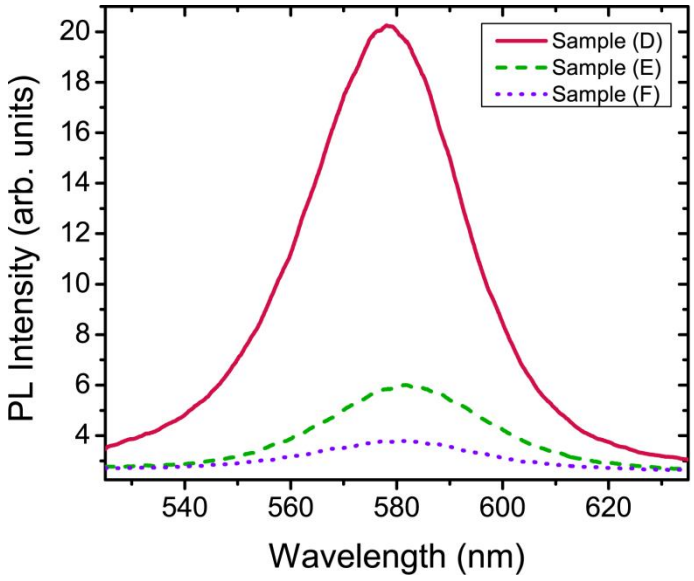

Figure 8-3 Fluorescence quenching of QDs in the presence of low concentration of Au NPs (dashed green line) and high concentration of Au NPs (dotted blue line) with respect to the pure QDs (solid red line).

The observed emission quenching in both mixed samples at a fixed point of pump energy can create this thought in mind that such PL quenching phenomena are simply originated from radiative absorption process by gold NPs. In order to clarify this point, the emission spectra of main samples have been measured with respect to reference sample by changing the energy of pumped pulses. Figure 8-4(a) represents the trends of the PL spectra of sample (E) in comparison to reference sample (D) as a function of the impinging energy/pulse. The quenching behavior of emission spectra related to the mixed QDs with Au NPs versus to change of pump energy is clear from this graph. In addition, in order to demonstrate a different PL quenching behavior of two samples, the emission maxima of QDs in both samples as a function of each investigated energy

value have been plotted in Figure 8-4(b). As this graph shows, while the emission intensity of the pure QD sample increases when the exciting light intensity increases, in the case of the mixed sample the ratio between emitted and exciting light intensity changes with different rate with respect to the case of pure QDs. The same sorts of experiments have been performed on sample (F) which contains higher concentration of Au NPs in comparison to sample (E). As it is evident from Figure 8-4(c) and (d), high concentration of Au NPs influences the optical response of the QDs in a different way with respect to the optical behavior of sample (E), in which a stronger emission quenching in all the investigated energy points is occurred. However, similar to sample (E), the rate of PL quenching is completely different in comparison to the pure QDs, in which light intensity of sample (F) remains unvaried.

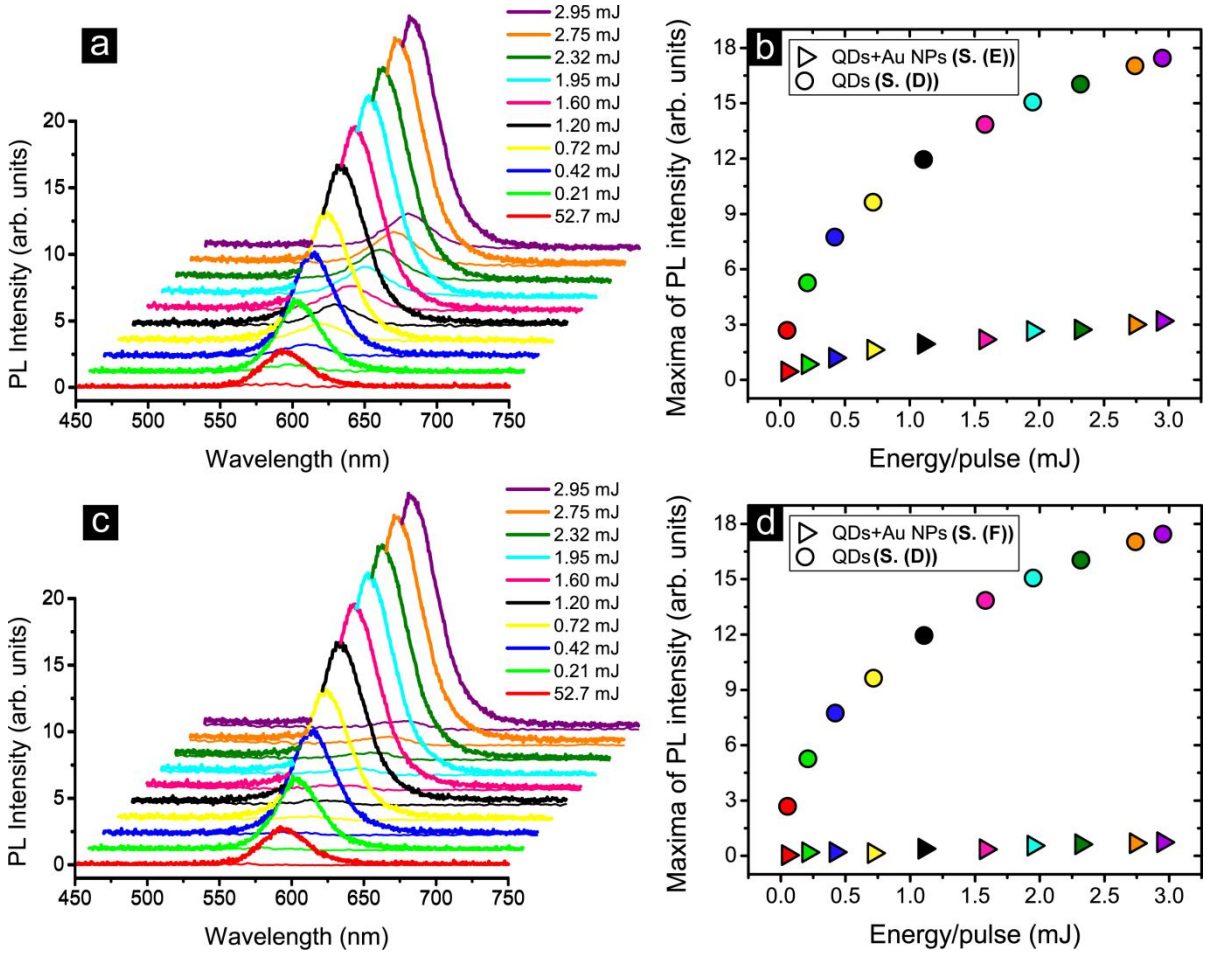

Figure 8-4 Emission spectra of QDs in the presence of Au NPs in **(a)** sample (E) and **(c)** sample (F) with respect to pure QDs (sample (D)). Optical behavior of the PL maxima of **(b)** sample (B) and **(d)** sample (F) with respect to sample (D) as a function of the incident pump energy/pulse. Dots refer to QDs only and triangles to the hybrid systems based on the mixed QD + Au NP.

The observed reduction behavior in PL light intensity of both main samples, can be correlated to the influence of the consisted components absorption (Au NPs and QDs) and as

well as the nonradiative resonance coupling between plasmonic Au NPs and emitting core-shell QDs. In order to clarify this point and provide persuasive explanations for the observed optical phenomena a time-resolved spectroscopy and quantum yield measurements have been performed. The results of these experiments on both hybrid systems as compared to the reference sample (D) are demonstrated in next section.

8.4 Quantum Yield Measurements and Time-resolved Spectroscopy Results

In order to explain the physical mechanism behind the experienced optical behaviors regarding PL quenching process in both main samples, performing the emission intensity decay rate quantum yield measurements are unavoidable. By combining the results of these two characterizations it is possible to inquire the participations of radiative and nonradiative decay rates in the modification of PL intensity and lifetime of the synthesized materials in PDMS host matrix with respect to the pure QDs dispersed in reference sample (D).

The first set of experiments was focused on the measurement of the fluorescence quantum yield of pure QDs (sample (D)) and QDs in the presence of the low concentration (sample (E)) and high concentration (sample (F)) of Au NPs in the PDMS matrices. As it has already been mentioned, the fluorescence quantum yield is defined as the ratio between the number of emitted photons through fluorescence and the number of photons absorbed. In other words, quantum yield gives the probability of the excited state being deactivated by fluorescence rather than by another non-radiative mechanism. Both hybrid systems and as well as reference sample are excited at wavelength of 375 nm, since at this wavelength the absorption of QDs as compared to Au NPs is significant (Figure 8-8). Furthermore, the emission spectra of reference and both main samples are acquired at 580 nm, which is the wavelengths correspond to the maximum emission spectrum of CdSe@ZnS QDs in main and reference systems. It is worth to mention that for measuring the quantum efficiency of sample (D), sample (A) (PDMS matrix) is used as reference sample, while in the case of main samples (E) and (F), the reference samples are applied as sample (B) and (C), respectively, which are NPs dispersed in PDMS matrix at the corresponding concentration of main samples (see Data analysis in the chapter 5, section 5.3.3).

The measured quantum yields of mixed QDs with gold NPs in both hybrid systems are decreased remarkably with respect to the pure QDs dispersed in PDMS matrix. However, the observed quenching of quantum yield in sample (F) is more pronounced as compared to that of

sample (E). Such fact can be also inferred by comparing Figure 8-4(c) with the plotted results in Figure 8-4(D). In fact, the quantum efficiency of sample (D) is decreased by more than 20 times, moving from 16.5%, down to only 0.8% when QDs are mixed with low concentration of Au NPs, while mixed QDs with high concentration of Au NPs experiences 40 folds lowering of quantum efficiency with respect to reference sample (D) by changing from 16.5% to the value of 0.4%.

Time-resolved fluorescence spectroscopy was carried out on both composite systems of (E) and (F) and as well as on reference system of (D), in order to obtain insight into possible QD–NP coupling and energy transfer processes. Fluorescence lifetime measurements indicate a faster decay of QDs PL in the presence of Au NPs, consistent with a strong resonant coupling between QDs and the NPs surface plasmons. The TCSPC data were obtained by exciting the two samples at 375 nm and emission intensity was recorded at 580 nm for reference and QD–Au NP mixed samples (see section 5.3.2 for setup details). The acquired results of time-resolved fluorescence spectroscopy for pure QDs and in the same condition for the hybrid systems of (E) and (F) are demonstrated in Table 8-1.

Samples	$\lambda_{exc/em}$ (nm)	Reduced χ^2	τ_1 (ns) (α_1/%)	τ_2 (ns) (α_2/%)	τ_3 (ns) (α_3/%)
Sample (D)	375(580)	1.15	-	4.39 (21)	61.7 (79)
Sample (E)	375(580)	1.05	1.43 (34)	5.80 (13)	34.7 (52)
sample (F)	375(580)	1.05	1.28 (35)	6.30 (14)	37.5 (51)

Table 8-1 Quantum yields and time resolved fluorescence decay times of hybrid systems of QDs mixed with two different concentrations of Au NPs (samples (E) & (F)) with respect to the pure QDs solutions and dispersed in PDMS host matrix.

In order to study the possible modification in the optical behavior of dispersed quantum dots in PDMS medium, the decay time of QDs dissolved in hexane solution has been measured. The obtained results of that measurement could be fitted by using a single exponential function, giving in a lifetime of 10.3 ns (χ^2=0.985). However, the presence of QDs in PDMS matrix results in two decay time values that can be extracted by applying a bi-exponential fitting function (Figure 8-5). The appearance of two lifetime components can be explained by the possibility for the formation of QDs micro-aggregates [5]. In fact, aggregated chromophores present longer lifetime as compared to mono-dispersive ones. In such condition, by considering different sizes of the formed micro-aggregates, the FRET mechanim among them can yields in the second

decay time compononent. The next set of decay time measurements confirm the presence of such micro-aggregates of QDs in PDMS matrices of all three samples of (D), (E) and (F).

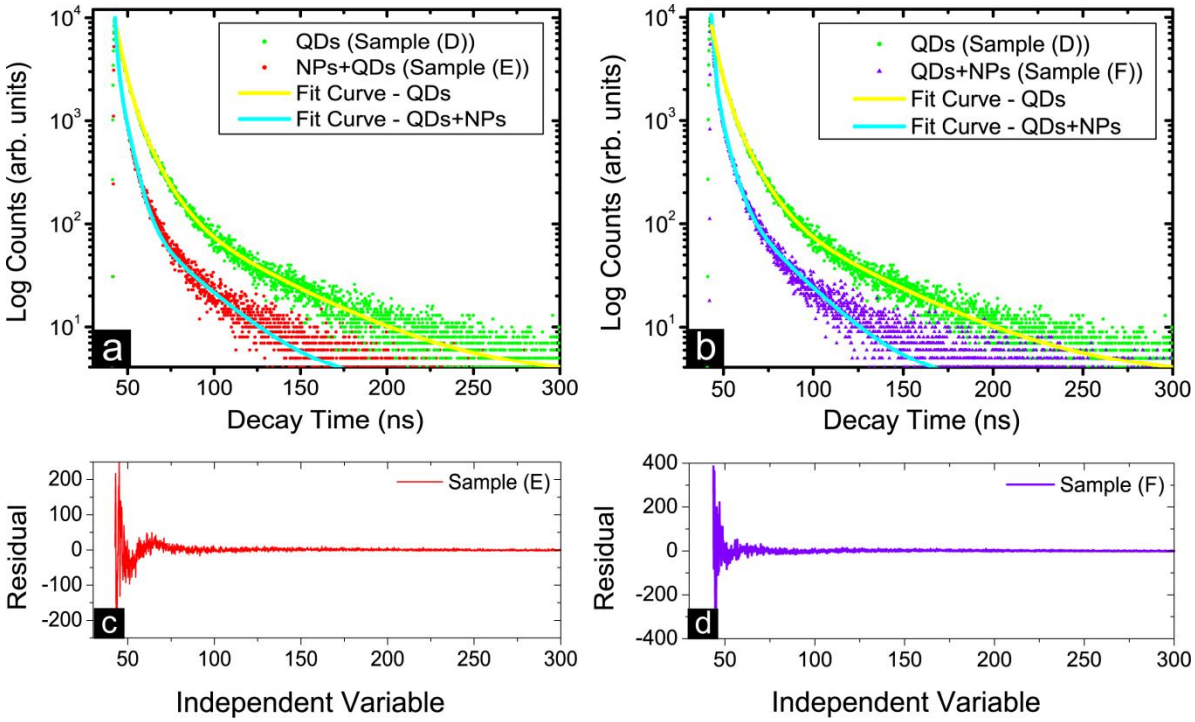

Figure 8-5 Time-resolved fluorescence spectroscopy results and applied tri-exponential fit functions for **(a)** sample (E) **(b)** Sample (F) in comparison to decay profile of sample (D). The observed difference in both decay times slop is the signature for the occurrence of the nonradiative energy transfer process among Au NPs and luminescence core-shell QDs. In addition, the residual of the decay fit for both **(c)** sample (E) and **(d)** sample (F) are demonstrated.

The recorded time-resolved data of both hybrid systems requires to be effectively fitted by a multi-exponential function, namely three exponential decay components are necessary, consistent with the relevant literature [6,7]. A typical examples of fitted results for the acquired TCSPC data of samples (E) and (F) in comparison to pure QDs dispersed in PDMS (sample (D)) are represented in Figure 8-5 (a) and (b), respectively. Also, the corresponding residual for the decay fit of both QD–Au NP mixed samples are demonstrated in Figure 8-5(E) and (F). In definition of these three measured lifetimes, the shortest decay time (τ_1) could be related to the presence of DMPET process among Au NPs and core-shell NCs within PMDS matrix. The comparison of τ_1 for both composite systems shows that the sample (F) with higher concentration of Au NPs experiences a faster decay rate as compared to sample (E), expressing a stronger resonant interplays between Au NPs and QDs in sample (F). The intermediate lifetime value (τ_2) is a quenched luminescence originated by an energy transfer between the nearest-neighbor QDs aggregates, which both are still in the same range of τ_2 for pure QDs. Finally the

longest decay time (τ_3) is originated from those agglomerated QDs which are not participated in any kind of RET processes neither FRET nor DMPET. The values of lifetime τ_3 are almost equal for both (E) and (F) systems. However, the reduction of this decay time of both main samples as compared to that of reference sample shows that simultaneous presence of Au NPs and QDs in PDMS matrix reduce the chance of the formation for very big aggregated structures of QDs.

8.5 Radiative and Nonradiative Decay Rates Enhancement Factors

Here, the role played by the presence of Au NPs in the de-excitation paths of the QDs can be effectively inferred. In fact, calculating the average lifetime by applying equation (3-8) can provide information concerning the rate of the RET within QDs-NPs in both plasmonic hybrid systems. For the QDs in PDMS (sample (D)) an average lifetime value $<\tau>$ of 60.6 ns was calculated, while for the samples containing less concentration (sample (E)) and more concentration (sample (F)) of plasmonic resonators a $<\tau>$ value of 32.7 ns and 35.4 ns was found, respectively. Such evidence clearly suggests that the PL quenching in the presence of Au-NPs is related to a faster relaxation dynamics, due to the presence of additional non-radiative de-excitation channels. Therefore a mechanism of resonant energy transfer from QDs to Au NPs for the QDs in proximity with metal NPs can be thought to take place.

Samples	$<\tau>$ (ns)	Φ (%)	k_r(1/s)	k_{nr}(1/s)	k_t(1/s)
Sample (D)	60.6	16.5	27×10^5	1.38×10^7	1.65×10^7
Sample (E)	32.7	0.8	2.4×10^5	3×10^7	3.06×10^7
sample (F)	35.4	0.4	1.1×10^5	2.8×10^7	2.82×10^7

Table 8-2 Calculated values of the average lifetime, total, radiative and nonradiative decay rates of reference sample (D) and main composite systems (E) and (F).

However, in order to reveal the physical mechanisms behind the modifications of the PL intensity, quantum yield and lifetime of the QDs in both composite systems with respect to that of the reference system, a precise investigation can be performed by calculating radiative and nonradiative decay rates. Table 8-2 shows the obtained values for the calculated decay rates by applying equations (3-12) and (3-13). The acquired data can be used to interpret the observed optical behavior of hybrid samples such as quenching in their photoluminescence or quantum efficiency with respect to each other and as well as to the reference one.

In order to describe these processes more quantitatively, the PL quenching of the QDs mixed with Au NP respect to the equation (4-21) is written as:

$$\eta_{PL} = \frac{\mathrm{R}_{ex}\,\Phi}{\mathrm{R}_{ex0}\,\Phi_0} = \eta_{ex}\frac{\eta_r}{\eta_t} \qquad (8-1)$$

where the component enhancement factors can be defined as

$$\eta_{ex} = \frac{\mathrm{R}_{ex}}{\mathrm{R}_{ex0}}, \qquad (8-2)$$

$$\eta_r = \frac{k_r}{k_{r0}} \qquad (8-3)$$

and by considering $k_t = k_r + k_{nr}$ the enhancement factor of total decay rate is referred as

$$\eta_t = \frac{k_t}{k_{t0}} \qquad (8-4)$$

Here in these equations, subscript 0 always refers to the bare QD. Within an order of magnitude, we may equate the excitation and radiative enhancements,

$$\eta_{ex} = \eta_r \qquad (8-5)$$

which leads to

$$\eta_{PL} = \frac{\eta_r^{\,2}}{\eta_t} \qquad (8-6)$$

Also, the enhancement factor of nonradiative decay rate can be extracted from the following equation.

$$\eta_{nr} = \frac{k_{nr}}{k_{nr0}} \qquad (8-7)$$

As it is evident from Table 8-2, the radiative decay rate in both main samples has reduced respect to the reference sample (D), while as a result of RET processes including both FRET and DMPET mechanisms within composite systems the rate of nonradiative decay rates has increased. By applying equations (8-3) and (8-7), the enhancement factors of radiative and nonradiative decays for sample (E) are calculated as 0.09 and 2.17, respectively, whereas, these parameters for sample (F) are extracted as 0.04 and 2.03. As it is clear from these values, while the decrease of radiative decay rate can increase lifetime value, the more prominent increase of the nonradiative decay rate outweighs this effect, so that in the case of both composite samples the average lifetime of the QDs has reduced. Such modification in average lifetime magnifies the

influence of the reduced radiative decay rate resulting in reduction of the quantum efficiency of both samples (E) and (F). Moreover, by referring to equations (8-4) and (8-6), the enhancement factor of emission intensity is calculated as 4.4×10^{-3} for sample (E) and for 9.4×10^{-4} sample (F). The obtained values confirm the observed quenching in emission intensity of QDs incorporated in samples (E) and (F) in comparison to sample (D). These sentences can be made much clear by the following expression.

$$k_r \downarrow \quad \tau_{QDs-NPs} \downarrow\downarrow \quad \Rightarrow \quad \Phi_{QDs-NPs} \downarrow \quad PL_{QDs-NPs} \downarrow$$

In addition, the calculated values of enhancement factor of emission intensity for both hybrid systems are consistent with the observed more pronounced PL quenching of sample (F) with respect to sample (E) (Figure 8-3). On the other hand, the enhancement factor of nonradiative decay rate of sample (F) is almost equal with respect to sample (E). This means that in the designed systems, the increase in the concentration of Au NPs has not modified nonradiative decay rate through energy transfer processes. This fact can be verified by inferring energy transfer efficiency parameter in both prepared hybrid systems according to the equation (4-8). In fact, this parameter creates an image of the RET processes including FRET and DMPET among emissive QDs and plasmonic NPs incorporated in PDMS matrix. This factor for sample (E) and (F) is calculated as 0.46 and 0.41, respectively. The comparable values of this parameter for both systems confirm again this fact that all of the plasmonic quenchers in sample (F) could not be participated in RET processes with QDs. This can arise from this matter that the concentration of QDs for such amount of plasmonic nano-resonators is not enough to provide the possibility for resonant coupling with all of NPs. Thus, the observed more pronounced quenching in PL and as well as quantum yield of sample (F) respect to sample (E) is originated only from the reduction in radiative decay rate of the system. Such strong reduction in radiative decay rate of sample (F) can be explained by absorptive nature of Au NPs and enhanced absorbance of QDs in the presence of Au NPs in sample. The enhancement of the absorption cross sections related to QDs that are presented in sample (F) will be explained in section (8-8).

8.6 Time-resolved Spectroscopy as a Function of Emission Wavelength

A second set of experiments was performed by investigating the two samples with time-resolved fluorescence spectroscopy as a function of the emission wavelength. Measurements were performed at five emission wavelengths ((a) = 548, (b) = 558, (c) = 575, (d) = 593 and (e) =

602 nm) to clarify the behavior of decay times when the emission wavelength moves towards the region of higher overlap with the plasmonic band of gold NPs in PDMS. Figure 8-6 (a) and (b) present TCSPC data obtained by exciting the sample of pure QDs (D) and the mixed sample (F) at 375 nm, and recording the emission intensity at different wavelengths. An increase in the decay time moving from the high energy to low energy region is measured for a sample of QDs in PDMS, consistent with the occurrence of the energy transfer mechanism from smaller to larger nanocrystals inside the same QD population. [8] Such a phenomenon corroborates the presence of micro-aggregates of QDs inside of the soft matrix, allowing the larger QDs to absorb the emission of the smaller ones, at higher energy by means of nonradiative FRET process. The same behavior is observed in the presence of metal NPs (Figure 8-6 (b)), along with a generally faster decay of the PL in the presence of Au NPs, as observed before (Figure 8-7(b)). This occurrence evidences how the mechanism of energy transfer among QDs co-exists with the plasmonic coupling with the metal NPs.

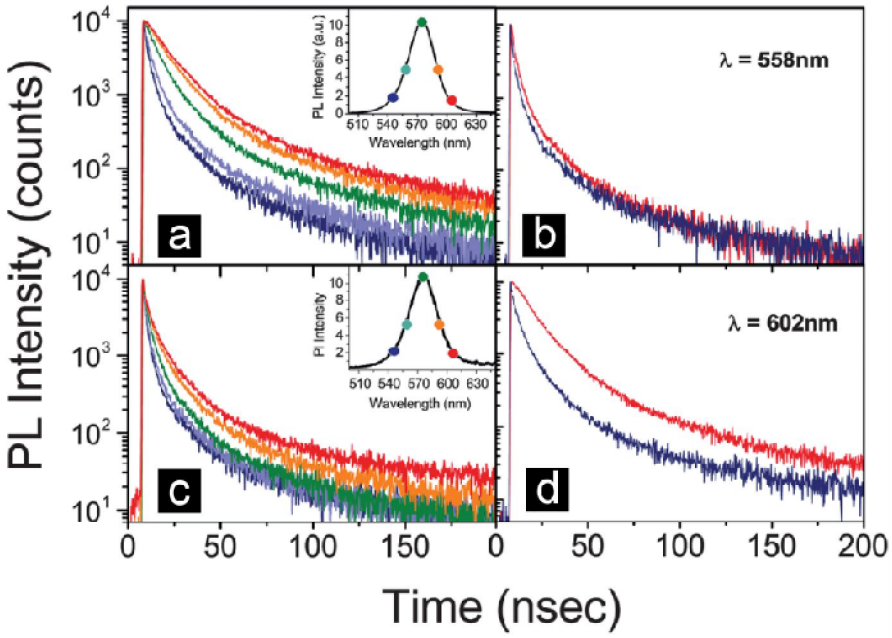

Figure 8-6 Time-resolved fluorescence intensity decays as a function of emission wavelength. **(a)** QDs **(b)** QDs + Au NPs in sample (F). The modification of the decay rate profiles in sample (F) as compared to sample (D) by detecting emission at **(c)** 558 nm **(d)** 602 nm. In (c) and (d) the red line refers to QDs, while the blue line refers to QDs + Au NPs in sample (F).

Figure 8-6(c) and (d) represent the same decay profiles at only two emission wavelengths (558 nm and 602 nm), in order to make a direct comparison between two samples. On moving towards the overlapping region between the QD emission and Au NP absorption band (both in PDMS), a larger gap between the two decay curves (red and blue lines) can be observed as

wavelength increases. Such an effect can be due to a stronger coupling off-resonance between the two systems when dispersed in the plastic matrix as demonstrated also by Komarala [9], due to a direct energy transfer from excitons in QDs to plasmons in Au NPs, which causes the rapid PL quenching in the mixed sample with respect to the pure QDs. Similar effects observed in sample (F) are expected to be present in sample (E) which contains less concentration of the plasmonic nano-resonators.

8.7 Pump-Probe Rayleigh Scattering Experiments

Steady-state fluorescence spectroscopy accompanied by time-resolved spectroscopy results confirmed the occurrence of the nonradiative energy transfer process from fluorescent QDs to plasmonic Au NPs in both hybrid systems of (E) and (F). However, in order to complete the systematic study of the prepared hybrid systems in the direction of optical loss mitigation purposes, simultaneous enhancement of Rayleigh scattering and optical transmittance of hybrid systems must be observed. The pump-probe experimental setup explained in section 5-4 of chapter 5 has been applied to perform those opto-physical characterizations. Figure 8-7 illustrates the achieved results of the Rayleigh scattering and optical transmission of probe beam at 532 nm as a function of the impinging pump energy (λ=355 nm) for both composite systems of (E) and (F).

The obtained results for optical transmission signal show that after providing certain value of the pump energy the transmittance of both systems starts to increase. However, as it is evident from Figure 8-7(a) at higher energy of the pumped pulses the transmission of sample (E) undergoes to reduction. The dropping of the transmitted signal for that sample can be ascribed by photo-bleaching phenomenon which can happen for chromophore in high energy values of the incident light [10]. Take into account that the aggregation of QDs are presented within PDMS matrix which can emphasize the possibility for occurrence of such phenomenon. On the hand, respect to the hybrid systems in solution, in a bulk composite system, the chromophore cannot move freely in dispersed environment, and continuously only a particular portion of chromophores are irradiated by impinging pulses. Hence, pump-probe experiments for bulk samples should be performed by considering some more practical points as compared to the hybrid systems in solution. Therefore, to avoid the occurrence of photo-bleaching processes for the QDs of sample (F), the impinging energy of incident pulses are limited to a particular value (Figure 8-7(c)). Consequently, the enhancement of the optical transmission signal for both hybrid

systems with less and more concentration of Au NPs can be observed. Such enhancement is the signature of the improvement in the optical transparency of the system.

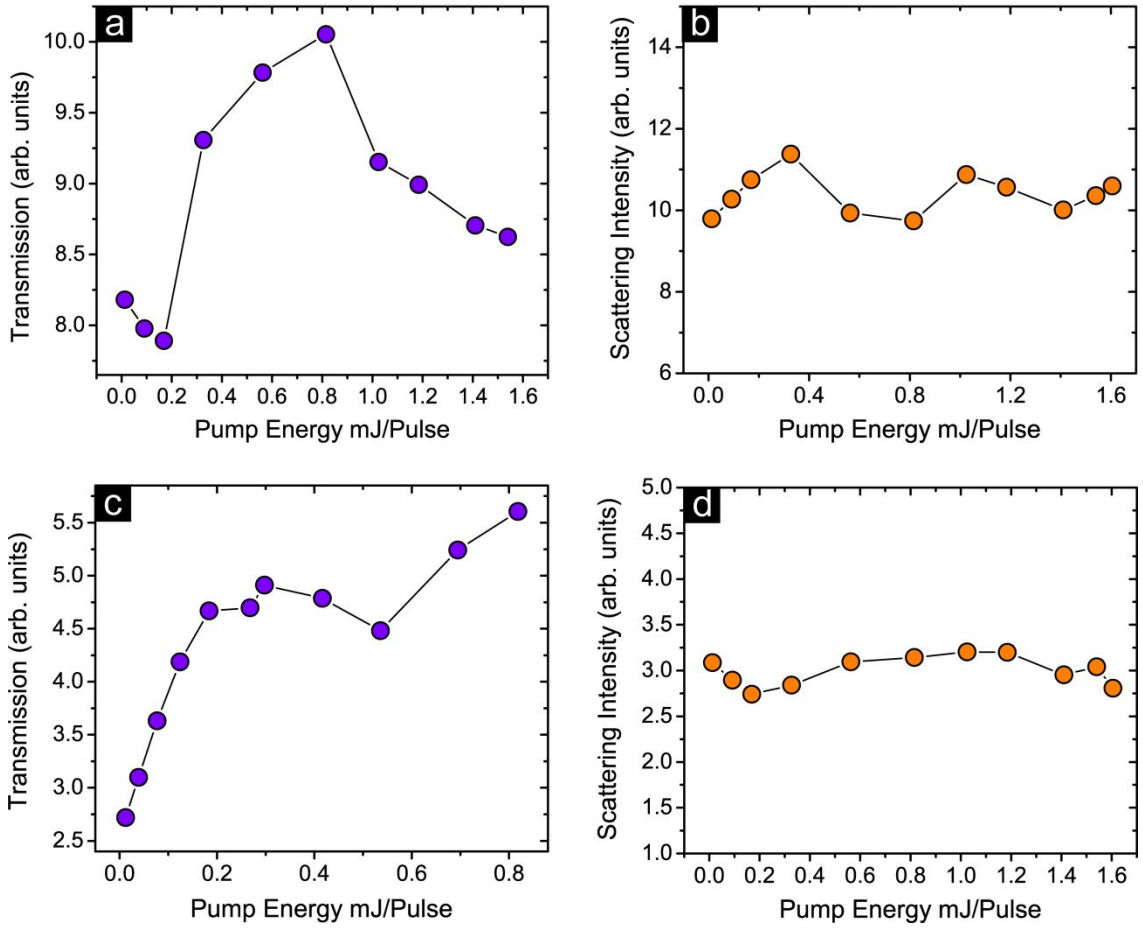

Figure 8-7 Rayleigh scattering and transmission signals of the (a and b) QDs+Au NPs with less concentration of NPs (sample (E)) and (c and d) QDs+Au NPs with more concentration of NPs (sample (F)). The normalized transmission signal of a probe beam at λ = 532 nm for **(a)** sample (E) and for **(c)** sample (F) as a function of pump energy (λ = 355 nm). Normalized Rayleigh scattering of a probe beam as a function of pump energy acquired at 532 nm for **(b)** sample (E) and for **(d)** sample (F).

Furthermore, the recorded signal for the scattering of the probe beam from both sample (E) and (F) are demonstrated in Figure 8-7(b) and (d), respectively. These graphs illustrate by increasing the energy of the impinging pump beam, the scattering signal from both composite system are remained almost unaffected. The observed optical feature of both samples can be ascribed by the geometry of the sample in macro scale, which obligates to not consider the scattered signal in elastic regime to obtain Rayleigh scattering. However, the presence of constant values of scattering in particular in resonance band in combination with the observed enhancement in transparency of both systems are convincing evidences for optical loss

mitigation in both sample (E) and (F). This claim can be explained more evidently by the following expression.

$$A\downarrow + Sc\,(cte) + Tr\uparrow = I_0\ (cte) \qquad (8-7)$$

In fact, due to the constant intensity of the incident light and by considering the constant value of the scattered signal, the enhancement of the transmission can be occurred if only the absorption of the corresponding hybrid system is diminished.

8.8 Extinction Band Enhancement

Beside the target of achieving a loss compensated macro-scaled hybrid system which has been followed in this research study, an interesting phenomenon has been observed in the case of sample (F). In fact, a strong absorbance enhancement of core-shell QDs incorporated in the PDMS matrix in the presence of resonant plasmonic Au NPs has been recorded. In this section, the occurrence of this phenomenon in sample (F) and the physical explanations behind such process are investigated.

The optical study for such process was performed by primarily investigating the spectroscopic dispersion of pure QDs and Au NPs, dissolved in a PDMS matrix, respectively. The extinction band of pure QDs in PDMS presents the typical behavior of a bare QDs (sample (D)), with a relative maximum around 568 nm (solid black line in Figure 8-8). The red-shifting of the absorption peak with respect to what measured in solution (Figure 8-1, blue dotted line) can be attributed to both an electronic reorganization of the QD energy levels, when dispersed in a different host environment, and the presence of aggregation states of the QDs inside of the PDMS matrix [11]. In Figure 8-8 the blue dotted line represents the extinction band of Au NPs with higher concentration in PDMS (sample (C)). The two pictures on the right side show the actual transparency of the two self-standing PDMS based composite films (incorporating Au NPs (C) and QDs (D)) obtained by acquiring an image of an “A” letter written on a white sheet of paper. The mathematical sum of the two extinction curves (i.e. sample (C) and sample (D)), represented by the dashed-dotted green line (and relative picture (C)+(D)), coincided with the spectrum obtained by physically overlapping the two PDMS samples. Instead, the measured extinction spectrum of the PDMS composite film, simultaneously containing QDs and Au NPs (sample (F)), at the same concentration of the samples (C) and (D), is depicted by the dashed red line in Figure 8-8.

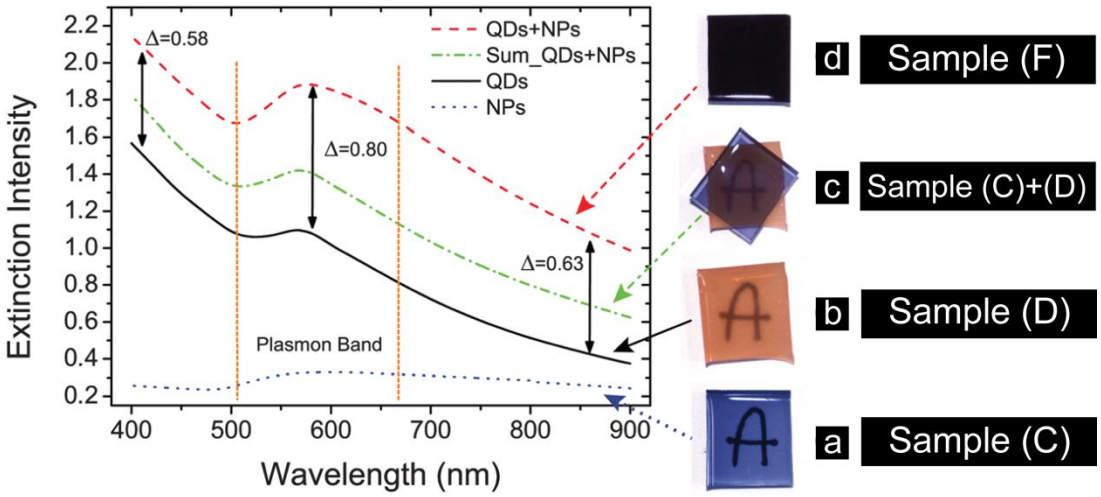

Figure 8-8 Extinction curves for QDs embedded in sample (D) (black solid line), Au NPs of sample (C) (dotted blue line) and the mixed sample (F) (dashed red line) in the PDMS matrix. The mixed sample presents an extinction curve that is much higher than the mathematical summation of the two separated curves (dashed-dotted green line). The images (a) – (d) refer to pictures of the real plastic matrices over an "A" written on a white paper. **(a)** Sample (C) Au NP based reference sample, **(b)** QD based reference sample, **(c)** overlap between (C) and (D), and **(d)** QD + Au NP based hybrid system.

Strikingly, in the presence of both nano-objects, the extinction curve differs from the bare mathematic sum. In particular, a distinct enhancement of the extinction curve with respect to the addition of the two curves corresponding to the two components is observed. Such an enhancement appears stronger in the overlapping region between the emission band of QDs and the Au NP plasmon band. Thus experimental investigation reported in Figure 8-8 evidenced a strong absorbance enhancement of QDs embedded in the plastic matrix in the presence of resonant plasmonic Au NPs. Indeed the effective overlap between the fluorescence emission of QDs and the Au NP plasmonic band (see Figure 8-1(d)) can create a strong resonance between the two systems, causing the occurrence of a modified local field that is able to interact with QDs and modify both their absorption and emission properties. From a quantitative point of view, whereas the mathematical sum presents an increase of about 22% inside the plasmon region (delimited by the orange vertical dashed lines), the observed increase became higher than 38% in the case of the mixed sample (F).

Picture (d) clearly shows how difficult it is to distinguish the letter "A" across this sample. Experimental evidence of a similar phenomenon observed in the case of organic dyes in the presence of Au NPs was already presented by Lawandy in 2005 [12]. Now it is crucial to distinguish, in the extinction spectrum, the contribution of scattering and absorption, respectively, and to verify whether the presence of plasmonic field due to Au NPs can affect the absorption cross section of QDs. For this reason, the absorption of QDs in the absence and

presence of Au NPs embedded in the PDMS matrix was measured by means of a 102mm-diameter integrating sphere. The absorbance value A was measured at each value of the wavelength in the 310–580 nm range by means of equation (5-9) reported in the chapter 5, section 5.3.3, and refers to the emitting species only, i.e. the QDs, excluding the NP scatter contribution(see Figure 8-9).

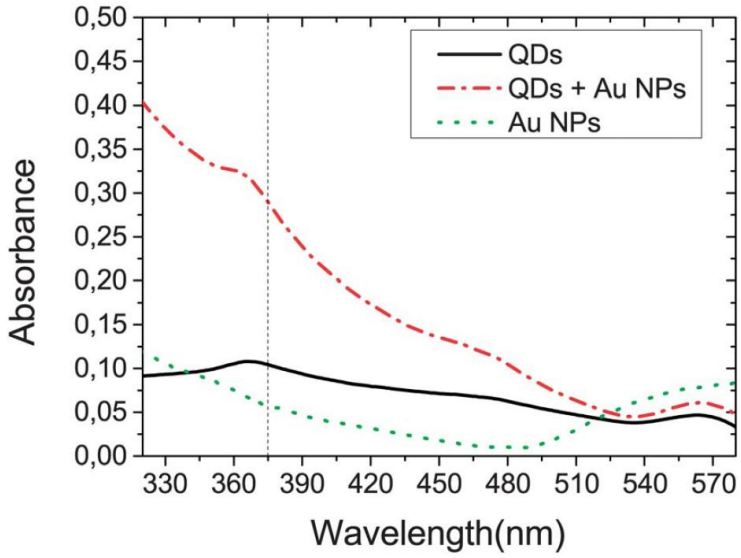

Figure 8-9 Absorption spectra of the PDMS samples recorded by means of an integrating sphere (black line QDs, red dashed-dotted QDs + Au NPs in sample (F)). Green dots refer to the Au NPs in PDMS (sample (C)).

Whereas QDs in PDMS show an absorbance of only 0.10 at 375 nm (i.e. the exciting wavelength of the QDs), a mixed sample of QDs and Au NPs presents a threefold increasing absorbance (0.27), which clearly gives evidence of the strong plasmonic field present in the vicinity of QDs, effectively modifying their absorption cross-section. In the same figure it is reported the absorbance of Au NPs in PDMS (green dots), determined by following the criterion explained in chapter 5, section 5.2.2.

It is clearly seen that the red dashed-dotted curve (QDs + Au NPs) is lower than the green dotted one (Au NPs only) right in the plasmon band. This is due to the strong cross talking present between the Au NP plasmonic resonance and QD absorption cross-section, which causes a feedback interaction between the two species. By taking into account that the increased concentration of Au NPs in sample (F) with respect to sample (E) can induce an aggregation of Au NPs, the EBE of sample (F) could be caused both by an enhanced scattering from those aggregated Au NPs, and as well as by a nonradiative coupling between the two components.

8.9 QDs and NPs Synthesis processes and Fabrication of PDMS Based Composite Films

8.9.1 Synthesis of CdS@ZnS QDs

Monodispersed CdSe nanocrystals (NCs) were synthesized by the injection of a solution of Se dissolved in TBP into a hot solution of CdO, OLEA, HDA, and of trioctylphosphine oxide (TOPO). Subsequently, the rapid cooling of the flask generates CdSe NCs of about 3 nm in size with the first absorption peak around 560–570 nm [13]. The CdSe NCs were purified by repeated centrifugation, after precipitation with methanol, and re-dissolution in chloroform. The NC concentration was evaluated by absorbance spectra calculating the extinction coefficient as reported elsewhere [4]. The ZnS shell was grown on the CdSe NC surface by means of a dropwise injection of a ZnS precursor stock solution into a hot mixture of pre-synthesized CdSe NCs dissolved in TOPO–TOP (trioctylphosphine) coordinating agents [14]. Finally, the solution was cooled at room temperature and the resulting highly luminescent CdSe@ZnS QDs were isolated and purified by centrifugation after precipitation with methanol, and finally dissolved in chloroform.

8.9.2 Synthesis of OA Capped Au NPs

Spherical Au NPs were prepared by the injection of a solution of $HAuC_{l4}.3H_2O$ dissolved in OA into a refluxing solution of OA and toluene [13]. The particle growth was carried out at 110 °C over the course of 120 min. The Au NPs, collected and purified with methanol from unreacted precursors, were finally dispersed in hexane. The NP concentration was evaluated by absorbance spectra calculating the extinction coefficient according the approach reported by X. Liu *et al*. [15]. The average size of Au NPs was measured from TEM investigation to be 11 nm.

8.9.3 Preparation of PDMS Based Composite Films

The elastomer was mixed thoroughly with the curing agent in the weight ratio of 10:1 and then degassed under vacuum to remove entrapped air bubbles. The pre-polymer mixtures were prepared by preliminarily mixing PDMS oligomers and curing agents, and allowing the cross linking reaction, based on vinyl end capped siloxane oligomers reacting with the dimethylmethylhydrogen siloxane curing agent by platinum catalyzed hydrosilation, to take place. Both the TOPO capped QD and the OA-capped Au NP hexane solutions (100 mL) were dispersed in the pre-polymer mixture (2 g) and vigorously stirred for 1h to obtain a homogeneous mixture. In particular, composite systems were obtained by adding the appropriate volume of QDs and Au NPs to the PDMS pre-polymer matrix. The reference samples were also prepared,

namely PDMS incorporating 1×10^{-6} M (sample (B)) and 3×10^{-6} M (sample (C)) of Au NPs and 6×10^{-5} M of QDs (sample (D)), respectively. The resulting mixtures were cast into a support template (2. cm × 2.5 cm) and the films were cured at 70 °C for 24 h to obtain ca. 3 mm thick self-standing films. Sketches of the nano-composite fabrication strategies and pictures of the resulting films are reported in Figure 8-10.

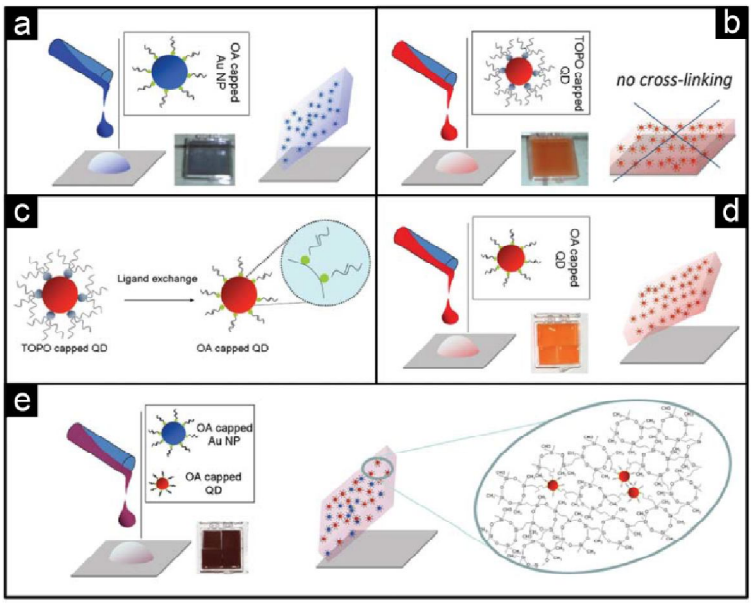

Figure 8-10 Sketches of the fabrication of the **(a)** composite films based on PDMS and Au NPs, **(b)** as-synthesized QDs **(c)** ligand-exchanged **(d)** composite films based on PDMS and **(e)** CdSe@ZnS QDs and the mixture of Au NPs and QDs, respectively. Pictures of the final freestanding films are also reported.

It should be noted that, after the addition of Au NPs into the PDMS, the dark-red color characteristic of the spherical Au NP solutions turned light violet, a color which was retained in the final solid films. Such a change in color can be explained by taking into account both the variation of the local dielectric constant of the medium surrounding the NPs, clearly different moving from hexane to the PDMS matrix, and their possible micro-aggregation in the polymer matrix (Figure 8-10(a)). Remarkably, a different behavior was obtained for the "as-synthesized" TOPO-capped QDs. In fact, when the TOPO-capped QD solution was incorporated into the PDMS pre-polymer mixture, inhibition of the cross-linking of the elastomer was observed. Such a behavior resulted in a QD–PDMS material which remains fluid and opaque even upon prolonged thermal treatment, preventing the fabrication of free-standing films (Figure 8-10(b)). As the OA-capped Au NPs were successfully incorporated in PDMS providing a curable composite film, a change in the QD surface chemistry was thought to be a possible method to overcome the observed crosslinking inhibition. Therefore a ligand exchange reaction was

performed to replace the pristine TOPO molecules coordinating the QD surface with OA, keeping unchanged the QD optical properties (Figure 8-10(d)). Subsequently OA-capped QDs were incorporated into the PDMS matrix, under the same standard experimental conditions used for the fabrication of Au NP composite films. Interestingly the change of QD surface chemistry resulted in an effective dispersion of the QDs into the polymer host matrix, which was effectively cross-linked, resulting in clear PDMS based bright orange films (Figure 8-10(d)).

The presence of a double bond in the aliphatic chain of OA, which was used as a pristine capping agent for Au NPs and as a new ligand in the surface-exchanged QDs, does not inhibit the crosslinking process. Therefore the presence of OA-capped nano-objects, far from being detrimental, appears even advantageous, as the ligand internal unsaturation could participate in the successful PDMS curing process, promoting cross-linking, and ultimately enabling NP and QD incorporation into the polymer. Looking at the morphology of the obtained composites, it can be seen how the proposed process, although allowing a quite uniform dispersion of the NPs and QDs in the PDMS. However, as macroscopically detected by the optical transparency of the obtained composite films, the formation of micro-aggregates of nano-objects could not be completely prevented, which finally affecting short range interactions among the NPs and QDs, and, hence, the related optical properties [16]. In fact this issue was overcome neither with the alternative routes proposed by Shojaei-Zadeh *et al.* that also reported a tendency for aggregation of the NPs in the matrix [11].

All the samples were prepared and synthesized by chemist collaborators in CNR IPCF UOS, University of Bari, Italy [17].

REFERENCES

1. D. I. Uhlenhaut, P. Smith, and W. Caseri, *Adv. Mater.*, **2006**, 18, 1653.
2. I. Pastoriza-Santos, J. Perez-Juste, G. Kickelbick, and L. M. Liz-Marzan, *J. Nanosci. Nanotechnol*., **2006**, 6, 414.
3. M. A. Hines, and P. Guyot-Sionnest, *J. Phys. Chem.*, **1996**, 100, 468.
4. W. W. Yu, L. Qu, W. Guo, and X. Peng, *Chem. Mater*., **2003**, 15, 2854.
5. S. Shankara Narayanan, and Samir Kumar Pal**.** *J. Phys. Chem. B*, **2006**, 110, 24403.
6. A. A. Salman, A. Tortschanoff, G. van der Zwan, F. van Mourik, and M. Chergui, *Chem. Phys*., **2009**, 357, 96.
7. M. Jones, S. S. Lo, and G.D. Scholes, *Proc.Natl. Acad. Sci.U. S. A.*, **2009**, 106, 3011.
8. N. Reitinger, A. Hohenau, S. Kstler, J. R. Krenn ,and A. Leitner, *Phys. Status Solidi A*, **2011**, 208, 710.
9. V. K. Komarala, Y. P. Rakovich, A. L. Bradley, S. J. Byrne, Y. K. Gunko, N. Gaponik, and A. Eychmüller, *Appl. Phys. Lett.*, **2006**, 89, 253118.
10. W. G. J. H. M. van Sark, *et al., J. Phys. Chem. B*, **2001**, 35, 8281.
11. S. Shojaei-Zadeh, J. F. Morris, A. Couzis, and C. Maldarelli, *J. Colloid Interface Sci*., **2011**, 363, 25.
12. N. M. Lawandy, *Proc. SPIE*, **2005**, 59240, 59240G.
13. H. Hiramatsu, and F. E. Osterloh, *Chem. Mater*., **2004**, 16, 2509.
14. P. Reiss, J. Bleuse, and A. Pron, *Nano Lett*., **2002**, 2, 781.
15. X. Liu, M. Atwater, J. Wang, and Q. Huo, *Colloids Surf. B*, **2007**, 58, 3.
16. Y. Liu, E. N. Mills, and R. J. Composto, *J. Mater. Chem.*, **2009**, 19, 2704.
17. A. De Luca, N. Depalo, E. Fanizza, M. Striccoli, M. L. Curri, M. Infusino, A. R. Rashed, M. La Deda, and G. Strangiea, *Nanosc.*, **2013**, 5, 6097.

Conclusions

The final goal of this research study was to provide an efficient solution for mitigating the absorptive losses of plasmonic nanostructures to improve their optical properties for optical metamaterial applications. The performed studies on resonance energy transfer processes among chromophore-chromophore and chromophore-plasmon pairs have paved the path to apply such effects in the direction of loss compensation purposes. In fact, transferring energy by nonradiative pathways over absorptive metallic components could be an effective method to overcome the absorptive nature of plasmonic NPs. However, in order to investigate applicability of such solution, an organized experimental investigation has been performed over all synthesized samples to explore their optical properties as optical loss compensated structures. With the presence of the spectral overlap between absorption band of plasmonic structures and emission spectrum of gain material, the experimentally observations such as quenched emission of gain material in close vicinity of plasmonic NPs by means of steady-state experiments and their reduced emission lifetime observed by applying time-resolved fluorescence spectroscopy have provided evidences for energy transfer processes among active chromophores and absorptive plasmonic objects. However, the key experiments have been performed by using Rayleigh scattering experimental setups in which simultaneous enhancement of Rayleigh scattering and optical transmission could reveal striking absorptive losses mitigation effects.

The strategy that has been followed regarding the fabricated samples by chemist collaborators was passing through three different spatial stages from nano to macro scales. In this regards, three different nano-scaled solution based hybrid system have been studied. First of all, Gain-assisted system which is the solution of plasmonic NPs with proper concentration of gain materials such as dye molecules has been investigated. The step by step performed experimental study has provided convincing evidences concerning mitigation of optical loss of NPs in the presence of active materials. In the second step, dye molecules have been encapsulated within

silica shell of NPs to provide a new nano-scaled system well-known as Gain-functionalized system. The controlled interparticle distance and concentration of gain elements in such structure have been provided more efficient optical loss mitigation results as compared to gain-assisted system. In the third step of nano-scaled spatial stage, multimeric nanostructures have been synthesized by attaching the single NPs to each other. The performed experimental results demonstrate that shorter gaps between plasmonic resonators and adjacent fluorescent molecules lead to more efficient nonradiative RET processes from donor molecules to acceptors. Furthermore, these systematic investigations show that the constructive interferences occurring between local fields in multimer nanostructures can improve the efficiency of the coherent coupling between gain materials and metal absorbers. The obtained simulation results have been confirmed the presence of much strong electrical local field of multimers as result of plasmonic hybridization effect within constituent NPs of a multimeric structure.

After acquiring successful results from nano-scaled hybrid systems, we could pave confidence to explore loss compensations effects in meso-scaled systems. Plasmonic nanoshells dispersed in ethanol as an example of this spatial stage have been investigated by means of the mentioned systematic experimental study. Such structures which have been composed of a dye doped silica core in the heart of gold shell have showed some interesting optical properties presence, resulting from plasmonic hybridization effects due to the interacting sphere and cavity plasmons of this structure. Modification of lifetime and enhanced transmission in particular wavelength range were convincing regarding the presence of meso-scaled optical loss mitigated structure.

The final spatial stage which has been followed in this research study was in macro-scale range. In fact, the intention of this stage was to fabricate a bulk sample as a real example of optical loss mitigated system for practical applications. Concerning this matter, the emissive QDs have been incorporated within PDMS flexible host in presence of two different concentrations of plasmonic NPs. The performed systematic investigations over these hybrid systems revealed the successful achievement regarding a macro-scaled absorptive losses mitigated systems. However, we have been observed that the energy transfer process almost have been occurred with the same rate in both systems, revealing the necessity for concerning a proper concentration of gain elements with respect to the amount of absorptive NPs.

In short, the observed experimental evidences imply this fact that at operative frequencies of resonant plasmonic nanostructures, where fascinating optical metamaterials properties are expected, optical loss can be reduced and controlled by placing gain units right at the heart of the nanostructure enabling extraordinary meta-properties of designed artificial materials. Thus, in the framework of bottom-up systems approach based on plasmonic materials this would represent a relevant step forward towards real applications of plasmonic metamaterials at optical frequencies.